CONTINUUM-BASED MULTISCALE COMPUTATIONAL DAMAGE MODELING OF CEMENTITIOUS COMPOSITES

A Dissertation

by

SUN-MYUNG KIM

Submitted to the Office of Graduate Studies of
Texas A&M University
in partial fulfillment of the requirements for the degree of

DOCTOR OF PHILOSOPHY

May 2010

Major Subject: Civil Engineering

CONTINUUM-BASED MULTISCALE COMPUTATIONAL DAMAGE MODELING OF CEMENTITIOUS COMPOSITES

A Dissertation

by

SUN-MYUNG KIM

Submitted to the Office of Graduate Studies of
Texas A&M University
in partial fulfillment of the requirements for the degree of

DOCTOR OF PHILOSOPHY

Approved by:

Chair of Committee,	Rashid K. Abu Al-Rub
Committee Members,	Eyad Masad
	Zachary Grasley
	Anastasia Muliana
Head of Department,	John Niedzwecki

May 2010

Major Subject: Civil Engineering

ABSTRACT

Continuum-based Multiscale Computational Damage Modeling of

Cementitious Composites.

(May 2010)

Sun-Myung Kim, B.En., Sejong University; M.En., Sejong University

Chair of Advisory Committee: Dr. Rashid K. Abu Al-Rub

Based on continuum damage mechanics (CDM), an isotropic and anisotropic damage model coupled with a novel plasticity model for plain concrete is proposed in this research. Two different damage evolution laws for both tension and compression are formulated for a more accurate prediction of the plain concrete behavior. In order to derive the constitutive equations, the strain equivalence hypothesis is adopted. The proposed constitutive model has been shown to satisfy the thermodynamics requirements, and detailed numerical algorithms are developed for the Finite Element implementation of the proposed model. Moreover, the numerical algorithm is coded using the user subroutine UMAT and then implemented in the commercial finite element analysis program Abaqus, and the overall performance of the proposed model is verified by comparing the model predictions to various experimental data on macroscopic level.

Using the proposed coupled plasticity-damage constitutive model, the effect of the micromechanical properties of concrete, such as aggregate shape, distribution, and volume fraction, the ITZ thickness, and the strength of the ITZ and mortar matrix on the

tensile behavior of concrete is investigated on 2-D and 3-D meso-scale. As a result of simulation, the tensile strength and thickness of the ITZ is the most important factor that control the global strength and behavior of concrete, and the aggregate shape and volume fraction has somewhat effect on the tensile behavior of concrete while the effect of the aggregate distribution is negligible. Furthermore, using the proposed constitutive model, the pull-out analysis of the single straight and curved CNT embedded in cement matrix is carried out. In consequence of the analysis, the interfacial fracture energy is the key parameter governing the CNT pull-out strength and ductility at bonding stage, and the Young's modulus of the CNT has also great effect on the pull-out behavior of the straight CNT. In case of the single curved CNT, while the ultimate pull-out force of the curved CNT at sliding stage is governed by the initial sliding force when preexisting normal force is relatively high, the ultimate pull-out force, when the preexisting normal force is not significant, is increased linearly proportional to the curvature and the Young's modulus of the CNT due to the additionally induced normal force by the bending stiffness of the curved CNT.

DEDICATION

To my beloved wife, Hyunjung and daughter, Hannah

ACKNOWLEDGEMENTS

First and foremost, I would like to warmly express sincere appreciation to my advisor, Professor Rashid K. Abu Al-Rub, for his continuous support, invaluable advice, and warm encouragement throughout the course of this research. Without his instruction, passion, time and patience, this work would never have been accomplished. I thank him sincerely for being a true mentor and a good friend.

Special appreciation is extended to my dissertation committee members, Professor Eyad Masad, Professor Zachary Grasley, and Professor Anastasia Muliana for many valuable comments and their time and effort in evaluating my dissertation.

Additionally, I would like to thank my parents and parents-in-law for their love, support, and encouragement. Especially, my beloved daughter who was born in hot summer of 2009, Hannah, is the delight of my life. Last but not least, I would like to say to my wife, Hyunjung, thanks, sorry, and love you.

TABLE OF CONTENTS

CHAPTER Page

LIST OF FIGURES

FIGURE Page

FIGURE Page

FIGURE Page

FIGURE Page

FIGURE Page

FIGURE Page

FIGURE Page

LIST OF TABLES

CHAPTER I

INTRODUCTION

1.1 Problem Statement

Concrete is a widely used material in numerous civil engineering structures due to the capability to be cast in site and the flexibility in different shapes. Although concrete material has longer history than other construction materials, such as steel and fiber reinforced polymer (FRP), the accurate understanding of its mechanical behavior under complex loading paths still represents a challenging task mainly due to its material characteristic. That is, concrete is not homogeneous material composed of entirely one material but heterogeneous composite material made of several distinctive components, such as coarse and fine aggregates, cement, water, and chemical admixture if necessary. Furthermore, it is well known that the failure of modern concrete structures is mainly caused by the material damage rather than the inadequate structural design. Therefore, it is crucial to understand the relationship among stress, material damage, stiffness reduction, and fracture at macro-scale, the role of each components, such as mortar matrix, aggregates, and interfacial transition zone (ITZ) and interaction among components at meso-scale, and the interaction between reinforcements, such as fiber and carbon nanotubes (CNTs) and mortar matrix or the ITZ at nano scale in order to predict more precisely the behavior of cementitious material and structures under various loading conditions.

This dissertation follows style of the *ASCE Journal of Engineering Mechanics.*

One of the most important characteristics of concrete is its low tensile strength compared to the compressive strength. The low strength for tension causes micro tensile cracks in material at the very low stress state, and governs dominantly global strength and behavior of concrete material or structures. Therefore, the accurate modeling of damage evolutions and crack propagations in concrete is very crucial. Two distinct mechanical processes: plasticity (slippage along grain boundaries, etc) and damage (micro-cracks and voids, crack nucleation and coalescence, and grain boundary cracks) can be attributed to the non-linear behavior of concrete. Therefore, theses two degradation processes should be considered simultaneously in order to account for the distinctive behavior of concrete for tension and compression, and it is important to develop a robust constitutive and computational model that can effectively describe the micro-crack nucleation and growth in plain concrete that lead to stiffness degradation of material and irreversible (plastic) deformations.

Concrete, based on the theory of micromechanics, can be considered as a three-phase composite material consisting of mortar matrix, aggregate, and the ITZ between the aggregate and mortar matrix. Among three constituents, the ITZ is the weakest region, and the weakness of the ITZ under loading, since the global strength of concrete is governed by the strength of the weakest region, is the main reason of the low tensile strength of concrete. Therefore, the clear comprehension of the characteristics and behavior of the ITZ under loading should be preceded in order to understand and predict the behavior of concrete as a composite material. Moreover, the micromechanical properties of concrete such as, the Young's modulus and yield strength of matrix,

aggregates, and the ITZ, aggregate shape, distribution, and volume fraction, and the thickness of the ITZ have great effect on the strength and behavior of concrete. However, it is impossible to investigate the effect of the micromechanical properties on concrete in macro-scale that concrete is considered as homogeneous material. Therefore, concrete should be considered as a composite material in the analysis to study the micromechanical properties effect, and mesoscopic level analysis is the most practical and useful method for evaluating a composite behavior of concrete.

Since concrete was used for the construction material, numerous experimental, analytical, and numerical researches have been developing the properties of concrete itself, such as stiffness, strength, and ductility. Generally, concrete is weak in tension, no matter how stronger concrete is, and this characteristic of plain concrete causes sudden collapse of structure after yielding. Therefore, a steel reinforcing bar is embedded in concrete in order to enhance the load resistance capacity against tension, and the reinforced concrete with steel rebar became the most successful concept in the history of construction. Even though the reinforcement of concrete with rebar increases the loading capacity of concrete members dramatically, however, concrete itself still has low tensile strength and shows a brittle behavior under tension. With this reason, numerous researches have been carried out from a few decades ago in order to control the properties of concrete itself, such as strength, ductility, fracture toughness, shrinkage, and impact resistance through adding special ingredients, such as meso and micro fibers in the cement matrix (Gopalaratnam and Gettu 1995; Zollo 1997; Nataraja *et al.* 1999). More recently, the enhancement of material properties of the cement matrix through

integration of nano fibers and filaments as reinforcements has become an active area of research. With these outstanding material properties, CNTs can be used for more effective reinforcement of cement matrix than any other conventional fibers by providing large interfacial contact area with mortar matrix. Thus, it is very important and strongly needed to investigate the pull-out process of CNTs embedded in matrix, the bridging effect of CNTs at crack surfaces, and the failure mechanism of the CNTs reinforced composites analytically in nano-scale which cannot be understood clearly by experimental tests in order to improve the properties of cement matrix.

In this research, on the basis of phenomenological observation that the damaged stiffness varies nonlinearly by the change of the damage density as argued by Cicekli et al. (2007), the modified constitutive model based on the coupled anisotropic damage and plasticity model is proposed. Two different damage evolution laws for both tension and compression are proposed and examined for a more accurate prediction of concrete behavior. Furthermore, in order to validate and demonstrate the capability of the proposed model and calibrated material constants, analysis results obtained with the proposed model are compared with experimental results at macroscopic level. And then, the proposed coupled plasticity-damage model for plain concrete is adopted for the meso-scale analysis of concrete. Considering concrete as a three-phase composite material considering of mortar matrix, aggregates, and the ITZ, the proposed constitutive model is applied to each phase with different material constants. The effect of the micromechanical properties of concrete, such as aggregate shape, distribution, and volume fraction, the Young's modulus and strength of each constituent, and the ITZ

thickness on the behavior of concrete under tensile loading is investigated in mesoscopic level. Lastly, the reinforcing effect of cementitious material with straight and curved single CNT, as a preliminary study of the macromechanical behavior of the CNTs reinforced cementitious material, is investigated analytically.

1.2 Background

In order to clarify the aim of this research, limited literatures related to the constitutive model for plain concrete, macro- and meso-scale analysis of concrete, and the CNTs/ cement matrix composite material are reviewed.

1.2.1 Constitutive Model for Plain Concrete

The idealized stress-strain diagram of material under the uniaxial compression is illustrated in Figure 1.1. During an ideal plastic deformation, the slop of the unloading path is not changed, and identical to the initial Young's modulus, E_0 of the material as seen in Figure 1.1(a). However, a perfectly brittle material, as shown in Figure 1.1(b), returns to the origin point upon unloading, and there exists no residual strain due to the continuous change of the internal microstructure with the nucleation and growth of micro cracks ($E_1 < E_0$). On the other hand, a general cementitious material displays both residual strain due to partial plastic deformation and the reduced Young's modulus due to the evolution of micro cracks ($E_1 < E_2 < E_0$), and Figure 1.1(c) represents loading-unloading path for concrete observed experimentally.

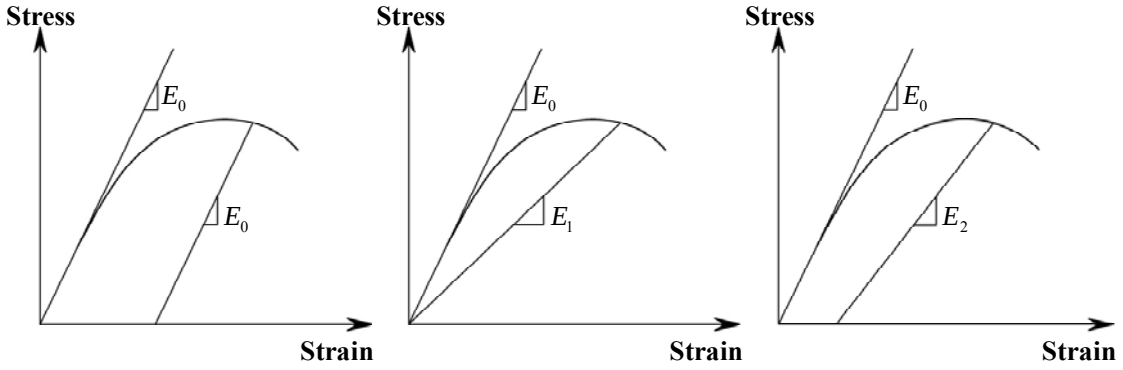

(a) (b) (c)

Figure 1.1 Schematic representation of material behavior: (a) Ideal plastic deformation, (b) perfectly brittle behavior, and (c) combined plastic and brittle behavior of concrete

Additional to the combined behavior of concrete upon unloading and reloading, concrete shows distinctive behavior for tension and compression, and the representation of the characteristics of concrete is one of the most important and critical issues in the field of analytical research. Many theories have been introduced in order to predict the behavior of cementitious material, and the theories that have been commonly used for the description of concrete constitutive behavior are plasticity, continuum damage mechanics, fracture mechanics, elastic-damage, and combined plasticity and damage mechanics. The mathematical theory of plasticity is thoroughly established and some of these works were far superior to elastic approaches. These works, however, failed to address the degradation of the material stiffness due to micro-cracking as seen in Figure 1.1(a) (Chen and Chen 1975; Bazant 1978; Voyiadjis and Abu-Lebdeh 1994; Feenstra and De Borst 1996; Grassl *et al.* 2002). Fracture mechanics (FM) has also been widely used to predict the behavior of concrete, especially to study how cracks form and the existing cracks propagate through materials. However, the facture mechanics approach

requires an initially defined or modeled crack, and this approach failed to describe the nucleation of numerous micro-cracks and the growth of the micro-cracks to macro-cracks (Bažant and Oh 1983; Jenq and Shah 1985; Planas and Elices 1991). Continuum damage mechanics (CDM) (Kachanov 1958; Lemaitre 1985; Lemaitre and Chaboche 1990) has also been used alone with elasticity to model the material nonlinear behavior of concrete. However, several facets of concrete behavior, such as irreversible deformations and inelastic volumetric expansion in compression cannot be described by this approach (Løland 1980; Ortiz and Popov 1982; Krajcinovic 1984; Krajcinovic 1985; Simo and Ju 1987a, 1987b; Mazars and Pijaudier-Cabot 1989). Therefore, since both micro-cracking and irreversible deformations are contributing to the nonlinear response of concrete, a constitutive model should address simultaneously the two physically distinct modes of irreversible changes in order to simulate the concrete nonlinear behavior properly up to fracture.

Combinations of plasticity and damage are usually based on isotropic hardening combined with either isotropic (scalar) or anisotropic (tensor) damage variables. One type of combination relies on stress-based plasticity formulated in the effective (undamaged) space (Simo and Ju 1987a, 1987b; Lee and Fenves 1998; Wu *et al.* 2006; Cicekli *et al.* 2007; Voyiadjis *et al.* 2008), where the effective stress is defined as the average micro-scale stress acting on the undamaged material between micro-defects. Another type is based on stress-based plasticity in the nominal (damaged) stress space (Bazant and Kim 1979; Ortiz 1985; Lubliner *et al.* 1989; Ananiev and Ožbolt 2004), where the nominal stress is defined as the macro-scale stress acting on both damaged

and undamaged material. However, it is shown by Abu Al-Rub and Voyiadjis(2003) that coupled plastic-damage models formulated in the effective space are numerically more stable and attractive. On the other hand, for better characterization of the concrete damage behavior, anisotropic damage effects, i.e. different micro-cracking in different directions, should be characterized (Ju 1990). However, anisotropic damage in concrete is complex and the coupling with plasticity and the application to structural analysis is not straightforward (Ju 1989; Ju 1990; Voyiadjis and Abu-Lebdeh 1994; Voyiadjis and Kattan 2006; Cicekli *et al.* 2007).

The model by Cicekli et al. (2007) is successfully used to predict the concrete distinct behavior in tension and compression. However, the model proposed by Cicekli et al. has few critical weaknesses. The model, unlike phenomenological observation, assumed the relation between the damaged stiffness and the damage density as linear. That is, they assumed that the decrease of the damage stiffness is directly proportional to the increase of the damage density. Moreover, the model couldn't predict the behavior of concrete material when both the global stress-strain relation and the loading-unloading paths on the stress-strain curve are considered, while showed good performance when only the global stress-strain relation is considered.

1.2.2 Macro-scale Analysis of Concrete

Since concrete is used for the construction material, the analytic study about concrete material and structures has been mainly focused on macroscopic level through the homogenization process of a heterogeneous cementitious material. This is because the analysis and modeling are less complicated than meso or smaller-scale analysis, and

computational cost can be reduced. Although the macroscopic level analysis is the most common analysis type, this scale analysis have critical weaknesses: (1) the stiffness reduction and the crack initiation are totally dependent on the stress level and distribution generated by the external or internal loads; (2) the crack paths are always perpendicular to the principal stress direction in case of plain concrete; and (3) it is not allowed to establish the microstructure-property relationship for designing better and superior fracture resistant cementitious materials. In spite of these weaknesses, the macro-scale analysis of concrete structures is the most widely used method because it is possible to get enough information with the macro-scale analysis alone for the prediction of the global response, such as displacement and deflection, the failure load, and the collapse mechanism of the structure. With these reasons, almost analytic researches of concrete structures have been focused on the macroscopic level even now.

1.2.3 Meso-scale Analysis of Concrete

In order to overcome the weakness of the concrete analysis at macro-scale and to verify the effect of each constituent on the behavior of concrete material and fracture process of structures, the mesoscopic level analysis considering concrete as a three-phase composite material consisting of mortar matrix, aggregate, and ITZ have been performed. Although the properties of the ITZ, which plays a very important role in the concrete fracture behavior, was not easy to be measured experimentally in the past, the recent advances in understanding the chemical composition, thickness, and strength of the ITZ as well as the developments in computational power made it possible to effectively simulate the micro-mechanical behavior of concrete materials at mesoscopic level in

order to get insights about the effect of various microstructure features (e.g. aggregate size, shape, gradation, and distribution, ITZ thickness, and etc).

The mesoscopic level analysis of concrete is the most practical and useful method for evaluating the composite behavior of concrete, and several numerical models have been proposed: (1) the random particle model (Bazant *et al.* 1990); (2) the random packing particle model (Fu and Dekelbab 2003); (3) the random two-dimensional natural shape aggregate model (Wittmann *et al.* 1985); (4) the lattice model (Schlangen and Garboczi 1997; van Mier 1997); and (5) the beam-particle model (Zhang *et al.* 2004). Currently, meso-scale analysis of cementitious material has been mainly focused on simulating the effect of aggregate shape and distribution, where randomly distributed circular particles are commonly used for the aggregate shape because it is practically very difficult to consider actual shape of the aggregate in every numerical simulation (Lilliu and van Mier 2007; Grassl and Rempling 2008). However, the arbitrary polygon shape and the elliptical shape aggregate model have also been used for more reasonable simulations by other researches (Kwan *et al.* 1999; Wang *et al.* 1999; Du and Sun 2007).

1.2.4 Nano-reinforced Cementitious Composites

The carbon nanotube (CNT), discovered by Iijima in 1991, is a nano-reinforcement, and has an extremely high specific strength and stiffness. The modulus of elasticity of the single walled CNT is approximately 1 TPa, yield strength varies generally from 20 to 60 GPa. Furthermore, the aspect ratio of the CNT could exceed 10^7, while the density is less than 1500 kg/m^3. With these specific material properties, the CNTs can be used as a more effective reinforcement of cement matrix than any other conventional fibers by

providing large interfacial contact area with the mortar matrix. While most attention has been paid to polymer based composite materials to date, CNT/cement composite material is recognized as a new area of research. Although it is beginning, a few experimental studies ascertain that the CNTs can strongly modify and reinforce the cement paste matrix with a variety of macro and nanoscopic observations. The CNTs increase the global strength, stiffness, and fracture toughness at macro-scale, delay crack opening due to the bridging effect of the CNTs at crack surfaces, and yield different crack patterns due to the CNT pull-out or breakage at nano-scale as observed by the scanning electron microscope (SEM) (Makar and Beaudoin 2003; Li *et al.* 2005; Makar *et al.* 2005; Li *et al.* 2007; Shah *et al.* 2009; Yazdanbakhsh *et al.* 2009; Konsta-Gdoutos *et al.* 2010). However, one cannot make sure of the failure mechanism or process of the CNTs embedded in the cement matrix at the crack surface through the experimental test. Therefore, one numerical analysis, recently, was conducted using the commercial finite element software ANSYS to investigate the effect of the interfacial and elastic properties of the CNT on the pull-out strength and ductility of cementitious composites (Chan and Andrawes 2009). The single CNT embedded representative volume element technique was employed. They revealed that the pull-out strength and ductility are proportional to the shear strength of the interface between the CNT and the cement matrix. They also concluded that the Young's modulus of the CNT is also a critical parameter that controls the pull-out behavior. A single CNT pull-out analysis could be a key to understand the load transfer mechanism between the CNT and cement matrix, and to determine the global properties of the CNT-based composite materials.

CNT pull-out process is composed of three stages - bonded, debonding, and sliding stage. In the bonded stage, the CNT and matrix are perfectly bonded, and the force and stress induced mainly by the crack opening and propagation on the matrix can be transferred entirely from the CNT to the matrix and vice versa. Besides, the initial pull-out strength of the CNT is governed by the interfacial characteristics between the CNT and the matrix at the bonded stage, the well-bonded stage, however, occupies infinitesimal pull-out displacement range compared to the whole pull-out displacement or the length of the CNT. In the second stage, called the debonding stage, the separation between the CNT and the matrix at interface of them begins to occur, and the debonded part coexists with the well-bonded part in this stage. Generally, the pull-out stiffness begins also to be decreased in the debonding stage, some amount of the pull-out force is charged to the interfacial friction force between the CNT and the matrix. Although the debonding stage occupies the wider pull-out displacement range than the bonded stage, this second stage is also relatively small compared to the total pull-out displacement. The last stage, so called sliding stage, is commenced as soon as the whole interface between the CNT and the matrix is fully damaged, and the friction force at interface resists the pull-out force of the CNT. Although the pull-out strength of the straight fiber or the straight CNT in the sliding stage is smaller than bonded or debonding stage, the fracture energy absorbed in the sliding stage is much higher than that in prior two stages, and almost the pull-out displacement lies in the sliding stage.

Considering the modeling techniques of a single CNT pull-out analysis, there are two types of models; the *discrete* model and the *continuum* model. In the *discrete* model,

such as the molecular dynamics, the individual carbon atoms are considered as particles, and the strength of the CNT is determined by the covalent bonds among the atoms. The nano-scale simulations using the *discrete* model have provided numerous data for understanding the behavior of the CNTs under various loading conditions (Yao *et al.* 2001; Frankland and Harik 2003; Mylvaganam and Zhang 2004; Chowdhury and Okabe 2007). The *discrete* model, however, is not a proper model for the conducting large scale simulations, such as the verification of the reinforcing effect of the CNT in the nanocomposite materials due to the difficulties in modeling and the computer power limitations. Therefore, the *continuum* model for the CNT was proposed about a decade ago such that the *continuum mechanics* approach has been successfully applied for the simulation of the CNT itself and the CNT/polymer composites considering the CNTs as beams, cylindrical shells or solids (Zhang *et al.* ; Sohlberg *et al.* 1998; Harik 2002; Li and Chou 2003; Odegard *et al.* 2003; Odegard 2007; Tserpes *et al.* 2008). Although the *continuum* models have some drawbacks due to the impossibility in predicting the size effect and the interactions between atoms, it is well known that the *continuum mechanics* approach is applicable if the global behaviors of the single CNTs or the CNT-based composite materials, such as the global strength and stiffness, deformations, and the failure mechanisms of the composite materials are of interest (Liu and Chen 2003). However, modeling the interfacial behavior between the CNT and the matrix using cohesive zone models allows one to incorporate intrinsic material length scales that can be used effectively to predict size-scale effects.

1.3 Research Objectives

The research includes five major objectives for the development, verification, and application of the coupled-plasticity-damage constitutive model for plain concrete and for the investigation of the behavior of the CNT reinforced cementitious composites.

- **Objective I: Development of robust constitutive and computational model for plain concrete**

It is needless to say that excellent constitutive model guarantees well prediction of material behavior. Especially, when the prediction of material failure is of interest, the need of the robust constitutive model and accurate modeling is greatly augmented. Although there are several constitutive models proposed to predict the behavior of concrete, all models have a little weakness. Therefore, based on continuum damage mechanics (CDM), an isotropic and anisotropic damage model coupled with a novel plasticity model is proposed in order to more effectively predict and simulate plain concrete fracture. Furthermore, detailed numerical algorithms are developed for the Finite Element implementation of the proposed coupled plasticity-damage model.

- **Object II: Identification of material parameters**

The application of the proposed model to the analysis of plain concrete needs identification of several material constants, such as tensile and compressive hardening modulus, h^+ and Q^-, tensile and compressive strength where uniaxial nonlinearity starts, $B^{\pm}$, compressive hardening rate constant, b^-, and constants for power tensile and

compressive damage evolution law, $q^{\pm}$. Once the yield strength of concrete is determined from monotonic or cyclic experimental tests, the cyclic loading-unloading uniaxial compressive stress-strain experimental curve should then be used in identifying unique values for the material constants listed above. Therefore, loading-unloading stress-strain data can be used to identify the material constants associated with the plasticity and damage constitutive equations simultaneously such that the reduction in Young's modulus can be used to identify the damage parameters. Once the damage law is calibrated, it can then be used to establish the effective stress-strain diagram which helps to identify the plasticity material constants in the effective configuration.

- **Object III: Verification of the proposed coupled plasticity-damage model in the macro-scale**

In order to investigate the predictive capability of the proposed model and the effectiveness of the numerical strategy, several numerical examples have been analyzed and comparisons with available experimental data have been made at the macroscopic level. The algorithmic model is coded as a UMAT user material subroutine and implemented in the commercial finite element software ABAQUS. The response of the constitutive model is compared to the results of experiments in uniaxial tensile and compressive loading, biaxial compressive loading, and mixed mode fracture for different types of concrete.

▪ **Object IV: Meso-scale simulation of cementitious composites**

At the macroscopic level, the crack nucleation and propagation in concrete material under loading is entirely dependent on the direction of principal stresses. At the mesoscopic level, however, the size and distribution of aggregate and the strength of each phase have a significant effect on the damage initiation and crack propagation. Especially, the accurate understanding of the properties and behavior of ITZ is one of the most important issues on meso-scale analysis because the damage is initiated at the weakest point and the ITZ is generally the weakest zone in concrete. Although the characteristic of the ITZ is not clearly understood currently, it can be assumed that the behavior of the ITZ, which has weaker mechanical properties, is similar to that of the mortar matrix. In this research, 2-D and 3-D meso-scale computational analysis is conducted in order to investigate the effect of aggregate shape, distribution, and volume fraction, the ITZ thickness, and the ITZ and mortar matrix strength in the tensile strength and the crack initiation and propagation of concrete. Moreover, the process of the crack penetration into the aggregate under uniaxial tensile loading is also investigated applying the proposed coupled plasticity-damage constitutive model to the aggregate as well as the ITZ and mortar matrix.

▪ **Objective V: Analysis of CNT/cement matrix composites**

CNT is the strongest known material that has ever developed, and its aspect ratio exceeds 10^7, while the density is reported as less than 1500 kg/m^3. With the specific material properties, CNTs can be used for more effective reinforcement of concrete than

any other conventional fibers by providing huge interfacial contact area with mortar matrix. With the experimental test results of CNTs itself and the composite effect between CNT and matrix, this research focused on the numerical analysis of CNT/cement composite material in order to validate the reinforcing effect of cement matrix with CNTs. As a simplest scenario, single straight CNT pull-out analysis is performed to find adequate interfacial model between CNT and mortar matrix, and investigate the effect of interfacial shear strength, stiffness, and fracture energy, the strength and the Young's modulus of the matrix, and the CNT mechanical properties and aspect ratio in the CNT pull-out strength and ductility. Moreover, the pull-out analysis of the single curved CNT embedded in the elastic body is performed in order to investigate the curvature effect of the CNT in the pull-out strength.

1.4 Outline of the Dissertation

The dissertation contains 9 Chapters and is organized as follows.

- **Chapter I** addresses the problem statement, background, and the objectives of the research.
- **Chapter II** presents the modified coupled plasticity-damage constitutive model for plain concrete. Based on the phenomenological observation, the coupled plasticity-damage model by Cicekli et al. (2007) is modified for better performance of the constitutive model. Moreover, both the isotropic and anisotropic damage model is considered, and the power damage evolution law is newly proposed in order to improve the predictability of the proposed constitutive model.

- **Chapter III** presents the thermodynamic admissibility of the proposed anisotropic damage model. The constitutive equations are derived from the second law of thermodynamics, the expression of Helmholtz free energy, the additive decomposition of the total strain rate into elastic and plastic components, the Clausius-Duhem inequality, and the maximum dissipation principle.
- **Chapter IV** presents the time descretization and numerical integration procedures for the presented elasto-plastic-damage model. The plastic multiplier is derived with both semi-explicit and semi-implicit algorithm, and the expression of the elasto-plastic tangent stiffness is obtained. Furthermore, the tensile and compressive damage multiplier, $\dot{\lambda}_d^{\pm}$, are also derived using damage consistency conditions.
- **Chapter V** is devoted in identifying material parameters, such as the tensile and compressive hardening modulus h^+ and Q^-, the tensile and compressive strength where uniaxial nonlinearity starts $B^{\pm}$, the compressive hardening rate constant b^-, and constants for the power tensile and compressive damage evolution law $q^{\pm}$ are calibrated in order for the application of the proposed coupled plasticity-damage model to the analysis of plain concrete.
- **Chapter VI** presents the verification of the proposed model in the macro-scale by comparing the response of the proposed constitutive model with various experimental data; monotonic uniaxial tension and compression, monotonic biaxial compression, and mixed mode fracture for different types of concrete.
- **Chapter VII** presents the application of the proposed constitutive model to the meso-scale simulation of cementitious composites. Using the proposed coupled plasticity-

damage model with different material constants for the ITZ, cement matrix, and aggregate, 2-D and 3-D meso-scale computational simulations are conducted in order to investigate the effects of aggregate distribution, aggregate volume fraction, and ITZ thickness and properties on the overall tensile strength and micro-crack initiation and propagation of concrete.

- **Chapter VIII** deals with the analysis of the carbon nanotube reinforced cementitious composites. The pull-out mechanisms of a single straight CNT from the cement matrix, the debonding process at the interface between the CNT and the matrix, and the damage initiation and propagations at the cement matrix surrounding the straight CNT are investigated through the single straight CNT pull-out simulations. Moreover, the pull-out simulation of the single curved CNT embedded in the elastic body is also performed in order to investigate the effect of the additional normal force induced by the bending stiffness of the curved CNT on the sliding behavior of the curved CNT.
- Finally, in **Chapter IX**, conclusions of this research and future recommendations regarding the research are presented.

CHAPTER II

COUPLED PLASTICITY AND DAMAGE MODEL

The coupled plasticity-damage model formulated recently by Cicekli *et al*. (2007) for plain concrete is recalled and modified. In order to predict the plastic behavior of plain concrete for tension and compression separately, the Lubliner yield criterion (Lubliner *et al.* 1989; Lee and Fenves 1998) expressed in the effective (undamaged) configuration is adopted. Moreover, the non-associative plasticity flow rule based on the Drucker-Prager potential and two distinct damage evolution surfaces; tensile and compressive damage surfaces are included in the model.

Damage in materials can be represented in many forms such as specific void and crack surfaces, specific crack and void volumes, the spacing between cracks or voids. The physical interpretation of the damage variable, however, is introduced as the specific damage surface area in this research.

2.1 Isotropic Damage Model

The definition of the damage variable φ in one-dimension proposed by Kachanov (1958) is adopted and recalled here for completeness. Consider a uniform bar subjected to a uniaxial tensile load T as shown in Figure 2.1(a). The whole cross-sectional area of the bar in the damaged configuration is A and the total damage area A^D is an area formed by both voids and cracks due to damage in the bar (Kattan and Voyiadjis 2001; Voyiadjis and Kattan 2006). Furthermore, a fictitious undamaged (effective)

configuration of the bar as shown in Figure 2.1(b) is considered in order to use the principles of continuum damage mechanics. In this effective configuration all types of damage, including both voids and cracks, are removed from the bar. The effective stressed cross-sectional area of the bar in this configuration is denoted by $\bar{A}$. The damage density φ is defined by the ratio of the total damaged area to whole cross-sectional area of the bar and is expressed simply as follows:

$$\varphi = \frac{A - \bar{A}}{A} = \frac{A^D}{A} \tag{2.1}$$

The damage density φ can be varied from 0 to 1. That the damage density is equal to zero means that the material is undamaged and one means that the material is fully damaged.

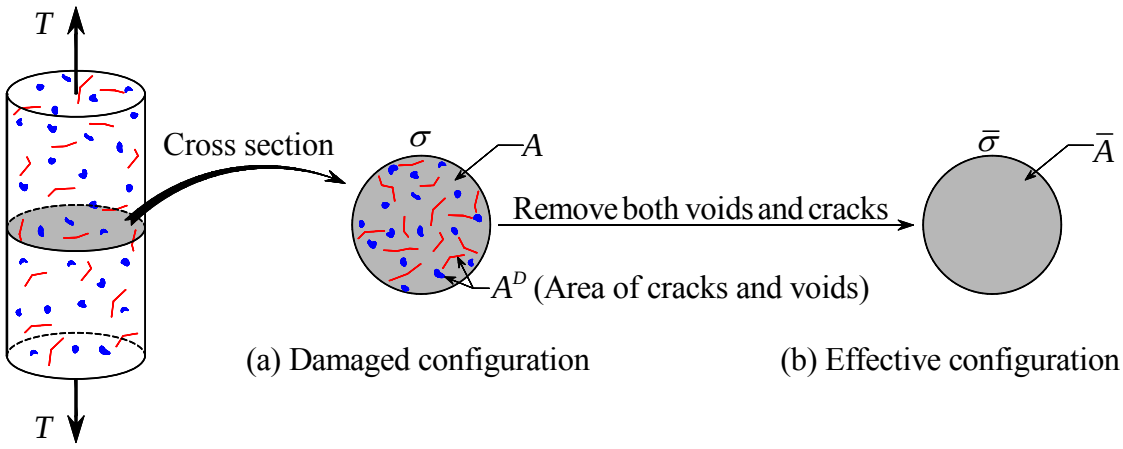

Figure 2.1 A cylindrical bar subjected to uniaxial tension

Because the bar in both the damaged and the effective configuration are subjected to the same tensile force T, the following expression for the uniaxial stress σ

(Kachanov 1958; Rabotnov 1968) of damaged configuration is derived considering the relation between the applied force and the resultant stress for both configurations:

$$\sigma = (1-\varphi)\bar{\sigma} \tag{2.2}$$

Similarly, the relation between the nominal stress tensor σ_{ij} and the effective stress tensor $\bar{\sigma}_{ij}$ for the isotropic damage (scalar damage variable) can be written as follows:

$$\sigma_{ij} = (1-\varphi)\bar{\sigma}_{ij} \tag{2.3}$$

Therefore, in the continuum damage mechanics framework, the effective stress means the average micro-level stress acting in the undamaged (intact) material between defects and is defined as the force divided by the undamaged part of the area, while the nominal stress means the macro-level stress and is defined as the force divided by the total area.

In order to derive the transformation relations between the damaged and the hypothetical undamaged states of the material, the strain equivalence hypothesis is adopted in this study for simplicity and ease in numerical implementation. This hypothesis states that the elastic and plastic strains in both the damaged and the effective configurations due to the applied force are equivalent. Therefore, the total strain tensor ε_{ij} is set equal to the corresponding effective strain tensor $\bar{\varepsilon}_{ij}$ (i.e. $\varepsilon_{ij} = \bar{\varepsilon}_{ij}$), which can be decomposed into an elastic strain $\varepsilon_{ij}^{e}\left(=\bar{\varepsilon}_{ij}^{e}\right)$ and a plastic strain $\varepsilon_{ij}^{p}\left(=\bar{\varepsilon}_{ij}^{p}\right)$, such that:

$$\varepsilon_{ij} = \varepsilon_{ij}^{e} + \varepsilon_{ij}^{p} = \bar{\varepsilon}_{ij}^{e} + \bar{\varepsilon}_{ij}^{p} = \bar{\varepsilon}_{ij} \tag{2.4}$$

The plastic strain in Eq. (2.4) incorporates all types of irreversible deformations whether they are due to tensile micro-cracking, breaking of internal bonds during shear loading, and/or compressive consolidation during the collapse of the micro-porous structure of the cement matrix.

Applying the hypothesis of the strain equivalence, the relation between the damaged elasticity tensor E_{ijkl} and the effective (undamaged) elasticity tensor $\bar{E}_{ijkl}$ can be expressed using the generalized Hooke's law as follows:

$$E_{ijkl} = (1-\varphi)\bar{E}_{ijkl} \tag{2.5}$$

This relation states that the damaged stiffness is decreased linearly as the damage density φ increases as shown in Figure 2.2. The concept of the isotropic damage model applying the hypothesis of the strain equivalence is very simple and has given a lot of inspirations to researchers. This damage model, however, is not fully capable of predicting the nonlinearity of the damaged stiffness degradation observed from the experiments due to the increase of the damage density (Cicekli *et al.* 2007).

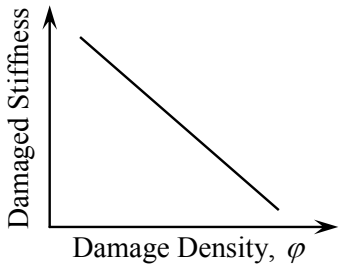

Figure 2.2 The linear relationship between the damage stiffness and density

2.2 Modified Isotropic Damage Model

The motivation of the modified isotropic damage model is that the damaged stiffness varies nonlinearly with the damage density as argued by Cicekli et al. (2007) as shown in Figure 2.3.

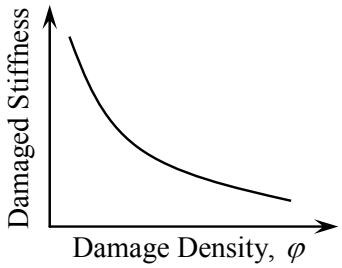

Figure 2.3 The nonlinear relationship between the damage stiffness and density

Therefore, in order to predict the nonlinear degradation of the damaged stiffness due to the increase of the damage density, a nonlinear relationship between the nominal and the effective stress tensor is assumed such that:

$$\sigma_{ij} = (1-\varphi)^{\alpha}\,\bar{\sigma}_{ij} \tag{2.6}$$

where α is a material constant. In the following development $\alpha = 2$ will be assumed such that

$$\sigma_{ij} = (1-\varphi)^{2}\,\bar{\sigma}_{ij} \tag{2.7}$$

By applying the strain equivalence hypothesis, the damaged elasticity tensor E_{ijkl} can be expressed as follows:

$$E_{ijkl} = \left(1-\varphi\right)^2 \bar{E}_{ijkl} \tag{2.8}$$

One can also use the strain energy equivalence hypothesis (Voyiadjis and Kattan 2006) to obtain a nonlinear relationship between stiffness and the damage density as in Eq. (2.8); however, this will complicate the constitutive models and the numerical implementation. This issue has been discussed thoroughly by Abu Al-Rub and Voyiadjis (2003).

Since concrete has a distinct behavior in tension and compression and, therefore, in order to adequately characterize the damage in concrete due to tensile, compressive, and/or cyclic loadings, the Cauchy stress tensor (in the nominal or effective configurations) is decomposed into positive and negative parts using the spectral decomposition technique (Simo and Ju 1987a, 1987b; Krajcinovic 1996). Hereafter, the superscripts "+" and "–" designate, respectively, tensile and compressive entities. Therefore, the nominal stress tensor σ_{ij} and the effective stress tensor $\bar{\sigma}_{ij}$ can be decomposed as follows:

$$\sigma_{ij} = \sigma_{ij}^{+} + \sigma_{ij}^{-}, \quad \bar{\sigma}_{ij} = \bar{\sigma}_{ij}^{+} + \bar{\sigma}_{ij}^{-} \tag{2.9}$$

where σ_{ij}^{+} and $\bar{\sigma}_{ij}^{+}$ are the tensile parts whereas σ_{ij}^{-} and $\bar{\sigma}_{ij}^{-}$ are the compressive parts of the stress tensor.

Using fourth-order tensile and compressive projection tensors P_{ijkl}^{+} and P_{ijkl}^{-}, the nominal tensile and compressive stress tensors $\bar{\sigma}_{ij}^{+}$ and $\bar{\sigma}_{ij}^{-}$ can be related to $\bar{\sigma}_{ij}$ by

$$\bar{\sigma}_{kl}^{+} = P_{klpq}^{+}\bar{\sigma}_{pq}\,, \quad \bar{\sigma}_{kl}^{-} = P_{klpq}^{-}\bar{\sigma}_{pq} \tag{2.10}$$

where the projection tensors are defined as follows:

$$P_{ijpq}^{+} = \sum_{k=1}^{3} H(\hat{\bar{\sigma}}^{(k)}) n_i^{(k)} n_j^{(k)} n_p^{(k)} n_q^{(k)}, \quad P_{ijpq}^{-} = I_{ijpq} - P_{ijpq}^{+} \tag{2.11}$$

where $H(\hat{\bar{\sigma}}^{(k)})$ denotes the Heaviside step function computed at *k*-th principal stress $\hat{\sigma}^{(k)}$ of σ_{ij} and $n_i^{(k)}$ is the *k*-th corresponding unit principal directions. In the subsequent development, the superimposed hat "^" designates a principal value.

Based on the decomposition in Eq. (2.9), the expression in Eq. (2.7) can be assumed to be valid for both tension and compression, such that:

$$\sigma_{ij}^{+} = \left(1-\varphi^{+}\right)^2 \bar{\sigma}_{ij}^{+}, \quad \sigma_{ij}^{-} = \left(1-\varphi^{-}\right)^2 \bar{\sigma}_{ij}^{-} \tag{2.12}$$

where φ^{+} and φ^{-} are the tensile and compressive damage densities, respectively. Therefore, by substituting Eqs. (2.12) into Eq. $(2.9)_1$, σ_{ij} can be expressed as follows:

$$\sigma_{ij} = \left(1-\varphi^{+}\right)^2 \bar{\sigma}_{ij}^{+} + \left(1-\varphi^{-}\right)^2 \bar{\sigma}_{ij}^{-} \tag{2.13}$$

In the above expression the explicit decoupling between the tensile and compressive damage density is assumed, but they are coupled implicitly such that degradation in the tensile strength will cause further degradation in the compressive strength and vice versa.

By substituting Eqs. (2.10) into Eq. (2.13), one can write the following relation between σ_{ij} and $\bar{\sigma}_{ij}$ in terms of φ^{+} and φ^{-}, such that:

$$\sigma_{ij} = \left[\left(1-\varphi^{+}\right)^{2} P^{+}_{ijkl} + \left(1-\varphi^{-}\right)^{2} P^{-}_{ijkl} \right] \bar{\sigma}_{kl} \tag{2.14}$$

2.3 Anisotropic Damage Model

Anisotropic damage is considered in this study for a more reliable representation of concrete damage behavior. Isotropic damage assumes that the strength and stiffness of the concrete material is degraded equally in different directions upon damage evolution which is not realistic. Therefore, in order to include damage-induced anisotropy (i.e. different degradation in different directions), the relation between σ_{ij} and $\bar{\sigma}_{ij}$ can be expressed as follows (Cordebois and Sidoroff 1979; Murakami and Ohno 1981; Voyiadjis and Kattan 2006):

$$\sigma_{ij} = M_{ijkl} \bar{\sigma}_{kl} \tag{2.15}$$

where M_{ijkl} is the fourth-order damage-effect tensor that is used to make the stress tensor symmetrical. There are several definitions for the tensor M_{ijkl} (Voyiadjis and Park 1997); however, a different definition is presented in this study as follows:

$$M_{ijkl} = \frac{1}{2}\left[\left(\delta_{im} - \varphi_{im}\right)\left(\delta_{jm} - \varphi_{jm}\right)\delta_{kl} + \delta_{ij}\left(\delta_{km} - \varphi_{km}\right)\left(\delta_{lm} - \varphi_{lm}\right) \right] \tag{2.16}$$

where δ_{ij} is the Kronecker delta and φ_{ij} is a second-order damage tensor.

Using the generalized Hooke's law, σ_{ij} and $\bar{\sigma}_{ij}$ are given as follows:

$$\sigma_{ij} = E_{ijkl}\varepsilon^{e}_{kl}, \quad \bar{\sigma}_{ij} = \bar{E}_{ijkl}\varepsilon^{e}_{kl} \tag{2.17}$$

For isotropic linear-elastic material, $\bar{E}_{ijkl}$ is given by

$$\bar{E}_{ijkl} = 2\bar{G}\delta_{ik}\delta_{jl} + \left(\bar{K} - \tfrac{2}{3}\bar{G}\right)\delta_{ij}\delta_{kl} \tag{2.18}$$

where $\bar{G} = \bar{E} / 2(1+\bar{\nu})$ and $\bar{K} = \bar{E} / 3\left(1-2\bar{\nu}\right)$ are the effective shear and bulk moduli, respectively, with $\bar{E}$ being the Young's modulus and $\bar{\nu}$ is the Poisson's ratio which are obtained from the stress-strain diagram in the effective configuration.

From the Eq. (2.17) and since the strain equivalence hypothesis is adopted, the elastic strain tensor ε^{e}_{kl} can be expressed as follows:

$$\varepsilon^{e}_{ij} = E^{-1}_{ijkl}\sigma_{kl} = \bar{E}^{-1}_{ijkl}\bar{\sigma}_{kl} \tag{2.19}$$

where E^{-1}_{ijkl} is the inverse (or compliance tensor) of the fourth-order damaged elastic tensor E_{ijkl}, which is a function of the damage variable φ_{ij}.

By substituting Eq. (2.15) into Eq. (2.17) or Eq. (2.19), one can express the damaged elasticity tensor E_{ijkl} in terms of the corresponding undamaged elasticity tensor $\bar{E}_{ijkl}$ by the following relation:

$$E_{ijkl} = M_{ijmn}\bar{E}_{mnkl} \tag{2.20}$$

Based on Eq. (2.9), the expression in Eq. (2.15) can be rewritten with decoupled damage evolution in tension and compression, such that:

$$\sigma_{ij}^{+} = M_{ijkl}^{+}\bar{\sigma}_{kl}^{+}, \quad \sigma_{ij}^{-} = M_{ijkl}^{-}\bar{\sigma}_{kl}^{-} \tag{2.21}$$

where M_{ijkl}^{+} is the tensile damage-effect tensor and M_{ijkl}^{-} is the corresponding compressive damage effect-tensor which can be expressed using Eq. (2.16) in a decoupled form as a function of the tensile and compressive damage variables, φ_{ij}^{+} and φ_{ij}^{-}, respectively, as follows:

$$\begin{aligned} M_{ijkl}^{+} &= \frac{1}{2}\left[\left(\delta_{im}-\varphi_{im}^{+}\right)\left(\delta_{jm}-\varphi_{jm}^{+}\right)\delta_{kl} + \delta_{ij}\left(\delta_{km}-\varphi_{km}^{+}\right)\left(\delta_{lm}-\varphi_{lm}^{+}\right)\right] \\ M_{ijkl}^{-} &= \frac{1}{2}\left[\left(\delta_{im}-\varphi_{im}^{-}\right)\left(\delta_{jm}-\varphi_{jm}^{-}\right)\delta_{kl} + \delta_{ij}\left(\delta_{km}-\varphi_{km}^{-}\right)\left(\delta_{lm}-\varphi_{lm}^{-}\right)\right] \end{aligned} \tag{2.22}$$

Now, by substituting Eq. (2.21) into Eq. $(2.9)_1$, one can express $\bar{\sigma}_{ij}$ as follows:

$$\bar{\sigma}_{ij} = \left(M_{ijkl}^{+}\right)^{-1}\sigma_{kl}^{+} + \left(M_{ijkl}^{-}\right)^{-1}\sigma_{kl}^{-} \tag{2.23}$$

Similarly, σ_{ij} can be expressed as follows:

$$\sigma_{ij} = M_{ijkl}^{+}\bar{\sigma}_{kl}^{+} + M_{ijkl}^{-}\bar{\sigma}_{kl}^{-} \tag{2.24}$$

By substituting Eqs. (2.10) into Eq. (2.23) and comparing the result with Eq. (2.15), the following relation for the damage-effect tensor M_{ijkl} can be obtained, such that:

$$M_{ijpq} = M^{+}_{ijkl} P^{+}_{klpq} + M^{-}_{ijkl} P^{-}_{klpq} \tag{2.25}$$

Using Eq. $(2.11)_2$, the above expression can be rewritten as:

$$M_{ijpq} = \left[M^{+}_{ijkl} - M^{-}_{ijkl} \right] P^{+}_{klpq} + M^{-}_{ijpq} \tag{2.26}$$

One should notice the following:

$$M_{ijkl} \neq M^{+}_{ijkl} + M^{-}_{ijkl} \tag{2.27}$$

or

$$\varphi_{ij} \neq \varphi^{+}_{ij} + \varphi^{-}_{ij} \tag{2.28}$$

It is also noteworthy that the relation in Eq. (2.26) enhances a coupling between tensile and compressive damage through the fourth-order projection tensor P^{+}_{ijkl}. Therefore, for isotropic damage Eq. (2.14) gives the following expression for the fourth-order damage-effect tensor:

$$M_{ijkl} = \left(1 - \varphi^{+}\right)^2 P^{+}_{ijkl} + \left(1 - \varphi^{-}\right)^2 P^{-}_{ijkl} \tag{2.29}$$

From the above expression, adopting the decomposition of the scalar damage variable φ into a positive φ^{+} part and a negative φ^{-} part still enhances a damage anisotropy through the spectral decomposition tensors P^{+}_{ijkl} and P^{-}_{ijkl}. However, this anisotropy is weak when compared to the anisotropic damage effect tensor presented in Eq. (2.26).

2.4 Plastic Yield Surface

Concrete materials exhibit plastic (irreversible) deformation upon unloading which implies that an elastic-damage model is not sufficient to model the concrete behavior even under tensile loading conditions. Therefore, an elasto-plastic-damage model should be developed. Thus, a plasticity yield surface and plasticity flow rules need to be developed. Furthermore, since concrete material behaves differently in tension and compression, the yield criterion of Lubliner et al. (1989) that accounts for both tension and compression plasticity is adopted in this study. However, since the stress state in the intact material is the one which drives the plasticity evolution, this yield criterion is expressed in the effective (undamaged) configuration as follows:

$$f = \sqrt{3\bar{J}_2} + \alpha \bar{I}_1 + \beta(\varepsilon_{eq}^{+}, \varepsilon_{eq}^{-})\mathrm{H}(\hat{\bar{\sigma}}_{\max})\hat{\bar{\sigma}}_{\max} - (1-\alpha)c^{-}(\varepsilon_{eq}^{-}) \le 0 \tag{2.30}$$

where $\bar{J}_2 = \bar{s}_{ij}\bar{s}_{ij}/2$ is the second-invariant of the effective deviatoric stress tensor $\bar{s}_{ij} = \bar{\sigma}_{ij} - \bar{\sigma}_{kk}\delta_{ij}/3$, $\bar{I}_1 = \bar{\sigma}_{kk}$ is the first-invariant of the effective Cauchy stress tensor $\bar{\sigma}_{ij}$, $\hat{\bar{\sigma}}_{\max}$ is the maximum principal effective stress, $\mathrm{H}(\hat{\bar{\sigma}}_{\max})$ is the Heaviside step function (H=1 for $\hat{\bar{\sigma}}_{\max} > 0$ and H=0 for $\hat{\bar{\sigma}}_{\max} < 0$), and the parameters α and β are dimensionless constants which are defined as follows:

$$\alpha = \frac{(f_{b0}/f_0^{-}) - 1}{2(f_{b0}/f_0^{-}) - 1}, \quad \beta = (1-\alpha)\frac{c^{-}(\varepsilon_{eq}^{-})}{c^{+}(\varepsilon_{eq}^{+})} - (1+\alpha) \tag{2.31}$$

with f_{b0} and f_0^{-} being the initial equi-biaxial and uniaxial compressive yield strengths, respectively.

According to Eq. (2.31), both tension and compression plasticity material parameters looks to be needed to calculate α and β and the damage parameters. However, simplifying Eqs. (2.30) and (2.31) for the case of pure tension or pure compression, one can get an expression for the yield function independent of the compressive material parameters for pure tension (i.e. $f = \sigma_{11}^{+} - c^{+} = 0$) and a yield function independent of the tensile material parameters for pure compression (i.e. $f = \sigma_{11}^{-} - c^{-} = 0$). Experimental values for f_{b0} / f_0^{-} lie between 1.10 and 1.16; yielding values for α between 0.08 and 0.12. The shape of the yield surface for two values of the dilatational constant α and its comparison with the experimental results by Kupfer et al. (1969) are shown in Figure 2.4.

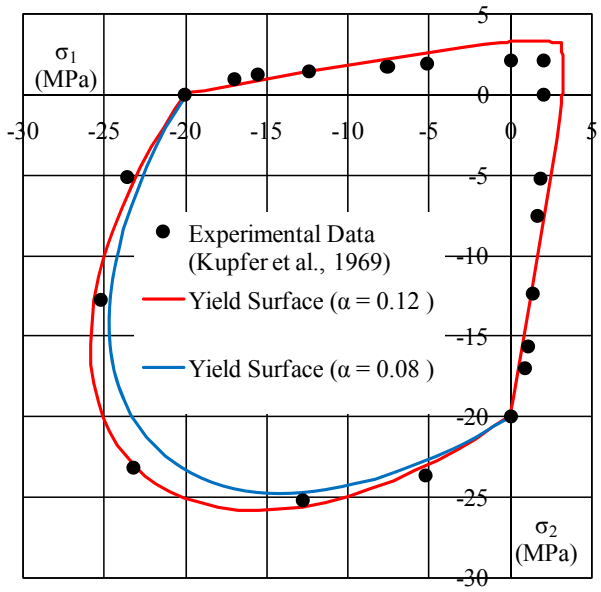

Figure 2.4 Lubliner plasticity yielding surface for different values of α, and its comparison with experimental results by Kupfer et al.(1969)

As seen, when the α constant is 0.12, the model gives a better prediction of the experimental results, and consequently, this value is used for α constant in this research.

The internal plastic state variables $\varepsilon_{eq}^{+} = \int_0^t \dot{\varepsilon}_{eq}^{+} \mathrm{d}t$ and $\varepsilon_{eq}^{-} = \int_0^t \dot{\varepsilon}_{eq}^{-} \mathrm{d}t$ are the equivalent plastic strains in tension and compression, respectively, where their rates are defined as follows:

$$\dot{\varepsilon}_{eq}^{+} = r(\hat{\bar{\sigma}}_{ij})\hat{\dot{\varepsilon}}_{\max}^{p}, \quad \dot{\varepsilon}_{eq}^{-} = -(1 - r(\hat{\bar{\sigma}}_{ij}))\hat{\dot{\varepsilon}}_{\min}^{p} \tag{2.32}$$

where $\hat{\dot{\varepsilon}}_{\max}^{p}$ and $\hat{\dot{\varepsilon}}_{\min}^{p}$ are the maximum and minimum principal values of the plastic strain rate $\dot{\varepsilon}_{ij}^{p}$ such that $\hat{\dot{\varepsilon}}_{1}^{p} > \hat{\dot{\varepsilon}}_{2}^{p} > \hat{\dot{\varepsilon}}_{3}^{p}$ with $\hat{\dot{\varepsilon}}_{\max}^{p} = \hat{\dot{\varepsilon}}_{1}^{p}$ and $\hat{\dot{\varepsilon}}_{\min}^{p} = \hat{\dot{\varepsilon}}_{3}^{p}$. Note that the superscript + or − designates a tensile or compressive quantity, $(\hat{\bullet})$ designates the principle value of $(\bullet)$, and the subscripts *eq*, min, and max are not indicial indices. The dimensionless parameter $r(\hat{\bar{\sigma}}_{ij})$ is a weight factor for tension or compression depending on the values of the principal stresses and is defined as follows:

$$r(\hat{\bar{\sigma}}_{ij}) = \frac{\sum_{k=1}^{3} \left\langle \hat{\bar{\sigma}}_{k} \right\rangle}{\sum_{k=1}^{3} \left| \hat{\bar{\sigma}}_{k} \right|} \tag{2.33}$$

where $\langle\ \rangle$ is the McAuley bracket presented as $\langle x \rangle = \frac{1}{2}(|x| + x)$. Note that $r(\hat{\bar{\sigma}}_{ij}) = r(\hat{\sigma}_{ij})$. Moreover, depending on the value of $r(\hat{\bar{\sigma}}_{ij})$: (a) if the loading is pure uniaxial tension $\hat{\bar{\sigma}}_{k} \geq 0$, then $r(\hat{\bar{\sigma}}_{ij}) = 1$, and (b) if the loading is pure uniaxial compression $\hat{\bar{\sigma}}_{k} \leq 0$, then $r(\hat{\bar{\sigma}}_{ij}) = 0$.

In the last term of Eq. (2.30), the isotropic hardening function c^- represents the material cohesion in uniaxial compression. Since the concrete behavior in compression is more of a ductile behavior as compared to its corresponding brittle behavior in tension, the evolution of the compressive and tensile isotropic hardening functions c^- and c^+ are defined by the following exponential and linear hardening laws, respectively:

$$c^- = f_0^- + Q^-\left[1-\exp(-b^-\varepsilon_{eq}^-)\right], \quad c^+ = f_0^+ + h^+\varepsilon_{eq}^+ \tag{2.34}$$

where f_0^- and f_0^+ are the initial yield stresses in compression and tension (i.e. when nonlinear behavior starts), respectively. The parameters Q^-, b^-, and h^+ are material constants obtained in the effective configuration of the uniaxial stress-strain diagram.

For realistic modeling of the volumetric expansion under compression of concrete, a non-associative plasticity flow rule should be used. This can be done by writing the evolution of the plastic strain tensor $\dot{\varepsilon}_{ij}^p$, in terms of a plastic potential F^p that is not equal to the plastic yield function f, such that:

$$\dot{\varepsilon}_{ij}^p = \dot{\lambda}^p \frac{\partial F^p}{\partial \bar{\sigma}_{ij}} \tag{2.35}$$

where $\dot{\lambda}^p$ is the plastic multiplier, which can be obtained using the standard plasticity consistency condition, $\dot{f} = 0$, such that:

$$f \le 0, \quad \dot{\lambda}^p \ge 0, \quad \dot{\lambda}^p f = 0, \quad \dot{\lambda}^p \dot{f} = 0 \tag{2.36}$$

The plastic potential F^p can be expressed in terms of the Drucker-Prager function as:

$$F^p = \sqrt{3\bar{J}_2} + \alpha_p \bar{I}_1 \tag{2.37}$$

where α_p is the dilation material constant. Then the plastic flow direction $\partial F^p / \partial \bar{\sigma}_{ij}$ in Eq. (2.35) is given by

$$\frac{\partial F^p}{\partial \bar{\sigma}_{ij}} = \frac{3}{2}\frac{\bar{s}_{ij}}{\sqrt{3\bar{J}_2}} + \alpha_p \delta_{ij} \tag{2.38}$$

2.5 Tensile and Compressive Damage Surfaces

The following damage growth function which is proposed by Chow and Wang (1987) and used by many others (Abu Al-Rub and Voyiadjis 2003, 2006) is adopted in this study. However, this function is generalized in Cicekli et al. (2007) in order to incorporate both tensile and compressive damage separately, such that:

$$g^{\pm} = \sqrt{\frac{1}{2} Y_{ij}^{\pm} L_{ijkl}^{\pm} Y_{kl}^{\pm}} - K^{\pm}(\varphi_{eq}^{\pm}) \le 0 \tag{2.39}$$

where $K^{\pm}$ is the tensile or compressive damage isotropic hardening function such that $K^{\pm} = K_0^{\pm}$ when there is no damage, where $K_0^{\pm}$ is the tensile or compressive initial damage parameter (i.e. damage threshold), and $L_{ijkl}^{\pm}$ is a fourth-order symmetric tensor and is presented in matrix form as follows:

$$L_{ijkl}^{\mp}=\begin{bmatrix} 1 & \mu^{\pm} & \mu^{\pm} & 0 & 0 & 0 \\ \mu^{\pm} & 1 & \mu^{\pm} & 0 & 0 & 0 \\ \mu^{\pm} & \mu^{\pm} & 1 & 0 & 0 & 0 \\ 0 & 0 & 0 & 2(1-\mu^{\pm}) & 0 & 0 \\ 0 & 0 & 0 & 0 & 2(1-\mu^{\pm}) & 0 \\ 0 & 0 & 0 & 0 & 0 & 2(1-\mu^{\pm}) \end{bmatrix} \tag{2.40}$$

where $\mu^{\pm}$ is a material constant satisfying $-1/2 \le \mu^{\pm} \le 1$. However, in what follows, $L_{ijkl}^{\pm}$ is taken as the fourth-order identity tensor I_{ijkl} in order to simplify the anisotropic damage formulation.

The damage driving force $Y_{ij}^{\pm}$ is interpreted as the energy release rate according to the notion of fracture mechanics as argued by Abu Al-Rub and Voyiadjis (2003), where the following expression is proposed:

$$Y_{rs}^{\pm}=-\frac{1}{2}\bar{E}_{ijab}^{-1}\bar{\sigma}_{ab}\frac{\partial M_{ijpq}}{\partial \varphi_{rs}^{\pm}}\bar{\sigma}_{pq} \tag{2.41}$$

The rate of the equivalent damage $\dot{\varphi}_{eq}^{\pm}$ (i.e. rate of damage accumulation) is defined as:

$$\dot{\varphi}_{eq}^{\pm}=\sqrt{\dot{\varphi}_{ij}^{\pm}\dot{\varphi}_{ij}^{\pm}} \quad \text{with} \quad \varphi_{eq}^{\pm}=\int_0^t \dot{\varphi}_{eq}^{\pm}\,\mathrm{d}t \tag{2.42}$$

where the evolution equation for $\dot{\varphi}_{ij}^{\pm}$ is defined by:

$$\dot{\varphi}_{ij}^{\pm}=\dot{\lambda}_d^{\pm}\frac{\partial g^{\pm}}{\partial Y_{ij}^{\pm}} \tag{2.43}$$

where $\dot{\lambda}_d^{\pm}$ is the damage multiplier such that one can easily show from Eqs. (2.39)-(2.43) that $\dot{\lambda}_d^{\pm} = \dot{\varphi}^{\pm}$. This multiplier can be obtained from the following damage consistency conditions:

$$g^{\pm} \le 0,\ \dot{\lambda}_d^{\pm} g^{\pm} = 0, \text{ and } \dot{g}^{\pm} \begin{cases} < 0 \Rightarrow \dot{\lambda}_d^{\pm} = 0 \\ = 0 \Rightarrow \dot{\lambda}_d^{\pm} = 0 \\ = 0 \Rightarrow \dot{\lambda}_d^{\pm} > 0 \end{cases} \Leftrightarrow \begin{cases} \text{effective (undamaged state)} \\ \text{damage initiation} \\ \text{damage growth} \end{cases} \tag{2.44}$$

2.6 Tensile and Compressive Damage Evolution Laws

In this research, two damage evolution laws, an exponential law and a power law, for both tensile and compressive loading cases are proposed and tested to see which one is more suitable than the other in predicting the damage behavior in concrete when compared to experimental data.

2.6.1 Exponential Damage Evolution Law

The following exponential tensile and compressive damage evolution laws are proposed for $\varphi_{eq}^{\pm}$ in Eq. (2.42):

$$\varphi_{eq}^{+} = 1 - \left(\frac{K_0^{+}}{K^{+}} \right) \exp\left[B^{+} \left(1 - \frac{K^{+}}{K_0^{+}} \right) \right] \tag{2.45}$$

$$\varphi_{eq}^{-} = 1 - \exp\left[B^{-} \left(1 - \frac{K^{-}}{K_0^{-}} \right) \right] \tag{2.46}$$

where $B^{\pm}$ is a material constant, which is related to the tensile and compressive fracture energies, and therefore can be calibrated from the uniaxial tensile and compressive

stress-strain diagrams. Both exponential damage evolution laws have similar form, however, the term K_0^+ / K^+, the ratio of the tensile damage threshold to the tensile damage hardening function, is multiplied to the tensile damage evolution law in order to control the tensile damage evolution rate. The main advantage of the exponential damage evolution law is that there is only one material constant in each law, $B^{\pm}$, which needs to be identified from experimental data. The above expressions are to a great extent similar to those proposed by Mazars and Pijaudier-Cabot (1989).

In the case of using the exponential damage evolution law, the evolution of the tensile and compressive damage isotropic hardening functions $\dot{K}^+$ and $\dot{K}^-$ in Eq. (2.39) can be derived by taking time derivative of Eqs. (2.45) and (2.46) as follows:

$$\dot{K}^+ = \frac{K^+}{B^+ + \dfrac{K_0^+}{K^+}} \exp\left[-B^+\left(1-\frac{K^+}{K_0^+}\right)\right]\dot{\varphi}_{eq}^+ \tag{2.47}$$

$$\dot{K}^- = \frac{K_0^-}{B^-} \exp\left[-B^-\left(1-\frac{K^-}{K_0^-}\right)\right]\dot{\varphi}_{eq}^- \tag{2.48}$$

The above evolution equations are useful in the development of numerical algorithms as is seen later in this research.

2.6.2 Power Damage Evolution Law

The following power tensile and compressive damage evolution laws are proposed in order to improve the capability of the damage model for the prediction of the concrete behavior and to compare it to the exponential damage low which is widely used in the literature, such that:

$$\varphi_{eq}^{+} = B^{+}\left(\frac{K_0^{+}}{K^{+}}\right)\left(\frac{K^{+}}{K_0^{+}}-1\right)^{q^{+}} \tag{2.49}$$

$$\varphi_{eq}^{-} = B^{-}\left(\frac{K^{-}}{K_0^{-}}-1\right)^{q^{-}} \tag{2.50}$$

where $B^{\pm}$ and $q^{\pm}$ are material constants. The expense of this proposition is that one needs to identify more material constant from experimental data as compared to the exponential damage laws. However, it will be shown in the analysis section that even setting $q^{\pm}=1$ gives better predictions than the exponential damage laws.

Similarly, for the power damage laws, one can obtain the evolution of the damage isotropic hardening functions $\dot{K}^{+}$ and $\dot{K}^{-}$ by taking the time derivative of Eqs. (2.49) and (2.50) as follows:

$$\dot{K}^{+} = \frac{K^{+}}{B^{+}\left(q^{+}K_0^{+}-1+\dfrac{K_0^{+}}{K^{+}}\right)}\left[\frac{K^{+}}{K_0^{+}}-1\right]^{1-q^{+}}\dot{\varphi}_{eq}^{+} \tag{2.51}$$

$$\dot{K}^{-} = \frac{K_0^{-}}{B^{-}q^{-}}\left[\frac{K^{-}}{K_0^{-}}-1\right]^{1-q^{-}}\dot{\varphi}_{eq}^{-} \tag{2.52}$$

It is noted that the tensile and compressive exponential and power damage evolution laws in Eqs. (2.45) and (2.46) and Eqs. (2.49) and (2.50) obey the fundamental principle that the damage is not initiated until the damage hardening function $K^{\pm}$ is greater than the damage threshold $K_0^{\pm}$. It is also noteworthy that when concrete is under tensile loading, the tensile yielding of the material is almost coincide with the damage

initiation. Therefore, the tensile yield strength f_0^+ and the tensile damage threshold K_0^+ have almost the same value, and the gap between the two parameters is not significant even though the tensile damage threshold K_0^+ is greater than the tensile yield strength f_0^+. When concrete is under compressive loading, however, the compressive damage is initiated later than the compressive yielding of the material. Therefore, the compressive damage threshold K_0^- is always greater than the compressive yield strength f_0^-.

CHAPTER III

CONSISTENT THERMODYNAMIC FORMULATION

The thermodynamic admissibility of the proposed anisotropic damage model is checked by following the internal variable procedure of Coleman and Gurtin (1967). The constitutive equations are derived from the second law of thermodynamics, the expression of Helmholtz free energy, the additive decomposition of the total strain rate in to elastic and plastic components, the Clausius-Duhem inequality, and the maximum energy dissipation principle.

3.1 Plasticity and Damage Internal State Variables

The Helmholtz free energy can be expressed in terms of a suitable set of internal state variables that characterize the elastic, plastic, and damage behavior of concrete. In this research the following internal variables are assumed to satisfactory characterize the concrete behavior both in tension and compression such that:

$$\psi = \psi\left(\varepsilon_{ij}^{e},\ \varphi_{ij}^{+},\ \varphi_{ij}^{-},\ \varphi_{eq}^{+},\ \varphi_{eq}^{-},\ \varepsilon_{eq}^{+},\ \varepsilon_{eq}^{-}\right) \tag{3.1}$$

where φ_{eq}^{+} and φ_{eq}^{-} are the equivalent (accumulated) damage variables for tension and compression , respectively, which are defined as $\varphi_{eq}^{\pm} = \int_0^t \dot{\varphi}_{eq}^{\pm}\,\mathrm{d}t$. Similarly, ε_{eq}^{+} and ε_{eq}^{-} are the equivalent tensile and compressive plastic strains that are used here to characterize the plasticity isotropic hardening, $\varepsilon_{eq}^{\pm} = \int_0^t \dot{\varepsilon}_{eq}^{\pm}\,\mathrm{d}t$.

The Helmholtz free energy is given as a decomposition of elastic ψ^e, plastic ψ^p, and damage ψ^d, parts such that:

$$\psi = \psi^e(\varepsilon_{ij}^e,\ \varphi_{ij}^+,\ \varphi_{ij}^-) + \psi^p(\varepsilon_{eq}^+,\ \varepsilon_{eq}^-) + \psi^d(\varphi_{eq}^+,\ \varphi_{eq}^-) \tag{3.2}$$

It can be noted from the above decomposition that damage affects only the elastic properties and not the plastic ones. However, for a more realistic description, one should introduce the damage variables in the plastic part of the Helmholtz free energy (Abu Al-Rub and Voyiadjis 2003). However, these effects are not significant for brittle materials and can, therefore, be neglected.

3.2 Analytical Form for the Helmholtz Free Energy Density

The elastic free energy ψ^e is given in term of the second-order damage tensors $\varphi_{ij}^{\pm}$ as follows:

$$\psi^e = \frac{1}{2}\varepsilon_{ij}^e E_{ijkl}(\varphi_{ij}^+, \varphi_{ij}^-)\varepsilon_{kl}^e = \frac{1}{2}\sigma_{ij}\varepsilon_{ij}^e = \frac{1}{2}(\sigma_{ij}^+ + \sigma_{ij}^-)\varepsilon_{ij}^e \tag{3.3}$$

Substituting Eqs. (2.21) along with Eqs. (2.15) and (2.25), considering Eq. (2.10) into Eq. (3.3) and making some algebraic simplifications, one obtains the following relation:

$$\psi^e = \frac{1}{2}M_{ijpq}\bar{\sigma}_{pq}\varepsilon_{ij}^e = \frac{1}{2}\sigma_{ij}\varepsilon_{ij}^e \tag{3.4}$$

The plastic part of the Helmholtz free energy function is postulated to have the following form (Abu Al-Rub and Voyiadjis 2003):

$$\rho\psi^{p} = f_0^{+}\varepsilon_{eq}^{+} + \frac{1}{2}h^{+}(\varepsilon_{eq}^{+})^2 + f_0^{-}\varepsilon_{eq}^{-} + Q^{-}\left(\varepsilon_{eq}^{-} + \frac{1}{b^{-}}\exp(-b^{-}\varepsilon_{eq}^{-})\right) \tag{3.5}$$

The damage part of the Helmholtz free energy functions for the exponential and the power damage evolution laws are postulated to have the following form:

(1) for the exponential damage evolution law

$$\rho\psi^{d} = K_0^{\pm}\left[\varphi_{eq}^{\pm} + \frac{1}{B^{\pm}}\left\{(1-\varphi_{eq}^{\pm})\ln(1-\varphi_{eq}^{\pm}) + \varphi_{eq}^{\pm}\right\}\right] \tag{3.6}$$

(2) for the power damage evolution law

$$\rho\psi^{d} = K_0^{\pm}\left[\varphi_{eq}^{\pm} + \left(\frac{q^{\pm}}{q^{\pm}+1}\right)\left(\frac{1}{B^{\pm}}\right)^{q^{\pm}} \varphi_{eq}^{\frac{1}{q^{\pm}}+1}\right] \tag{3.7}$$

where $K_0^{\pm}$ is the initial damage threshold and $B^{\pm}$ are material constants which are expressed in terms of the fracture energy.

3.3 Plasticity and Damage Thermodynamic Conjugate Forces

The Clausius-Duhem inequality for isothermal conditions (i.e. there is no change in temperature), which is the fundamental inequality for deriving constitutive equations, can be obtained through the thermodynamic requirement that the rate of the free energy should be less than or equal to the rate of external work, such that:

$$\frac{d}{dt}\int_{\Gamma}\rho\psi \; dV \le P_{\text{ext}} \tag{3.8}$$

where ρ is the material density, Γ is a sub-volume of the body V, d/dt indicates derivative with respect to time, and P_{ext} is the external power (rate of external work), which according to the first law of thermodynamics (i.e. conservation of energy) should be equal to the internal power P_{int} such that

$$P_{\text{ext}} = P_{\text{int}} \tag{3.9}$$

where P_{int} can be simply expressed as follows

$$P_{\text{int}} = \int_{\Gamma} \sigma_{ij} \dot{\varepsilon}_{ij} dV \tag{3.10}$$

Therefore, using the conservation of mass along with the conservation of energy, Eq. (3.9), into Eq. (3.8) along with Eq. (3.10) one can write the following inequality:

$$\int_{\Gamma} \left(\sigma_{ij} \dot{\varepsilon}_{ij} - \rho \dot{\psi} \right) dV \geq 0 \tag{3.11}$$

From the above equation one can express the Clausius-Duhem inequality for isothermal case as follows:

$$\sigma_{ij} \dot{\varepsilon}_{ij} - \rho \dot{\psi} \geq 0 \tag{3.12}$$

Taking the time derivative of Eq. (3.2), the following expression can be written:

$$\dot{\psi} = \frac{\partial \psi^e}{\partial \varepsilon_{ij}^e} \dot{\varepsilon}_{ij}^e + \frac{\partial \psi^e}{\partial \varphi_{ij}^+} \dot{\varphi}_{ij}^+ + \frac{\partial \psi^e}{\partial \varphi_{ij}^-} \dot{\varphi}_{ij}^- + \frac{\partial \psi^p}{\partial \varepsilon_{eq}^+} \dot{\varepsilon}_{eq}^+ + \frac{\partial \psi^p}{\partial \varepsilon_{eq}^-} \dot{\varepsilon}_{eq}^- + \frac{\partial \psi^d}{\partial \varphi_{eq}^+} \dot{\varphi}_{eq}^+ + \frac{\partial \psi^d}{\partial \varphi_{eq}^-} \dot{\varphi}_{eq}^- \tag{3.13}$$

By plugging the above equation into the Clausius-Duhem inequality, Eq. (3.12), and making some simplifications, one can obtain the following relations for any admissible states such that:

$$\sigma_{ij} = \rho \frac{\partial \psi^e}{\partial \varepsilon_{ij}^e} \tag{3.14}$$

and

$$\sigma_{ij}\dot{\varepsilon}_{ij}^p + Y_{ij}^+ \dot{\varphi}_{ij}^+ + Y_{ij}^- \dot{\varphi}_{ij}^- - c^+ \dot{\varepsilon}_{eq}^+ - c^- \dot{\varepsilon}_{eq}^- - K^+ \dot{\varphi}_{eq}^+ - K^- \dot{\varphi}_{eq}^- \geq 0 \tag{3.15}$$

where the damage and plasticity conjugate forces that appear in the above expression are defined as follows:

$$Y_{ij}^+ = -\rho \frac{\partial \psi^e}{\partial \varphi_{ij}^+} \tag{3.16}$$

$$Y_{ij}^- = -\rho \frac{\partial \psi^e}{\partial \varphi_{ij}^-} \tag{3.17}$$

$$K^+ = \rho \frac{\partial \psi^d}{\partial \varphi_{eq}^+} \tag{3.18}$$

$$K^- = \rho \frac{\partial \psi^d}{\partial \varphi_{eq}^-} \tag{3.19}$$

$$c^+ = \rho \frac{\partial \psi^p}{\partial \varepsilon_{eq}^+} \tag{3.20}$$

$$c^- = \rho \frac{\partial \psi^p}{\partial \varepsilon_{eq}^-} \tag{3.21}$$

3.4 Maximum Dissipation Energy Principle

The Clausius-Duhem inequality can be rewritten to yield the dissipation energy, Π, due to plasticity, Π^p, and damage, Π^d, such that

$$\Pi = \Pi^d + \Pi^p \geq 0 \tag{3.22}$$

with

$$\Pi^p = \sigma_{ij}\dot{\varepsilon}_{ij}^p - c^+\dot{\varepsilon}_{eq}^+ - c^-\dot{\varepsilon}_{eq}^- \geq 0 \tag{3.23}$$

$$\Pi^d = Y_{ij}^+\dot{\varphi}_{ij}^+ + Y_{ij}^-\dot{\varphi}_{ij}^- - K^+\dot{\varphi}_{eq}^+ - K^-\dot{\varphi}_{eq}^- \geq 0 \tag{3.24}$$

The rate of the internal variables associated with plastic and damage deformations are obtained by utilizing the calculus of functions of several variables with the plasticity and damage Lagrangian multipliers, $\dot{\lambda}^p$ and $\dot{\lambda}_d^{\pm}$, such that the following objective function can be defined:

$$\Omega = \Pi - \dot{\lambda}^p F^p - \dot{\lambda}_d^+ g^+ - \dot{\lambda}_d^- g^- \geq 0 \tag{3.25}$$

Using the well known maximum dissipation principle (Simo and Honein 1990; Simo and Hughes 1998), which states that the actual state of the thermodynamic forces (σ_{ij}, $Y_{ij}^{\pm}$, $c^{\pm}$, $K^{\pm}$) are that which maximizes the dissipation function over all other possible admissible states, hence, one can maximize the objective function Ω by using the necessary conditions as follows:

$$\frac{\partial\Omega}{\partial\sigma_{ij}} = 0,\ \frac{\partial\Omega}{\partial Y_{ij}^{\pm}} = 0,\ \frac{\partial\Omega}{\partial c^{\pm}} = 0,\ \frac{\partial\Omega}{\partial K^{\pm}} = 0 \tag{3.26}$$

Substituting Eq. (3.25) along with Eqs. (3.23) and (3.24) into Eqs. (3.26) yield the following thermodynamic laws:

$$\dot{\varepsilon}_{ij}^{p} = \dot{\lambda}^{p} \frac{\partial F^{p}}{\partial \sigma_{ij}} \tag{3.27}$$

$$\dot{\varphi}_{ij}^{+} = \dot{\lambda}_{d}^{+} \frac{\partial g^{+}}{\partial Y_{ij}^{+}} \tag{3.28}$$

$$\dot{\varphi}_{ij}^{-} = \dot{\lambda}_{d}^{-} \frac{\partial g^{-}}{\partial Y_{ij}^{-}} \tag{3.29}$$

$$\dot{\varepsilon}_{eq}^{+} = \dot{\lambda}^{p} \frac{\partial F^{p}}{\partial c^{+}} \tag{3.30}$$

$$\dot{\varepsilon}_{eq}^{-} = \dot{\lambda}^{p} \frac{\partial F^{p}}{\partial c^{-}} \tag{3.31}$$

$$\dot{\varphi}_{eq}^{+} = \dot{\lambda}_{d}^{+} \frac{\partial g^{+}}{\partial K^{+}} \tag{3.32}$$

$$\dot{\varphi}_{eq}^{-} = \dot{\lambda}_{d}^{-} \frac{\partial g^{-}}{\partial K^{-}} \tag{3.33}$$

3.5 Derivation of the Elastic, Plastic, Damage Constitutive Laws

The elastic part of the Helmholtz free energy function, ψ^{e}, as presented in Eq. (3.3) can be substituted into Eq. (3.14) to yield the following stress-strain relation:

$$\sigma_{ij} = E_{ijkl}\varepsilon_{kl}^{e} = E_{ijkl}(\varepsilon_{kl} - \varepsilon_{kl}^{p}) \tag{3.34}$$

Now, one can obtain expressions for the damage driving forces $Y_{ij}^{\pm}$ from Eqs. (3.3), (3.16), and (3.17) as follows:

$$Y_{rs}^{\pm} = -\frac{1}{2}\varepsilon_{ij}^{e}\frac{\partial E_{ijkl}}{\partial \varphi_{rs}^{\pm}}\varepsilon_{kl}^{e} \tag{3.35}$$

By taking the derivative of Eq. (2.20) with respect to the damage parameter $\varphi_{ij}^{\pm}$ one obtains:

$$\frac{\partial E_{ijkl}}{\partial \varphi_{rs}^{\pm}} = \frac{\partial M_{ijmn}}{\partial \varphi_{rs}^{\pm}}\overline{E}_{mnkl} \tag{3.36}$$

Now, by substituting Eq. (3.36) into Eq. (3.35), the expression for $Y_{ij}^{\pm}$ can be obtained:

$$Y_{rs}^{\pm} = -\frac{1}{2}\varepsilon_{ij}^{e}\frac{\partial M_{ijmn}}{\partial \varphi_{rs}^{\pm}}\overline{E}_{mnkl}\varepsilon_{kl}^{e} \tag{3.37}$$

where from Eq. (2.25), one can write the following expression:

$$\frac{\partial M_{ijmn}}{\partial \varphi_{rs}^{\pm}} = \frac{\partial M_{ijpq}^{\pm}}{\partial \varphi_{rs}^{\pm}}P_{pqmn}^{\pm} \tag{3.38}$$

One can also rewrite Eq. (3.37) in terms of the effective stress tensor by replacing ε_{kl}^{e} from Eq. $(2.17)_2$ as follows:

$$Y_{rs}^{\pm} = -\frac{1}{2}\overline{E}_{ijab}^{-1}\overline{\sigma}_{ab}\frac{\partial M_{ijpq}}{\partial \varphi_{rs}^{\pm}}\overline{\sigma}_{pq} \tag{3.39}$$

Substituting Eq. (3.5) into Eqs. (3.26) and (3.27) yields the following expressions for the plasticity conjugate forces c^+ and c^- that are equal to Eq. (2.34):

$$c^+ = f_0^+ + h^+ \varepsilon_{eq}^+ \tag{3.40}$$

$$c^- = f_0^- + Q^- \left[1 - \exp(-b^- \varepsilon_{eq}^-)\right] \tag{3.41}$$

Substituting Eq. (3.6) into Eqs. (3.18) and (3.19), the following expressions for the damage isotropic hardening function $K^\pm$ for the exponential damage evolution law can be easily obtained:

$$K^\pm = K_0^\pm \left[1 - \frac{1}{B^\pm} \ln(1 - \varphi_{eq}^\pm)\right] \tag{3.42}$$

Similarly, one can derive the damage isotropic hardening function $K^\pm$ for the power damage evolution law by substituting Eq. (3.7) into Eqs. (3.18) and (3.19) as follows:

$$K^\pm = K_0^\pm \left[1 + \left(\frac{1}{B^\pm} \varphi_{eq}^\pm\right)^{\frac{1}{q^\pm}}\right] \tag{3.43}$$

By taking the time derivative of the above Eqs. (3.42) and (3.43) separately, one retrieves the rate form of the damage hardening/softening function $\dot{K}^\pm$ for the exponential and the power damage evolution laws presented in Eqs. (2.47) - (2.52) such that:

(1) for the exponential damage evolution law

$$\dot{K}^{\pm} = \frac{K_0^{\pm}}{B^{\pm}} \exp\left[-B^{\pm}(1 - \frac{K^{\pm}}{K_0^{\pm}}) \right] \dot{\varphi}_{eq}^{\pm} \tag{3.44}$$

(2) for the power damage evolution law

$$\dot{K}^{\pm} = \frac{K_0^{\pm}}{B^{\pm} q^{\pm}} \left[\frac{K^{\pm}}{K_0^{\pm}} - 1 \right]^{1-q^{\pm}} \dot{\varphi}_{eq}^{\pm} \tag{3.45}$$

It is noteworthy that the expression of the tensile damage functions K^{+}, for the exponential and the power damage evolution law presented in Eqs. (2.47) and (2.51), is slightly different with the expression shown in Eqs. (3.44) and (3.45). However, in the remaining of this study, Eqs. (2.47) and (2.51) are used. This is attributed to the better representation of the stress-strain diagram under tensile loading.

CHAPTER IV

FINITE ELEMENT IMPLEMENTATION

The time descretization and numerical integration procedures for the presented elasto-plastic-damage model are presented in this chapter. The evolutions of the plastic and damage internal state variables can be obtained if the Lagrangian multipliers $\dot{\lambda}^p$ and $\dot{\lambda}_d^{\pm}$ are computed. Therefore, the plasticity and damage consistency conditions, Eqs. (2.36) and (2.44), are used for computing both $\dot{\lambda}^p$ and $\dot{\lambda}_d^{\pm}$. This is shown in the subsequent developments. Then, at the beginning of the step, by applying the given strain increment $\Delta\varepsilon_{ij} = \varepsilon_{ij}^{(n+1)} - \varepsilon_{ij}^{(n)}$ and knowing the values of the stress and internal variables from the previous step, $(\bullet)^{(n)}$, the updated values at the end of the step, $(\bullet)^{(n+1)}$, are obtained.

The implemented integration scheme is divided into two sequential steps, corresponding to the plastic and damage parts of the model. In the plastic part, the plastic strain ε_{ij}^p and the effective stress $\bar{\sigma}_{ij}$ at the end of the step are determined by using the classical radial return mapping algorithm (Simo and Hughes 1998), such that one can write from Eqs. $(2.17)_2$, (2.4), and (2.35) the following algorithmic step:

$$\bar{\sigma}_{ij} = \bar{\sigma}_{ij}^{tr} - \bar{\bar{E}}_{ijkl}\Delta\varepsilon_{kl}^p = \bar{\sigma}_{ij}^{tr} - \Delta\lambda^p \bar{\bar{E}}_{ijkl}\frac{\partial F^p}{\partial \bar{\sigma}_{kl}^{(n)}} \tag{4.1}$$

where $\bar{\sigma}_{ij}^{tr} = \bar{\sigma}_{ij}^{(n)} + \bar{\bar{E}}_{ijkl}\Delta\varepsilon_{kl}$ is the trial stress tensor, which is easily evaluated from the given strain increment. Also, substituting Eqs. (2.18) and (2.38) into Eq. (4.1), the above equation can be rewritten as follows:

$$\bar{\sigma}_{ij} = \bar{\sigma}_{ij}^{tr} - \Delta\lambda^{p}\left[\sqrt{6}\bar{G}\frac{\bar{s}_{ij}^{(n+1)}}{\left\|\bar{s}_{ij}^{(n+1)}\right\|} + 3\bar{K}\alpha_{p}\delta_{ij}\right] \tag{4.2}$$

where $\| \bar{s}_{ij} \| = \sqrt{\bar{s}_{ij}\bar{s}_{ij}}$ and $\bar{s}_{ij}$ is the deviatoric component of the effective stress tensor $\bar{\sigma}_{ij}$. If the trial stress is not outside the yield surface, i.e. $f\left(\bar{\sigma}_{ij}^{tr}, c_{c}^{(n)}\right) \le 0$, the step is elastic and one sets $\Delta\lambda^{p} = 0$, $\bar{\sigma}_{ij}^{tr} = \bar{\sigma}_{ij}^{(n+1)}$, $\varepsilon_{ij}^{p(n+1)} = \varepsilon_{ij}^{p(n)}$, $c^{\pm(n+1)} = c^{\pm(n)}$. However, if the trial stress is outside the yield surface, then $\bar{\sigma}_{ij}^{(n+1)}$, $\varepsilon_{ij}^{p(n+1)}$, and $c^{\pm(n+1)}$ are determined by computing $\Delta\lambda^{p}$.

In the damage part, the nominal stress σ_{ij} at the end of the step is obtained from Eq. (2.15) by knowing the damage variables $\varphi_{ij}^{\pm}$, which can be calculated once $\Delta\lambda_{d}^{\pm}$ are computed from the damage consistency conditions in Eq. (2.44). Therefore, a decoupled updating algorithm is proposed in this research where the constitutive equations are updated first in the effective configuration and then the damaged variables are calculated in terms of the effective quantities which are the used to update the constitutive equations in the damaged configuration.

4.1 Computation of the Plastic Multiplier with a Semi-explicit Algorithm

From the plasticity consistency condition in Eq. (2.36), one can write the following relation at $n+1$ step:

$$f^{(n+1)} = f^{(n)} + \Delta f = 0 \tag{4.3}$$

where since $f = f\left(\bar{\sigma}_{ij}, \bar{\sigma}_{\max}, \varepsilon_{eq}^{-}, \varepsilon_{eq}^{+}\right)$ from the Eq. (2.30), the increment of the plastic yield function Δf can be expressed as follows:

$$\Delta f = \frac{\partial f}{\partial \bar{\sigma}_{ij}} \Delta \bar{\sigma}_{ij} + \frac{\partial f}{\partial \hat{\bar{\sigma}}_{\max}} \Delta \hat{\bar{\sigma}}_{\max} + \frac{\partial f}{\partial \varepsilon_{eq}^{-}} \Delta \varepsilon_{eq}^{-} + \frac{\partial f}{\partial \varepsilon_{eq}^{+}} \Delta \varepsilon_{eq}^{+} = 0 \tag{4.4}$$

where

$$\Delta \bar{\sigma}_{ij} = \Delta \bar{\sigma}_{ij}^{tr} - \Delta \lambda^{p} \left[\sqrt{6} \bar{G} \frac{\left(\bar{\sigma}_{ij}^{tr} - \frac{1}{3} \bar{I}_1 \delta_{ij} \right)}{\left\| \bar{s}_{ij} \right\|} + 3 \bar{K} \alpha_p \delta_{ij} \right] \tag{4.5}$$

$$\Delta \hat{\bar{\sigma}}_{\max} = \Delta \hat{\bar{\sigma}}_{\max}^{tr} - \Delta \lambda^{p} \left[\sqrt{6} \bar{G} \frac{\left(\hat{\bar{\sigma}}_{\max} - \frac{1}{3} \bar{I}_1 \right)}{\left\| \bar{s}_{ij} \right\|} + 3 \bar{K} \alpha_p \right] \tag{4.6}$$

$$\Delta \varepsilon_{eq}^{+} = r \Delta \lambda^{p} \frac{\partial F^{p}}{\partial \hat{\bar{\sigma}}_{\max}} \tag{4.7}$$

$$\Delta \varepsilon_{eq}^{-} = -\left(1 - r\right) \Delta \lambda^{p} \frac{\partial F^{p}}{\partial \hat{\bar{\sigma}}_{\min}} \tag{4.8}$$

In order to go back radially to the yield surface, the following assumption is made (Simo and Hughes, 1998):

$$\frac{\bar{s}_{ij}^{(n+1)}}{\left\| \bar{s}_{ij}^{(n+1)} \right\|} = \frac{\bar{s}_{ij}^{tr}}{\left\| \bar{s}_{ij}^{tr} \right\|} \tag{4.9}$$

Substituting Eqs. (2.30), (2.37), (4.5)-(4.8) into Eqs. (4.4) and (4.3), and then by making few algebraic manipulations, one can obtain the plastic multiplier $\Delta \lambda^{p}$ from the following expression:

$$\Delta\lambda^{p} = \frac{f^{tr}}{H} \tag{4.10}$$

where f^{tr} and H are given as follows:

$$f^{tr} = \sqrt{\tfrac{3}{2}}\left\|\bar{s}_{ij}^{tr}\right\| + \alpha\bar{I}_1^{tr} + \beta^{tr}H(\hat{\bar{\sigma}}_{\max}^{tr})\hat{\bar{\sigma}}_{\max}^{tr} - (1-\alpha)c^{-(n)} \tag{4.11}$$

$$H = 3\bar{G} + 9\bar{K}\alpha_p\alpha + \beta^{tr}H\left(\hat{\bar{\sigma}}_{\max}^{tr}\right)Z + (1-r)\frac{\partial f}{\partial\varepsilon_{eq}^{-tr}}\frac{\partial F^{p}}{\partial\hat{\bar{\sigma}}_{\min}^{tr}} - r\frac{\partial f}{\partial\varepsilon_{eq}^{+tr}}\frac{\partial F^{p}}{\partial\hat{\bar{\sigma}}_{\max}^{tr}} \tag{4.12}$$

with

$$Z = \sqrt{6}\,\bar{G}\frac{\hat{\bar{\sigma}}_{\max}^{tr}}{\left\|\bar{s}_{ij}^{tr}\right\|} + 3\bar{K}\alpha_p - \sqrt{\tfrac{2}{3}}\bar{G}\frac{\bar{I}_1^{tr}}{\left\|\bar{s}_{ij}^{tr}\right\|} \tag{4.13}$$

$$\frac{\partial F^{p}}{\partial\hat{\bar{\sigma}}_{\min,\max}^{tr}} = \sqrt{\frac{3}{2}}\frac{(\hat{\bar{\sigma}}_{\min,\max}^{tr} - \frac{1}{3}\bar{I}_1^{tr})}{\left\|\bar{s}_{ij}^{tr}\right\|} + \alpha_p \tag{4.14}$$

$$\frac{\partial f}{\partial\varepsilon_{eq}^{-tr}} = -(1-\alpha)Q^{-}b^{-}\exp(-b^{-}\varepsilon_{eq}^{-}) \tag{4.15}$$

$$\frac{\partial f}{\partial\varepsilon_{eq}^{+tr}} = -\langle\hat{\bar{\sigma}}_{\max}^{tr}\rangle\frac{c^{-}(1-\alpha)h^{+}}{(c^{+})^{2}} \tag{4.16}$$

4.2 Computation of the Plastic Multiplier with a Semi-implicit Algorithm

4.2.1 Effective (Undamaged) Elastic Predictor

Assuming that the variables of the model at iteration i, the trial elastic stress can be given in the corotational frame by the following relation:

$$\bar{\sigma}_{ij}^{tr} = \bar{E}_{ijkl}(\bar{\varepsilon}_{kl}^{(n+1)} - \bar{\varepsilon}_{kl}^{p(n)}) = \bar{\sigma}_{ij}^{(n)} + \bar{E}_{ijkl}\Delta\bar{\varepsilon}_{kl} \tag{4.17}$$

Note that $\bar{\sigma}_{ij}^{(n)}$ is calculated from the previous step. If $f\left(\bar{\sigma}_{ij}^{tr}, c_c^{(n)}\right) < 0$ then:

$$\bar{\sigma}_{ij}^{(n+1)} = \bar{\sigma}_{ij}^{tr} \tag{4.18}$$

4.2.2 Effective Plastic Corrector

The plastic-corrector problem may then be stated as (the objective rates reduce to a simple time derivative due to the fact that the global configuration is held fixed), such that the effective plastic corrector is derived as follows:

$$\bar{\sigma}_{ij}^{(n+1)} = \bar{\sigma}_{ij}^{(n)} + \Delta\bar{\sigma}_{ij} = \bar{\sigma}_{ij}^{tr} - \bar{\bar{E}}_{ijkl}\Delta\bar{\varepsilon}_{kl}^{p} \tag{4.19}$$

4.2.3 Effective Plastic Consistency Condition

The plastic consistency condition (i.e., $f = 0$) is satisfied at the end of the loading step for the effective (undamaged) case presented here. The Drucker-Prager flow rule is used and presented below. In the approach followed in this study, the consistency condition is transformed into a linear set of equations that depends on the material parameters and on the current coordinates of the integration points.

To compute $\Delta\varepsilon_{kl}^{p}$ in Eq. (4.19), the generalized mid-point rule is used. The flow rule for $n+1$ step can be written as the following:

$$\Delta\bar{\varepsilon}_{kl}^{p} = \Delta\lambda^{p}\frac{\partial F}{\partial\bar{\sigma}_{kl}^{(n+1)}} \tag{4.20}$$

where $\dfrac{\partial F}{\partial\bar{\sigma}_{kl}^{(n+1)}}$ is given as the following:

$$\frac{\partial F}{\partial \bar{\sigma}_{kl}^{(n+1)}} = \sqrt{\frac{3}{2}} \frac{\bar{s}_{kl}^{(n+1)}}{\left\| s_{ij}^{(n+1)} \right\|} + \alpha_p \delta_{kl} \tag{4.21}$$

where $\left\| A_{ij} \right\| = \sqrt{A_{ij} A_{ij}}$ and λ^p is the plastic multiplier or also known as Lagrangian Multiplier.

The elasticity tensor in the undamaged configuration is given by:

$$\bar{E}_{ijkl} = 2\bar{G} I_{ijkl}^{dev} + \bar{K} \delta_{ij} \delta_{kl} \tag{4.22}$$

where $\bar{G}$ and $\bar{K}$ are the effective shear and bulk moduli, respectively, and $I_{ijkl}^{dev} = \delta_{ik}\delta_{jl} - \frac{1}{3}\delta_{ij}\delta_{kl}$.

By substituting Eq. (4.22) along with the identity tensor for the deviatoric case, one obtains the updated effective stress by the return mapping equation as follows:

$$\bar{\sigma}_{ij}^{(n+1)} = \bar{\sigma}_{ij}^{tr} - \left[2\bar{G} \Delta \bar{\varepsilon}_{ij}^{p} + (\bar{K} - \tfrac{2}{3}\bar{G}) \Delta \bar{\varepsilon}_{kk}^{p} \delta_{ij} \right] \tag{4.23}$$

where $\Delta \bar{\varepsilon}_{kk}^{p}$ can now be obtained from Eqs. (4.20) and (4.21) as follows:

$$\Delta \bar{\varepsilon}_{kk}^{p} = 3\alpha_p \Delta \lambda^p \tag{4.24}$$

By substituting Eqs.(4.20), (4.21), and (4.24) into Eq. (4.23), the updated effective stress can be rewritten as follows:

$$\bar{\sigma}_{ij}^{(n+1)} = \bar{\sigma}_{ij}^{tr} - \left[2\bar{G}\lambda^p \left\{ \sqrt{\tfrac{3}{2}} \frac{\bar{s}_{ij}^{(n+1)}}{\left\| \bar{s}_{ij}^{(n+1)} \right\|} + \alpha_p \delta_{ij} \right\} + (\bar{K} - \tfrac{2}{3}\bar{G})(3\alpha_p \Delta \lambda^p) \delta_{ij} \right] \tag{4.25}$$

Expanding and then simplifying the above equation, one can obtain the following form:

$$\bar{\sigma}_{ij}^{(n+1)} = \bar{\sigma}_{ij}^{tr} - \Delta\lambda^{p}\left[\sqrt{6}\bar{G}\frac{\bar{s}_{ij}^{(n+1)}}{\left\|\bar{s}_{ij}^{(n+1)}\right\|} + 3\bar{K}\alpha_{p}\delta_{ij}\right] \tag{4.26}$$

In order to return radially to the yield surface, one can use the radial return algorithm assumption such that:

$$\frac{\bar{s}_{ij}^{(n+1)}}{\left\|\bar{s}_{ij}^{(n+1)}\right\|} = \frac{\bar{s}_{ij}^{tr}}{\left\|\bar{s}_{ij}^{tr}\right\|} \tag{4.27}$$

where $\bar{s}_{ij}^{tr} = \bar{\sigma}_{ij}^{tr} - \frac{1}{3}\bar{\sigma}_{kk}^{tr}\delta_{ij}$. Therefore, at step $n+1$, one can write the following expressions for the deviatoric stress and the corresponding volumetric stress part, respectively:

$$\bar{s}_{ij}^{(n+1)} = \bar{s}_{ij}^{tr} - \Delta\lambda^{p}\sqrt{6}\bar{G}\frac{\bar{s}_{ij}^{tr}}{\left\|\bar{s}_{ij}^{tr}\right\|} \tag{4.28}$$

$$\bar{I}_{1}^{(n+1)} = \bar{I}_{1}^{tr} - 9\Delta\lambda^{p}\bar{K}\alpha_{p} \tag{4.29}$$

Multiplying both sides of Eq. (4.28) by $\frac{\left\|\bar{s}_{ij}^{tr}\right\|}{\bar{s}_{ij}^{tr}}$ and applying the assumption of Eq. (4.27), the deviatoric stress at Eq. (4.28) can be rewritten as follows:

$$\left\|\bar{s}_{ij}^{(n+1)}\right\| = \left\|\bar{s}_{ij}^{tr}\right\| - \sqrt{6}\bar{G}\Delta\lambda^{p} \tag{4.30}$$

4.2.4 Spectral Return-mapping Algorithm

A return-mapping algorithm based on a spectral decomposition of the stress is presented. It is considered that the spectral return-mapping algorithm has the advantage for a yield function which includes principal stress terms in addition to the stress tensor invariants (Lee and Fenves 2001). For this work similar to the work that conducted by Fenves and Lee (2001), a decoupled version of the return-mapping algorithm is derived using a spectral decomposition. A second-order tensor is used for the stresses and strains.

The spectral decomposition of the stress at step $n+1$ is given as follows:

$$\bar{\sigma}_{ij}^{(n+1)} = l_{ir}\hat{\bar{\sigma}}_{rs}^{(n+1)}l_{js} \tag{4.31}$$

Therefore, one can write $F(\bar{\sigma}_{ij}^{(n+1)}) = F(\hat{\bar{\sigma}}_{ij}^{(n+1)})$. As a result, one can express the following expressions in terms of the principal values as follows:

$$\Delta\hat{\bar{\varepsilon}}_{ij}^{p} = \Delta\lambda^{p}\frac{\partial F}{\partial\hat{\bar{\sigma}}_{ij}^{(n+1)}} \tag{4.32}$$

$$\Delta\bar{\varepsilon}_{ij}^{p} = \Delta\lambda^{p}l_{ir}\frac{\partial F}{\partial\hat{\bar{\sigma}}_{rs}^{(n+1)}}l_{js} \tag{4.33}$$

By substituting Eqs.(4.24), (4.31), and (4.33) into Eq. (4.23), one can write the return-mapping equation in the following form:

$$l_{ir}\hat{\bar{\sigma}}_{rs}^{(n+1)}l_{js} = \bar{\sigma}_{ij}^{tr} - \left[2\bar{G}\Delta\lambda^{p}l_{ir}\frac{\partial F}{\partial\hat{\bar{\sigma}}_{ij}^{(n+1)}}l_{js} + 3(\bar{K} - \tfrac{2}{3}\bar{G})\alpha_{p}\Delta\lambda^{p}\delta_{ij}\right] \tag{4.34}$$

and, one can use the following relation for Kronecker delta:

$$\delta_{ij} = l_{ir}\delta_{rs}l_{js} \tag{4.35}$$

Substitute Eq. (4.35) into Eq. (4.34), the trial stress can be obtained as follows:

$$l_{ir}\hat{\bar{\sigma}}_{rs}^{(n+1)}l_{js} = \bar{\sigma}_{ij}^{tr} - \Delta\lambda^{p}l_{ir}\left[2\bar{G}\frac{\partial F}{\partial\hat{\bar{\sigma}}_{rs}^{(n+1)}} + 3(\bar{K} - \tfrac{2}{3}\bar{G})\alpha_{p}\delta_{rs}\right]l_{js} \tag{4.36}$$

In the case that the symmetric matrices have repeated eigenvalues, they do not have a unique spectral decomposition form. Therefore, similar to Eq. (4.31) one can write the following relation:

$$\bar{\sigma}_{ij}^{tr} = l_{ir}\hat{\bar{\sigma}}_{rs}^{tr}l_{js} \tag{4.37}$$

where, σ_{ij}^{tr} is the diagonal eigenvalue matrix of the effective stress, and the orthogonal eigenvector matrix l_{ij} becomes an orthogonal eigenvector matrix of the trial stress matrix according to the Lemma. This leads the decomposition from of σ_{ij}^{tr} (at step $n+1$) as shown in the Eq.(4.37).

From Eq. (4.36) along with Eq. (4.37) one can write the decoupled form of the return-mapping equation as follows:

$$\hat{\bar{\sigma}}_{ij}^{(n+1)} = \hat{\bar{\sigma}}_{ij}^{tr} - \Delta\lambda^{p}\left[2\bar{G}\frac{\partial F}{\partial\hat{\bar{\sigma}}_{ij}^{(n+1)}} + 3(\bar{K} - \tfrac{2}{3}\bar{G})\alpha_{p}\delta_{ij}\right] \tag{4.38}$$

where, the derivative of the potential function with respect to the principal stress is given as follows:

$$\frac{\partial F}{\partial \hat{\bar{\sigma}}_{ij}^{(n+1)}} = \sqrt{\frac{3}{2}} \frac{\hat{\bar{s}}_{ij}^{(n+1)}}{\left\| \hat{\bar{s}}_{ij}^{(n+1)} \right\|} + \alpha_p \delta_{ij} \tag{4.39}$$

However, using Eq.(4.27), one can obtain the following expression:

$$\frac{\partial F}{\partial \hat{\bar{\sigma}}_{ij}^{(n+1)}} = \sqrt{\frac{3}{2}} \frac{\hat{\bar{\sigma}}_{ij}^{tr}}{\left\| \hat{\bar{s}}_{ij}^{tr} \right\|} + \left(\alpha_p - \sqrt{\frac{1}{6}} \frac{\bar{I}_1^{tr}}{\left\| \hat{\bar{s}}_{ij}^{tr} \right\|} \right) \delta_{ij} \tag{4.40}$$

where $\bar{I}_1^{tr} = \hat{\bar{I}}_1^{tr}$ and $\left\| \bar{s}_{ij}^{tr} \right\| = \left\| \hat{\bar{s}}_{ij}^{tr} \right\|$.

It should be noted that, the eigenvectors are preserved through the corrector steps which basically means that the eigenvectors are calculated at the predictor step. The principal stress is only needed to be computed at the plastic and degradation corrector steps.

Now, by substituting the final form of Eq. (4.40) into Eq. (4.38), one can obtain the following form:

$$\hat{\bar{\sigma}}_{ij}^{(n+1)} = \hat{\bar{\sigma}}_{ij}^{tr} - \Delta\lambda^p \left[\sqrt{6}\, \bar{G} \frac{\hat{\bar{\sigma}}_{ij}^{tr}}{\left\| \bar{s}_{ij}^{tr} \right\|} + \left(3\bar{K}\alpha_p - \sqrt{\frac{2}{3}}\, \bar{G} \frac{\bar{I}_1^{tr}}{\left\| \bar{s}_{ij}^{tr} \right\|} \right) \delta_{ij} \right] \tag{4.41}$$

In order to obtain $\hat{\bar{\sigma}}_{\max}^{(n+1)} = \hat{\bar{\sigma}}_{\max}^{tr}$, one can rewrite the above relation such that:

$$\hat{\bar{\sigma}}_{\max}^{(n+1)} = \hat{\bar{\sigma}}_{\max}^{tr} - \Delta\lambda^p \left[\sqrt{6}\, \bar{G} \frac{\hat{\bar{\sigma}}_{\max}^{tr}}{\left\| \bar{s}_{ij}^{tr} \right\|} + \left(3\bar{K}\alpha_p - \sqrt{\frac{2}{3}}\, \bar{G} \frac{\bar{I}_1^{tr}}{\left\| \bar{s}_{ij}^{tr} \right\|} \right) \right] \tag{4.42}$$

It should be noted that, if the plastic increment $\Delta\bar{\varepsilon}^{p}$ is obtained by a linear combination of $\hat{\bar{\sigma}}_{n+1}$ and I , e.g. for the Drucker-Prager model, the algebraic order of the effective (undamaged) principal stresses is maintained at the corrector steps (Lee and Fenves 2001). This can be proven by checking the Eq. (4.42). The stress is obtained only by a scalar multiplication and constant-vector addition on the trial stress. The order of the diagonal entries therefore in the trial stress matrix cannot be changed. This argument, however, is not valid for the case when the given yield criterion, f is used as a plastic potential function. This means that if one takes the derivative with respect of the maximum stresses, $\hat{\bar{\sigma}}_{\max}$, the algebraic order in the eigenvalue matrix does not preserve the same order, i.e., the order changes.

4.2.5 Updating of the Effective (Undamaged) Stress Tensor

Using the spectral form of the effective principal stress in Eq.(4.41), an implicit radial return-mapping algorithm is shown in order to evaluate the plastic multiplier, λ^{p} .

From the effective consistency condition, one can write the following relation at $n+1$ step:

$$f^{(n+1)} = f^{(n)} + \Delta f \tag{4.43}$$

where,

$$f^{(n+1)} = \sqrt{3\bar{J}_2^{(n+1)}} + \alpha \bar{I}_1^{(n+1)} - \beta^{(n+1)} H\left(\hat{\bar{\sigma}}_{\max}^{(n+1)}\right)\hat{\bar{\sigma}}_{\max}^{(n+1)} - (1-\alpha)c^{-(n+1)} \tag{4.44}$$

In the above equation, the third term of right side, $\beta^{(n+1)} H\left(\hat{\bar{\sigma}}_{\max}^{(n+1)}\right)\hat{\bar{\sigma}}_{\max}^{(n+1)}$ can be rewritten as follows:

$$\begin{aligned}\beta^{(n+1)} H\left(\hat{\bar{\sigma}}_{\max}^{(n+1)}\right)\hat{\bar{\sigma}}_{\max}^{(n+1)} &= \left(\beta^{(n)} + \Delta\beta\right) H\left(\hat{\bar{\sigma}}_{\max}^{(n+1)}\right)\hat{\bar{\sigma}}_{\max}^{(n+1)} \\ &= \beta^{(n)} H\left(\hat{\bar{\sigma}}_{\max}^{(n+1)}\right)\hat{\bar{\sigma}}_{\max}^{(n+1)} + \Delta\beta H\left(\hat{\bar{\sigma}}_{\max}^{(n+1)}\right)\hat{\bar{\sigma}}_{\max}^{(n+1)}\end{aligned} \tag{4.45}$$

where, the dimensionless constant β is already defined in Eq. $(2.31)_2$ and its increment has the form like below:

$$\begin{aligned}\Delta\beta &= \frac{(1-\alpha)}{c^+}\Delta c^- - \frac{(1-\alpha)c^-}{\left(c^+\right)^2}\Delta c^+ \\ &= \Delta\lambda^p\left[\frac{(1-r)}{c^+}\frac{\partial f}{\partial \varepsilon_{eq}^-}\frac{\partial F^p}{\partial \hat{\bar{\sigma}}_{\min}} + \frac{r}{\left\langle\hat{\bar{\sigma}}_{\max}\right\rangle}\frac{\partial f}{\partial \varepsilon_{eq}^+}\frac{\partial F^p}{\partial \hat{\bar{\sigma}}_{\max}}\right]\end{aligned} \tag{4.46}$$

where,

$$\frac{\partial f}{\partial \varepsilon_{eq}^+} = -\left\langle\hat{\bar{\sigma}}_{\max}\right\rangle\frac{c^-(1-\alpha)h^+}{\left(c^+\right)^2} \tag{4.47}$$

$$\frac{\partial f}{\partial \varepsilon_{eq}^-} = -(1-\alpha)\left[Q^- b^- \exp\left(-b^-\varepsilon_{eq}^-\right)\right] \tag{4.48}$$

and, the increment of the tensile and compressive isotropic hardening functions is expressed as follows from the Eq. (2.34):

$$\Delta c^+ = \frac{\partial c^+}{\partial \varepsilon_{eq}^+}\Delta\varepsilon_{eq}^+ = rh^+\Delta\lambda^p\frac{\partial F^p}{\partial \hat{\bar{\sigma}}_{\max}} \tag{4.49}$$

$$\Delta c^{-} = \frac{\partial c^{-}}{\partial \varepsilon_{eq}^{-}} \Delta \varepsilon_{eq}^{-} = -(1-r)\left[Q^{-} b^{-} \exp\left(-b^{-} \varepsilon_{eq}^{-}\right)\right] \Delta \lambda^{p} \frac{\partial F^{p}}{\partial \hat{\bar{\sigma}}_{\min}} \tag{4.50}$$

By substituting Eqs. (4.42) and (4.46) into Eq. (4.45), one can get the expression as follows:

$$\begin{aligned} \beta^{(n+1)} H\left(\hat{\bar{\sigma}}_{\max}^{(n+1)}\right) \hat{\bar{\sigma}}_{\max}^{(n+1)} = \beta^{(n)} H\left(\hat{\bar{\sigma}}_{\max}^{tr}\right) \hat{\bar{\sigma}}_{\max}^{tr} - \beta^{(n)} H\left(\hat{\bar{\sigma}}_{\max}^{tr}\right) Z \Delta \lambda^{p} \\ + r \Delta \lambda^{p} \frac{\partial f}{\partial \varepsilon_{eq}^{+tr}} \frac{\partial F^{p}}{\partial \hat{\bar{\sigma}}_{\max}^{tr}} \end{aligned} \tag{4.51}$$

where,

$$Z = \sqrt{6}\, \bar{G} \frac{\hat{\bar{\sigma}}_{\max}^{tr}}{\left\| \bar{s}_{ij}^{tr} \right\|} + 3 \bar{K} \alpha_{p} - \sqrt{\frac{2}{3}}\, \bar{G} \frac{\bar{I}_{1}^{tr}}{\left\| \bar{s}_{ij}^{tr} \right\|} \tag{4.52}$$

Moreover, the fourth term of Eq. (4.44) also can be rewritten as follows:

$$\begin{aligned} (1-\alpha) c^{-(n+1)} &= (1-\alpha) c^{-(n)} + (1-\alpha) \Delta c^{-} \\ &= (1-\alpha) c^{-(n)} + (1-r) \frac{\partial f}{\partial \varepsilon_{eq}^{-}} \Delta \lambda^{p} \frac{\partial F^{p}}{\partial \hat{\bar{\sigma}}_{\min}} \end{aligned} \tag{4.53}$$

By substituting Eqs.(4.29), (4.30), (4.51), and (4.53) into Eq. (4.44), and making few arithmetic manipulations, the plastic multiplier $\Delta \lambda^{p}$ can be expressed as follows:

$$\Delta \lambda^{p} = \frac{f^{tr}}{H} \tag{4.54}$$

where f^{tr} and H are given as:

$$f^{tr} = \sqrt{\tfrac{3}{2}}\left\|\bar{s}_{ij}^{tr}\right\| + \alpha \bar{I}_1^{tr} + \beta^{(n)} H(\hat{\bar{\sigma}}_{\max}^{tr})\hat{\bar{\sigma}}_{\max}^{tr} - (1-\alpha)c^{-(n)} \tag{4.55}$$

$$H = 3\bar{G} + 9\bar{K}\alpha_p\alpha + \beta^{(n)} H\left(\hat{\bar{\sigma}}_{\max}^{tr}\right) Z + (1-r)\frac{\partial f}{\partial \varepsilon_{eq}^{-tr}}\frac{\partial F^p}{\partial \hat{\bar{\sigma}}_{\min}^{tr}} - r\frac{\partial f}{\partial \varepsilon_{eq}^{+tr}}\frac{\partial F^p}{\partial \hat{\bar{\sigma}}_{\max}^{tr}} \tag{4.56}$$

4.3 The Elasto-plastic Tangent Stiffness

From the plastic yield criterion defined in Eq. (2.30) and the relation in Eq. (4.43), the increment of the yield function, Δf is expressed as follows:

$$\Delta f = \frac{\partial f}{\partial \bar{\sigma}_{ij}}\Delta\bar{\sigma}_{ij} + \frac{\partial f}{\partial \hat{\bar{\sigma}}_{\max}}\Delta\hat{\bar{\sigma}}_{\max} + \frac{\partial f}{\partial \varepsilon_{eq}^{-}}\Delta\varepsilon_{eq}^{-} + \frac{\partial f}{\partial \varepsilon_{eq}^{+}}\Delta\varepsilon_{eq}^{+} = 0 \tag{4.57}$$

Moreover, for the effective (undamaged) configuration, the relation between the effective stress increment $\Delta\bar{\sigma}_{ij}$ and the elastic strain increment $\Delta\bar{\varepsilon}_{ij}^{e}$ can be written in the following form from Eqs. $(2.17)_2$ and (2.35), such that:

$$\Delta\bar{\sigma}_{ij} = \bar{E}_{ijkl}\Delta\bar{\varepsilon}_{kl}^{e} = \bar{E}_{ijkl}\Delta\bar{\varepsilon}_{kl} - \Delta\lambda^p \bar{E}_{ijkl}\frac{\partial F^p}{\partial \bar{\sigma}_{kl}} \tag{4.58}$$

By substituting Eqs. (2.4) and (2.18) into the above equation, the above expression can be rewritten as follows:

$$\Delta\bar{\sigma}_{ij} = 2\bar{G}\Delta\bar{\varepsilon}_{ij} + \left(\bar{K} - \tfrac{2}{3}\bar{G}\right)\Delta\bar{\varepsilon}_{kk}\delta_{ij} - \Delta\lambda^p\left[2\bar{G}\frac{\partial F^p}{\partial \bar{\sigma}_{ij}} - 3\left(\bar{K} - \tfrac{2}{3}\bar{G}\right)\alpha_p\delta_{ij}\right] \tag{4.59}$$

Furthermore, based on a spectral decomposition of the stress tensor, Eq. (4.59) can be written for the increment of the effective principal stresses $\Delta\hat{\bar{\sigma}}_{ij}$ as follows:

$$\Delta\hat{\bar{\sigma}}_{ij} = 2\bar{G}l_{ri}\Delta\bar{\varepsilon}_{rs}l_{sj} + \left(\bar{K} - \tfrac{2}{3}\bar{G}\right)\Delta\bar{\varepsilon}_{kk}\delta_{ij} - \Delta\lambda^{p}\left[2\bar{G}\frac{\partial F^{p}}{\partial\hat{\bar{\sigma}}_{ij}} - 3\left(\bar{K} - \tfrac{2}{3}\bar{G}\right)\alpha_{p}\delta_{ij}\right] \quad (4.60)$$

where $l_{ij} = \left[n_i^{(1)} \quad n_i^{(2)} \quad n_i^{(3)}\right]^T$ is a second-order tensor that contains the principal directions of $\bar{\sigma}_{ij}$, where $n_i^{(1)}$, $n_i^{(2)}$, and $n_i^{(3)}$ are the eigenvectors that corresponds to $\hat{\bar{\sigma}}^{(1)} = \hat{\bar{\sigma}}_{\max}$, $\hat{\bar{\sigma}}^{(2)}$, and $\hat{\bar{\sigma}}^{(3)} = \hat{\bar{\sigma}}_{\min}$, respectively, and $[]^T$ designates the transpose. Thus, the increment in the maximum principal stress $\Delta\bar{\sigma}_{\max}$ can be written as follows:

$$\Delta\hat{\bar{\sigma}}_{\max} = 2\bar{G}n_i^{(1)}\Delta\bar{\varepsilon}_{ij}n_j^{(1)} + \left(\bar{K} - \tfrac{2}{3}\bar{G}\right)\Delta\bar{\varepsilon}_{kk} - \Delta\lambda^{p}\left[2\bar{G}\frac{\partial F^{p}}{\partial\hat{\bar{\sigma}}_{\max}} + 3\left(\bar{K} - \tfrac{2}{3}\bar{G}\right)\alpha_{p}\right] \quad (4.61)$$

By substituting Eqs. (4.59), (4.61), and (2.32) into Eq. (4.57) and making few algebraic manipulations, one can get the expression of the plastic multiplier $\Delta\lambda^{p}$ as a function of the strain rate $\Delta\bar{\varepsilon}_{ij}$ as follows:

$$\Delta\lambda^{p} = \frac{1}{H}\left\{\frac{\partial f}{\partial\bar{\sigma}_{ij}}\bar{E}_{ijkl} + 2\bar{G}\frac{\partial f}{\partial\hat{\bar{\sigma}}_{\max}}n_k^{(1)}n_l^{(1)} + \left(\bar{K} - \tfrac{2}{3}\bar{G}\right)\frac{\partial f}{\partial\hat{\bar{\sigma}}_{\max}}\delta_{kl}\right\}\Delta\bar{\varepsilon}_{kl} \quad (4.62)$$

Then, by substituting Eq. (4.62) into Eq. (4.58), the stress rate $\Delta\bar{\sigma}_{ij}$ can be rewritten as a function of the rate of the total strain $\Delta\bar{\varepsilon}_{ij}$ as follows:

$$\Delta\bar{\sigma}_{ij} = \bar{D}_{ijkl}\Delta\bar{\varepsilon}_{kl} \tag{4.63}$$

where the fourth-order tensor $\bar{D}_{ijkl}$ represents the elasto-plastic tangent stiffness in the effective configuration and is expressed as follows:

$$\bar{D}_{ijkl} = \bar{E}_{ijkl} - \frac{1}{H}\left\{\bar{E}_{mnkl}\frac{\partial f}{\partial\bar{\sigma}_{mn}} + \frac{\partial f}{\partial\hat{\bar{\sigma}}_{\max}}\left[2\bar{G}n_k^{(1)}n_l^{(1)} + \left(\bar{K} - \tfrac{2}{3}\bar{G}\right)\right]\delta_{kl}\right\}\bar{E}_{ijpq}\frac{\partial F^p}{\partial\bar{\sigma}_{pq}} \tag{4.64}$$

The above equation retains $\bar{D}_{ijkl} = \bar{E}_{ijkl}$ if the material is under elastic deformation or there is no plastic flow.

4.4 Computation of the Tensile and Compressive Damage Multiplier

In the following, the damage multipliers, $\dot{\lambda}_d^{\pm}$, are obtained using the consistency conditions in Eq. (2.44). The incremental expression for the damage consistency condition can be written as:

$$g^{\pm(n+1)} = g^{\pm(n)} + \Delta g^{\pm} = 0 \tag{4.65}$$

where $g^{\pm}$ is the tensile and compressive damage surface function given in Eq. (2.39) and $\Delta g^{\pm}$ is the increment of the damage function which is expressed by:

$$\Delta g^{\pm} = \frac{\partial g^{\pm}}{\partial Y_{ij}^{\pm}}\Delta Y_{ij}^{\pm} + \frac{\partial g^{\pm}}{\partial K^{\pm}}\Delta K^{\pm} \tag{4.66}$$

However, since $Y_{ij}^{\pm}$ is a function of $\sigma_{ij}^{\pm}$ and $\varphi_{ij}^{\pm}$ from Eq. (3.37), one can write the following:

$$\Delta Y_{ij}^{\pm} = \frac{\partial Y_{ij}^{\pm}}{\partial \sigma_{kl}^{\pm}} \Delta \sigma_{kl}^{\pm} + \frac{\partial Y_{ij}^{\pm}}{\partial \varphi_{kl}^{\pm}} \Delta \varphi_{kl}^{\pm} \tag{4.67}$$

where $\Delta \varphi_{kl}^{\pm}$ is obtained from Eqs. (3.28) and (3.29), such that:

$$\Delta \varphi_{kl}^{\pm} = \Delta \lambda_d^{\pm} \frac{\partial g^{\pm}}{\partial Y_{kl}^{\pm}} \tag{4.68}$$

and $\Delta \sigma_{kl}^{\pm}$ can be obtained from Eq. (2.21) as follows:

$$\Delta \sigma_{kl}^{\pm} = \frac{\partial M_{klrs}^{\pm}}{\partial \varphi_{mn}^{\pm}} \Delta \varphi_{mn}^{\pm} \bar{\sigma}_{rs}^{\pm} + M_{klrs}^{\pm} \Delta \bar{\sigma}_{rs}^{\pm} \tag{4.69}$$

By substituting Eqs. (4.67)-(4.69) into Eq. (4.66) and noticing that $\dot{\lambda}^{\pm} = \dot{\varphi}_{eq}^{\pm} = \sqrt{\dot{\varphi}_{ij}^{\pm} \dot{\varphi}_{ij}^{\pm}}$, one can obtain the following relation:

$$\begin{aligned} \Delta g^{\pm} = & \frac{\partial g^{\pm}}{\partial Y_{ij}^{\pm}} \frac{\partial Y_{ij}^{\pm}}{\partial \sigma_{kl}^{\pm}} \frac{\partial M_{klrs}^{\pm}}{\partial \varphi_{mn}^{\pm}} \bar{\sigma}_{rs}^{\pm} \frac{\partial g^{\pm}}{\partial Y_{mn}^{\pm}} \Delta \lambda_d^{\pm} + \frac{\partial g^{\pm}}{\partial Y_{ij}^{\pm}} \frac{\partial Y_{ij}^{\pm}}{\partial \sigma_{kl}^{\pm}} M_{klrs}^{\pm} \Delta \bar{\sigma}_{rs}^{\pm} \\ & + \frac{\partial g^{\pm}}{\partial Y_{ij}^{\pm}} \frac{\partial Y_{ij}^{\pm}}{\partial \varphi_{kl}^{\pm}} \frac{\partial g^{\pm}}{\partial Y_{kl}^{\pm}} \Delta \lambda_d^{\pm} + \frac{\partial g^{\pm}}{\partial K^{\pm}} \frac{\partial K^{\pm}}{\partial \varphi_{eq}^{\pm}} \Delta \lambda_d^{\pm} \end{aligned} \tag{4.70}$$

Substituting the above equation into Eq. (4.65), one obtains $\Delta \lambda_d^{\pm}$ by the following relation:

$$\Delta\lambda_d^{\pm} = \frac{g^{\pm tr}}{H_d^{\pm}} \tag{4.71}$$

where, $g^{\pm tr}$ is the trial value of the damage function, $H_d^{\pm}$ is the tensile or compressive damage modulus and is given as follows:

$$H_d^{\pm} = \frac{\partial g^{\pm}}{\partial Y_{ij}^{\pm}} \frac{\partial Y_{ij}^{\pm}}{\partial \sigma_{kl}^{\pm}} \frac{\partial M_{klrs}^{\pm}}{\partial \varphi_{mn}^{\pm}} \bar{\sigma}_{rs}^{\pm} \frac{\partial g^{\pm}}{\partial Y_{mn}^{\pm}} + \frac{\partial g^{\pm}}{\partial Y_{ij}^{\pm}} \frac{\partial Y_{ij}^{\pm}}{\partial \varphi_{kl}^{\pm}} \frac{\partial g^{\pm}}{\partial Y_{kl}^{\pm}} + \frac{\partial g^{\pm}}{\partial K^{\pm}} \frac{\partial K^{\pm}}{\partial \varphi_{eq}^{\pm}} \tag{4.72}$$

where,

$$\frac{\partial g^{\pm}}{\partial K^{\pm}} = -1 \tag{4.73}$$

$$\frac{\partial K^{\pm}}{\partial \varphi_{eq}^{\pm}} = \frac{K_0^{\pm}}{B^{\pm} q^{\pm}} \left(\frac{B}{\varphi_{eq}^{\pm}} \right)^{\frac{q^{\pm}-1}{q^{\pm}}} \tag{4.74}$$

$$\frac{\partial g^{\pm}}{\partial Y_{ij}^{\pm}} = \frac{L_{ijkl}^{\pm} Y_{kl}^{\pm}}{2\sqrt{\frac{1}{2} Y_{ij}^{\pm} L_{ijkl}^{\pm} Y_{kl}^{\pm}}} \tag{4.75}$$

CHAPTER V

IDENTIFICATION OF MATERIAL PARAMETERS

Material parameters, such as the tensile and compressive hardening modulus h^+ and Q^-, the tensile and compressive strength where uniaxial nonlinearity starts $B^\pm$, the compressive hardening rate constant b^-, and constants for the power tensile and compressive damage evolution law $q^\pm$ are calibrated in order for the application of the coupled plasticity-damage model to the analysis of plain concrete and to investigate the predictive capability of the proposed power damage evolution law. The algorithmic model presented in the previous chapter is coded as a UMAT user material subroutine and implemented in the commercial finite element software Abaqus, and the response of the constitutive model is compared to the uniaxial tensile and compressive loading-unloading experimental results.

5.1 Calibration of the Compressive Plasticity and Damage Evolution Laws from Loading-unloading Uniaxial Test

The identification of the plastic and damage material constants is commonly relied on monotonic stress-strain experimental curves in the field of continuum damage mechanics. Such an approach, however, results in a non-unique determination of these material constants. Therefore, a simple procedure for the identification of plasticity and damage material parameters is addressed.

Once the compressive yield strength f_0^- is determined from monotonic or cyclic experimental results, the cyclic loading-unloading uniaxial compressive stress-strain experimental curve should then be used in identifying unique values for the material constants Q^- and b^- in Eq. $(2.34)_1$ and B^-, K_o^-, and q^- in Eqs. (2.48) and (2.52). Therefore, loading-unloading stress-strain data can be used to identify the material constants associated with the plasticity and damage constitutive equations simultaneously such that the reduction in Young's modulus can be used to identify the damage parameters. Once the damage law is calibrated, it can then be used to establish the effective stress-strain diagram which helps to identify the plasticity material constants in the effective (undamaged) configuration. This is demonstrated in the following subsections for some experimental loading-unloading compressive stress-strain diagrams. However, it is noteworthy that the values of Q^- and b^- are crucial for the evolution of the compressive damage density when using either the exponential or the power damage compressive evolution equations, Eqs. (2.48) and (2.52), and hence they are crucial for the accurate prediction of the nominal stress-strain relationship. For example, Figures. 5.1 and 5.2 show the evolution of the compressive damage density versus the applied strain by changing the values of the compressive plasticity hardening parameters Q^- and b^-, respectively.

In the case of using the exponential damage evolution law, the damage evolution versus the applied strain, as expected, shows that the rate of damage growth is high initially and then decays to reach a constant value depending on Q^-.

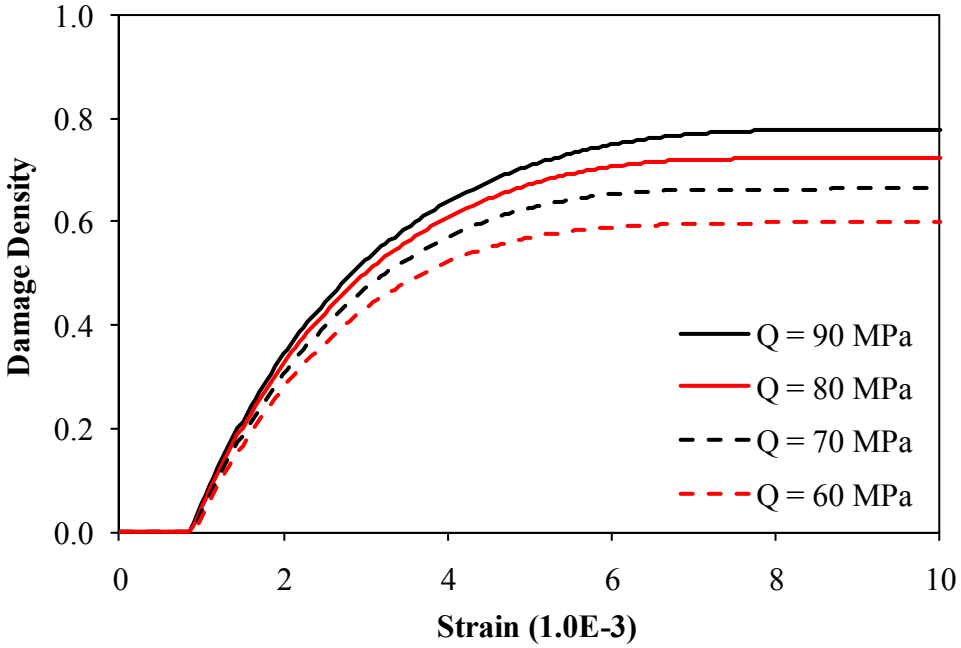

(a)

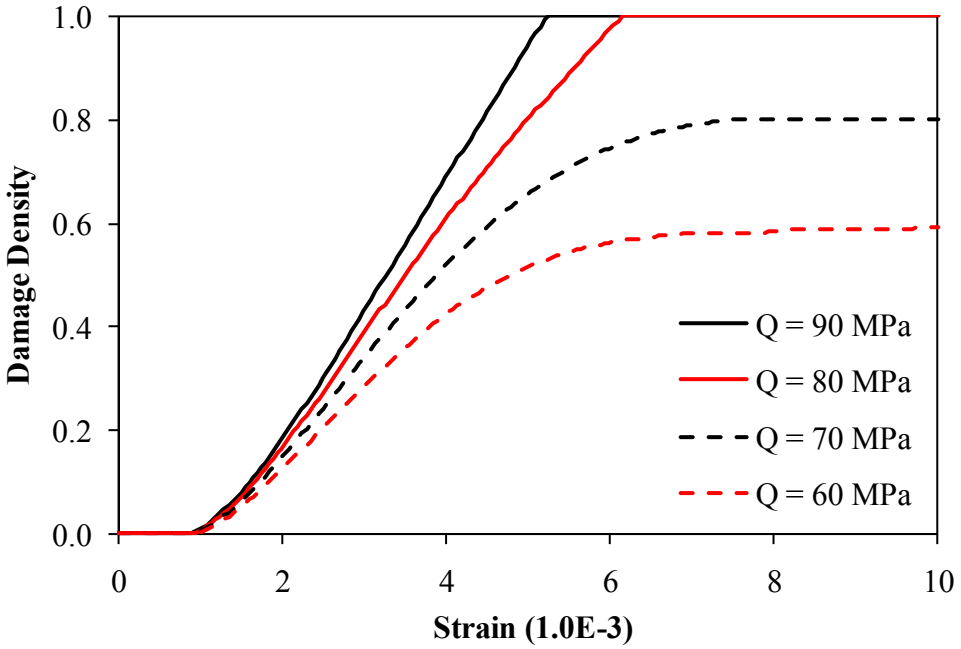

(b)

Figure 5.1 Evolution of the damage due to the change of the compressive hardening modulus Q^- for: (a) Exponential damage evolution law in Eq. (2.48) and (b) power damage evolution law in Eq. (2.52)

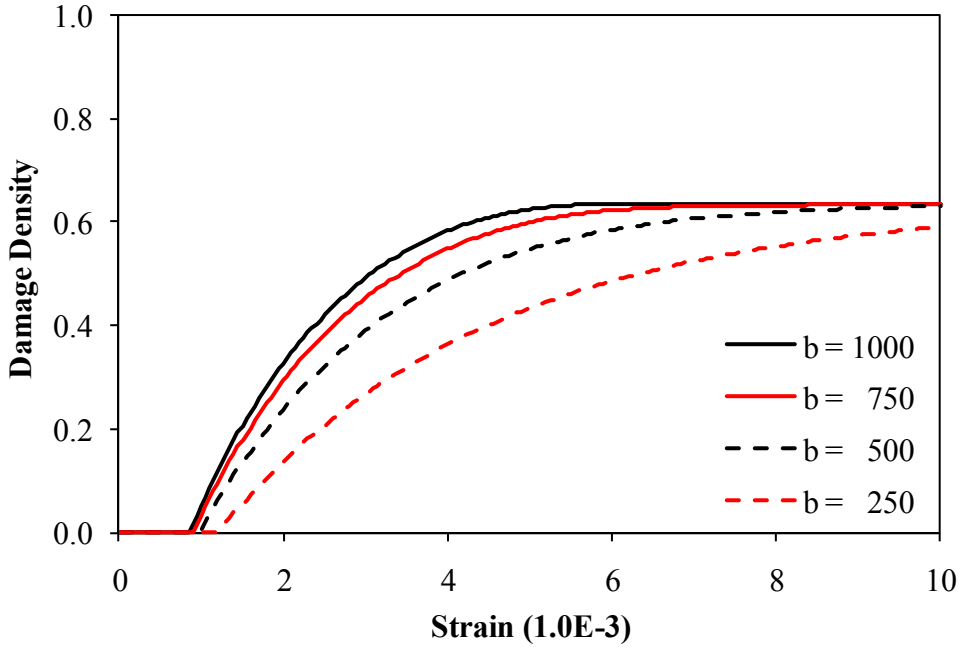

(a)

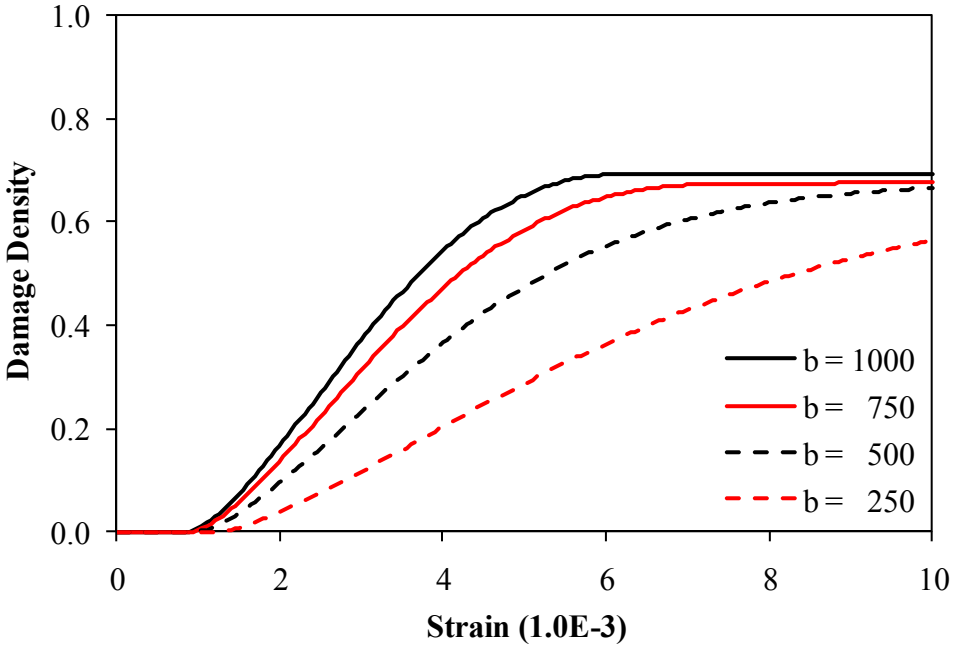

(b)

Figure 5.2 Evolution of the damage due to the change of the compressive hardening rate constant b^- for: (a) Exponential damage evolution law in Eq. (2.48) and (b) power damage evolution law in Eq. (2.52)

Meanwhile, when the power damage evolution law is used, the damage growth is slow initially and then increases with the strain, but decays at higher strains depending on the value of Q^- to give a desirable S-shape for the damage evolution. Moreover, for both damage evolution laws, the value of b^- affect the damage nucleation and growth rate whereas the value of Q^- affect the final damage value.

5.1.1 Prediction of the Test Result by Karsan and Jirsa (1969)

Since the plasticity constitutive equations are defined in the effective configuration, stress-strain data for an undamaged material is needed to indentify the plasticity material constants. One can establish such an effective stress-strain diagram from the nominal (damaged) loading-unloading stress-strain data by determining the damaged Young's modulus E, for each cycle which is shown in Figure 5.3. From Eqs. (2.7) and (2.8), one can define the effective stress $\bar{\sigma}$ as $\bar{\sigma} = (\bar{E} / E)\sigma$, where $\bar{E}$, E, and σ are measurable quantities such that at each unloading point (A to E) the damaged Young's moduli are determined by connecting each unloading and reloading points (A' to E').

As shown in Figure 5.3, the experimental effective stress-strain shows an almost linear relation, and the predicted effective stress-strain curve is in close agreement with the experimental result. Based on this analysis, the compressive yield strength f_0^-, compressive hardening modulus Q^-, and the compressive hardening rate constant b^-, although there can be numerous combinations, are determined as 15 MPa, 74 MPa, and 670, respectively. Moreover, from Eq. (2.8) and the measured damaged Young's modulus in Figure 5.3, one can plot the variation of the damage density with strain as

shown in Figure 5.4(b) such that $\varphi = 1 - \sqrt{E / \bar{E}}$. Hence, these data can be used in identifying the damage parameters B^- and q^- and the damage threshold K_0^- .

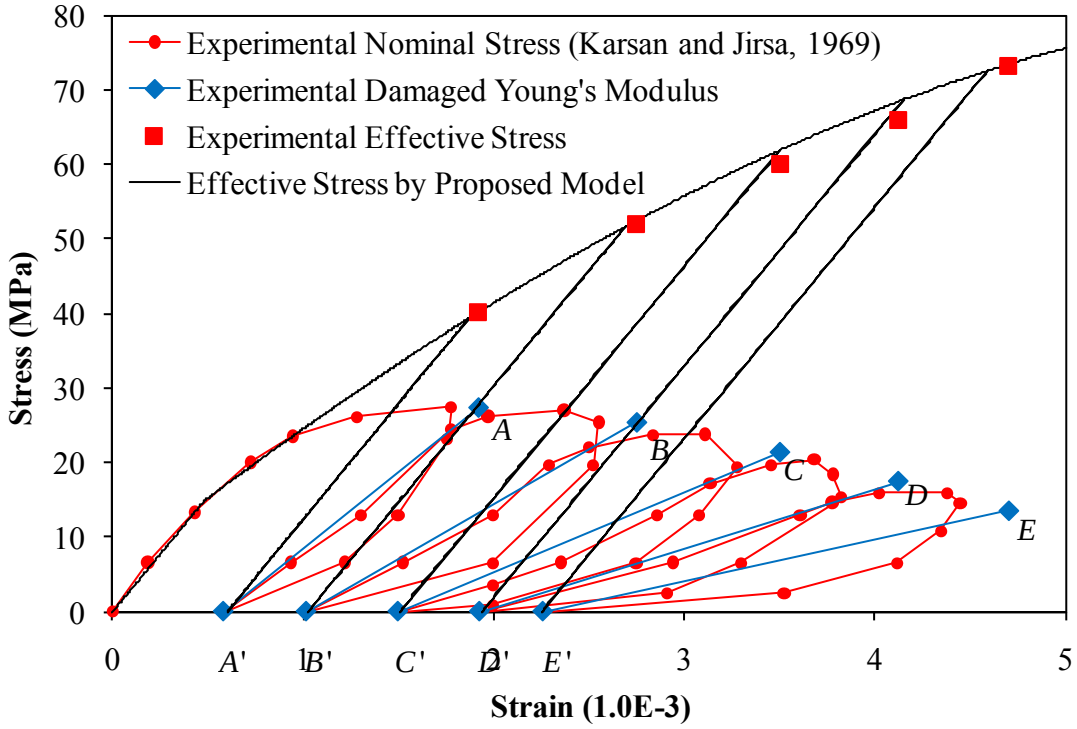

Figure 5.3 Experimental analysis and predicted stress-strain diagrams in the effective (undamaged) and nominal (damaged) configurations for Karsan and Jirsa (1969) experimental data

The predicted nominal stress-strain curves and the damage densities using the exponential and power damage evolution laws as compared to the experimental results are shown in Figures 5.4 and 5.5, and the identified compressive plasticity and damage material constants are listed in Table 5.1.

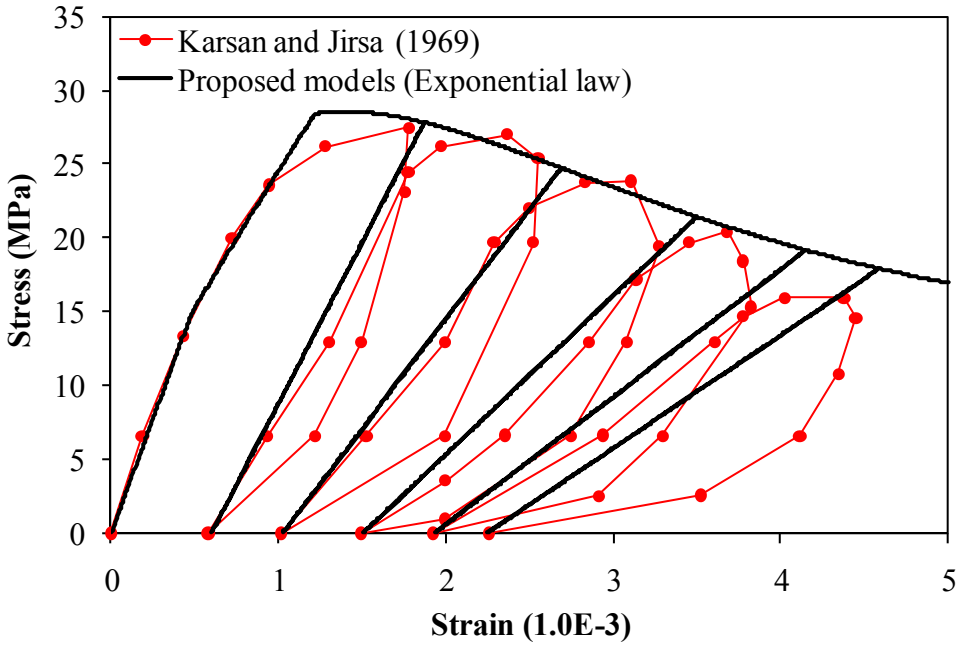

(a)

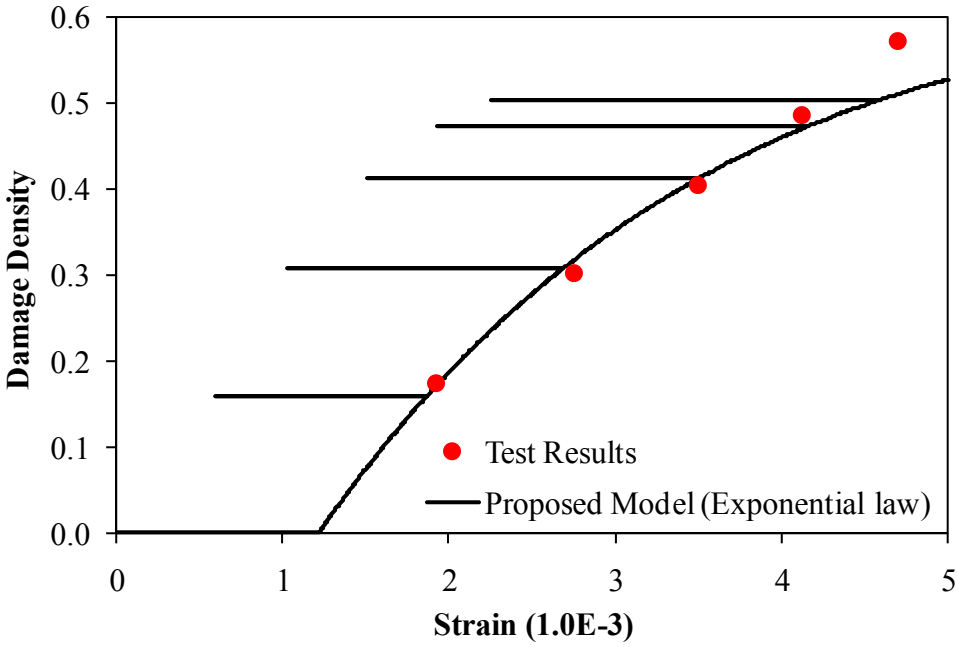

(b)

Figure 5.4 Comparison of the compressive loading-unloading analysis results with the experimental data by Karsan and Jirsa (1969) using the exponential damage evolution law: (a) Nominal stress-strain curve and (b) damage density

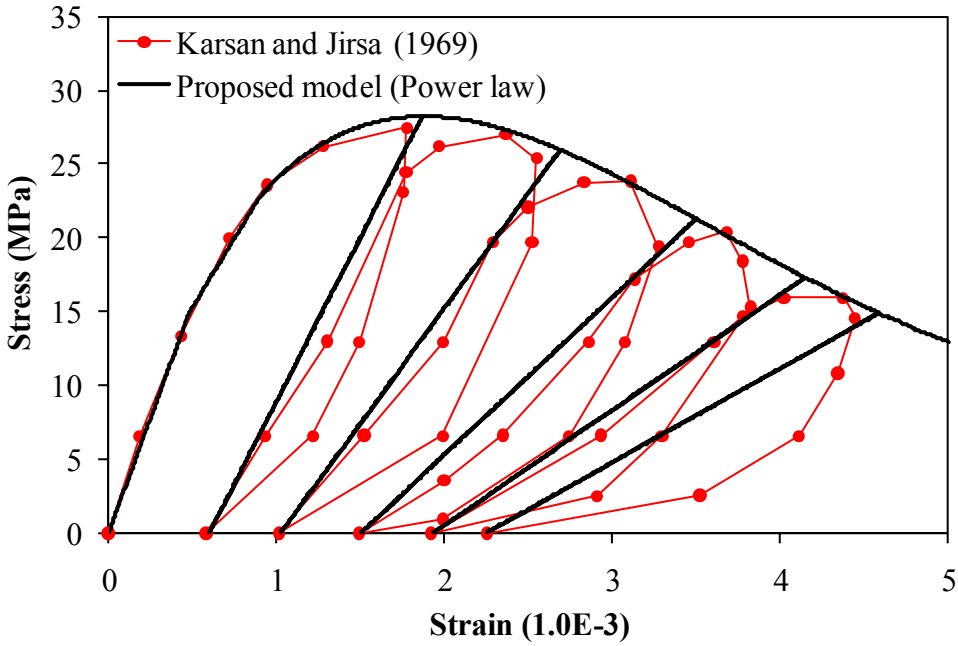

(a)

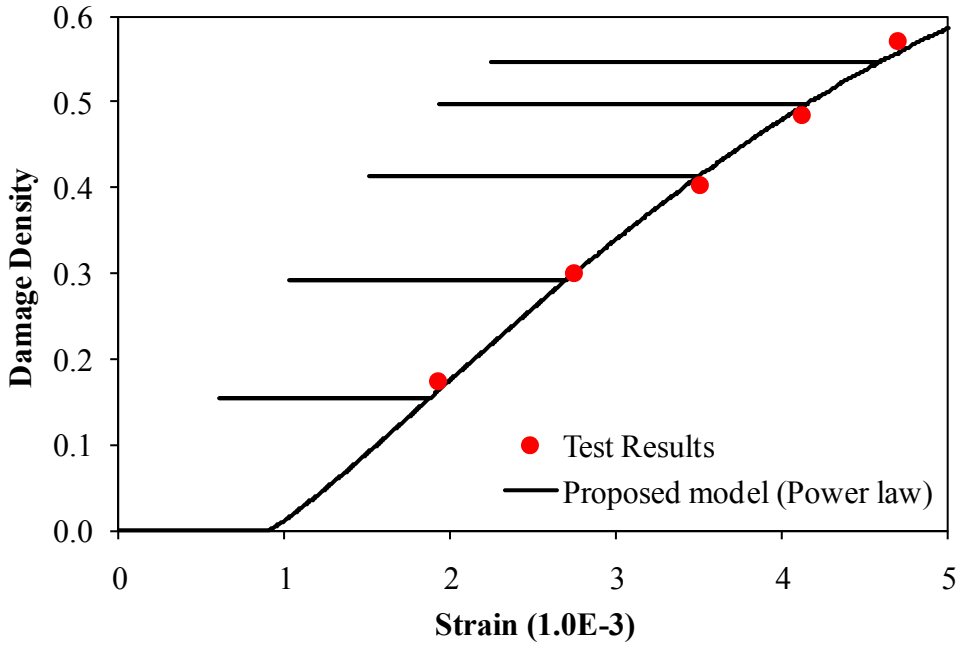

(b)

Figure 5.5 Comparison of the compressive loading-unloading analysis results with the experimental data by Karsan and Jirsa (1969) using the power damage evolution law: (a) Nominal stress-strain curve and (b) damage density

Table 5.1 Material constants identified from the experimental results by Karsan and Jirsa (1969)

	$\bar{E}$ (MPa)	ν	f_0^- (MPa)	Q^- (MPa)	b^-	K_0^- (MPa)	B^-	q^-
Exponential law	31,000	0.2	15	74	670	25	0.45	-
Power law						20	0.22	1.16

One can see that the power damage evolution law as in Figure 5.5 gives much better predictions of both the nominal stress-strain diagram and the damage density as compared to the predictions of the exponential damage law as in Figure 5.4. However, one may argue that the power damage law is associated with three material constants (B^-, q^-, and K_0^-) whereas the exponential damage law is as associated with only two material constants (B^- and K_0^-) such that one can obtain better predictions with more material constants.

In fact, in this study, setting $q^- = 1$ (i.e. linear damage law) in all the numerical examples yielded much better predictions than the exponential damage law. Moreover, the smoothness of the stress-strain diagram, the accurate prediction of the damaged modulus, and the S-shape of the variation of the damage density with strain are highly desirable predicted features by the power law (or linear law when $q^- = 1$).

5.1.2 Prediction of the Test Result by Sinha et al.(1964)

Following the same procedure as in the previous subsection, the effective stress-strain diagram for the experimental result carried by Sinha et al. (1964) is established from the nominal stress-strain loading-unloading diagram as shown in Figure 5.6. The predicted

effective stress-strain relation agrees well with the established effective stress-strain diagram if the values of the material constants f_0^-, Q^-, and b^- are identified as 14 MPa, 41 MPa, and 430, respectively. Furthermore, the compressive damage parameters are identified through fitting the established damage density versus strain from the nominal stress-strain loading-unloading experimental curve (see Figure 5.7(b)). The identified compressive plasticity and damage material constants associated with fitting the experimental data by Sinha et al. (1964) are listed in Table 5.2. These constants are then used to predict the nominal stress-strain diagram and damage density as shown in Figures 5.7 and 5.8 when using the exponential and power damage laws, respectively.

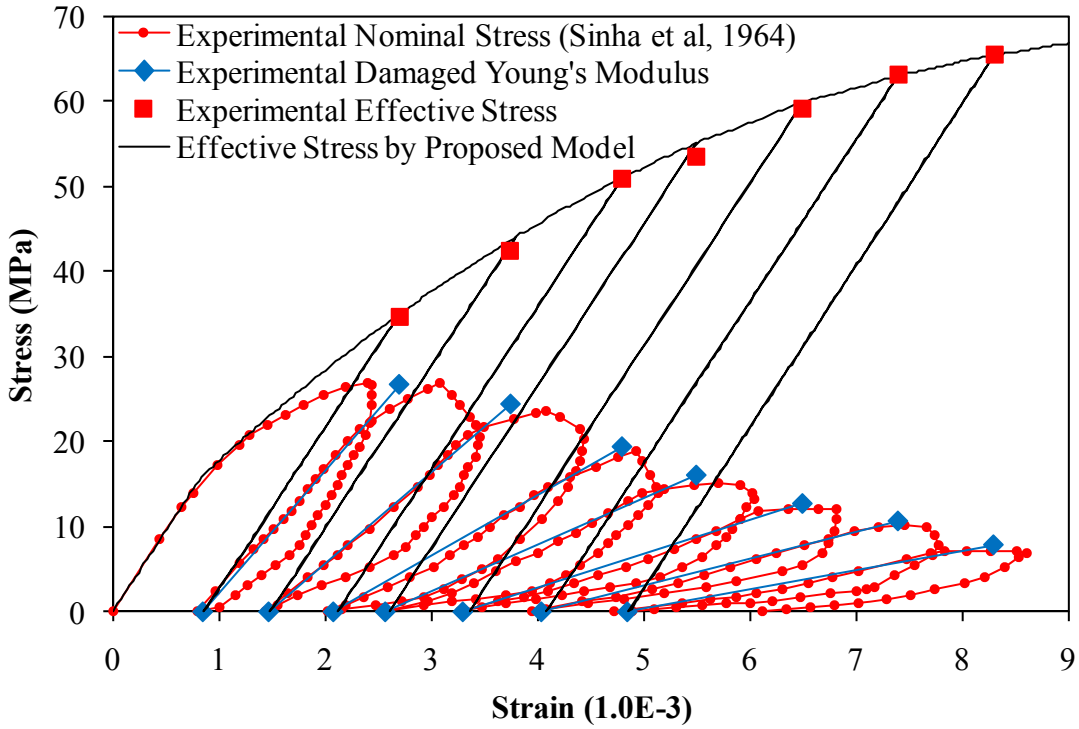

Figure 5.6 Experimental analysis and predicted stress-strain diagrams in the effective (undamaged) and nominal (damaged) configurations for Sinha et al. (1964) experimental data

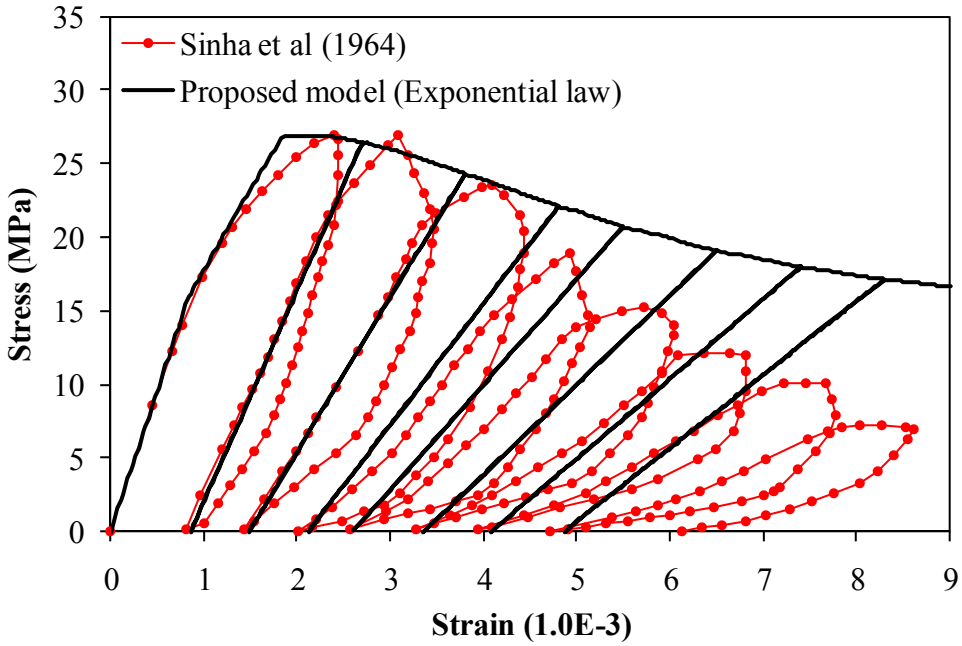

(a)

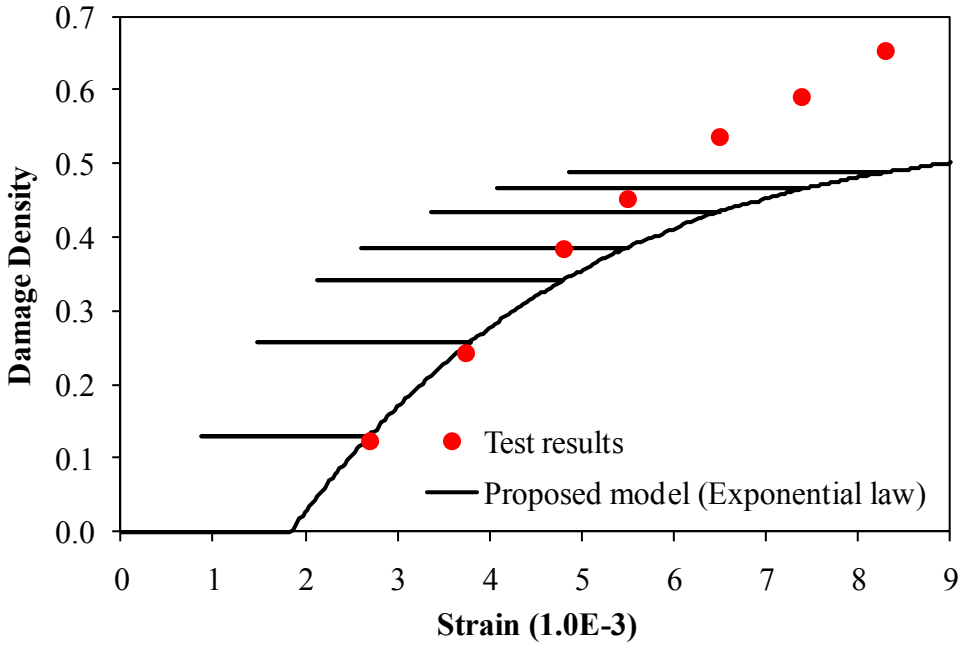

(b)

Figure 5.7 Comparison of the compressive loading-unloading analysis results with the experimental data by Sinha et al. (1964) using the exponential damage law: (a) Nominal stress-strain curve and (b) damage density

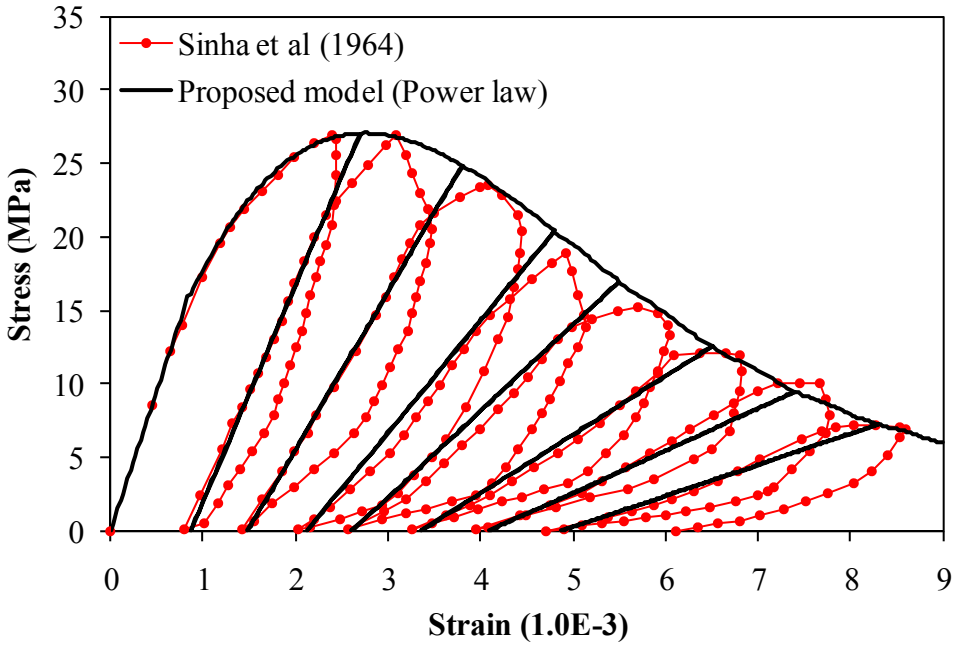

(a)

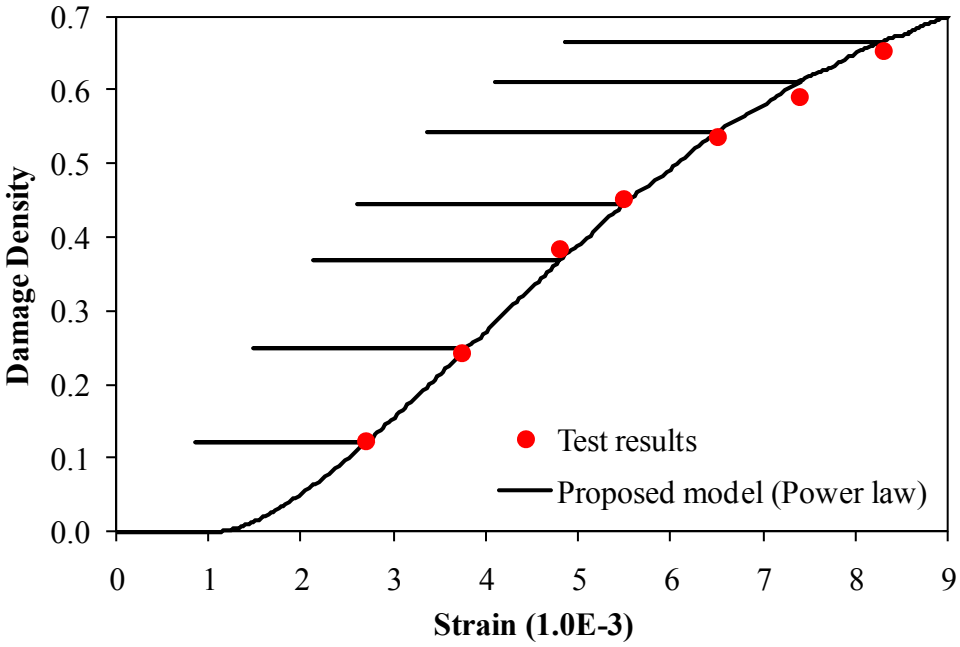

(b)

Figure 5.8 Comparison of the compressive loading-unloading analysis results with the experimental data by Sinha et al. (1964) using the power damage law: (a) Nominal stress-strain curve and (b) damage density

Table 5.2 Material constants identified from the experimental results of Sinha et al. (1964)

	$\bar{E}$ (MPa)	ν	f_0^- (MPa)	Q^- (MPa)	b^-	K_0^- (MPa)	B^-	q^-
Exponential law	19,000	0.2	14	41	430	9	0.5	-
Power law						14.1	0.2	1.57

It can be seen, as concluded from the previous analysis of Karsan and Jirsa (1969) data, that the power damage evolution law gives a more accurate description of the softening part of the stress-strain diagram, degradation of the Young's modulus, and the S-shape curve for the damage density versus the applied strain.

5.2 Calibration of the Tensile Plasticity and Damage Evolution Laws from Loading-unloading Uniaxial Tests

The procedure in section 5.1 for the identification of the material constants associated with the compressive plasticity and damage constitutive equations is also followed here for calibration of the tensile plasticity and damage constitutive equations. The loading-unloading uniaxial tensile tests by Taylor (1992) are adopted in order to identify the material constants in Eqs. $(2.34)_2$, (2.47), and (2.51) (i.e. f_0^+, h^+, B^+, K_0^+, and q^+).

Figures 5.9 and 5.10 show the analysis results where the identified material constants are listed in Table 5.3 for both exponential and power damage evolution laws, respectively. Although the two laws give similar results for the case of tensile loading, the power damage evolution law gives closer predictions of the softening part of the stress-strain diagram as compared to the corresponding prediction by the exponential

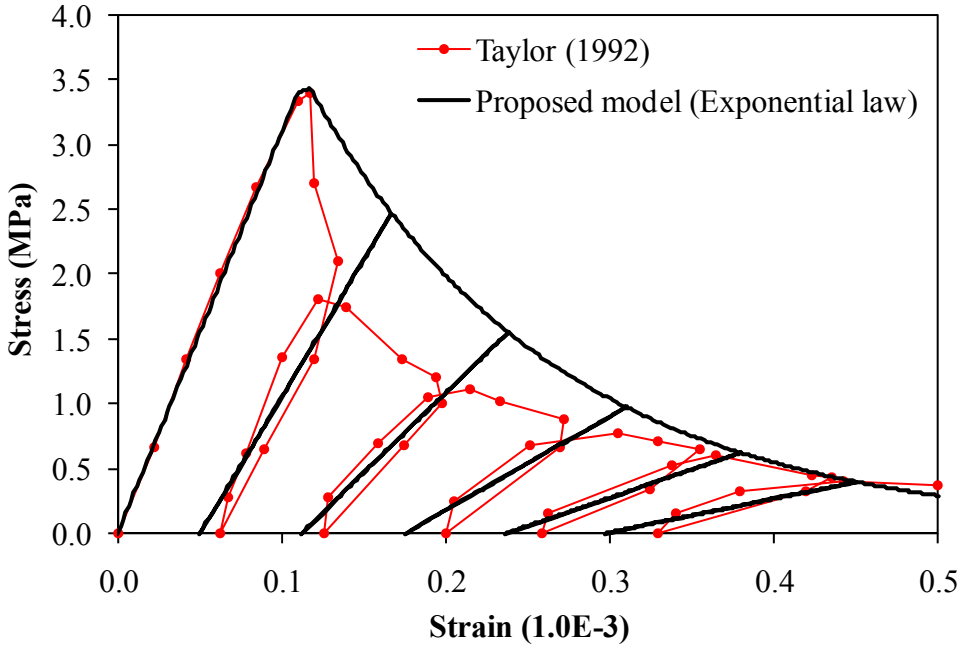

(a)

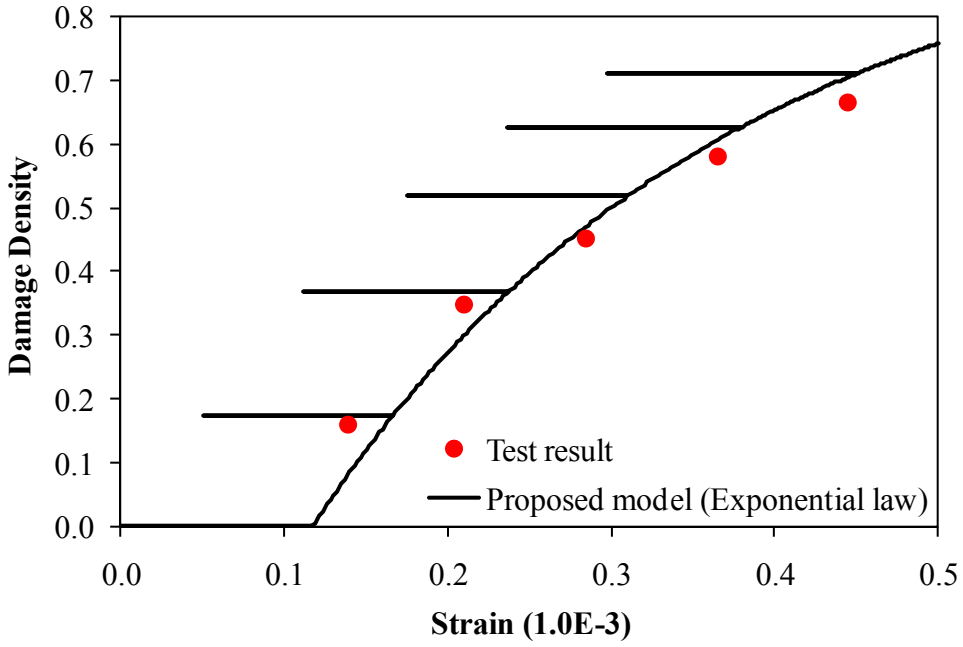

(b)

Figure 5.9 Comparison of the uniaxial tensile loading-unloading analysis results with the experimental data by Taylor (1992) using the exponential damage law: (a) Nominal stress-strain curve and (b) damage density

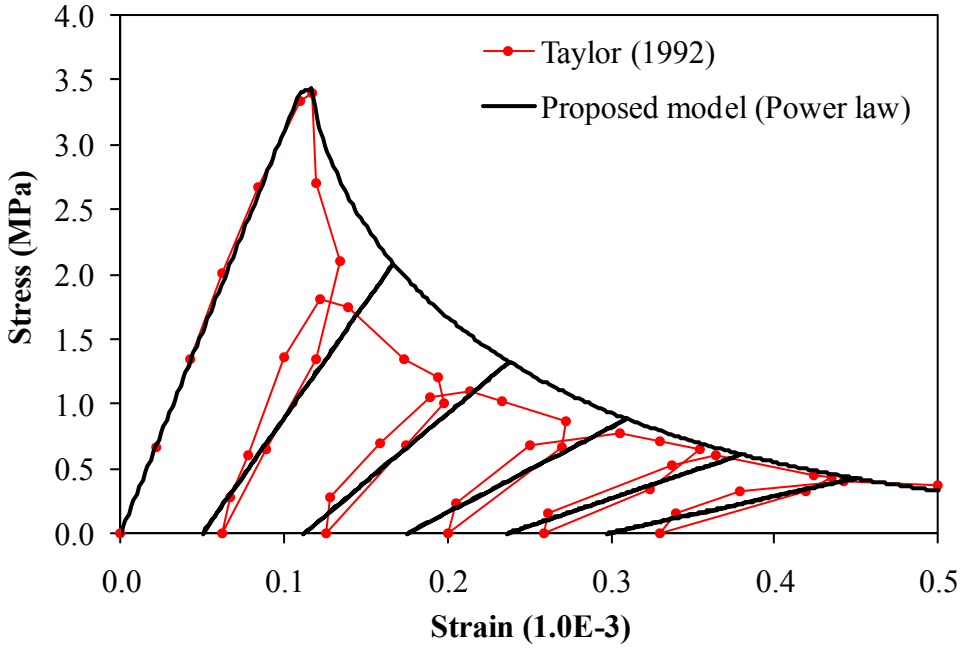

(a)

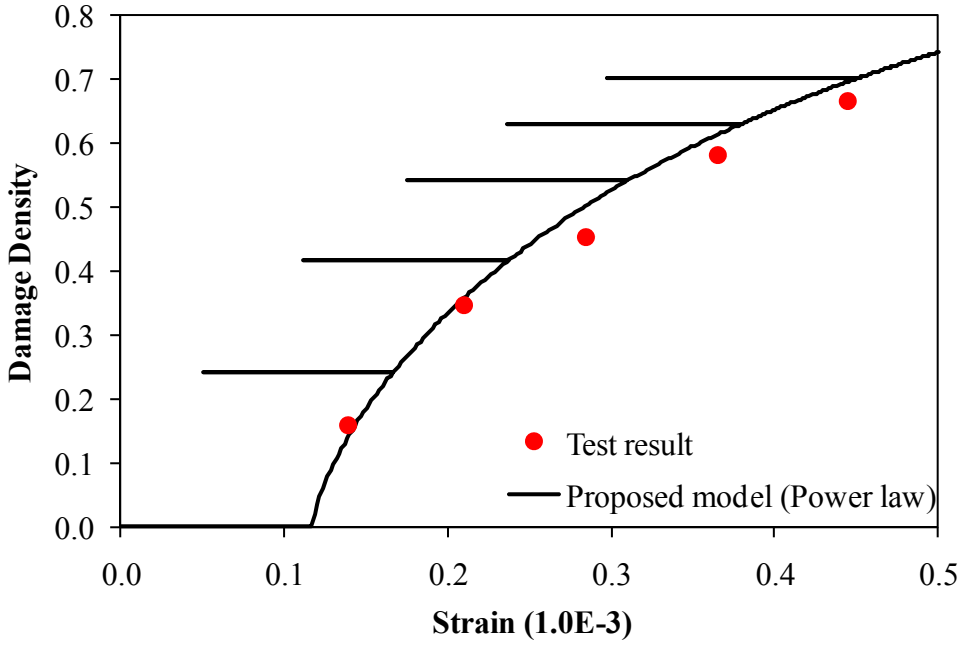

(b)

Figure 5.10 Comparison of the uniaxial tensile loading-unloading analysis results with the experimental data by Taylor (1992) using the power damage law: (a) Nominal stress-strain curve and (b) damage density

Table 5.3 Material constants identified from the experimental data by Taylor (1992)

	$\bar{E}$ (MPa)	ν	f_0^+ (MPa)	K_0^+ (MPa)	h^+ (MPa)	B^+	q^+
Exponential law	31,000	0.2	3.40	3.43	4,500	2.4	-
Power law						1.9	0.7

damage evolution equation. For the result using the power damage law in Figure 5.10(a), the difference between the experimental and numerical stress-strain curve at the softening region still exists. This is because both the nominal stress-strain relation and the loading-unloading paths are considered simultaneously in calibrating the tensile constitutive equations. If the unloading parts are disregarded as in the case of monotonic uniaxial tensile loading, one can get a more precise prediction by using the power damage law, and those cases are considered in the next chapter.

CHAPTER VI

VERIFICATION OF THE PROPOSED MODEL IN THE MACRO-SCALE

The proposed coupled plasticity-damage model for plain concrete is verified on macroscopic level by comparing the response of the proposed constitutive model with various experimental data; monotonic uniaxial tension and compression, monotonic biaxial compression, and mixed mode fracture for different types of concrete. Moreover, as a result of the uniaxial loading-unloading tensile and compressive analysis performed at previous chapter, the power damage evolution law shows a better ability to predict the softening behavior of concrete for both compressive and tensile loading-unloading results. Therefore, the power damage evolution law, instead of the exponential damage law that has been used widely in the literature, is used in all of the following predictions and simulations.

6.1 Monotonic Uniaxial Compressive Loading

Two different monotonic uniaxial compressive experimental results (Karsan and Jirsa 1969; Zhang 2001) are employed. The analysis results using the power damage evolution law are compared with the test results in Figures 6.1 and 6.2, and the material constants used for the prediction of the two test results are listed in Table 6.1. For both cases, the softening behaviors of concrete under compressive loading as well as the hardening regime are well predicted. However, it is noteworthy that since the loading-unloading experimental data are not available for uniaxial compressive loading for the

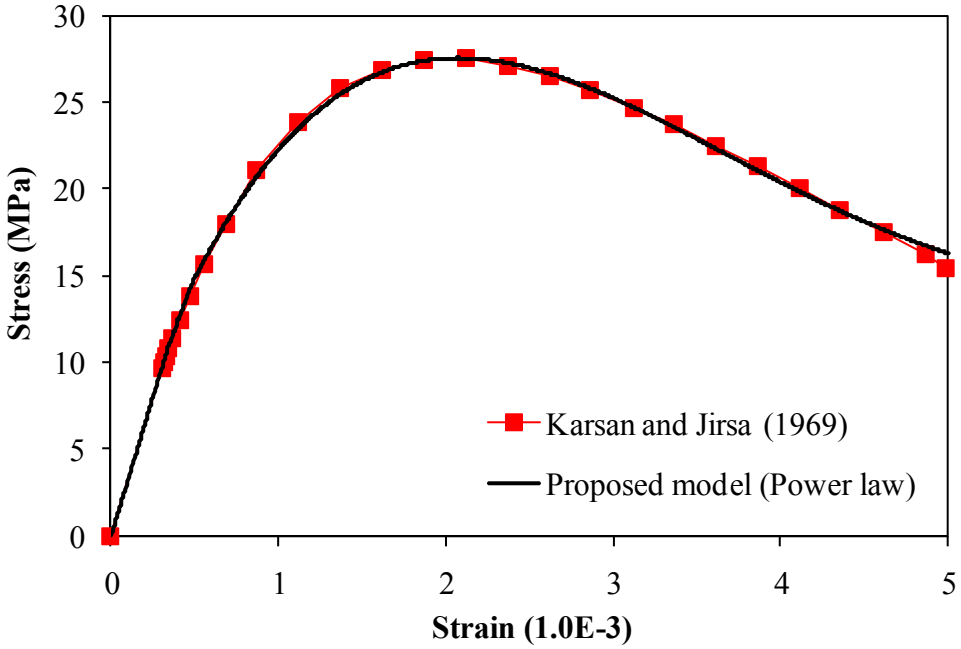

(a)

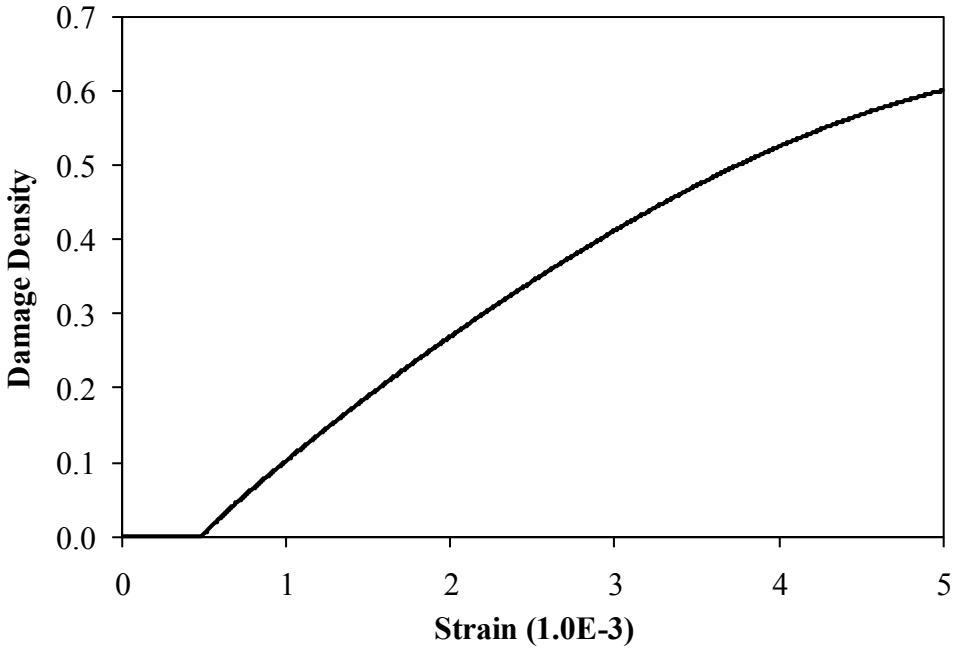

(b)

Figure 6.1 Prediction of the monotonic uniaxial compressive experimental data by Karsan and Jirsa (1969): (a) Stress-strain relation and (b) damage density

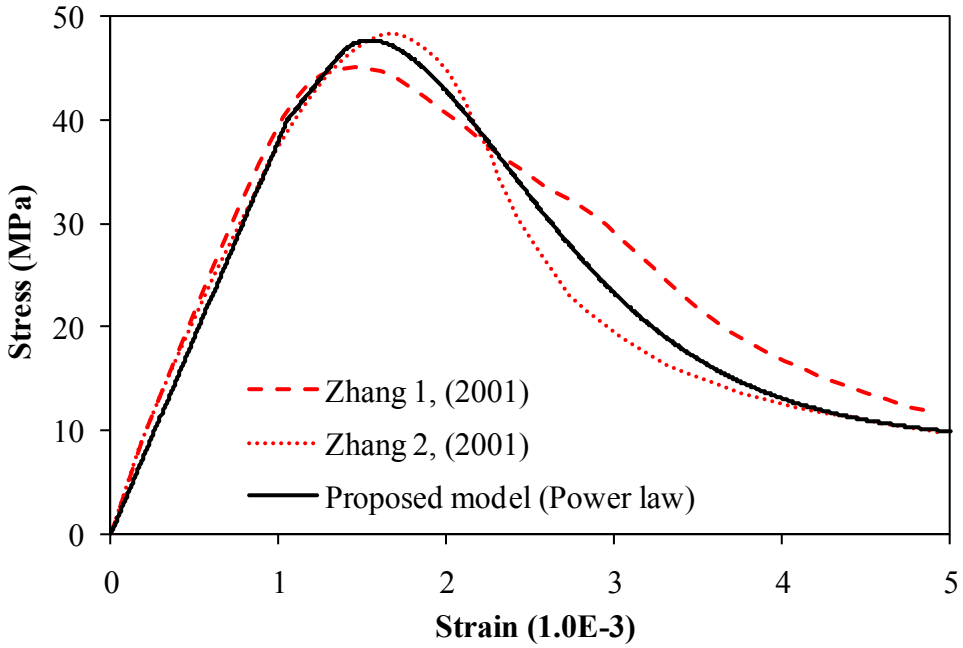

(a)

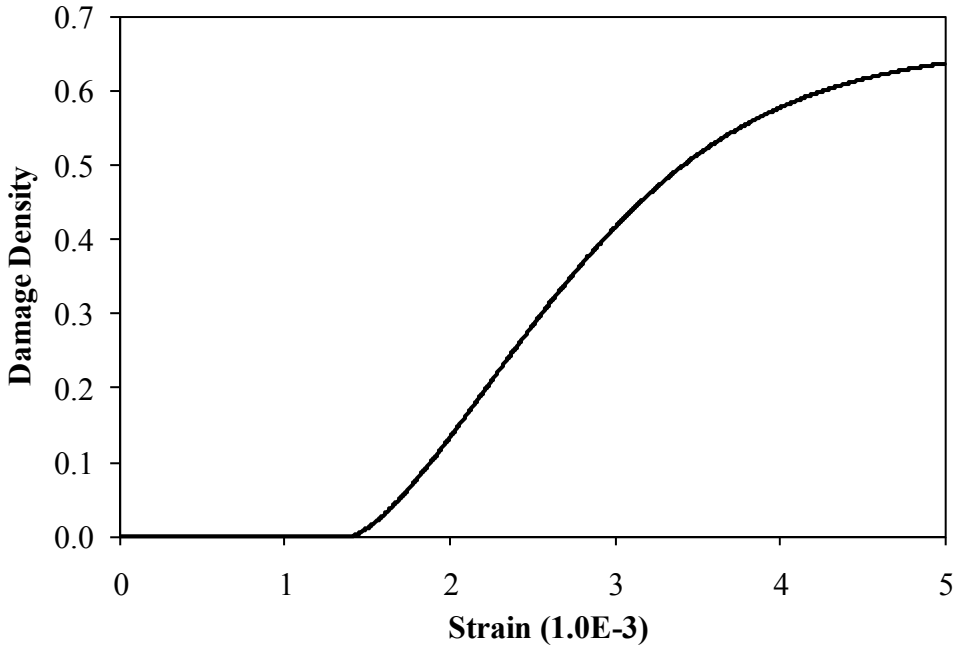

(b)

Figure 6.2 Prediction of the monotonic uniaxial compressive experimental data by Zhang (2001): (a) Stress-strain relation and (b) damage density

Table 6.1 Material constants used for the monotonic uniaxial compressive loading analysis

	$\bar{E}$ (MPa)	ν	f_0^- (MPa)	K_0^+ (MPa)	Q^- (MPa)	b^-	B^-	q^-
Karsan and Jirsa (1969)	32,000	0.2	11	12.8	100	1350	0.11	0.93
Zhang (2001)	38,000	0.2	40	41	36	1300	1.35	1.55

concrete considered in Figures 6.1(a) and 6.2(a), which are crucial for identifying the material parameters of the compressive damage law, one may use another set of material constants in Table 6.1 to get analogous predictions. Hence, the loading-unloading experimental results are indispensable to obtain a unique set of material parameters. This is also true for the following monotonic uniaxial tensile loading predictions.

6.2 Monotonic Uniaxial Tensile Loading

Two representative monotonic uniaxial tensile tests (Gopalaratnam and Shah 1985; Zhang 2001) are compared with the analysis results using the proposed tensile damage evolution law. The tensile material constants used to predict the two test results are listed in Table 6.2, and Figures 6.3 and 6.4 show the analysis results. As seen, the predicted nominal stress-strain relations by the proposed constitutive model using the power tensile damage evolution law are in close agreement with the experimental results.

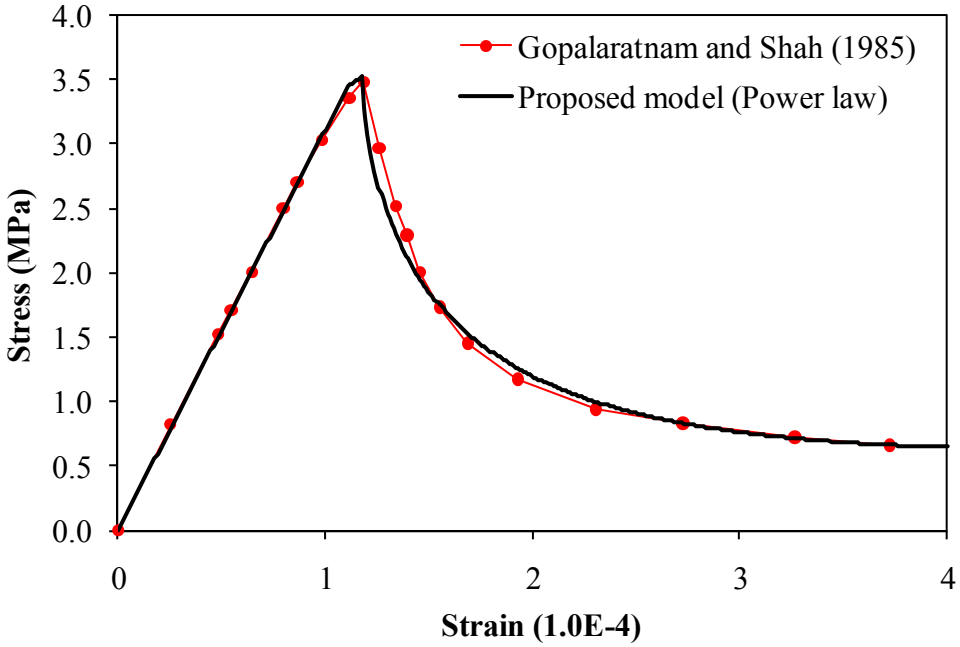

(a)

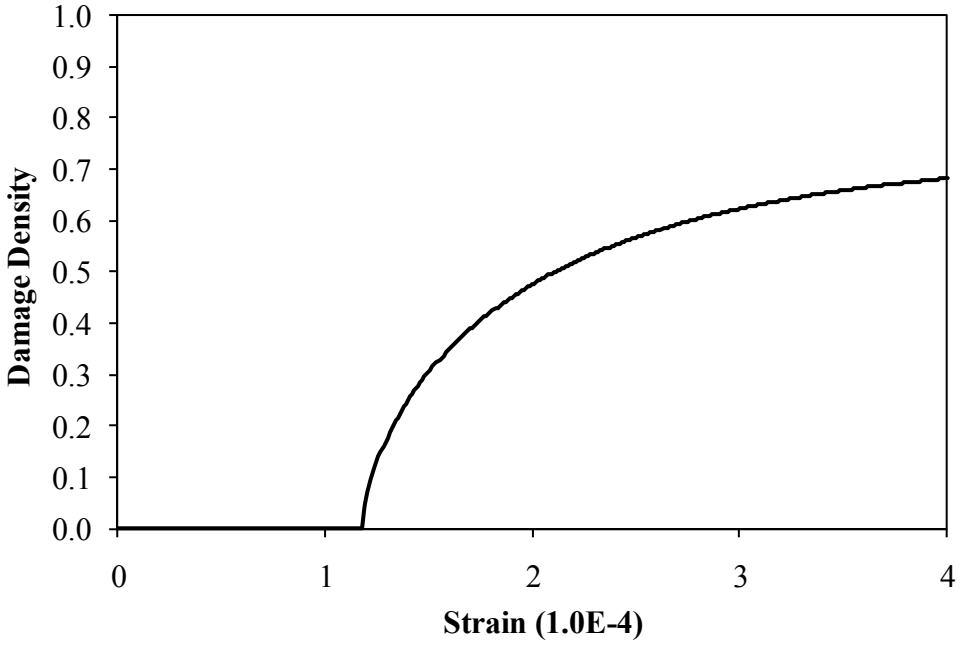

(b)

Figure 6.3 Prediction of the monotonic uniaxial tensile experimental data by Gopalaratnam and Shah (1985): (a) Stress-strain relation and (b) damage density

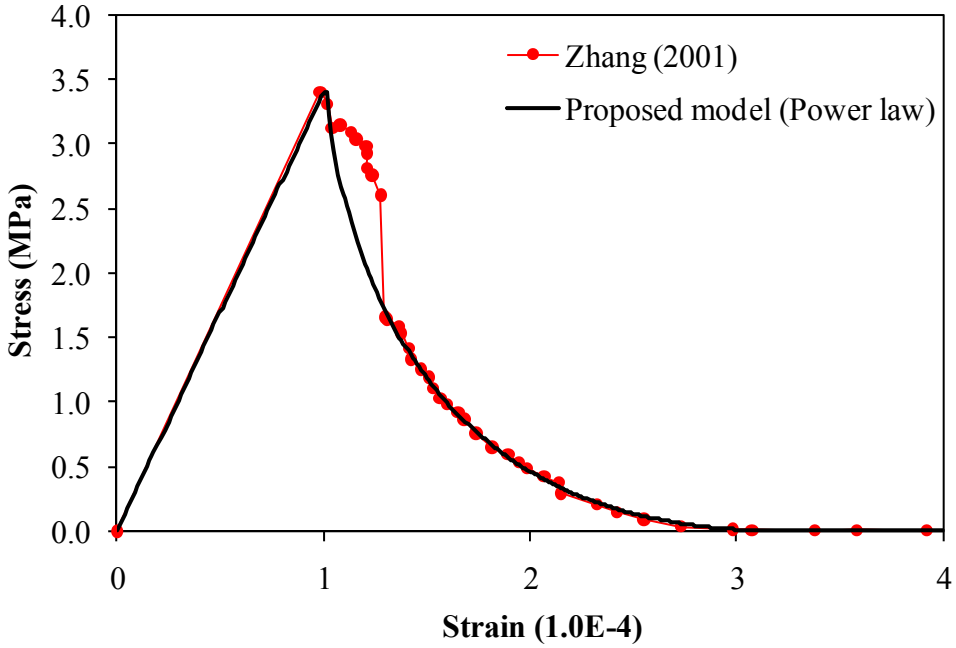

(a)

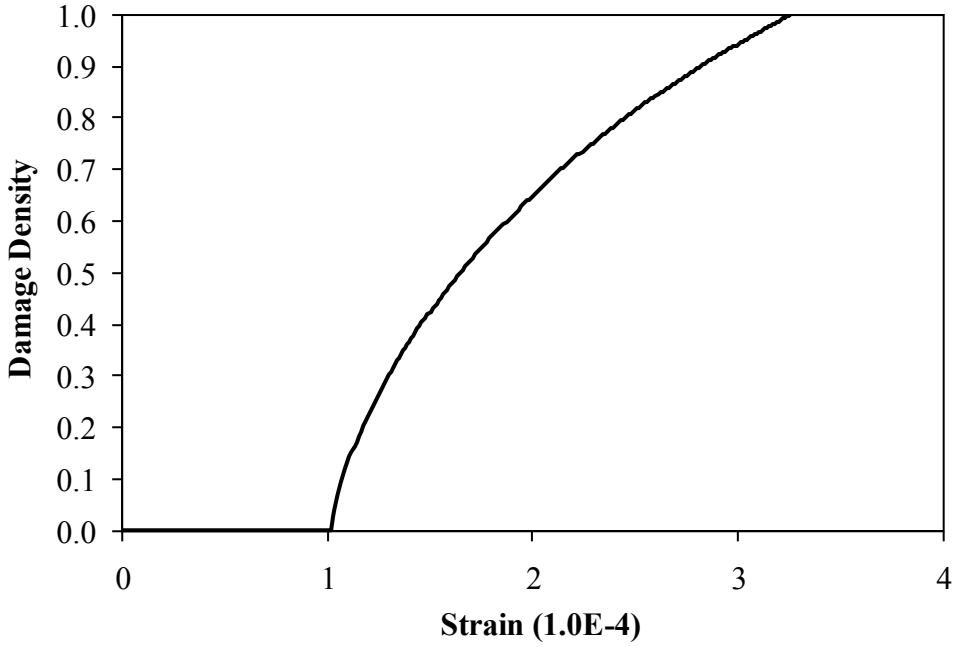

(b)

Figure 6.4 Prediction of the monotonic uniaxial tensile experimental data by Zhang (2001): (a) Stress-strain relation and (b) damage density

Table 6.2 Material constants used for the monotonic uniaxial tensile loading analysis

	$\bar{E}$ (MPa)	ν	f_0^+ (MPa)	K_0^+ (MPa)	h^+ (MPa)	B^+	q^+
Gopalaratnam and Shah(1985)	31,000	0.2	3.45	3.52	15,000	1.4	0.6
Zhang (2001)	34,000	0.2	3.39	3.40	4,500	3.1	0.67

6.3 Monotonic Biaxial Compressive Loading

The biaxial compressive test results carried out by Kupfer et al. (1969) are adopted in this research in order to validate the proposed model. The analysis results are compared with the experimental results in Figures 6.5(a)-(c) and the damage densities of each case are compared in Figure 6.5(d). The material constants used in this simulation are listed in Table 6.3. Those material constants are determined from the monotonic uniaxial compressive loading test in Figure 6.5(a) and then the same properties are used in predicting the biaxial compressive experimental results in Figures 6.5(b) and (c).

The predicted results in Figures 6.5(b) and (c) agree well with the test results although the ultimate stress is somewhat over predicted. Moreover, the damage density of the specimen under loading condition $\sigma_2 / \sigma_1 = -1/-1$ is slightly higher than that of the specimen under uniaxial loading $\sigma_2 / \sigma_1 = 1-/0$, while the damage density of the specimen under the loading condition $\sigma_2 / \sigma_1 = -1/-0.52$ is lower. This implies that the lump sum of damage densities in all directions is the highest for equi-biaxial compressive loading.

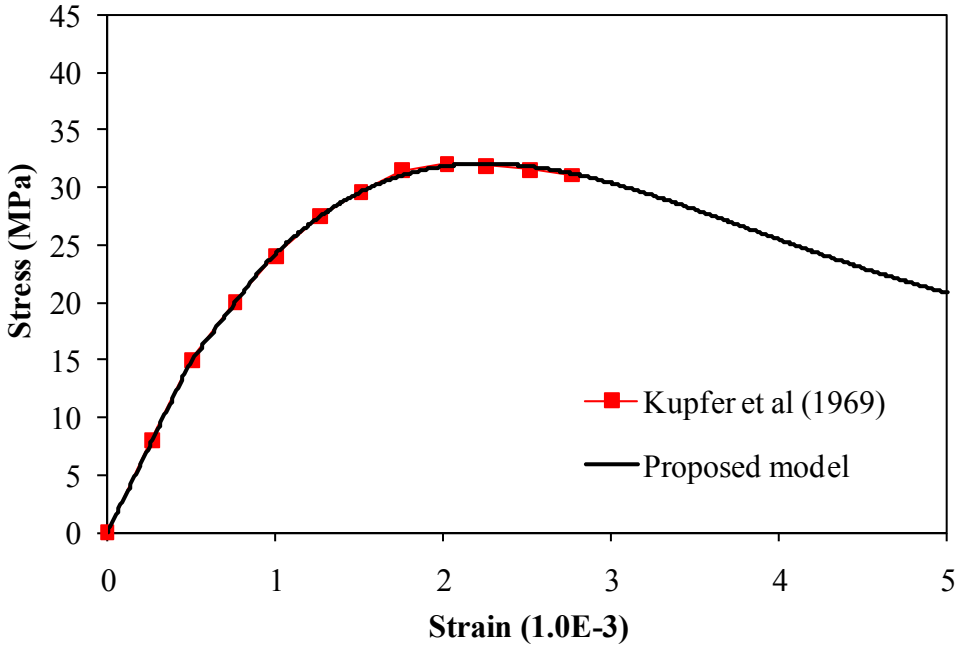

(a)

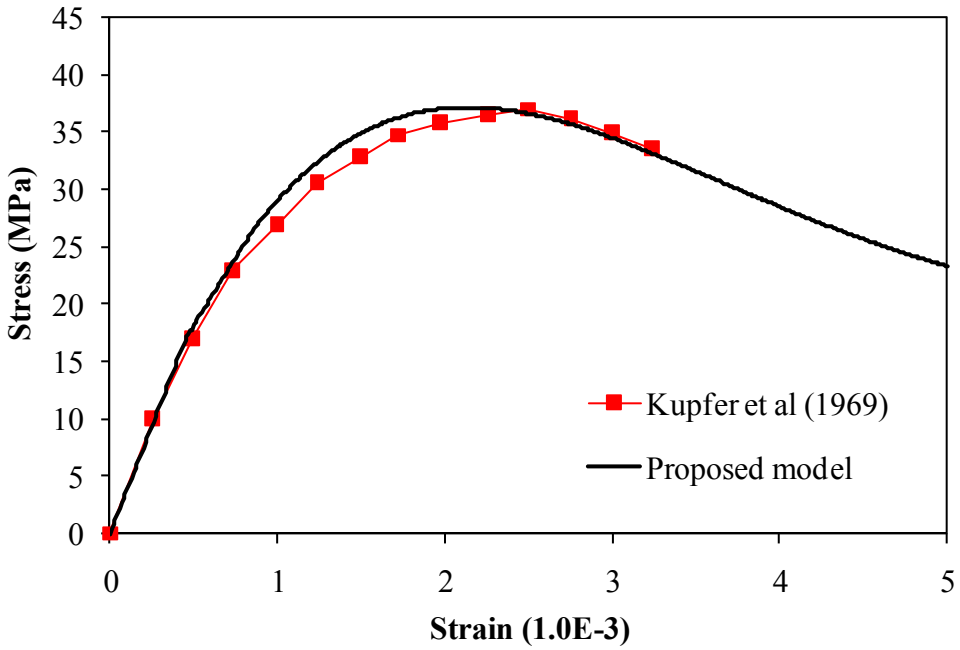

(b)

Figure 6.5 The model response in uniaxial and biaxial compressive loading compared to experimental results reported by Kupfer et al. (1969): (a) $\sigma_2 / \sigma_1 = -1/0$, (b) $\sigma_2 / \sigma_1 = -1/-1$, (c) $\sigma_2 / \sigma_1 = -1/-0.52$, and (d) damage density versus strain

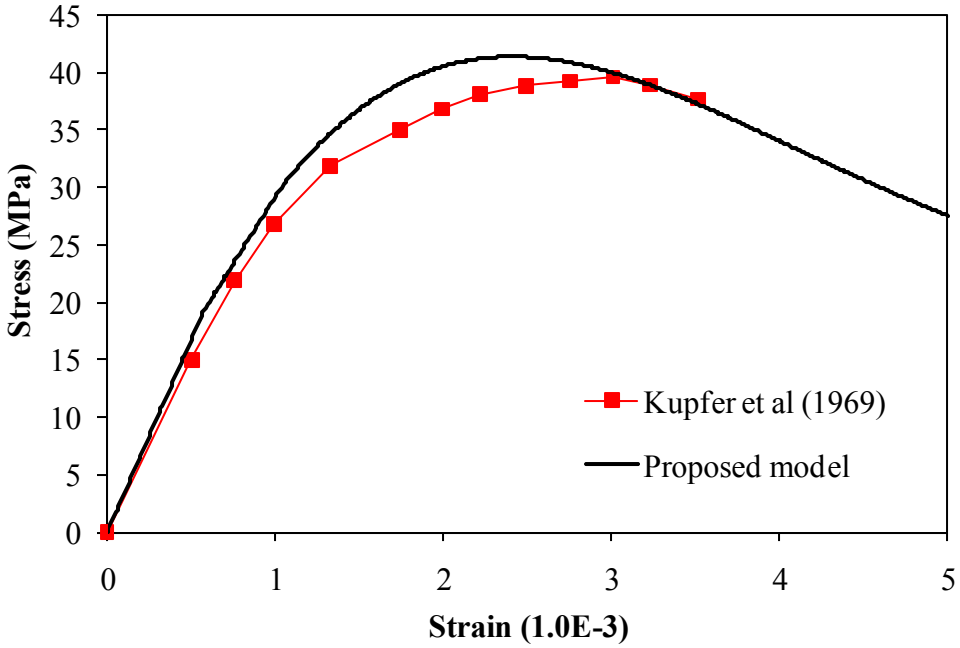

(c)

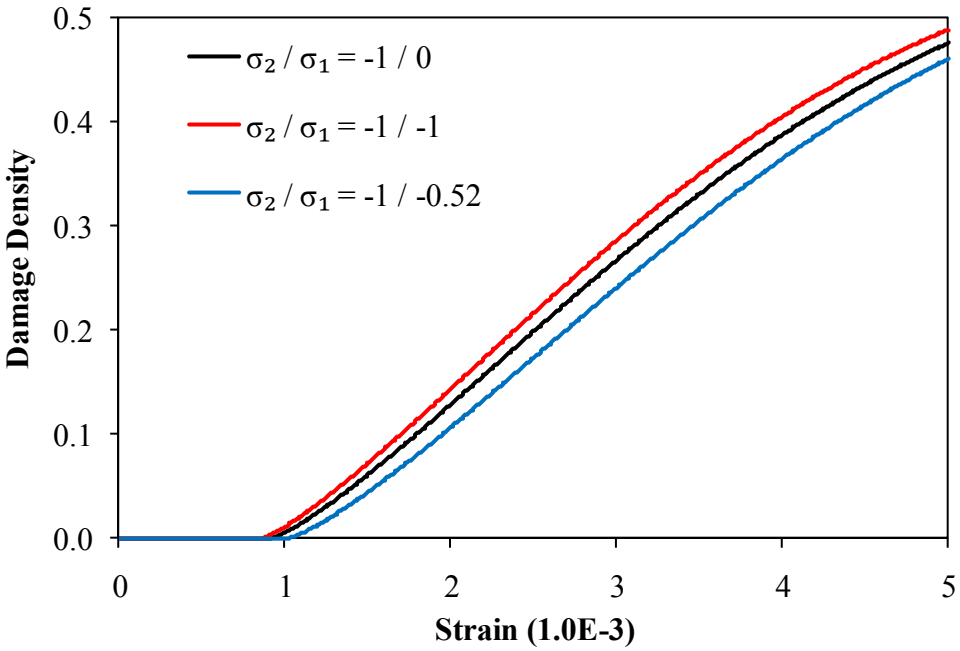

(d)

Figure 6.5 Continued

Table 6.3 Material constants used for the biaxial compressive loading analysis

$\bar{E}$ (MPa)	ν	f_0^- (MPa)	K_0^- (MPa)	Q^- (MPa)	b^-	B^-	q^-
29,000	0.2	15.0	20.0	70.0	810	0.16	1.29

The variation of the ultimate compressive strength and the damage density according to the change of the biaxial stress ratio $S_{11} / S_{22} = \sigma_1 / \sigma_2$ are shown in Figure 6.6. For this analysis, the maximum transverse directional displacement δ_2 is fixed to -0.005 mm, and the maximum longitudinal displacement δ_1, considering the Poisson's effect, is varied from 0.001 mm to -0.005 mm for the biaxial stress ratio to be varied from 0 to 1. Each point in Figure 6.6 is obtained at a strain level of 3×10^{-3}. One can notice that the ultimate compressive strength has a maximum value at a biaxial stress ratio of 0.4 while the damage density is minimum at a biaxial stress ratio of 0.3 and tends to increase as the biaxial stress ratio increases to a maximum value for equi-biaxial stress (i.e. stress ratio of 1) as concluded above. When the biaxial stress ratio is shifted from 0.0 to 0.1, both the ultimate compressive strength and the damage density of the element shows sudden change. This is due to the additional tensile damage induced by the longitudinal displacement δ_1 when the biaxial stress ratio is zero in order to maintain a zero biaxial stress ratio taking into consideration the Poisson's effect such that the tensile damage accelerates the transverse directional compressive damage.

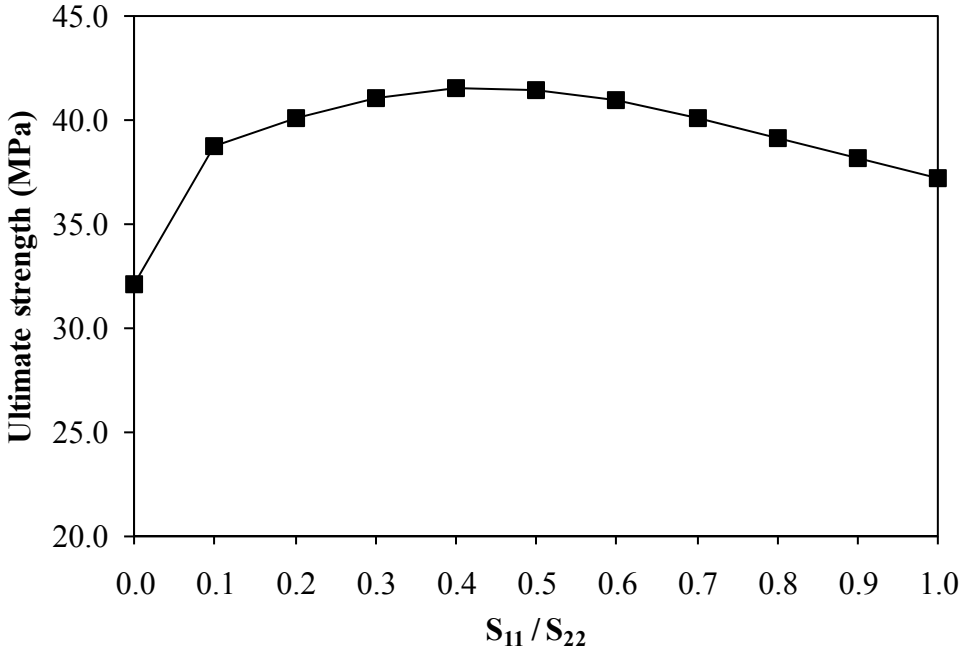

(a)

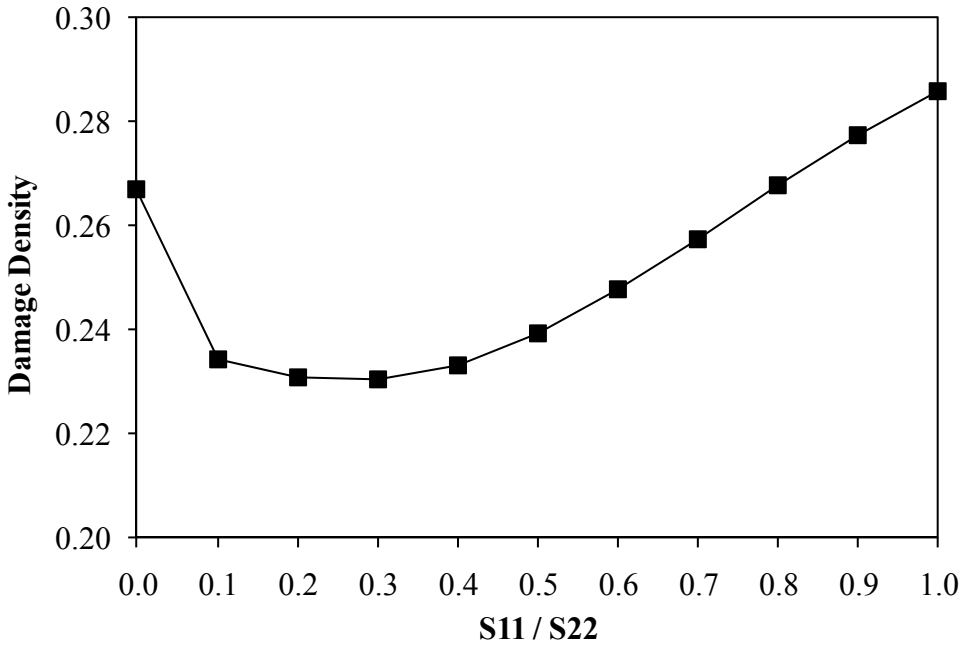

(b)

Figure 6.6 Variation of the model response by the change of the biaxial stress ratio. (a) Ultimate compressive strength, and (b) damage density

6.4 Simulation of the Mixed-mode Fracture of Plain Concrete

The mixed-mode fracture of the double-edge-notched (DEN) specimen tested by Nooru-Mohamed (1992) is simulated to verify the efficiency of the proposed constitutive model. The geometry of the DEN specimens and the loading setup are presented in Figure 6.7. The specimen dimensions are 200 mm × 200 mm square, 50 mm thick, and the length and height of the two notches are 25 mm and 5 mm, respectively. Although only two lading plates, top and left upper parts, were attached in the experimental set up, one more loading plate on the right upper part is attached additionally in the simulation in order to prevent the premature failure on the upper right and lower left-hand corners of the DEN specimen due to stress concentration. The vertical displacement δ_v of the specimen is an average displacement of $\delta_{MM'}$ and $\delta_{NN'}$.

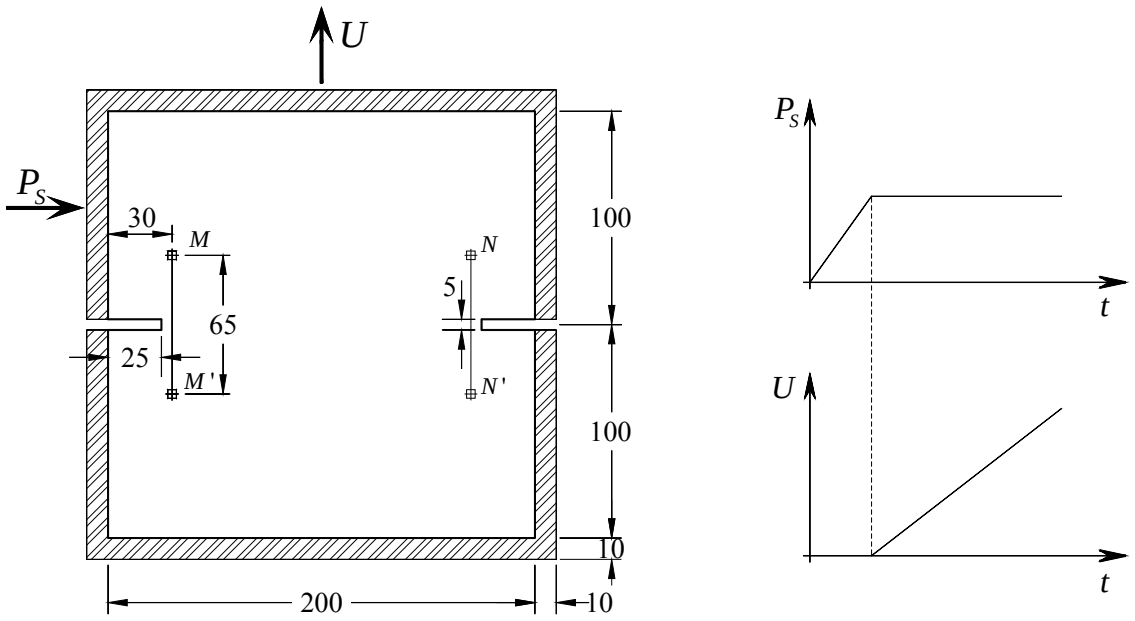

Figure 6.7 Geometry and loading of the DEN specimen (units: mm)

Figure 6.8 shows the plots of the initial mesh configurations of the performed FE analysis. Three mesh densities are used: coarse mesh with 1550 elements, medium mesh with 4704 elements, and fine mesh with 16052 elements and the size of the smallest element for coarse, middle, and fine mesh are 5.0 mm × 5.0 mm, 2.5 mm × 2.5 mm, and 1.25 mm × 1.25 mm, respectively.

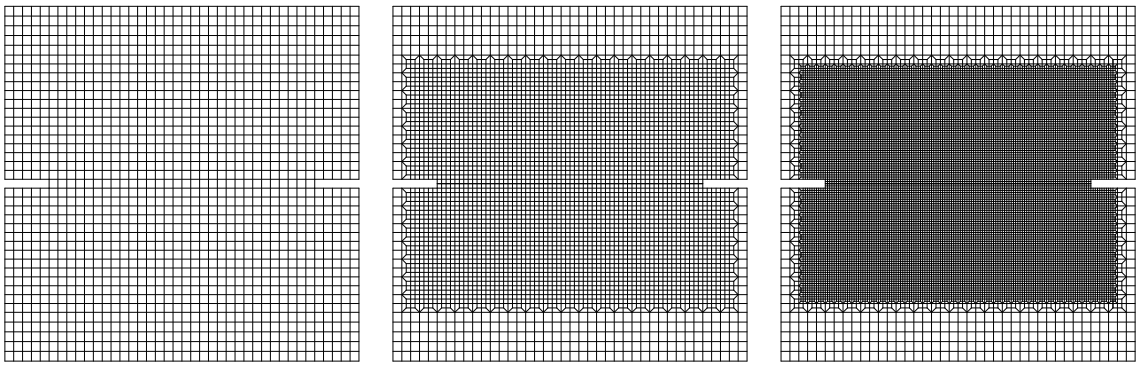

(a) (b) (c)

Figure 6.8 Meshes used in the simulations: (a) coarse mesh, (b) medium mesh, and (c) fine mesh

Table 6.4 Material constants used for the DEN specimen fracture simulation

Elastic Constants		Yield Criterion		Tensile Material Constants				
$\bar{E}$ (MPa)	ν	α	α_p	f_0^+ (MPa)	K_0^+ (MPa)	h^+ (MPa)	B^+	q^+
30,000	0.2	0.12	0.2	3.5	3.55	4,500	0.71	1.17

Compressive Material Constants					
f_0^- (MPa)	Q^- (MPa)	b^-	K_0^- (MPa)	B^-	q^-
15.0	120	1000	22	0.15	1.14

A three-dimensional (3D) stress 8-node linear brick element with one integration point is used. Although 3D simulations are performed, a 2 mm out-of-plane thickness is assumed instead of 50 mm actual thickness, and one element is taken through the thickness in order to reduce the simulation time. Same with the experimental set-up, bottom and right lower parts are fixed during whole loading steps, and a lateral (shear) force, P_S, is applied first up to the specified value of 5 kN or 10 kN with a zero vertical force, and then a vertical displacement, U, is loaded while the P_S remains constant (see Figure 6.7). The material parameters that are used in this simulation are listed in Table 6.4. These material constants are assumed in light of the numerical comparisons in the previous sections and that matches qualitatively the observed experimental crack trajectories in Nooru-Mohamed (1992).

The crack propagation for two loading cases are shown in Figure 6.9 for the fine mesh, where the final shape of the crack patterns are compared to the crack patterns experimentally reported in Nooru-Mohamed (1992) as overlapping each other. As shown, the initial slop of the crack increases in proportion to a rise in lateral shear force, P_S, and the trajectories of the crack of the analysis are in close agreement with the experimental results for both lateral loading cases. The tensile damage patterns for the three mesh densities are compared for both loading cases in Figures 6.10 and 6.11. As can be shown, the model predicts qualitatively the crack patterns and trajectories almost independent of the mesh size. However, Figure 6.12 shows plots of the reaction force versus the average displacement δ_v in which the solution is dependent on the mesh density; particularly, the ultimate load and the post-peak response.

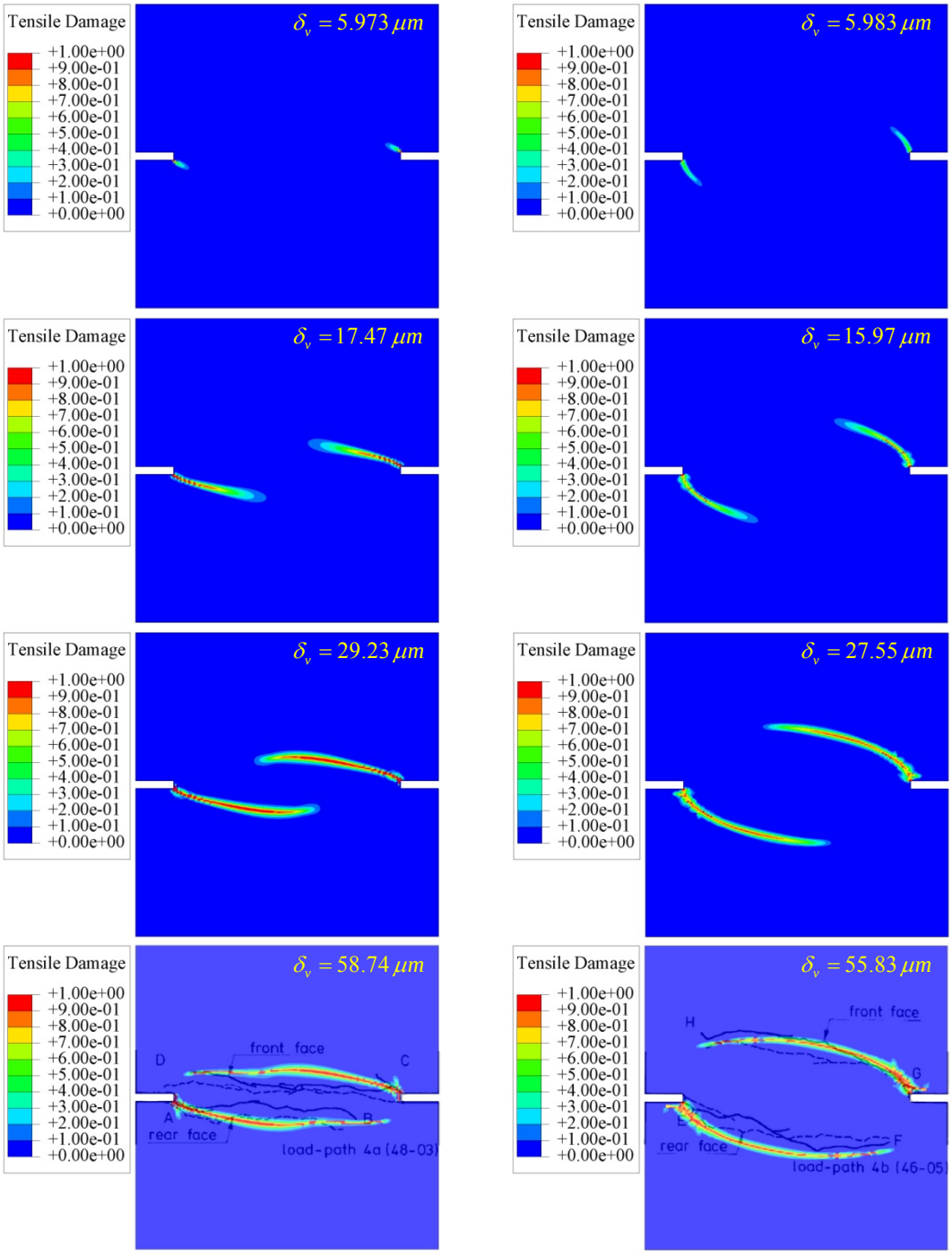

(a) (b)

Figure 6.9 Damage evolution showing the trend of crack propagation for two loading conditions: (a) P_S = 5.0 kN and (b) P_S = 10.0 kN. The figures at the bottom show the final crack propagation path as compared to the reported experiments by Nooru-Mohamed (1992)

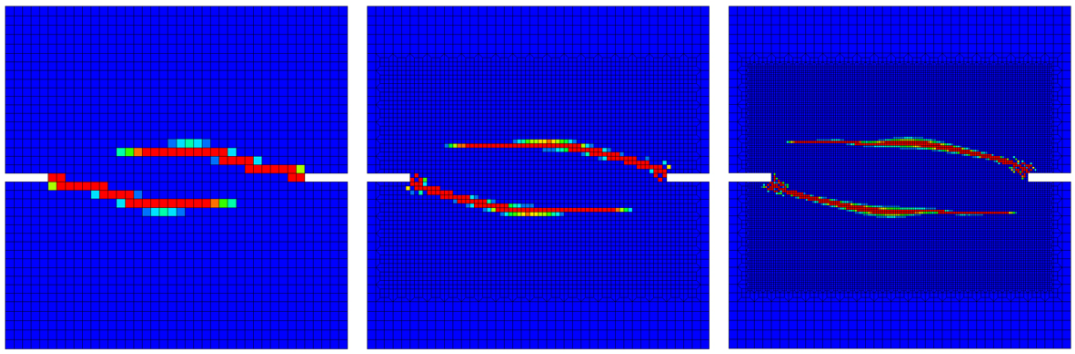

(a) (b) (c)

Figure 6.10 Simulated crack trajectories for the load case P_S = 5.0 kN for three mesh densities: (a) coarse, (b) medium, and (c) fine

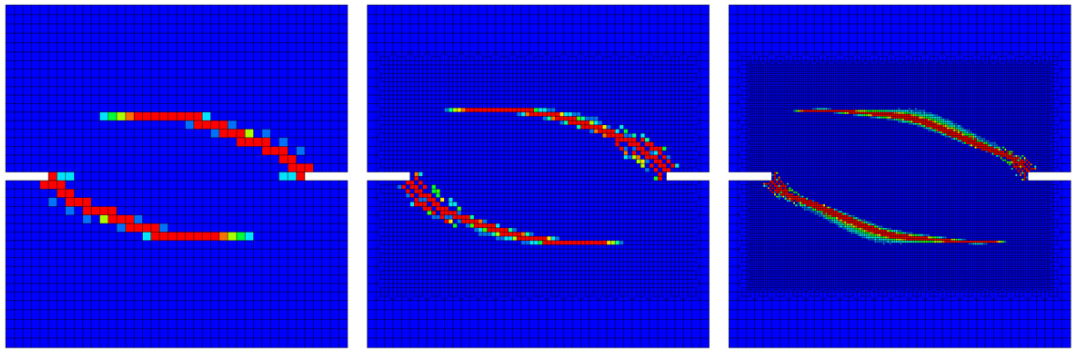

(a) (b) (c)

Figure 6.11 Simulated crack trajectories for the load case P_S = 10.0 kN for three mesh densities: (a) coarse, (b) medium, and (c) fine

As the mesh density increases, the load capacity decreases due to damage localization and higher damage density. This implies that the proposed local constitutive model with damage localization and softening cannot provide an objective description of the failure results quantitatively, but to a less extent qualitatively.

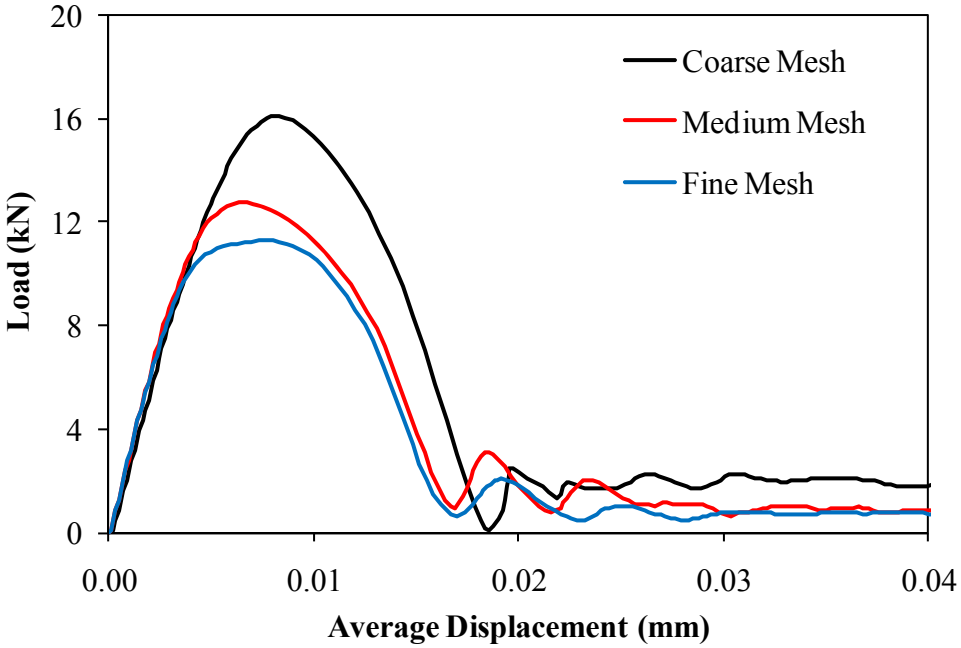

(a)

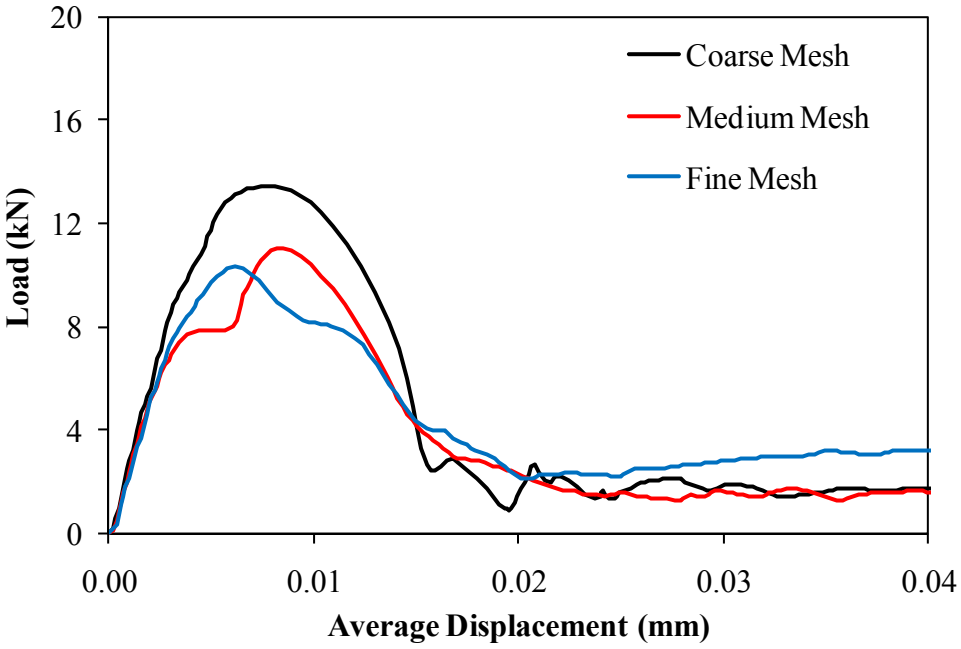

(b)

Figure 6.12 Load versus displacement curves for different mesh densities and for the loading cases: (a) P_S = 5.0 kN and (b) P_S = 10.0 kN

CHAPTER VII

MESO-SCALE SIMULATION OF CEMENTITIOUS COMPOSITES

Concrete can be considered as a three-phase composite material consisting of mortar matrix, aggregate, and interfacial transition zone (ITZ) between the aggregate and the mortar matrix. However, the majority of the conducted research on the inelastic and damage behavior of concrete materials and structures has been focused on treating concrete as a homogeneous material at the macroscopic scale which did not allow one to establish the microstructure-property relationship for designing better and superior fracture-resistant cementitious materials. Micromechanical modeling of the inelastic and damage behavior of each phase in the concrete material is not a trivial task since: (1) the properties of the ITZ, which plays a very important role in the concrete fracture behavior, are not easy to be measured experimentally; and (2) the computational cost is very high. However, due to the recent advances in understanding the chemical composition, thickness, and strength of the ITZ and the developments in computational power, one can effectively simulate the micromechanical behavior of concrete materials in order to get insights about the effect of various microstructure features (e.g. aggregate size, shape, gradation, and distribution, ITZ thickness and mechanical properties, the mortar mechanical properties, etc). This will ultimately guide the design of better and superior fracture resistant concrete materials and structures.

At the macroscopic level, the crack nucleation and propagation in concrete material under loading is entirely dependent on the direction of principal stresses. At the

mesoscopic level, however, the size and distribution of aggregate and the strength of each phase have a significant effect on the damage initiation and crack propagation. Especially, the accurate understanding of the properties and behavior of ITZ is one of the most important issues in the meso-scale analysis because the damage is initiated at the weakest region and the ITZ is generally the weakest link in concrete. Although the characteristic of the ITZ is not clearly understood currently (Scrivener *et al.* 2004; Mondal *et al.* 2008, 2009), it can be assumed that the behavior of the ITZ, which has weaker mechanical properties, is similar to that of the mortar matrix but with reduced stiffness and strength. Based on this assumption, the material properties of the mortar matrix and the ITZ should be chosen carefully. Moreover, the aggregate is modeled as a linear elastic material since the aggregate shows more brittle behavior than the mortar matrix, and has a higher Young's modulus and yield strength.

In this study, two- and three-dimensional meso-scale computational simulations are conducted in order to investigate the effects of aggregate distribution, aggregate volume fraction, and ITZ thickness and properties on the overall tensile strength and micro-crack initiation and propagation of concrete. The proposed coupled plasticity-damage model is adopted in order to simulate the inelastic and damage behavior of the mortar matrix and the ITZ separately.

7.1 2-D Meso-scale Analysis Model of Concrete

The representative volume element of size 100 mm × 100 mm, which is found to be representative of the statistical distribution of aggregates in concrete is shown in Figure

7.1. The well-known finite element code Abaqus via the user material subroutine UMAT is used for the meso-scale analysis and a 4-node bilinear plane stress quadrilateral element (CPS4R) is used for all models.

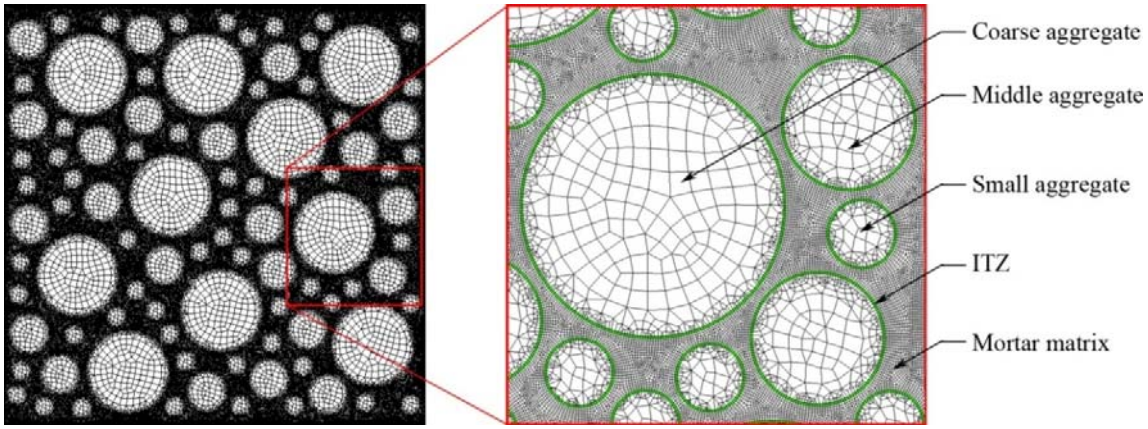

Figure 7.1 2-D meso-scale analysis model of a concrete

The radius of the coarse, middle, and fine aggregate are 10, 5, and 2.5 mm, respectively, and the aggregate gradation is 5:3:2. Since there is very limited experimental data on the thickness and mechanical properties of the ITZ, in this study the thickness of ITZ is assumed to be 200 μm and its behavior described with the presented elasto-plastic-damage model with weaker mechanical properties as compared to the cement matrix.

7.2 Material Properties of the ITZ and Mortar Matrix

At mesoscopic level, it is crucial to understand the material mechanical properties and behavior of each phase and the interaction between the aggregate and the mortar matrix because the change in each material property has a great effect on the global

macroscopic behavior of concrete. Because micro-cracks are initiated at the weakest link, where the ITZ is the weakest link, it is one of the most important tasks to define the tensile and compressive behavior of the ITZ for predicting the overall mechanical properties of concrete composites. However, it is difficult to determine the local mechanical properties of ITZ because of the complexity of their microstructure and the constraints of the existing measurement techniques (Ramesh et al., 1998; Scrivener et al., 2004; Mondal et al., 2008, 2009). Based on a systematic nano-indentation testing of the ITZ in concrete, Mondal et al. (2009) have shown that the Young's modulus of the ITZ is comparable to the Young's modulus of the mortar matrix. However, they also showed through using electron microscopy imaging that the microstructure of the ITZ is highly heterogeneous and highly damaged due to pre-existence micro-voids and micro-cracks within this zone. Hence, one can assume that the tensile/compressive strength of the ITZ is weaker than that of the mortar matrix. Thus, although the mechanical characteristic of the ITZ is not clearly understood currently, it can be assumed that the behavior of the ITZ, which has weaker mechanical properties (Scrivener et al., 2004; Mondal et al., 2009), is similar to that of the mortar matrix. Based on this assumption, the material properties of the mortar matrix and the ITZ are chosen carefully such that the properties of the ITZ are chosen to be less than that of the mortar by a constant factor.

In this study, the presented coupled plasticity-damage model is adopted for modeling the tensile and compressive behavior of the ITZ and the mortar matrix, whereas the aggregate is modeled as a linear elastic material (E = 55,500 MPa, ν = 0.2) since the aggregate shows a more brittle behavior than the mortar matrix, and has a higher

Young's modulus and yield strength. It is noteworthy that the cyclic or monotonic uniaxial loading-unloading tensile and compressive stress-strain experimental curve, as discussed in Chapter 5, should be used to identify unique values for the material parameters of the ITZ and the mortar matrix, such as $K_0^{\pm}$, $B^{\pm}$, $q^{\pm}$, h^{+}, b^{-}, and Q^{-}. The aim of the mesoscopic level analysis, however, is not in predicting the behavior of a specific concrete structure. Therefore, the material constants of the ITZ and the matrix used in the analysis are assumed to show suitable tensile and compressive loading-unloading behavior based on the monotonic tensile and compressive loading-unloading experimental result by Taylor (1992) and Karsan and Jirsa (1969). The predicted tensile and compressive stress-strain relations based on these material constants of the mortar matrix and the ITZ are shown in Figure 7.2, and the material parameters used in the meso-scale analysis are listed in Table 7.1.

Table 7.1 Material constants used in the meso-scale analysis

	Elastic Constants		Tensile Material Constants					Yield Criteria	
	$\bar{E}$ (MPa)	ν	f_0^{+} (MPa)	K_0^{+} (MPa)	h^{+} (MPa)	B^{+}	q^{+}	α	α_p
Mortar	26,000	0.20	3.0	3.0	10,000	1.30	1.10	0.12	0.20
ITZ	25,000	0.16	2.0	2.0	10,000	1.40	1.05		

	Compressive Material Constants					
	f_0^{-} (MPa)	Q^{-} (MPa)	b^{-}	K_0^{-} (MPa)	B^{-}	q^{-}
Mortar	15.0	80.0	820.0	20.0	0.15	1.40
ITZ	12.0	50.0	820.0	16.0	0.20	1.60

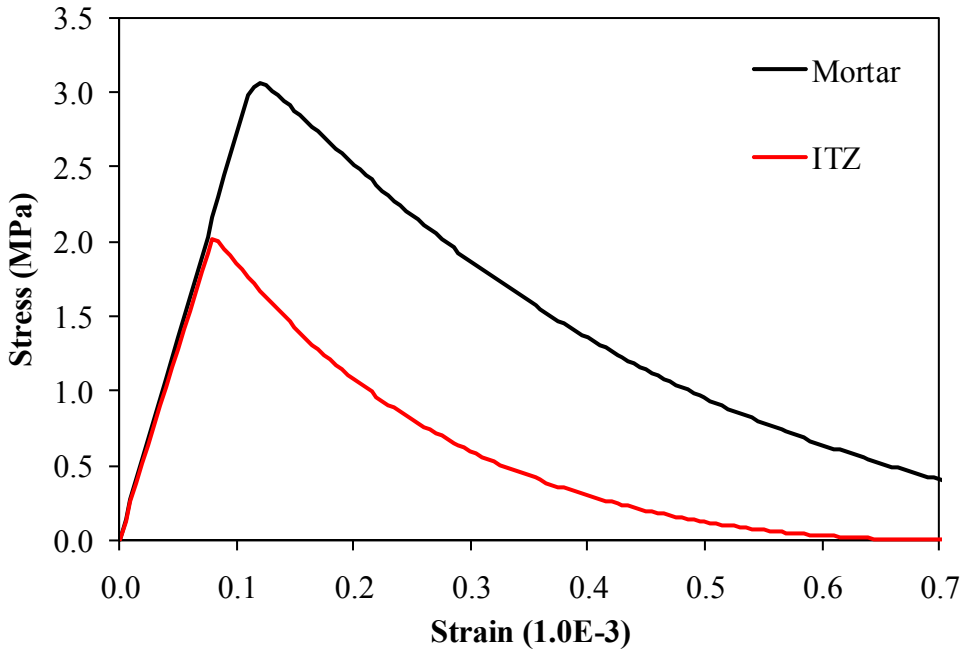

(a)

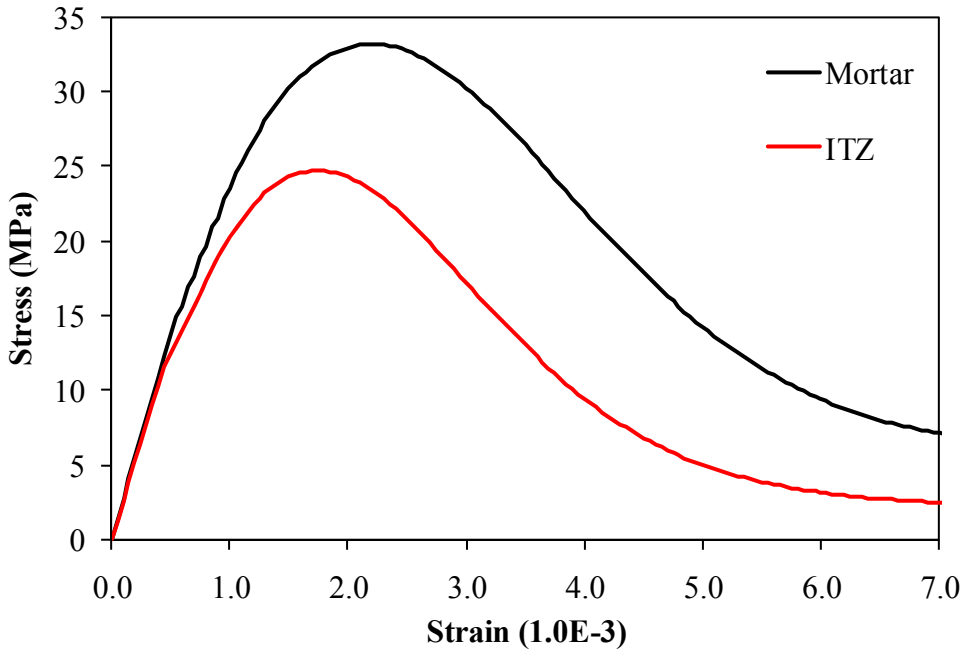

(b)

Figure 7.2 Stress-strain relation of mortar and the ITZ: (a) tensile and (b) compressive

7.3 The Effect of the Aggregate Shape

Currently, circular or spherical aggregate shape is commonly used for 2-D or 3-D meso-scale finite element analysis because of simplicity. However, it is found that the meso-scale concrete model using circular shape of aggregate tends to give higher strength compared to the model using irregular actual shape of aggregate (Du and Sun, 2007). This is attributed to the increased levels of stress concentration when modeling the actual shape of the aggregate. Therefore, the effect of the aggregate shape on the tensile strength of 2-D meso-scale concrete model is investigated in this section. Five different aggregate shapes; circular, hexagonal, pentagonal, tetragonal, and arbitrary polygonal shapes are considered as shown in Figure 7.3.

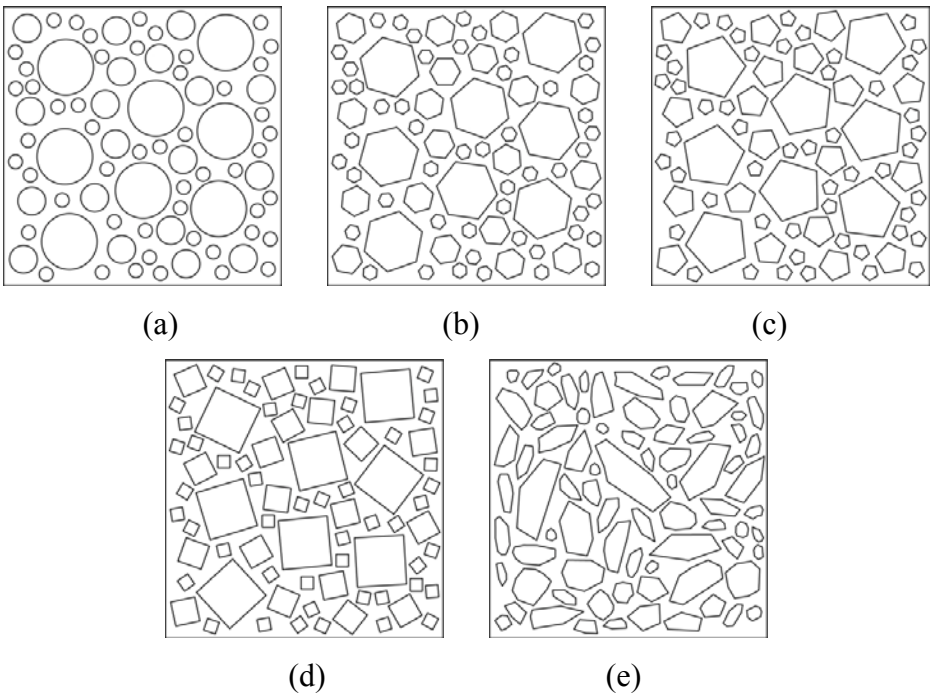

Figure 7.3 Aggregate shape sensitivity analysis micro-structures: (a) Circular, (b) hexagonal, (c) pentagonal, (d) tetragonal, and (e) arbitrary polygonal RVEs

For all these cases, the aggregate volume fraction is assumed 50%, and the aggregate gradation of models except for the arbitrary polygonal shape (Figure 7.3(e)) is assumed 5:3:2. The arbitrary polygonal shape model generated by Wang et al. (1999) based on X-ray tomography is utilized in this work.

Micro-crack distribution for the aggregate shape sensitivity analyses at vertical displacement of 10 μm are shown in Figure 7.4. Also, the corresponding load-displacement diagrams and the normalized values of the tensile strength and the strain capacity at the onset of damage are shown in Figure 7.5. In this study, the strain at damage-onset is defined as the strain at which micro-cracks are initiated and degradation in strength and elastic modulus occurs. Therefore, by predicting this strain as a function of the material's microstructure, one can investigate the key microstructural parameters that mitigate damage onset and decreases cracking potential. It is obvious that the aggregate shape has a weak effect on the ultimate strength of concrete and on the strain to damage-onset as shown in Figure 7.5, but significantly affects the crack initiation, propagation, and distribution as shown in Figure 7.4. However, one can notice that due to the stress concentration at the sharp edges of polygonal aggregate shape, both the ultimate tensile strength and the strain at onset of damage of the circular shape aggregate model are higher than those of the other aggregate shapes. Specifically, the ultimate tensile strength of the circular aggregate model shows larger than 6% increase than that of the arbitrary polygonal shape aggregate model.

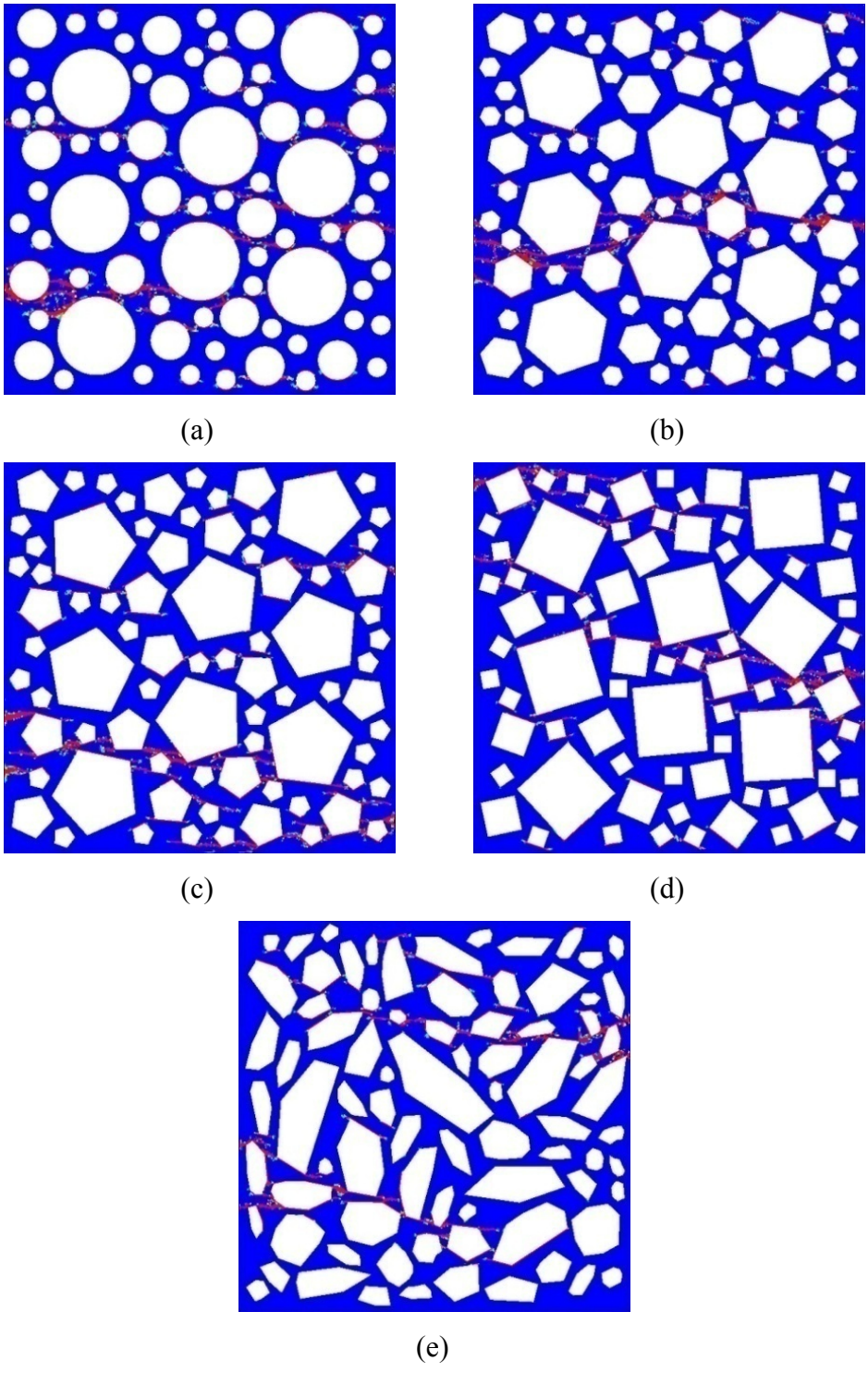

(a) (b)

(c) (d)

(e)

Figure 7.4 Final micro-crack distributions for the aggregate shape effect analyses: (a) Circular, (b) hexagonal, (c) pentagonal, (d) tetragonal, and (e) arbitrary polygonal shapes

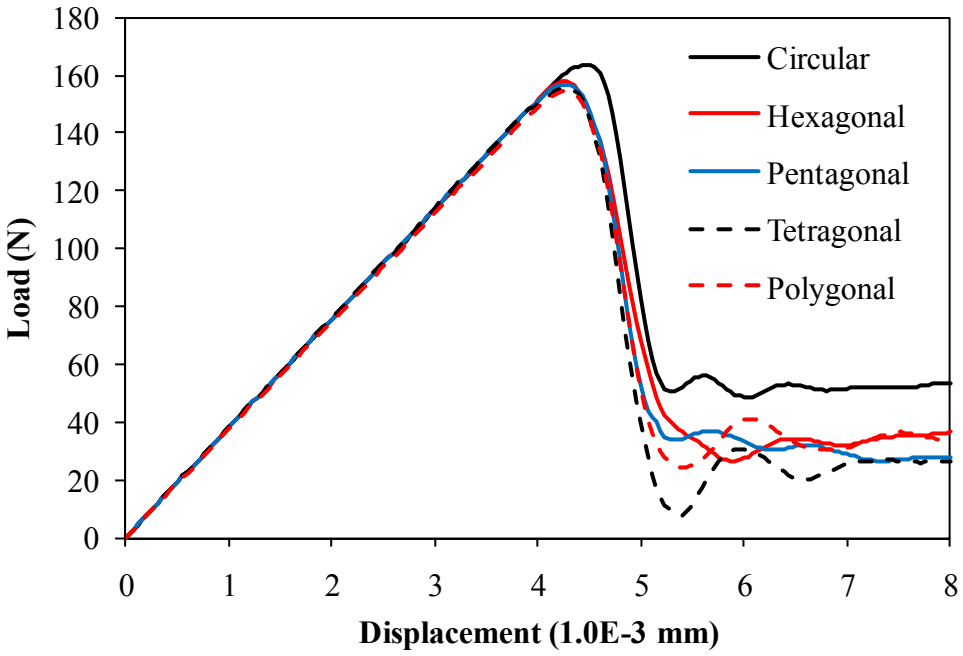

(a)

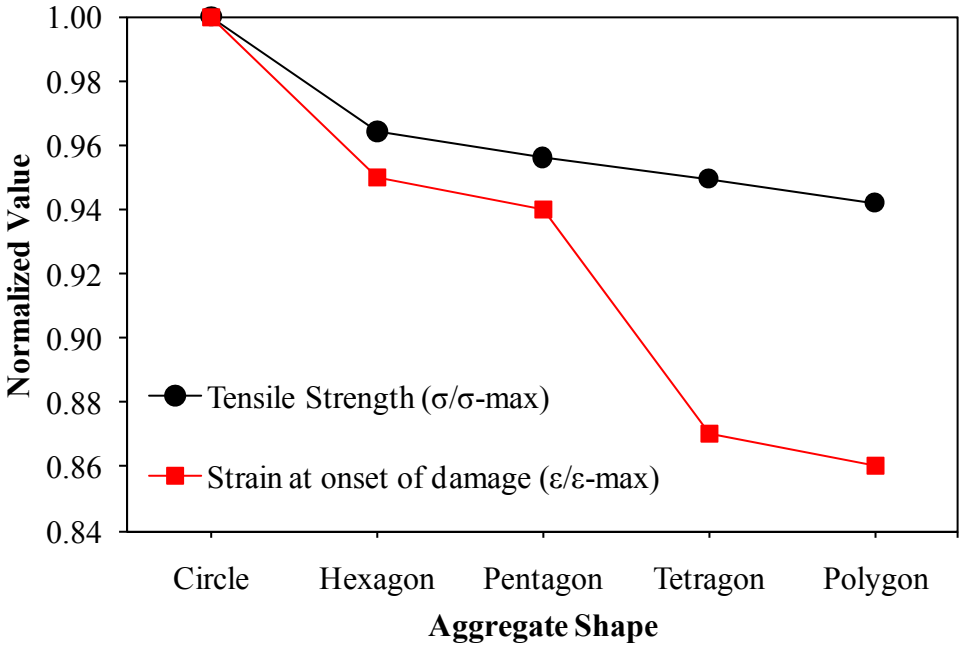

(b)

Figure 7.5 Results of the aggregate shape effect analyses: (a) Load-displacement relation and (b) variation of the ultimate strength and the strain at onset of damage as a function of the aggregate shape

Due to the small differences in the predictions of the overall tensile strength and strain capacity of the concrete when considering different aggregate shapes, in the following simulations a circular aggregate shape is assumed for simplicity in carrying out the finite element simulations.

7.4 The Effect of the Aggregate Distribution

Although the maximum and minimum aggregate size, the aggregate gradation, and volume fraction, depending on the purpose, can be controlled in the concrete mix design, it is actually impossible to control the distribution of aggregate. Furthermore, the concentration of the aggregates on a localized region due to poor mix or segregation may have effect on the strength of concrete. Mixing and pouring concrete is based on the basic assumption that aggregate is randomly and uniformly distributed, and the aggregate distribution has little effect on the strength and behavior of concrete. Therefore, the aggregate distribution effect is investigated with four different aggregate distribution models as shown in Figure 7.6.

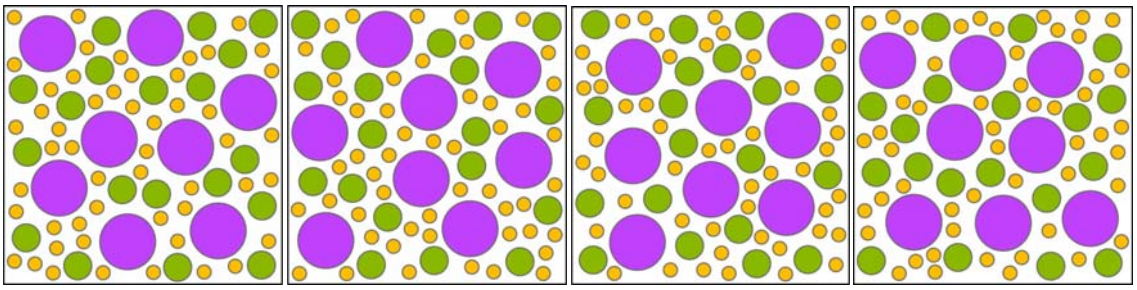

(a) (b) (c) (d)

Figure 7.6 Aggregate distribution sensitivity analyses with aggregate volume fraction of 50 %: (a) Model 1, (b) model 2, (c) model 3, and (d) model 4

The size of the RVE is 100 mm × 100 mm, and the aggregate volume fraction of the models is identical with 50%. The number of coarse, middle, and fine aggregates used in the analysis is 8, 19, and 51, respectively, and all aggregates are randomly distributed with the same aggregate gradation of 5:3:2.

The final crack patterns and the load-displacement relations for the change of the aggregate distribution of the four simulated RVEs are shown in Figures. 7.7 and 7.8.

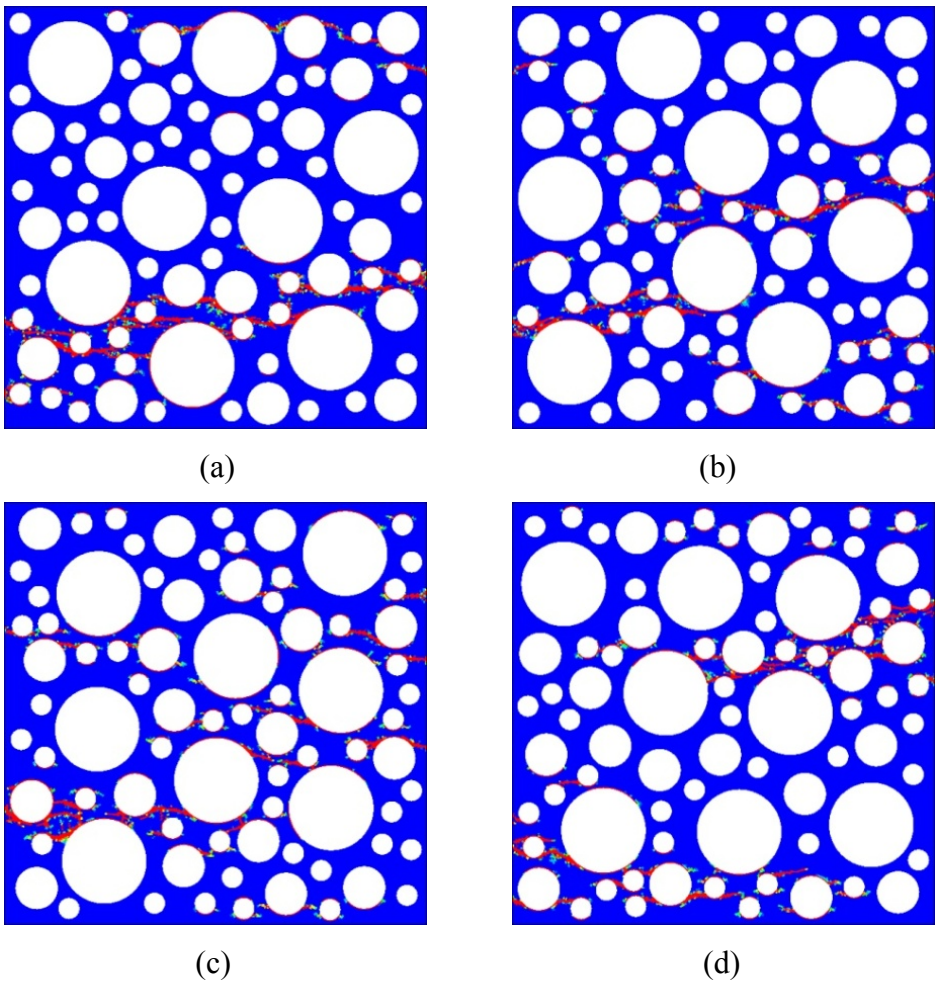

Figure 7.7 Final micro-crack distributions for the aggregate distribution effect: (a) model 1, (b) model 2, (c) model 3, and (d) model 4 shown in Figure 7.6

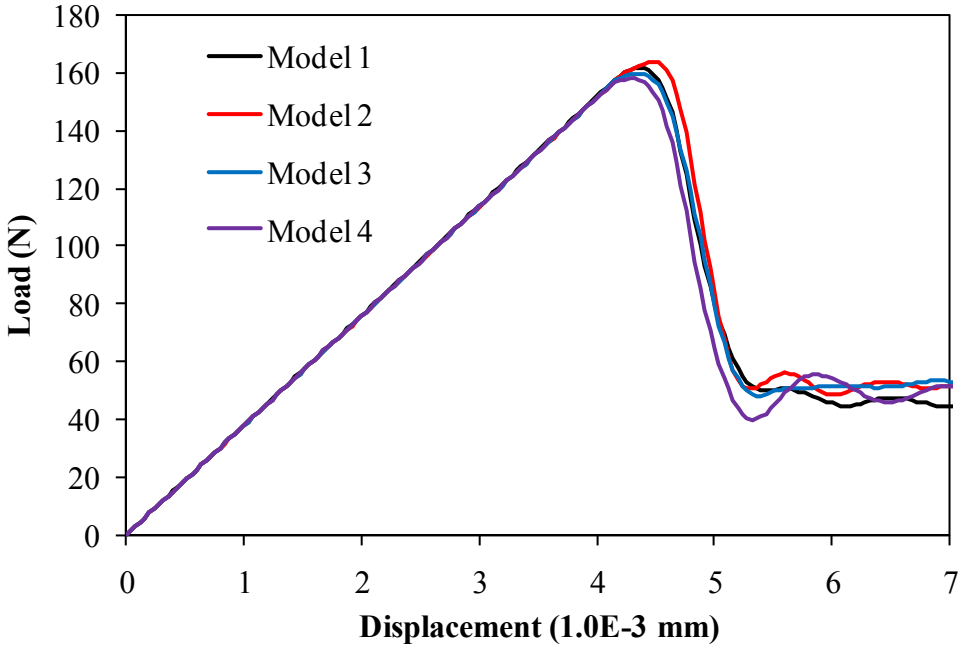

Figure 7.8 Load-displacement relations for the different aggregate distributions in Figure 7.6

As seen in Figure 7.7, the micro-crack distribution is totally dependent on the distribution of aggregates. However, it is obvious from Figure 7.8 that the tensile strength and strain capacity under tensile loading is less dependent on the aggregate distribution. This result can be explained with the global damage density, and the fraction of damaged element at 5 μm of vertical displacement as listed in Table 7.2. It can be seen from Table 7.2 that although the crack distribution of each model is quite different, the difference of the fraction of damaged elements is insignificant. Therefore, it can be concluded that the aggregate statistical distribution has a negligible effect on overall mechanical response of concrete composites.

Table 7.2 The fraction of damaged elements for the different aggregate distributions in Figure 7.6

Model	1	2	3	4
ITZ	18.5 %	20.1 %	23.9 %	22.1 %
Mortar	2.7 %	2.5 %	2.3 %	2.1 %

7.5 The Effect of the Aggregate Volume Fraction

It is obvious that aggregate plays a vital role in the fracture of concrete because aggregate takes up to 75% of the total volume of concrete, and the aggregate volume fraction is one of the most important factors governing the failure mechanism of concrete. It is well known through experimental tests that the Young's modulus of normal strength concrete is proportional to the aggregate volume fraction, whereas the compressive strength of concrete generally is inversely proportional to that (Tasdemir and Karihaloo, 2001; Amparano et al., 2000). However, there is little information how the aggregate volume fraction affects the tensile strength of concrete since the direct tensile test is not that easy to perform (Stock et al., 1979). Therefore, the effect of the aggregate volume fraction on the tensile behavior of concrete is examined in this section.

In order to investigate the effect of aggregate volume fraction, Figure 7.9 shows different RVEs with increasing aggregate volume fractions from 10% to 60%. The number and fraction of aggregates used in this analysis are summarized in Table 7.3. Each RVE in Figure 7.9 is subjected to a vertical tensile displacement. However, Figure 7.9(g-l) show the same considered aggregate volume fractions, but with different aggregate distributions.

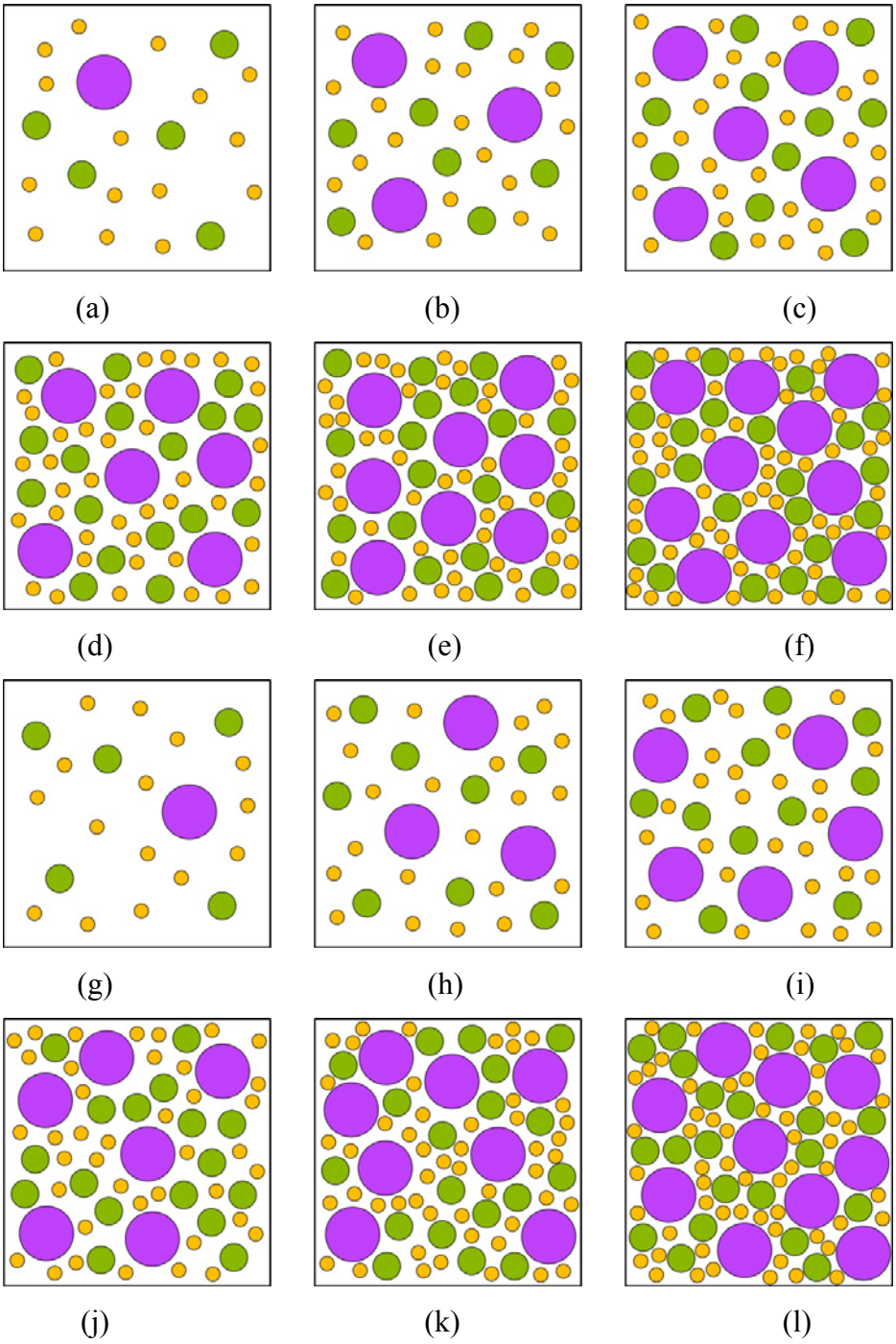

Figure 7.9 Aggregate volume fraction sensitivity analysis models: (a) Set 1 - 10 %, (b) set 1 - 20 %, (c) set 1 - 30 %, (d) set 1 - 40 %, (e) set 1 - 50 %, (f) set 1 - 60 %, (g) set 2 - 10 %, (h) set 2 - 20 %, (i) set 2 - 30 %, (j) set 2 - 40 %, (k) set 2 - 50 %, and (l) set 2 - 60 %

Table 7.3 The number and fraction of aggregates used in the aggregate volume fraction simulations

Volume fraction (%)	Coarse aggregate (%)	Middle aggregate (%)	Fine aggregate (%)	Total area (mm^2)	Actual volume fraction (%)
10	1 (31.4)	5 (39.3)	15 (29.5)	1001.38	10.01
20	3 (47.1)	8 (31.4)	21 (20.6)	1983.13	19.83
30	5 (52.4)	11 (28.8)	29 (19.0)	3004.15	30.04
40	6 (47.1)	17 (33.4)	40 (19.6)	4005.53	40.06
50	8 (50.3)	19 (29.8)	51 (20.0)	5006.92	50.07
60	10 (52.4)	22 (28.8)	60 (19.6)	6047.57	60.48

This second set of RVEs are simulated in order to make sure that altering the aggregate distribution does not have significant effect on the drawn conclusions on the effects of aggregate volume fraction as concluded from the previous section. Also, it should be noted that the obtained results in this section are obtained from performing four simulations: (1) by applying tensile *vertical* displacement to the RVEs in *set 1* in Figures 7.9 (a-f); (2) by applying tensile *vertical* displacement to the RVEs in *set 2* in Figures 7.9 (g-l); (3) by applying tensile *horizontal* displacement to the RVEs in *set 1* in Figures 7.9 (a-f); and (4) by applying tensile *horizontal* displacement to the RVEs in *set 2* in Figures 7.9 (g-l). This is equivalent to simulating four different distributions for each considered aggregate volume fraction.

The micro-crack distributions at 0.02 mm of tensile vertical displacement are shown in Figure 7.10, and the process of micro-crack initiation and propagation is shown in Figure 7.11.

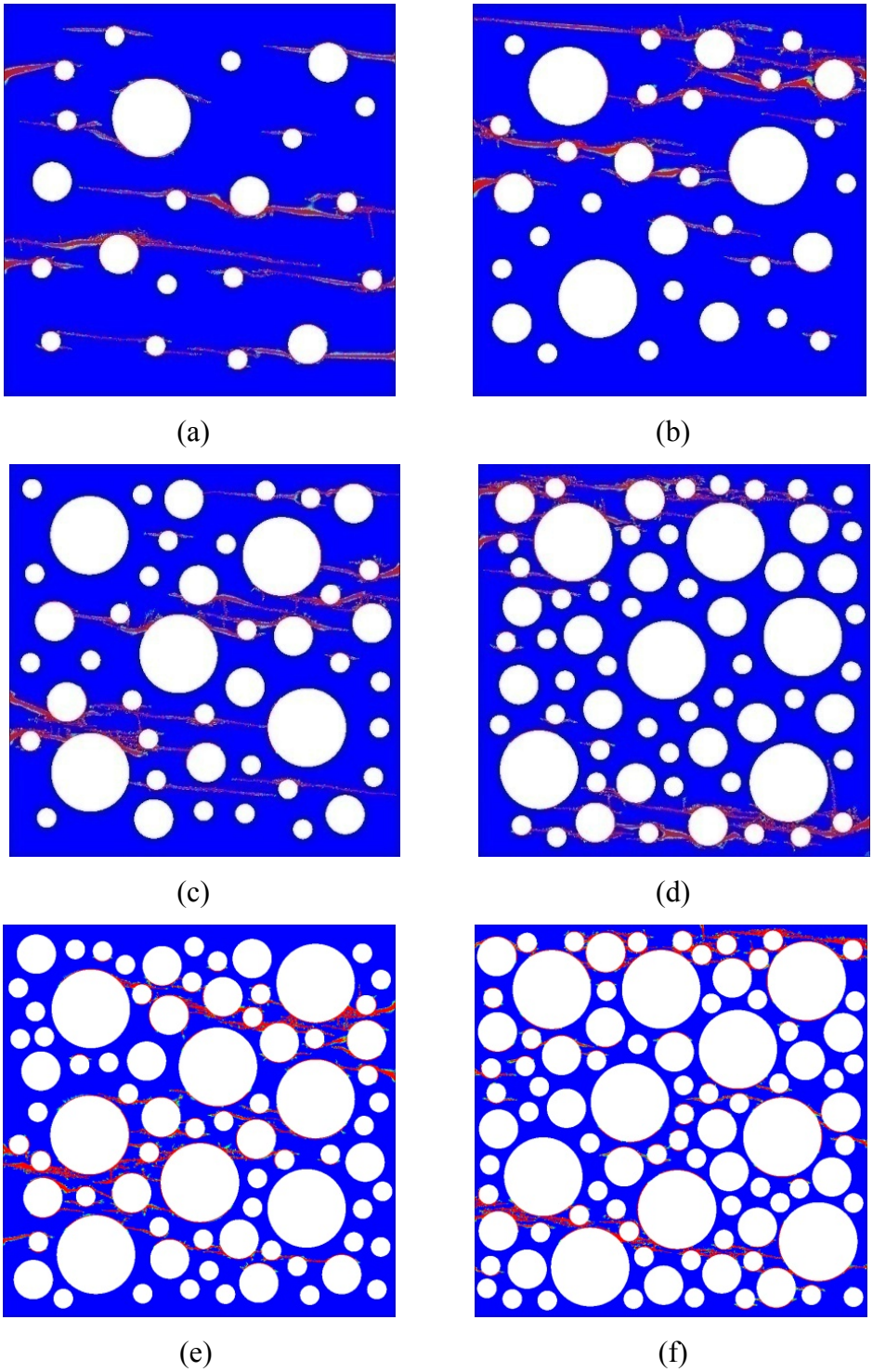

Figure 7.10 Micro-crack distributions due to applied tensile loading for different aggregate volume fractions of set 1 in Figure 7.9: (a) 10 %, (b) 20 %, (c) 30 %, (d) 40 %, (e) 50 %, and (f) 60 %

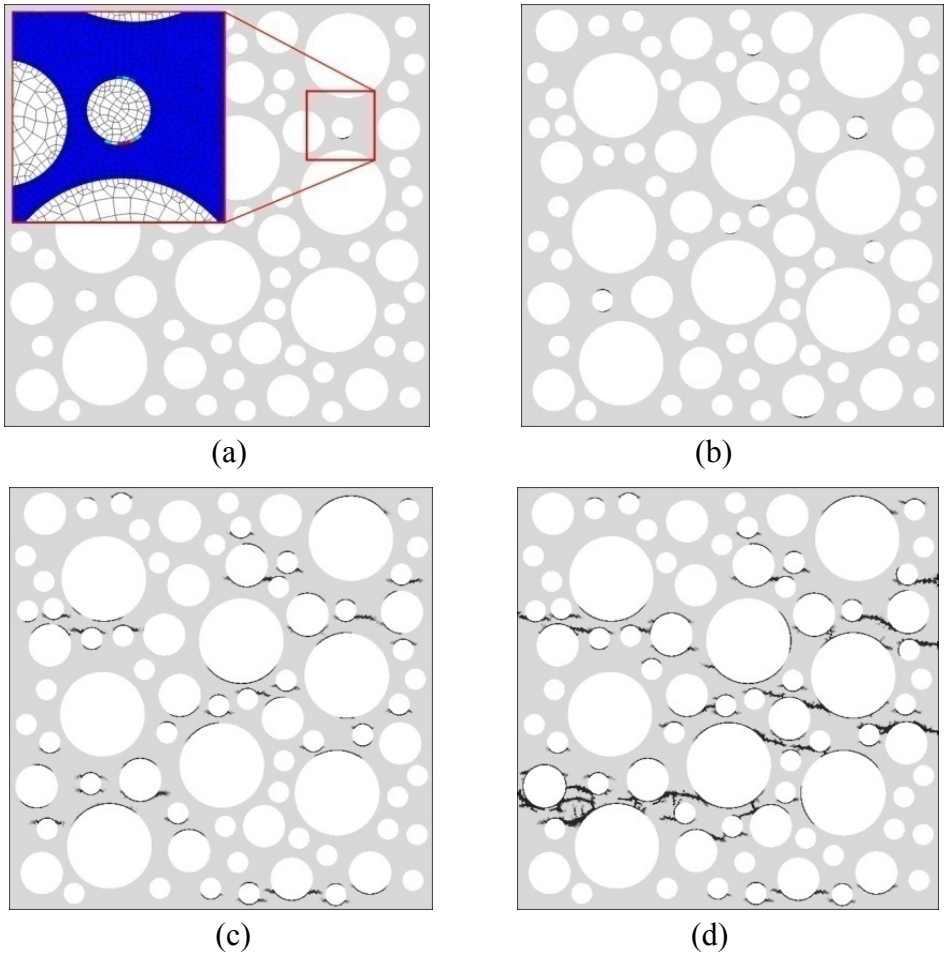

Figure 7.11 Micro-crack nucleation and propagation for a RVE with aggregate volume fraction of 50%. Micro-crack distribution at increasing deformations: (a) 4.2 μm (onset of damage), (b) 4.5 μm (peak), (c) 5.0 μm, and (d) u=10.0 μm

As shown in Figure 7.10, the crack distributions are totally dependent on the aggregate volume fraction and distribution, and tend to be more localized as the aggregate volume fraction increases. Furthermore, the tensile damage is initiated at the ITZ, the weakest region at a vertical displacement of 4.2 μm. Subsequently, a number of micro-cracks are developed at the ITZ regions simultaneously after damage initiation, and the micro-cracks are then propagated to the mortar matrix, coalesced with each other, and developed to macro-cracks as the vertical displacement increases.

The effects of varying the aggregate volume fraction on the overall mechanical response of the concrete composite are shown in Figure 7.12. It can be seen from Figure 7.12(b) that the Young's modulus of concrete is almost linearly proportional to the aggregate volume fraction and is not affected by the aggregate distribution. It can also be seen from Figure 7.12(d) that the strain at the onset of damage is inversely proportional to the aggregate volume fraction and is not significantly influenced by the aggregate distribution.

Whereas, the ultimate tensile strength of concrete as a function of aggregate volume fraction, unlike the Young's modulus and strain at damage initiation, is not monotonic such that the concrete capacity is found to be minimum at 40 % volume fraction. As can be seen from Figure 7.12(c) that although the aggregate distribution has a slight effect on the tensile strength of concrete, the distribution of aggregates cannot be the reason for the observed response in Figure 7.12(c). This observed behavior can be attributed to sever localized damage distribution leading to clear macro-crack evolution at the top and bottom of the 40% aggregate volume fraction RVE as shown in Figure 7.10(d). Therefore, the load carrying capacity is mainly localized within small regions of the mortar matrix while the surrounding material is elastically unloaded. On the other hand, more distributed micro-damage evolution and propagation is seen for other volume fractions such that the loading carrying capacity is more distributed within the mortar matrix. Furthermore, it is believed that at volume fractions greater than 40% the aggregates are more closely packed to each other inducing confinement effects on the surrounding matrix and making the response stronger.

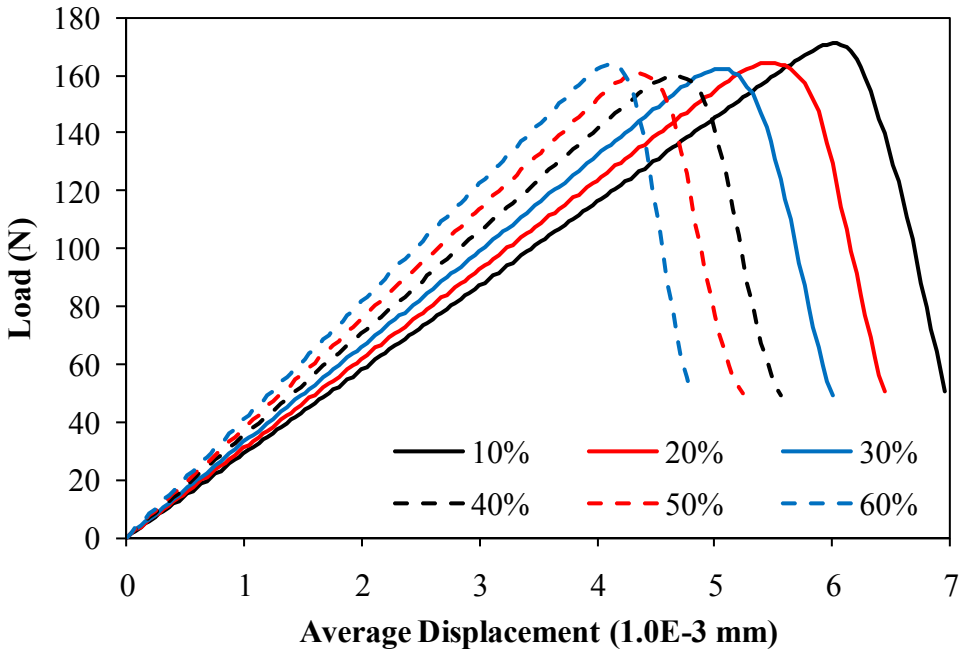

(a)

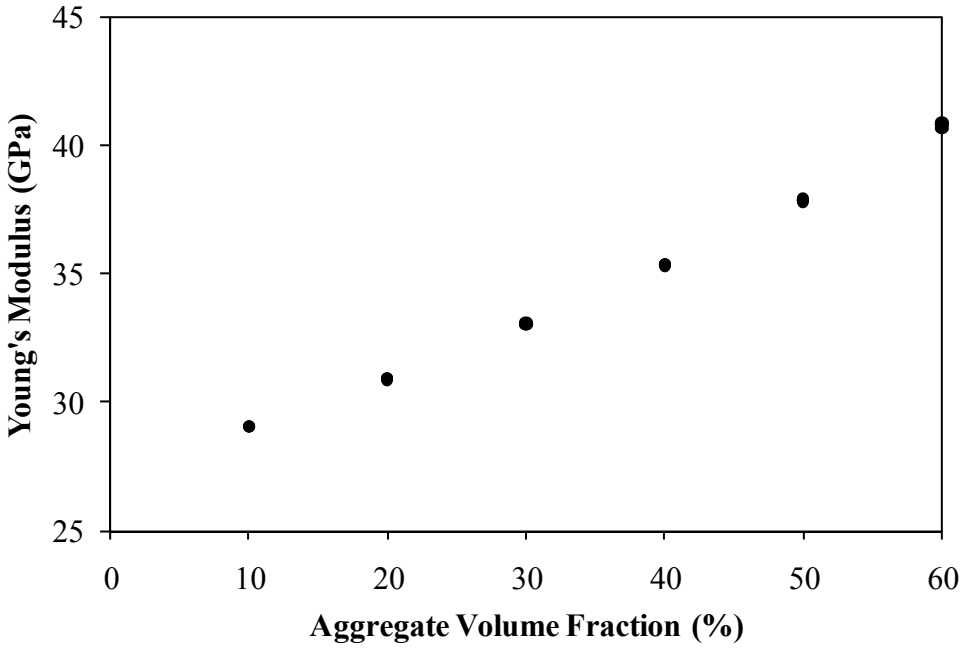

(b)

Figure 7.12 Aggregate volume fraction on (a) load-displacement response, (b) Young's modulus, (c) tensile strength, and (d) strain at onset of damage

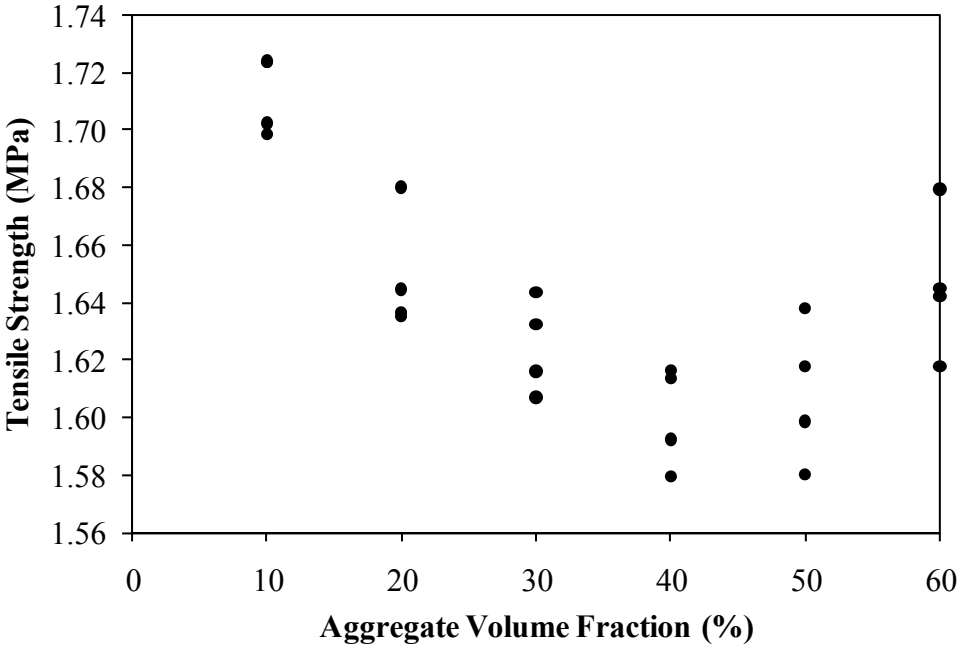

(c)

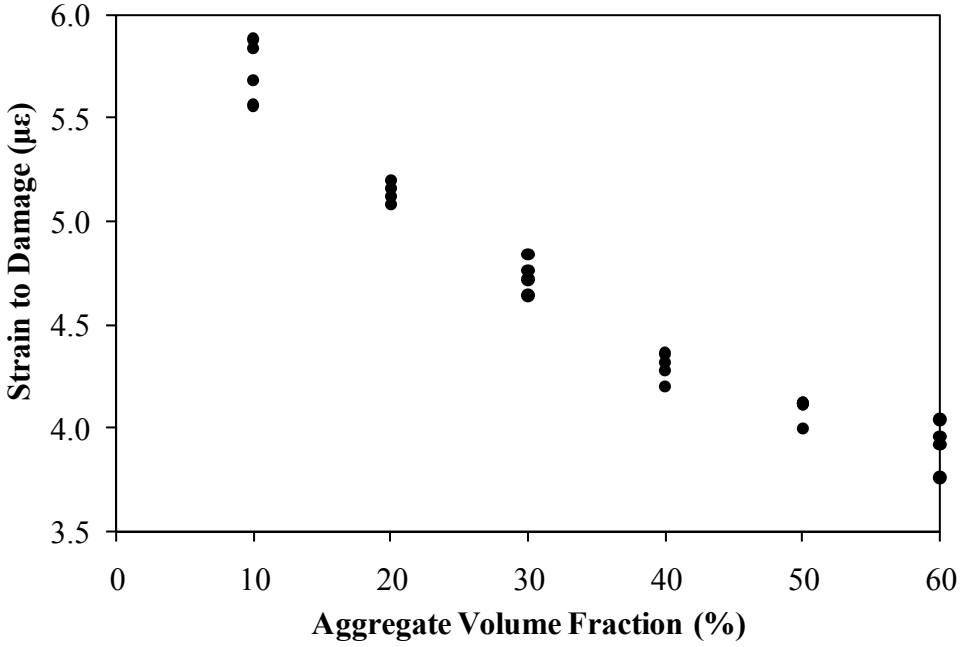

(d)

Figure 7.12 Continued

7.6 The Effect of the ITZ Thickness

Understanding the characteristics of the ITZ is one of the most critical issues in predicting the overall mechanical response of concrete composites based on meso-scale simulations since the ITZ is the weakest region in concrete such that the strength and behavior of concrete is mainly governed by the properties of the ITZ (Scrivener *et al.* 2004; Mondal *et al.* 2008, 2009). The ITZ as a constituent of concrete can be considered as an initial defect, and the increase of the ITZ thickness or volume may lower the global strength of concrete. The effect the ITZ thickness on the tensile strength of concrete is investigated in this section. Five thicknesses are simulated in this section as shown in Figure 7.13. The thickness of the ITZ varies from 0.1 mm to 0.8 mm.

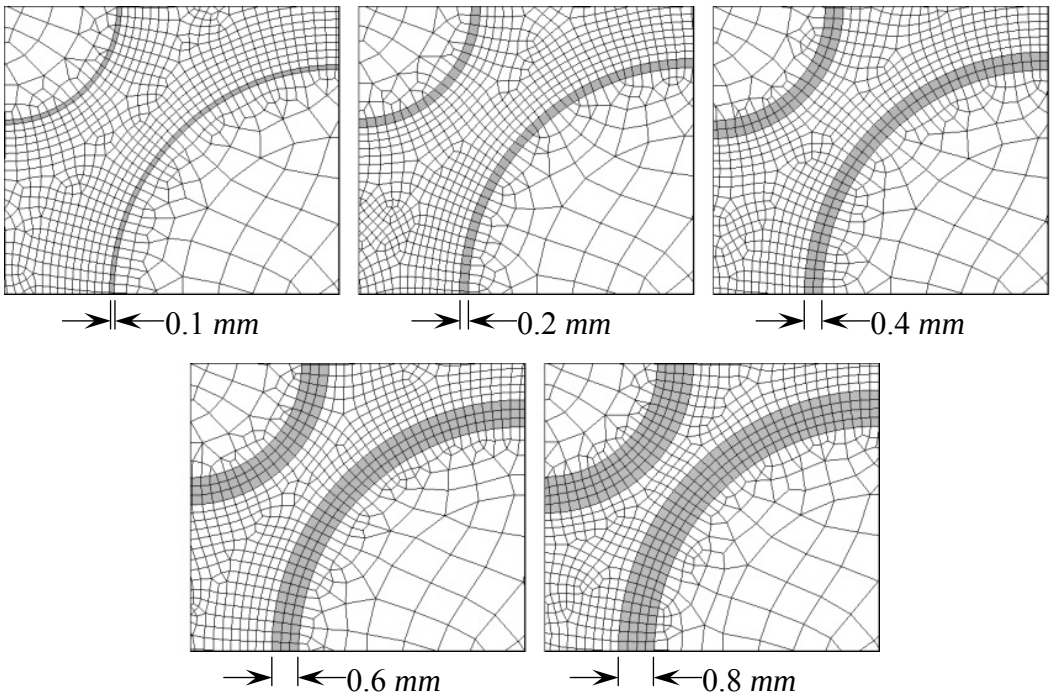

Figure 7.13 Geometry and finite element meshes for studying the effect of varying the ITZ thickness

The ITZ thickness sensitivity analysis results are shown in Figure 7.14. As shown in Figure 7.14(a), the increase in the ITZ thickness has a slight effect on the post-peak behavior such that the brittleness of concrete increases as the ITZ thickness increases. However, as shown in Figure 7.14(b) that the decrease in the tensile strength with increasing the thickness of the ITZ is not that significant and reaches a constant value with further increase in the ITZ thickness. This result indicates that further increase in the thickness of the ITZ may have no effect on the global strength of concrete. As seen in Figure 7.14(c), the strain at onset of damage is not affected by increasing the ITZ thickness, whereas changing the aggregate volume fraction has a more significant effect on the strain to damage, which is the conclusion from the previous section.

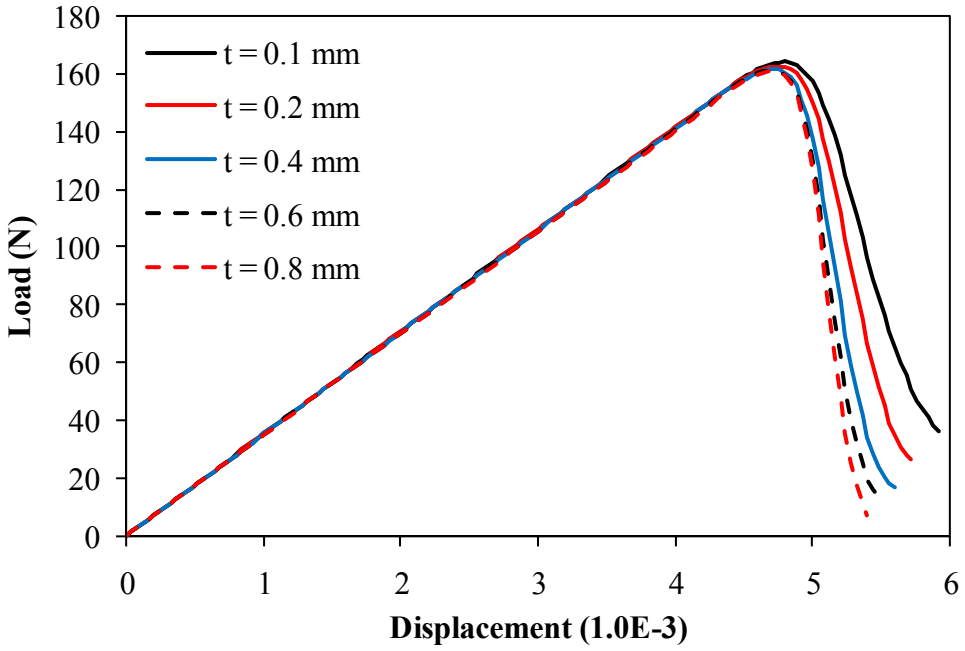

(a)

Figure 7.14 The effect of varying the ITZ thickness on (a) the load-displacement relation for an aggregate volume fraction (AVF) of 40%, (b) the normalized tensile strength for different AVFs, and (c) the strain at onset of damage for different AVFs

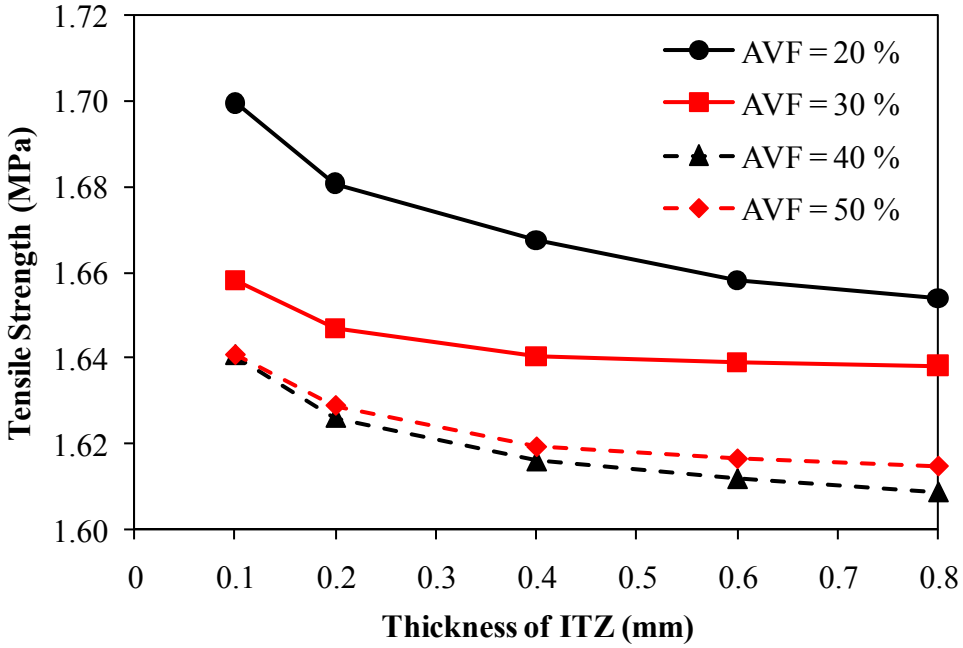

(b)

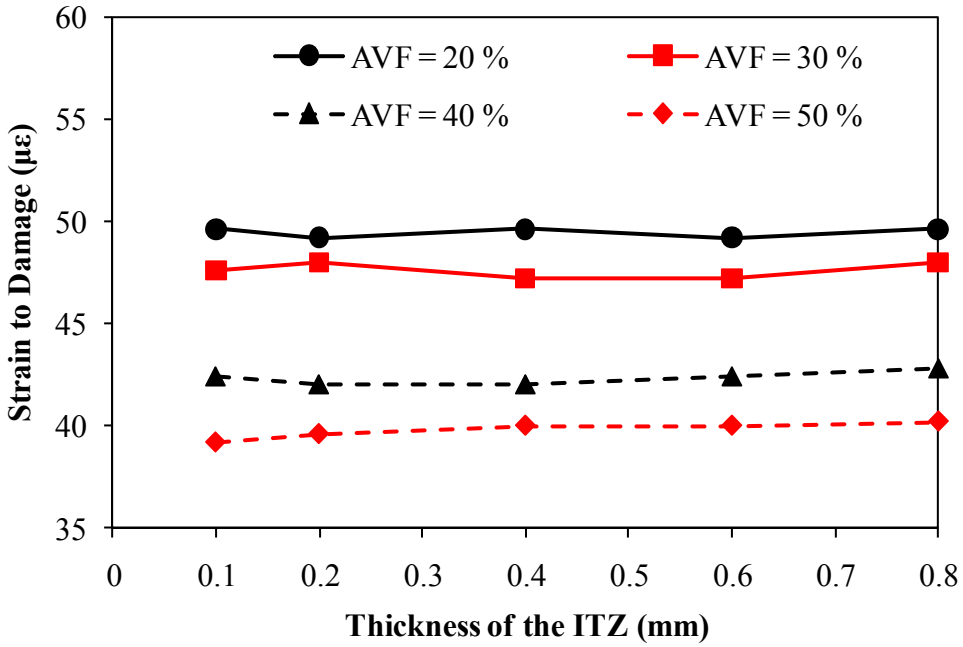

(c)

Figure 7.14 Continued

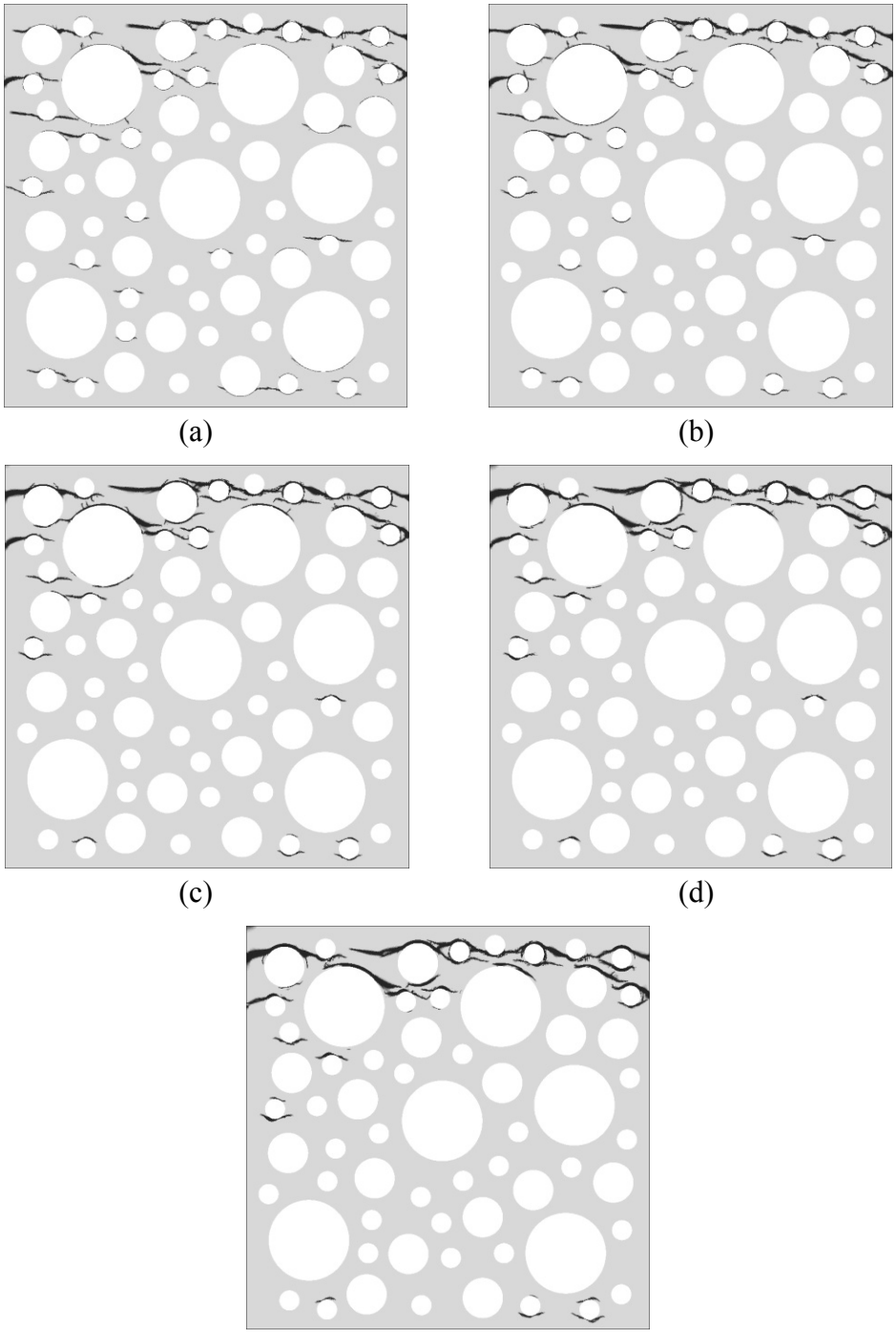

Figure 7.15 Micro-crack distributions for ITZ thicknesses of (a) 0.1 mm, (b) 0.2 mm, (c) 0.4 mm, (d) 0.6 mm, and (e) 0.8 mm. The simulations are obtained at 6 μm displacement and for an aggregate volume fraction of 50 %

Figure 7.15 shows the micro-crack distribution for varying the ITZ thickness. Although the crack distribution and initiation points are almost the same for each change in the ITZ thickness, macro-cracks are more localized and wider as the thickness of the ITZ increases.

7.7 The Effect of the ITZ and Mortar Matrix Strength

The global ultimate tensile strength of concrete as a function of the ITZ and mortar matrix tensile strengths is analyzed in this section. Although the ITZ strength cannot be in excess of the strength of mortar matrix for normal concrete, cases where the ITZ strength is higher than that of the mortar matrix are considered too. The ITZ strength may be greater than the matrix strength through surface treatment of aggregates and nano-modification of the cement paste (e.g. the use of nano silica fume, nano fibers, nano tubes). In the following simulations, the reference tensile strengths (100 % of strength) of the ITZ and mortar matrix are assumed to be 2.0 MPa and 3.0 MPa, respectively. The strength of the ITZ varies from 10% (σ_{y-ITZ} = 0.2 MPa) to 200% (σ_{y-ITZ} = 4.0 MPa) of the reference strength of ITZ, whereas the strength of the mortar matrix varies from 70% ($\sigma_{y-Mortar}$ = 2.1 MPa) to 200% ($\sigma_{y-Mortar}$ = 6.0 MPa) of the reference strength of matrix.

The analysis results of varying the ITZ and mortar matrix tensile strengths assuming 50% aggregate volume fraction is shown in Figure 7.16. It can be seen from Figure 7.16(a) that the variation in the ITZ strength has a significant effect on the global response of concrete. However, in case that the ITZ tensile strength is less than 40% of

its reference strength (i.e. the ITZ tensile strength is equal or less than 0.8 MPa), the variation of the ITZ strength does not affect the ultimate tensile load as shown in Figure 7.16(b). This is because the ITZ is easily damaged whereas the mortar matrix is still elastically loaded and can resist additional loading, which explains the observed subsequent hardening response in Figure 7.16(b). Then, after the load is redistributed and transferred to the mortar matrix due to the complete damage of the ITZ region, one can start seeing micro-cracking of the mortar matrix. When the ITZ tensile strength lies in the range of 40% (0.8 MPa) and 150% (3.0 MPa) of reference strength, the ultimate tensile strength of concrete increases linearly with the increase of the ITZ strength.

Figure 7.17 shows the variation of micro-crack distributions as a function of the ITZ strength at 10 μm of applied vertical displacement. As seen, almost all ITZ elements are damaged when the strength of the ITZ is very low compared to the mortar matrix strength, and this distributed tensile damage on the ITZ yields higher ductility. As the ITZ strength increases, the more tensile cracks are propagated through the mortar matrix, and the model shows more brittle behavior. Also, one can notice from Figs. 7.17(a) and (b) that the majority of micro-cracking occurs at the ITZ region and much less within the mortar matrix as compared to the micro-crack distributions in Figs. 7.17(c-f). Therefore, increasing the ITZ strength will mitigate the micro-cracking from the interface (adhesive) to the matrix (cohesive), which leads to a stronger response as shown in Figure 7.16. However, the additional increase in the ITZ strength over the mortar's strength has no effect on the ultimate strength of concrete because in this case the concrete strength is governed by the mortar's tensile strength of 3.0 MPa, which is the weakest link.

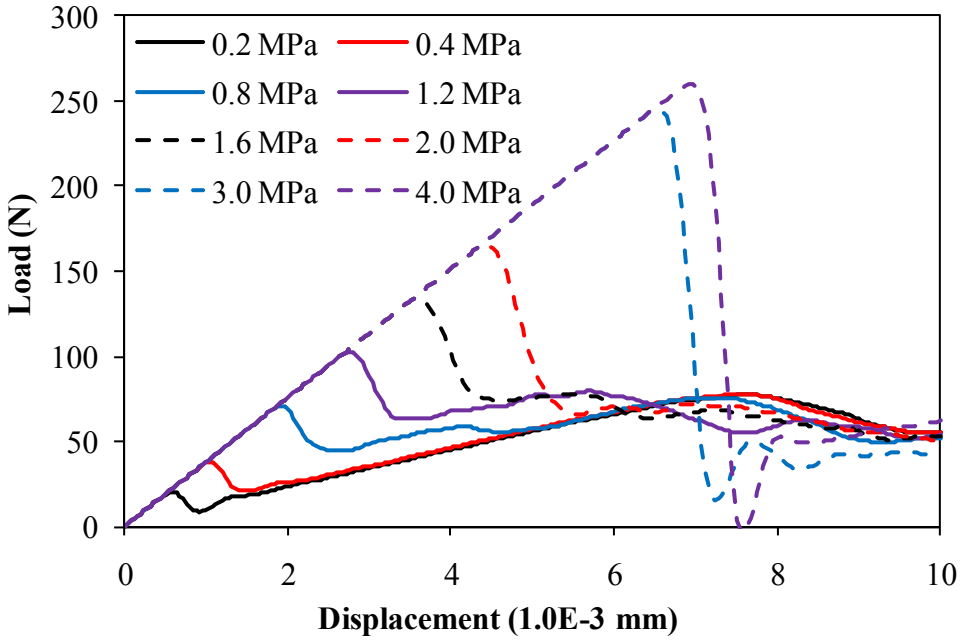

(a)

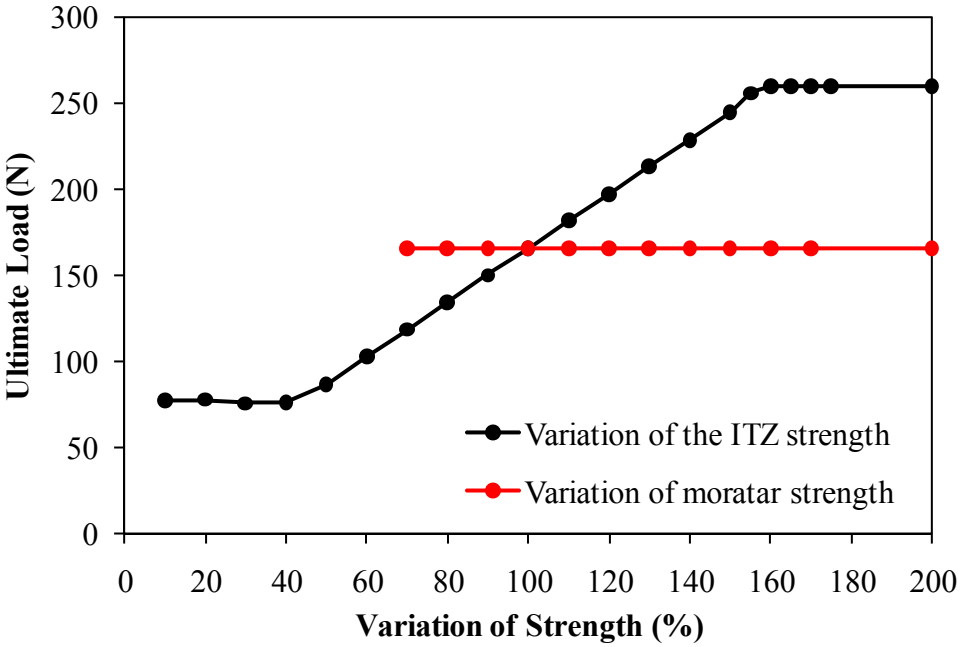

(b)

Figure 7.16 The effect of varying the ITZ and mortar matrix tensile strengths on (a) the load-displacement response assuming $\sigma_{y-Mortar}$ =3.0 MPa, and (b) the ultimate load. 50% aggregate volume fraction is assumed

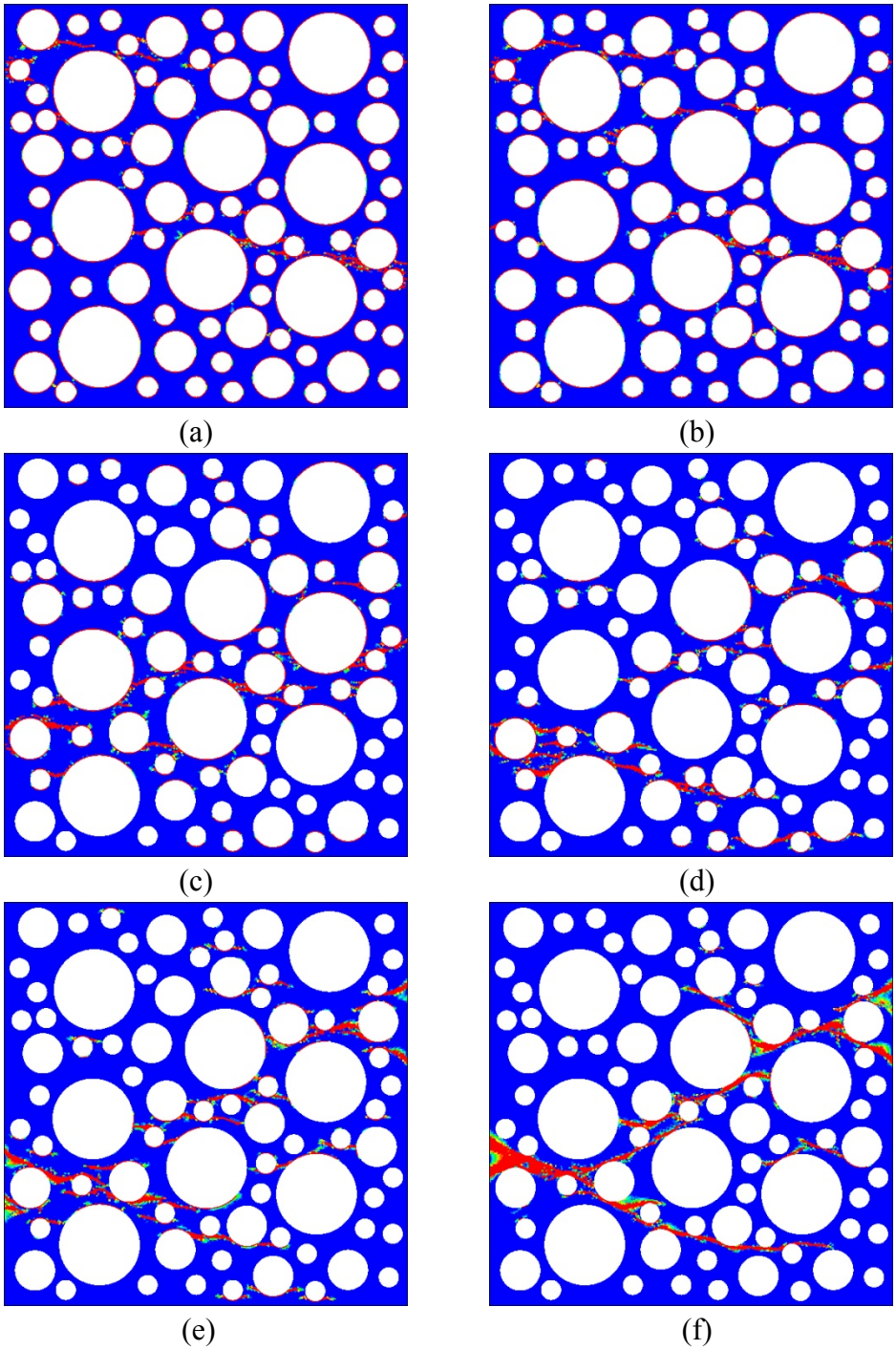

Figure 7.17 Micro-crack distributions as a function of the ITZ strength for aggregate volume fraction of 50% and applied vertical displacement of 10 μm: (a) 10% (0.2 MPa), (b) 40% (0.8 MPa), (c) 70% (1.4 MPa), (d) 100% (2.0 MPa), (e) 130% (2.6 MPa), and (f) 150% (3.0 MPa, same as the mortar strength)

Although the variation of the ITZ strength influences the yield and the ultimate strength of concrete, the increase in the mortar matrix strength with assuming constant ITZ strength has no effect on the variation of the tensile strength of concrete. This is because the tensile strain at onset of damage at the ITZ is unchanged regardless of the increase in the mortar's strength due to the constant strength of the ITZ. Furthermore, the force resisted by the ITZ and aggregates is suddenly transmitted to the mortar matrix as the strain increases after damage initiation at the ITZ, and then the loss of the interaction between aggregates and mortar matrix due to the damage at the ITZ.

7.8 Simulation of the Crack Penetration into Aggregate Phase

In case of the normal strength concrete which compressive strength is about 30 MPa, the aggregate can be considered as a linear elastic material because the Young's modulus and strength of the aggregate is so high compared to those of mortar matrix that the micro cracks initiated at the ITZ or initially damaged mortar at low stress is mainly propagated through the ITZ surrounding the aggregates. With this reason, the global strength of concrete is connected directly with the ITZ strength, and the majority of meso-scale analytical researches dealing with the concrete fracture or the crack propagation in concrete, including the papers reviewed in section 1.2.3, have been focused on the variation of the ITZ properties with considering aggregates as a linear elastic material. On the other hand, for high strength concrete which compressive strength is over 40 MPa as *American Concrete Institute* defines, the thickness and the porosity of the ITZ is decreased and the strength of the ITZ is increased as the strength

of the concrete increases (Poon *et al.* 2004), and then the micro-cracks initiated at the ITZ or mortar matrix can cause the aggregate breakage due to the improved ITZ strength. Relating to the aggregate fracture, a few experimental and analytical results were reported. Wu et al. (1999) presented that the shape and size of aggregate have effect considerably on the rupture probability of coarse aggregate, and Rosselló and Elices (2004) reported experimentally the effect of the ITZ strength on the aggregate damage. Mohamed and Hansen (1999) showed analytically that the tensile strength ratio between the aggregate and the matrix plays an important role in determining the possibility of crack penetration into the aggregate. They, however, assumed that the ITZ strength is always 90% of the matrix strength, and the meso-scale analysis model is limited to the circular shape aggregate model.

In order to investigate more clearly the process of the crack propagation into the aggregate under tensile loading, 2-D meso-scale analysis is performed applying the proposed coupled plasticity-damage model to the aggregate phase as well as the ITZ and mortar matrix. Two different aggregate shape models, circular and arbitrary polygonal shape models, are considered, and the effect of the ITZ strength on the crack penetration into the aggregate is investigated. The effect of notches on both sides of the meso-scale analysis model is also observed. The tensile stress-strain relation of the aggregate and mortar matrix are shown in Figure 7.18, and the material constants of each phase used in the simulation are also listed in Table 7.4. As seen, the aggregate shows much brittle behavior after yielding compared to the behavior of the mortar matrix.

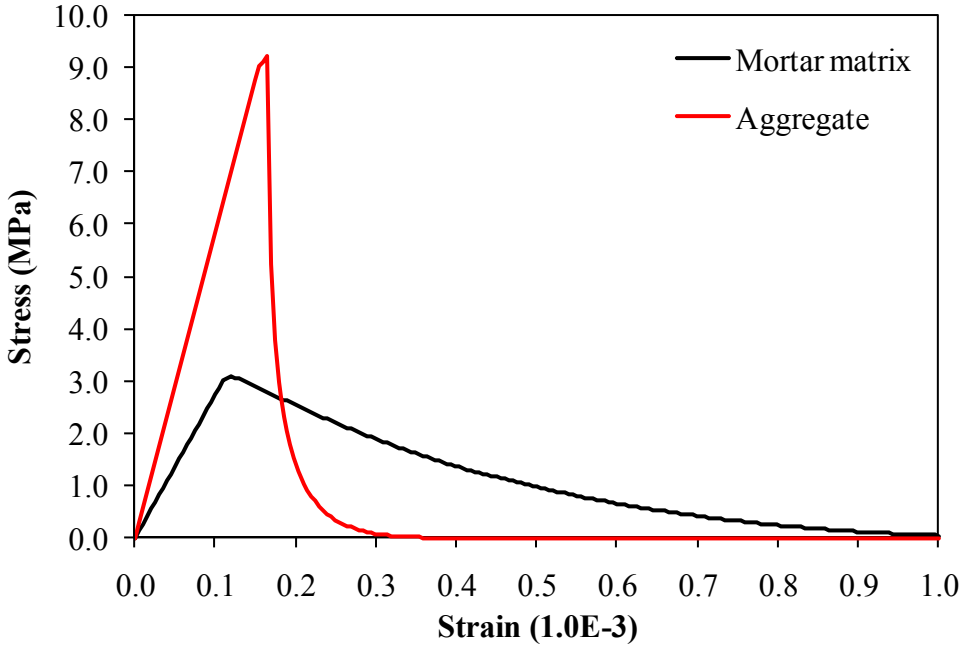

Figure 7.18 Tensile stress-strain relation of the aggregate and mortar matrix for the simulation of the crack penetration process into the aggregates

Table 7.4 Material constants of the aggregate and mortar matrix

	Elastic Constants		Tensile Material Constants					Yield Criteria	
	$\bar{E}$ (MPa)	ν	f_0^+ (MPa)	K_0^+ (MPa)	h^+ (MPa)	B^+	q^+	α	α_p
Mortar	26,000	0.22	3.0	3.0	10,000	1.30	1.10	0.12	0.20
Agg.	55,500	0.16	9.0	9.0	25,000	2.00	0.40		

	Compressive Material Constants					
	f_0^- (MPa)	Q^- (MPa)	b^-	K_0^- (MPa)	B^-	q^-
Mortar	15.0	80.0	820.0	20.0	0.15	1.40
Agg.	23.0	90.0	1200.0	25.0	0.20	1.50

The behavior and crack distribution of the elastic damage aggregate model under the uniaxial tensile loading is compared with those of the elastic aggregate model. Moreover, two notches at both sides of the meso-scale analysis model, as Figure 7.19, are generated in order to investigate the effect of the notch on the process of the crack propagation, and the size of the notch is 10mm × 1mm. The properties of the ITZ assumed to be identical to the properties of the mortar matrix in this simulation.

Figure 7.19 shows the tensile crack distribution of the elastic and elastic damage circular and arbitrary polygonal shape aggregate models without the notches. In case of the meso-scale analysis model without the notch, the property of the aggregate, although several cracks on the aggregate of the elastic damage aggregate model are observed, has little effect on the condition of the tensile crack propagation, and the tensile cracks are distributed widely for both models. This is because several tensile cracks are initiated simultaneously at several places of the mortar matrix, and the cracks are propagated to different directions. The tensile crack distribution of the elastic and elastic damage circular and arbitrary polygonal shape aggregate models with the notches is shown in Figure 7.20. Unlike the results of the analysis model without the notch, the distribution of the tensile cracks is remarkably localized in the middle of the model for both cases because the initial damage is localized at the tip of the notches acting as an initial defect, and the stress is also concentrated in the middle of the model. Especially, the macro tensile crack on the elastic damage arbitrary aggregate shape model is propagated almost horizontally from the end of the both notches with penetrating coarse aggregate. Moreover, comparing the elastic damage arbitrary shape aggregate model (Figure 7.20

(d)) with the elastic damage circular shape aggregate model (Figure 7.20 (b)), since the tensile crack on the circular shape aggregate model can be propagated readily following the smooth surface of the circular aggregate, the intensity of the aggregate damage of the arbitrary shape aggregate model is more severe than that of the circular shape aggregate model.

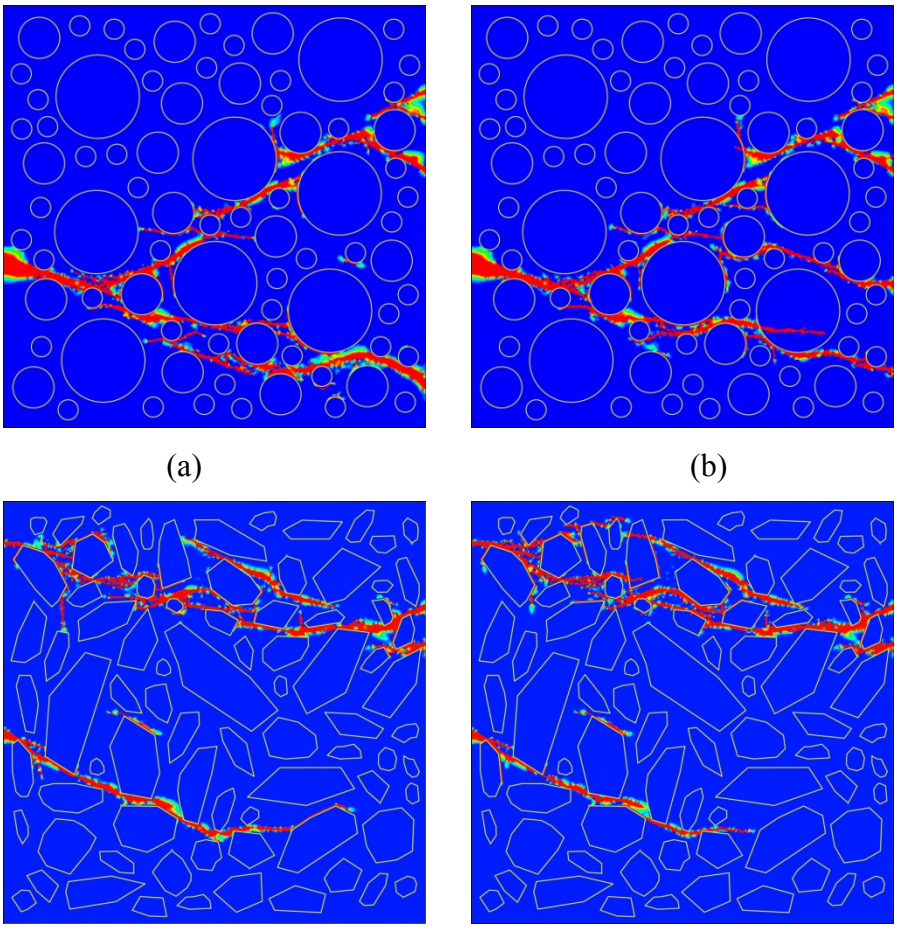

Figure 7.19 Tensile crack distribution of the circular shape aggregate model; (a) Elastic aggregate model without the notch, (b) elastic damage aggregate model without the notch, (c) elastic aggregate model with the notches, and (d) elastic damage aggregate model with the notches

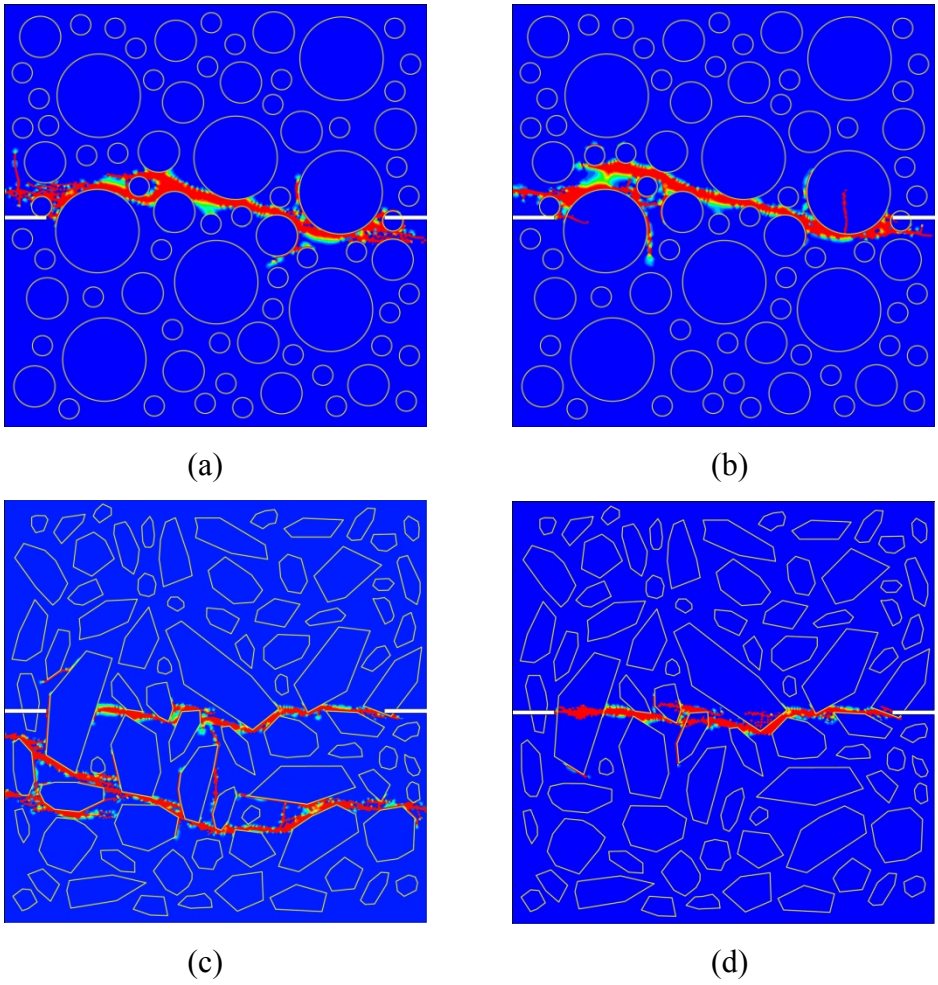

Figure 7.20 Tensile crack distribution of the arbitrary polygonal shape aggregate model; (a) Elastic aggregate model without the notch, (b) elastic damage aggregate model without the notch, (c) elastic aggregate model with the notches, and (d) elastic damage aggregate model with the notches

The tensile load-displacement curves of eight analysis models discussed above are shown in Figure 7.21. As discussed at section 7.3, the circular shape aggregate model gives the higher tensile strength then the arbitrary polygonal shape aggregate model. In case of the models without the notch, the tensile behavior of the model, although the elastic aggregate model shows little higher tensile strength, is almost the same.

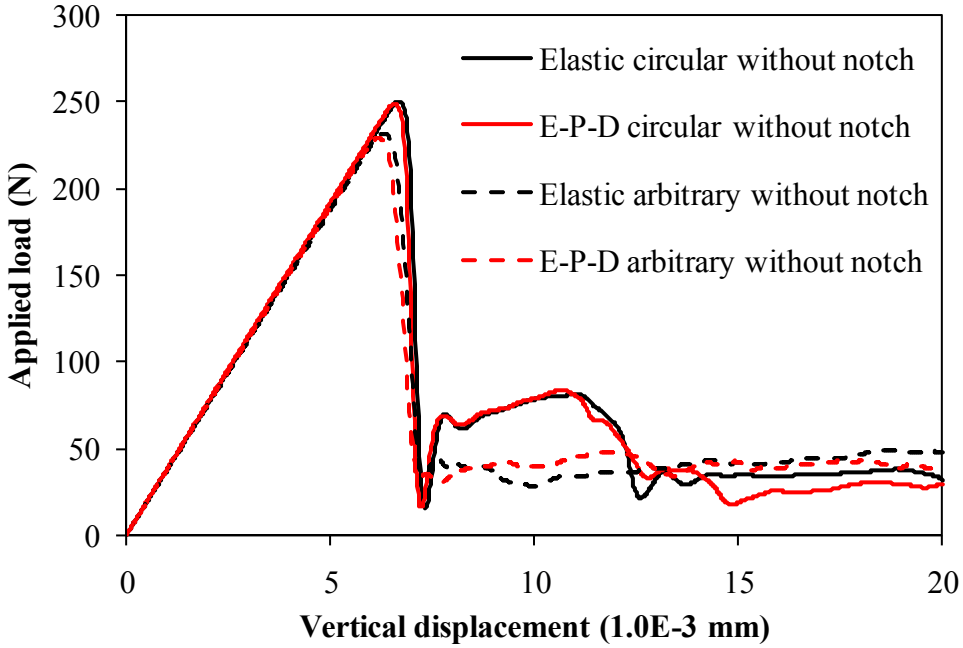

(a)

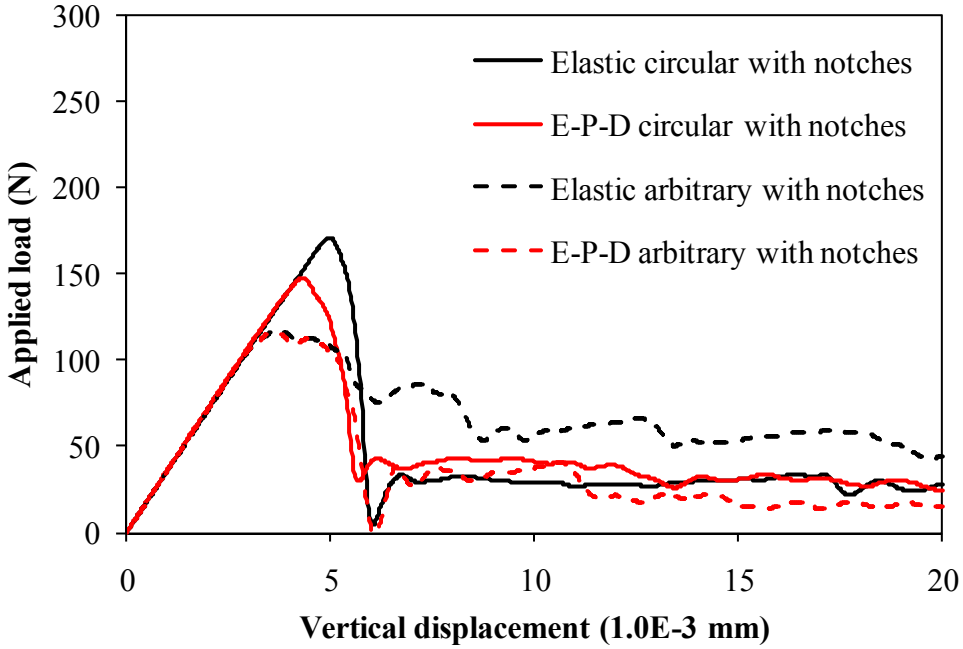

(b)

Figure 7.21 Load-displacement curves; (a) Models with notches and (b) models without notch

On the other hand, in case of the models with the notches at both sides, the tensile strength of the elastic aggregate model is much higher than that of the elastic-damage aggregate model for the circular shape aggregate model. For the arbitrary shape aggregate model, since the tensile crack propagation mechanism of the two models is totally different, the different post-yielding behavior of the two models is noticeable while the tensile strength of the two models is almost the same.

Since the condition of the crack penetration into the aggregates is more apparent on the arbitrary polygonal shape aggregate model with the notches as discussed above, the effect of the tensile strength variation of the ITZ is investigated with the arbitrary polygonal shape aggregate model with the notches. The stress-strain curve for the ITZ is shown in Figure 7.22. The tensile strength of the ITZ varies from 2.1 MPa (70% of the mortar matrix strength) to 3.0 MPa (100% of the mortar matrix strength).

The crack distribution of the arbitrary shape aggregate models with notches under the uniaxial tensile loading by the change of the ITZ strength is shown in Figure 7.23. As the result of the analysis, the tensile crack distribution and condition of the crack penetration into the aggregate is considerably different by the change of the ITZ strength. Although few minor cracks penetrate into the aggregates even when the ITZ strength is less than 80 % of the mortar strength, the dominant tensile crack on the aggregates is occurred when the ITZ strength is greater than 90 % of the mortar strength. Moreover, in case that the ITZ strength is less than 80 % of the mortar strength, even though the aggregate shows the elastic-damage response, the tensile cracks are mainly propagated through the ITZ surrounding the aggregates, while the tensile crack tends to

localized on the middle of the RVE as the ITZ strength increased. The tensile load-displacement relation is shown in Figure 7.24. Whereas the yield strength and the first peak stress are proportional to the ITZ strength, the second peak stress, that is the ultimate strength caused by the crack bridging of the aggregate does not linearly proportional to the ITZ strength, and the model which ITZ strength is 90% of the matrix strength (2.7 MPa) gives the highest ultimate strength. It means that the yield and ultimate strength of the meso-scale concrete analysis model considering aggregate fracture can be affected by the aggregate distribution. Furthermore, in case that the tensile crack passes through the aggregate clearly, that is, when the yield strength of the ITZ is 3.0 and 2.7 MPa, the post-yielding strength drops greatly as the displacement increases.

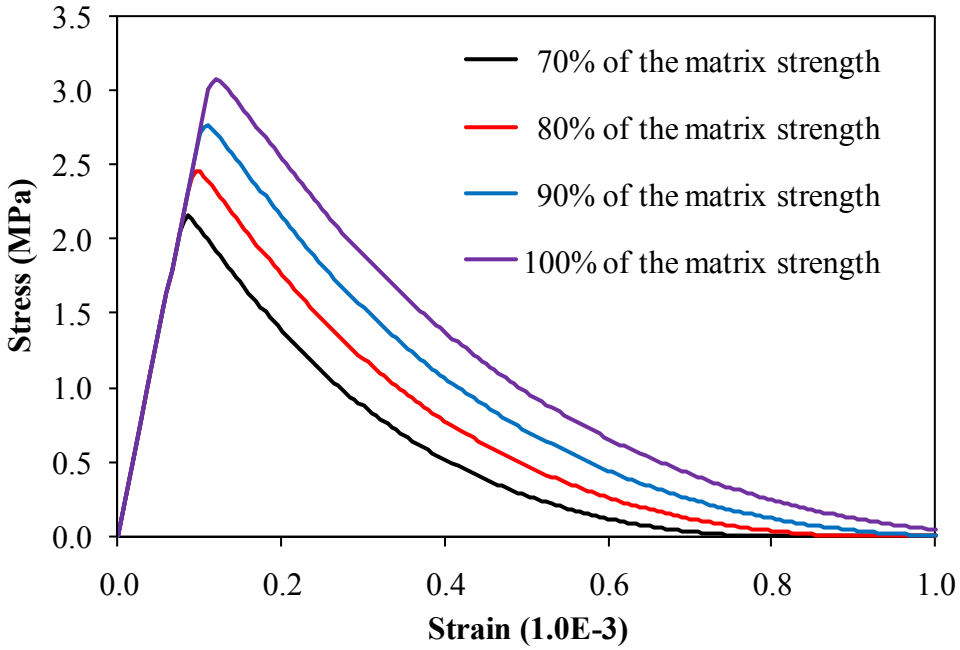

Figure 7.22 Variation of the ITZ tensile strength

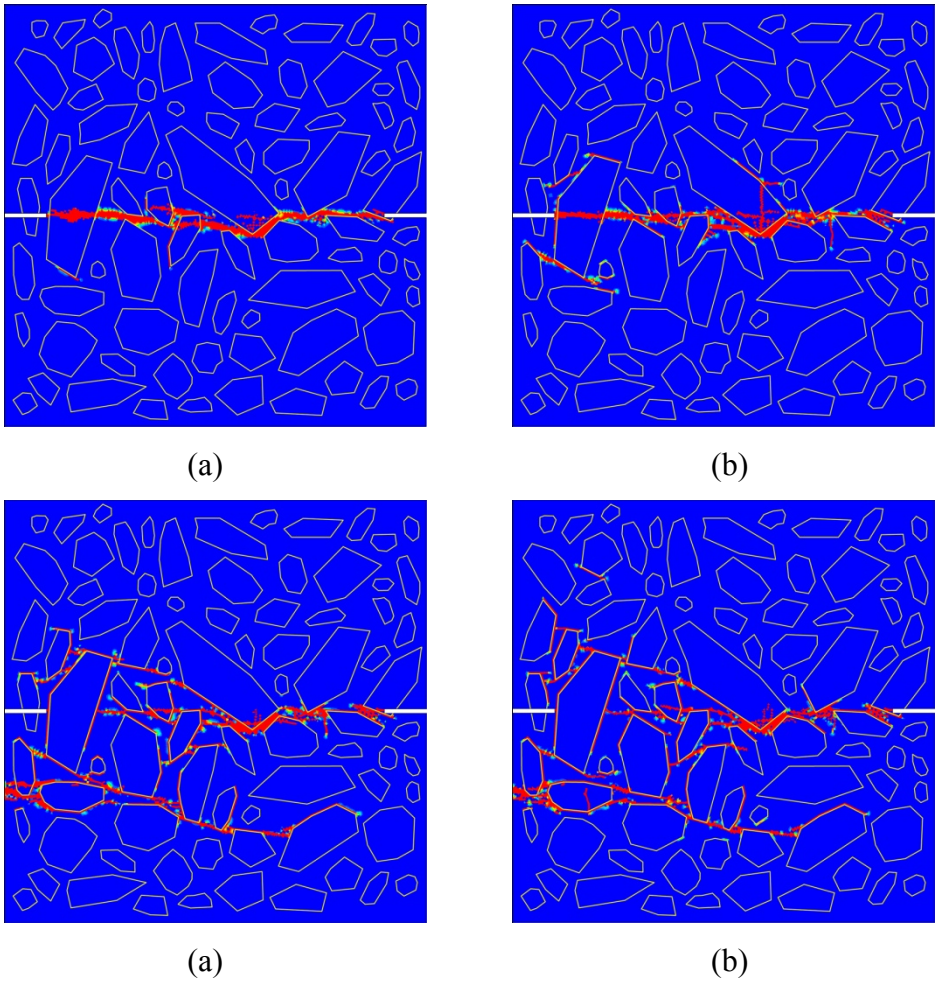

Figure 7.23 Tensile crack distribution on the arbitrary polygonal shape aggregate models with the notches by the change of the ITZ strength. (a) σ_{ITZ} = 3.0 MPa, (b) σ_{ITZ} = 2.7 MPa, (c) σ_{ITZ} = 2.4 MPa, and (d) σ_{ITZ} = 2.1 MPa

The processes of the tensile crack propagation for two different ITZ strength models (σ_{ITZ} = 3.0 MPa and σ_{ITZ} = 2.1 MPa) are compared with each others and shown in Figure 7.25. For both analysis models, the crack is initiated at the end of the right notch due to the crack bridging effect of coarse aggregate existing just ahead of the left notch. In case of the model which the ITZ strength is 2.1 MPa, the tensile crack initiated

at the end of the right notch, as the vertical displacement increases, is developed quickly through the ITZ surrounding aggregates. On the other hand, the crack is propagated relatively slowly through the aggregates when the ITZ strength of the model is 3.0 MPa. As the result of the research, it is noteworthy that the crack approaching angle to the aggregate that can be altered by the aggregate distribution as well as the size and shape of aggregate is also important factor that controls the condition of the crack penetration into the aggregates.

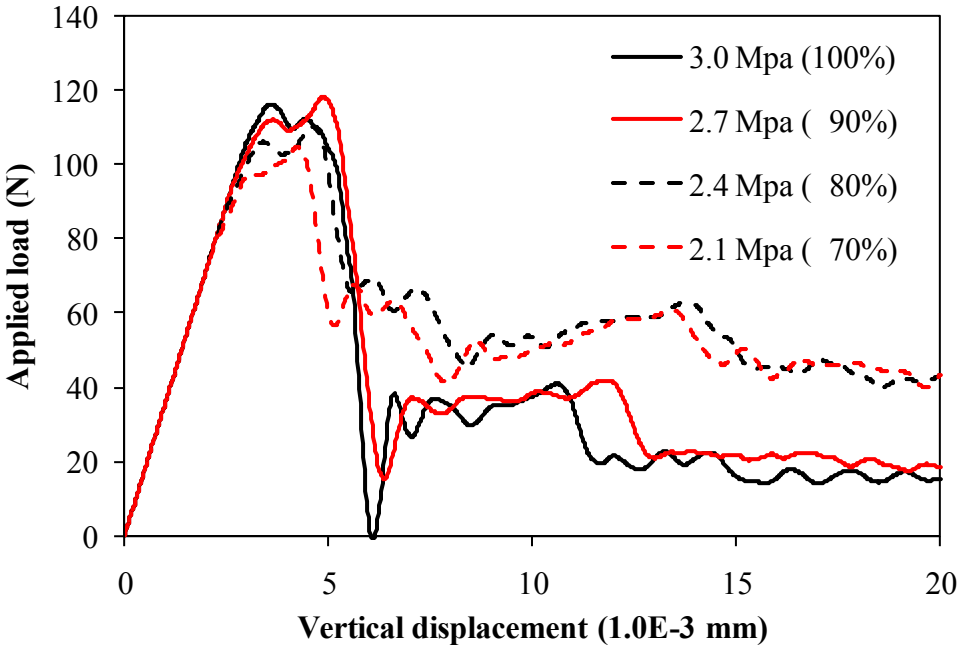

Figure 7.24 Load-displacement relation of the arbitrary shape aggregate models with notches according to the change of the ITZ strength

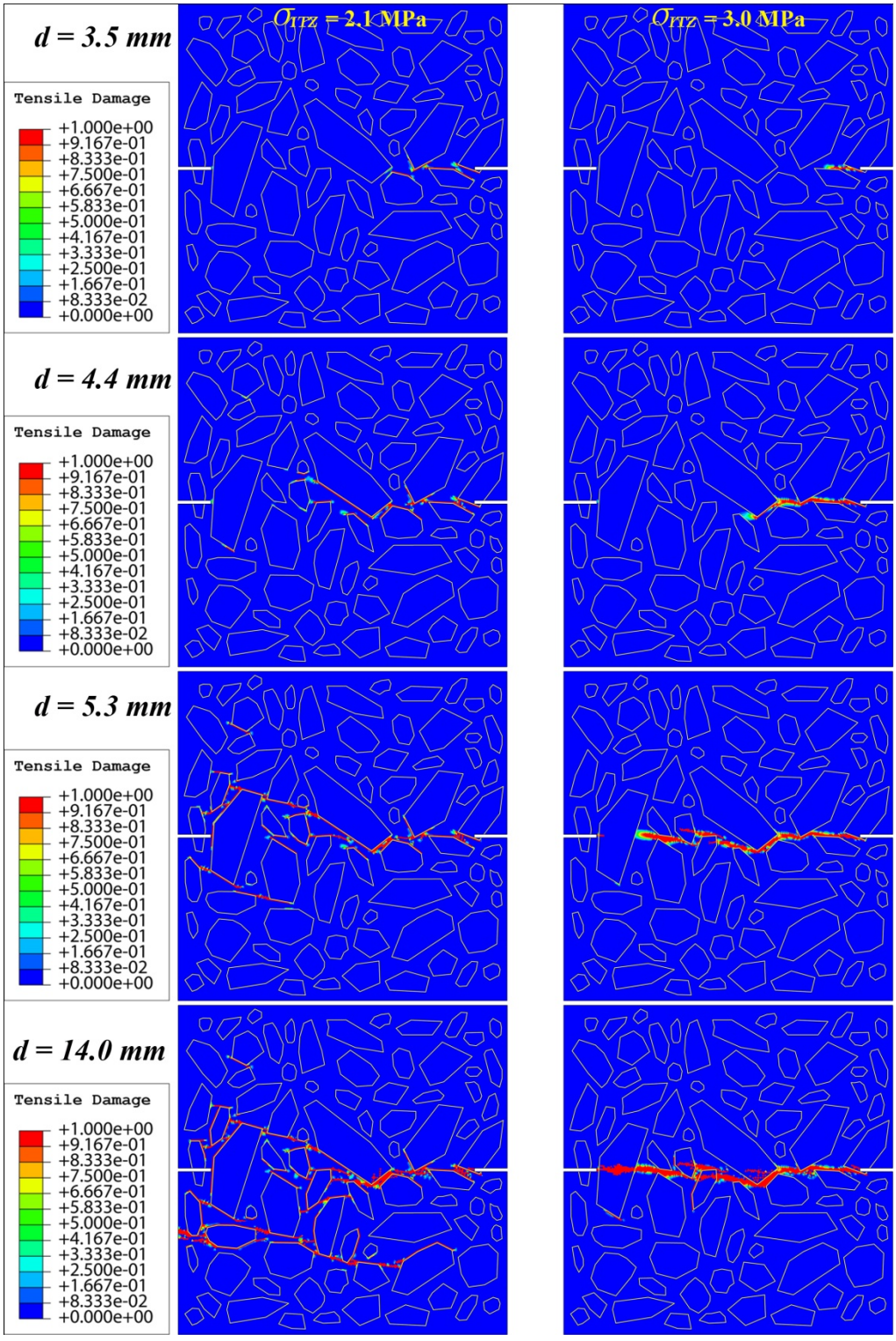

Figure 7.25 Crack propagation processes of the elastic and elastic damage arbitrary shape aggregate models with notches

7.9 3-D Meso-scale Simulation of Concrete

In order to use the proposed coupled plasticity-damage constitutive model for the comparison with the simplified 2-D meso-scale analysis results, the tensile behavior of concrete is investigated with a 3-D meso-scale analysis model. Figure 7.26 shows the 3-D meso-scale RVE of concrete, and the distribution of coarse, middle, and fine aggregates is shown in Figure 7.27.

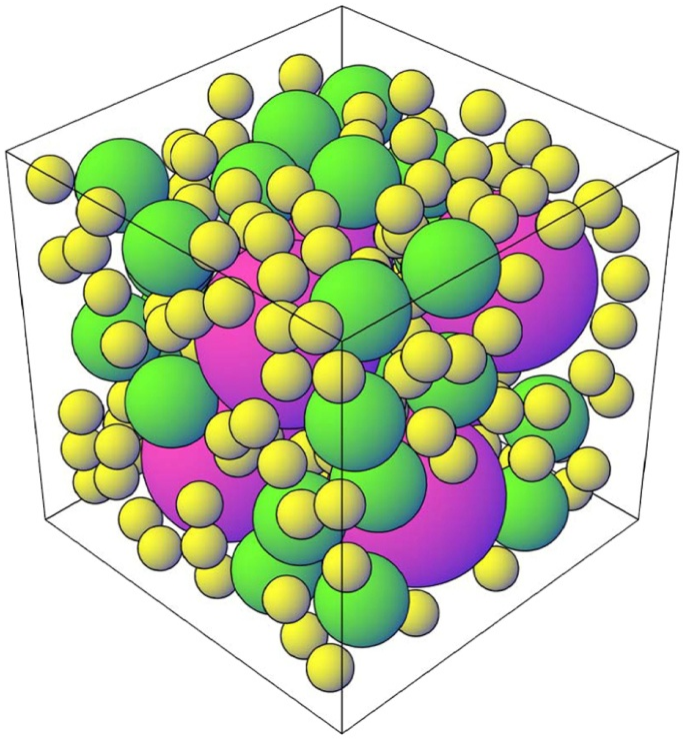

Figure 7.26 3-D meso-scale analysis model for concrete

In order to reduce the computational cost, only the size of the 3-D RVE is reduced to 50 mm × 50 mm × 50 mm, and all other micromechanical properties, such as the size of coarse, middle, and fine aggregate, the aggregate gradation, the ITZ thickness,

and the material properties of the ITZ, aggregate, and mortar matrix are identical to those of the 2-D meso-scale analyses. A 40 % of aggregate volume fraction is assumed for conducting the 3-D meso-scale analysis, and the number of coarse, middle, and fine aggregates used for the generation of the 3-D model is 6, 28, and 154, respectively. This 3-D simulation will show the applicability of the conducted 2-D simulations in that the later provide very meaningful simulations as compared to more realistic 3-D models.

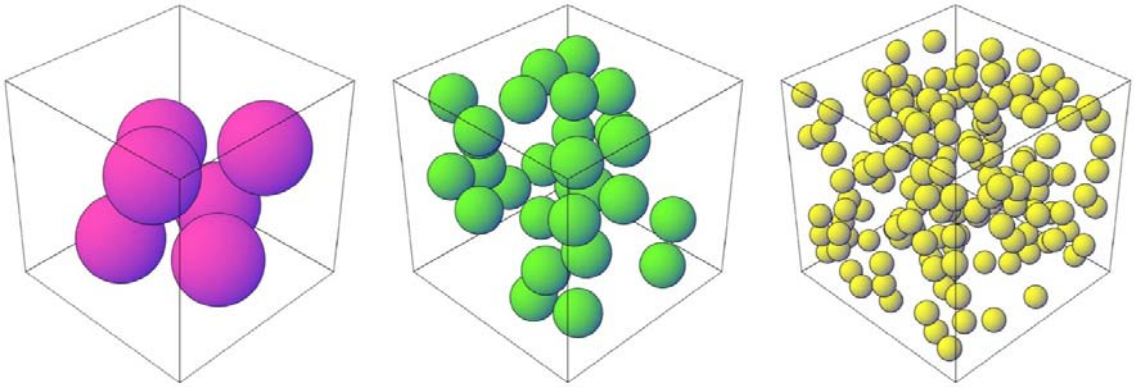

(a) (b) (c)

Figure 7.27 Distribution of aggregates. (a) Coarse aggregates, (b) middle aggregates, and (c) fine aggregates

The stress-strain responses from the 3-D and 2-D simulations are shown in Figure 7.28. As can be seen, the 3-D analysis gives the lower ultimate tensile strength but the higher ductility compared to the 2-D meso-scale analysis. This is because the ITZ volume fraction of the 3-D model is about 50% greater than that of the 2-D meso-scale model although the aggregate volume fraction and the ITZ thickness of the 2-D and 3-D models are the same for both models.

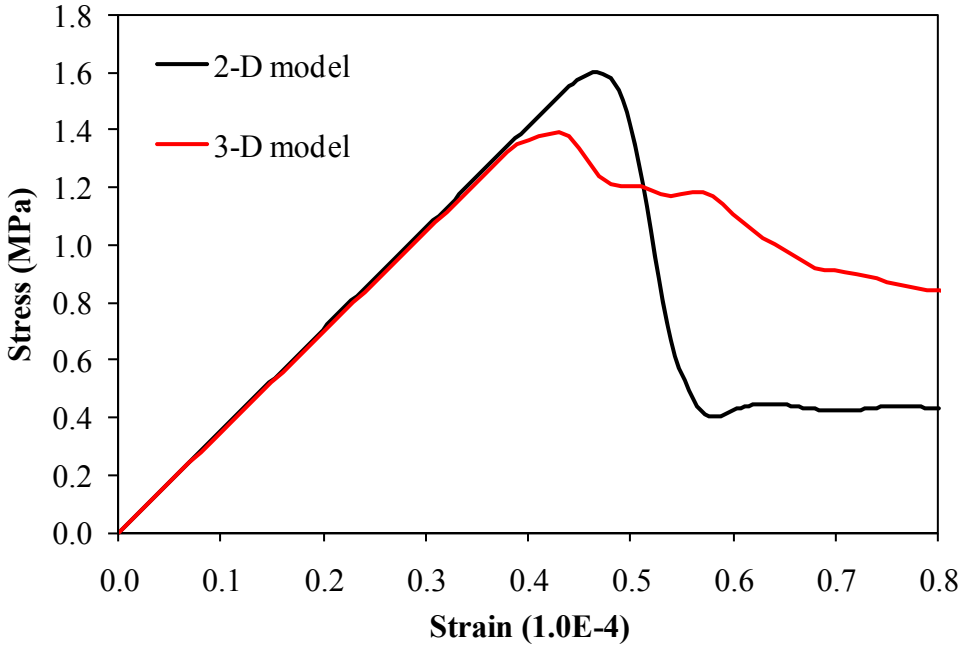

Figure 7.28 Comparison between the 2-D and 3-D meso-scale analysis results

The distribution of the tensile damage in the mortar matrix and the ITZ are shown in Figure 7.29. Although the tensile damage is initiated at the ITZ when the vertical strain is 0.30×10^{-4}, the initial micro tensile damage at the ITZ has a marginal effect on the reduction of the Young's modulus of concrete, and the Young's modulus of the 3-D meso-scale concrete analysis model begins to reduce when the vertical strain is 0.38×10^{-4} which causes initial tensile damage in the mortar matrix. Due to the vertically applied tensile displacement, the ITZ region existing on the top and bottom of aggregates is mainly damaged, and the damaged ITZ region is localized with forming a plane on the top part of the analysis model although the tensile damage at the ITZ is initiated at several regions simultaneously.

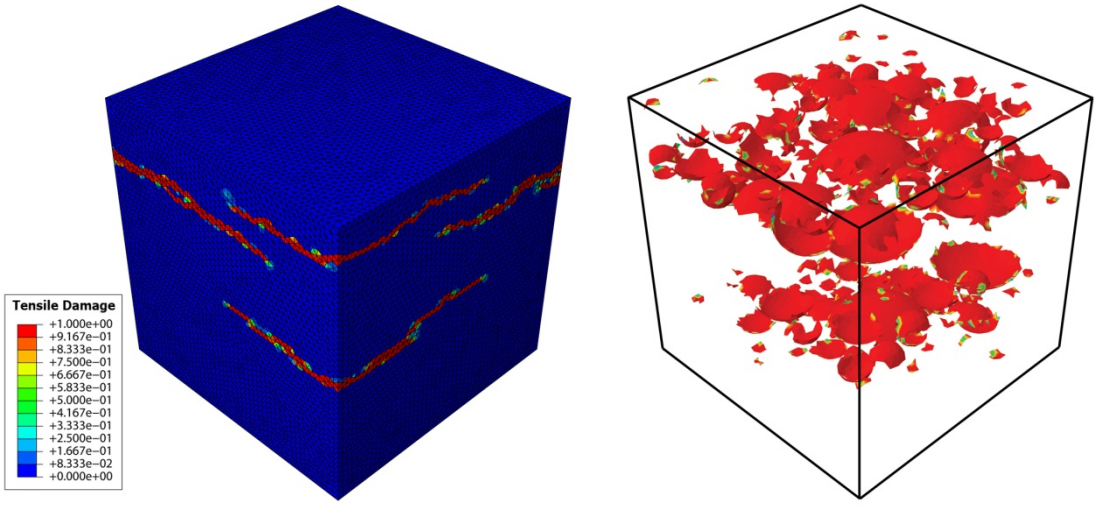

(a) (b)

Figure 7.29 Distribution of the tensile damage. (a) Outside of the mortar matrix , and (b) the ITZ

The progressive tensile damage propagation in the mortar matrix with the increase of the vertical displacement is shown in Figure 7.30. Although the initial tensile damage in the mortar matrix occurs randomly at the several regions simultaneously, the tensile damage is propagated with forming one overwhelming damaged plane as the vertical displacement increases.

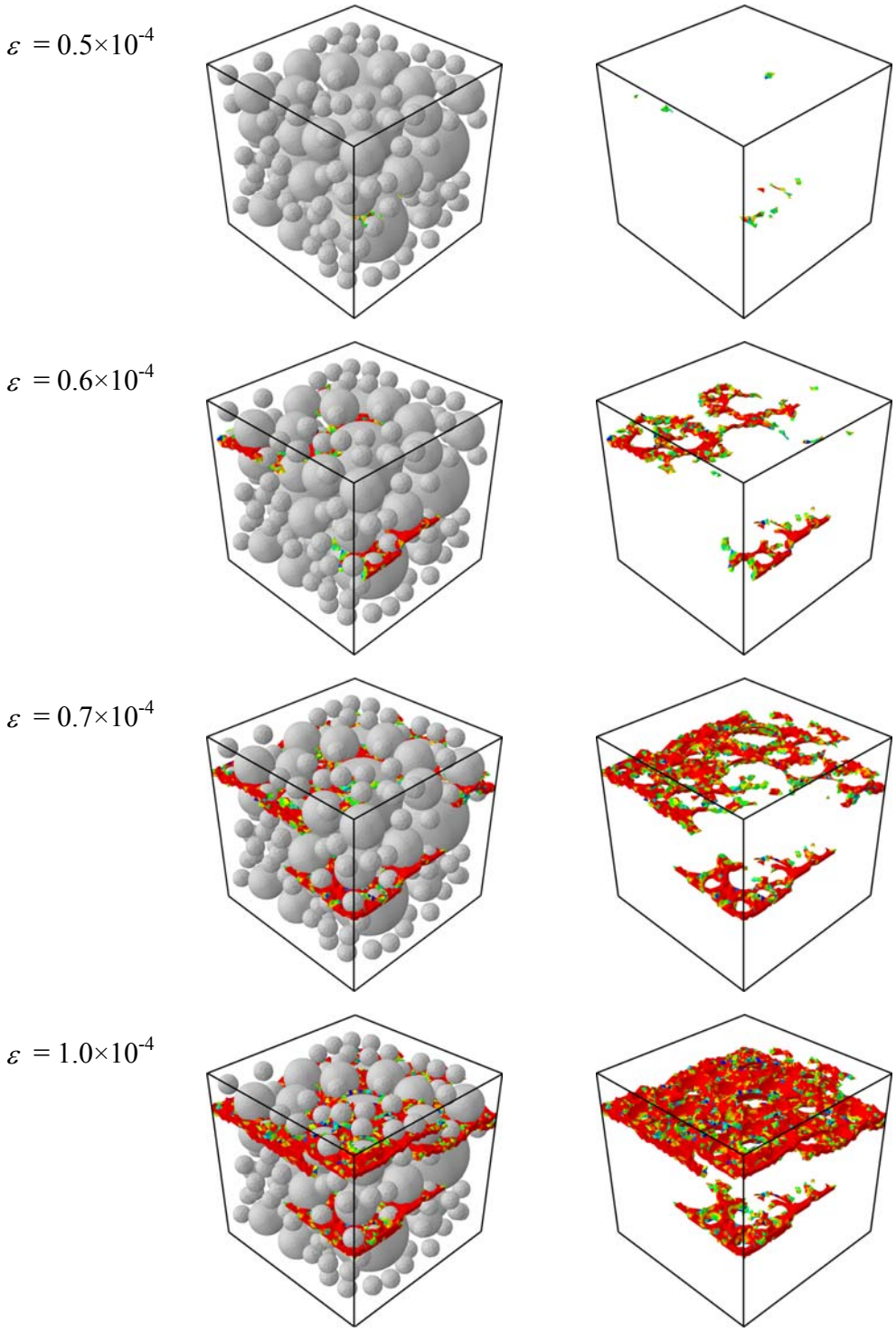

Figure 7.30 Tensile damage propagation. (a) with aggregates and (b) without aggregates

CHAPTER VIII

ANALYSIS OF NANOTUBE REINFORCED CEMENT COMPOSITES

As mentioned, the CNT pull-out process is composed of three stages - bonded, debonding, and sliding stage. In the bonded stage, the CNT and the matrix surrounding the CNT are perfectly bonded, in the debonding stage, the separation between the CNT and the matrix at interface of them begins to occur, and the debonded part coexists with the well-bonded part in this stage, and the last stage, sliding stage, is commenced as soon as the whole interface between the CNT and the matrix is fully debonded, and the friction force at interface resists the pull-out force of the CNT.

Since the ultimate pull-out strength of the straight CNT is determined by the bonding strength of the interface between the CNT and the matrix, the first stage, well-bonded stage is the most important for the straight CNT while the other two stages – debonding and sliding stage – can be neglected if the pull-out strength is the only matter of concern. For the curved CNT, however, the sliding stage can be more interesting and important stage even though the ultimate pull-out strength is of unique interest. This is because the bending stiffness of the CNT due to the extremely high modulus of elasticity can cause extra friction force during the sliding stage.

Therefore, based on the existing experimental and numerical research results of the CNTs itself and the composite effect between the CNT and the matrix, this chapter is focused on the verification of the pull-out mechanisms of the single straight CNT from the cement matrix, the debonding process at the interface between the CNT and the

matrix, and the damage initiation and propagations at the cement matrix surrounding the CNT through the single straight CNT pull-out simulations. The simulations will be conducted with varying a variety of parameters such as the interfacial shear strength, stiffness, and fracture energy, the strength and the Young's modulus of the matrix, and the CNT mechanical properties and aspect ratio.

Moreover, the pull-out mechanisms of the single curved CNT embedded in the elastic body is investigated. Since the third stage, sliding stage can be more important for the single curved CNT pull-out analysis, the first and second stages, bonding and debonding stages are not considered. With the 3-dimensional analysis model, the effect of the friction force, the Young's modulus of the CNT and the matrix, and the radius of curvature of the CNT on the sliding behavior of the CNT during pull-out process are also investigated.

8.1 Single Straight CNT Pull-out Analysis

8.1.1 Single Straight CNT Pull-out Analysis Model

With the proposed coupled plasticity-damage model for cement matrix, the single CNT pull-out analysis is performed. Figure 8.1 shows the representative volume element (Cervenka and Papanikolaou) finite element model for the CNT/cement matrix composite. From the literature review, the outer diameter and thickness of the embedded CNT are chosen to be 20 nm and 0.34 nm, respectively. Besides, the diameter of the cement matrix surrounding the CNT is 292 nm, and the embedded length of the CNT is assumed to be 1000 nm.

Since both the CNT and mortar matrix are the axisymmetric with respect to the longitudinal axis, the axisymmetric model is generated as shown in Figure 8.2. The commercial FE analysis software, Abaqus v6.9 is used for the analysis. Moreover, a 4-node bilinear axisymmetric quadrilateral element with reduced integration (CAX4R) is used for the cement matrix and a 2-node linear axisymmetric shell element (SAX1) is used for the CNT. The minimum element size of the mortar matrix is 2.5 nm × 2.5 nm, and the mesh density is coarsened towards the outer surface boundary in order to reduce the computational time.

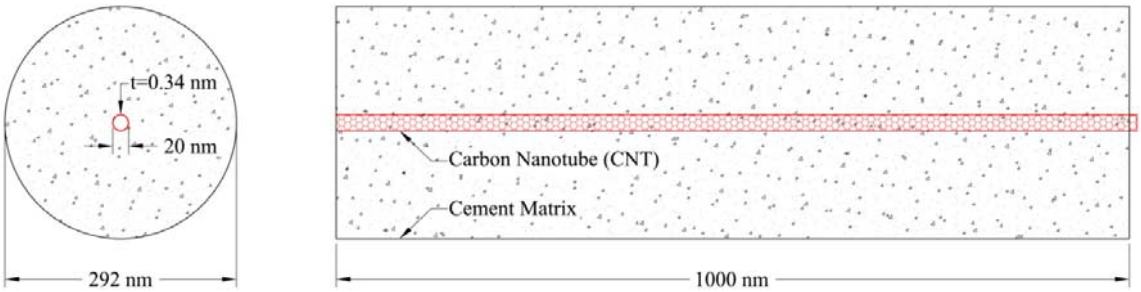

Figure 8.1 RVE of the CNT/cement matrix composite: (a) Sectional and (b) side view

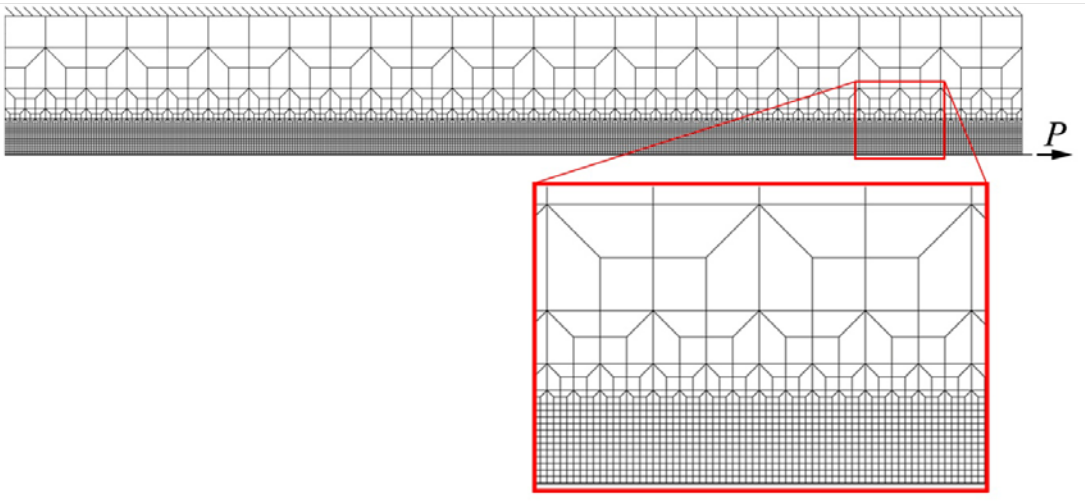

Figure 8.2 Finite element pull-out analysis mesh and boundary conditions

Since the CNT is much stronger than the cement matrix, the Young's modulus and Poisson's ratio of the CNT is assumed to be 1.0 TPa and 0.1, respectively, and the material properties of the cement matrix used in the analysis are listed in Table 8.1. Since the CNT is much stronger than the cement matrix, the CNT is modeled as a linear elastic material, while the tensile and compressive stress-strain relation of the mortar matrix and the damage evolution by the increase of the strain are shown in Figure 8.3.

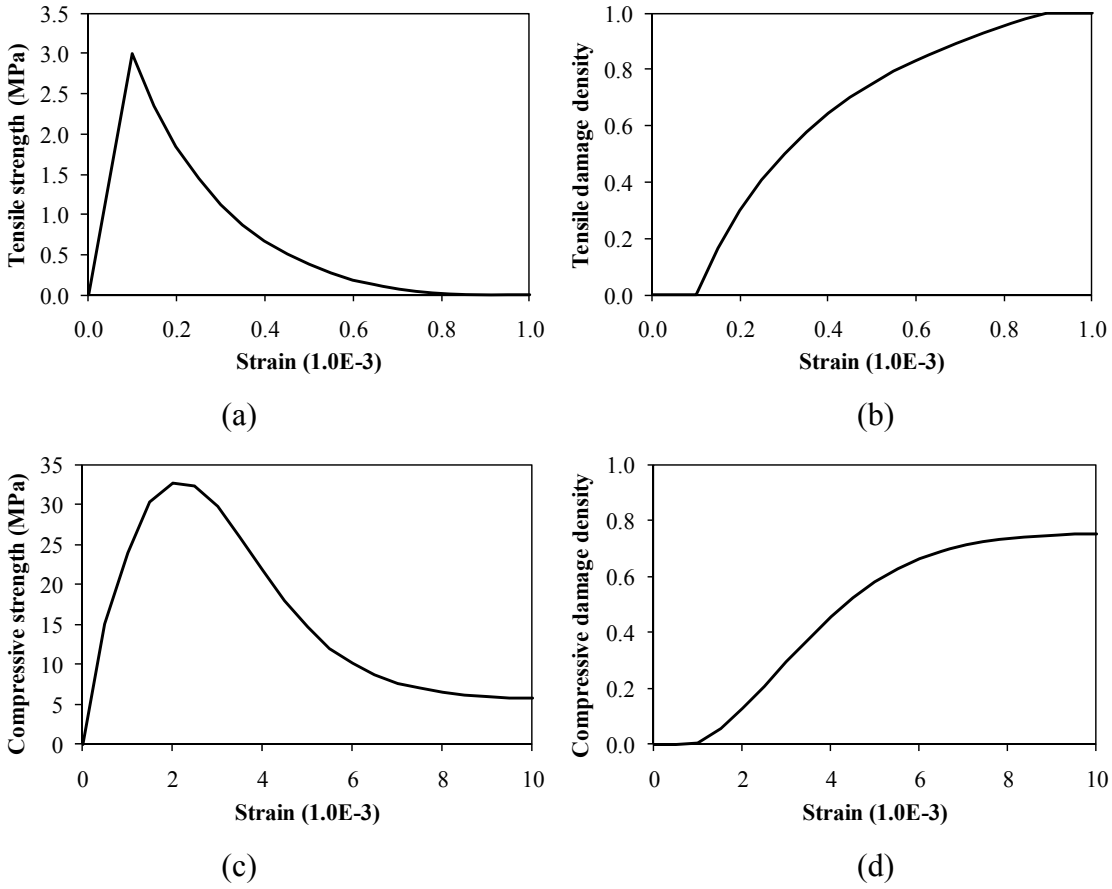

Figure 8.3 Material properties of the mortar matrix: (a) Tensile stress-strain relation, (b) tensile damage density evolution, (c) compressive stress-strain relation and (d) compressive damage evolution

Table 8.1 Material properties used in the single CNT pull-out analysis

Elastic Constants		Yield Criterion		Tensile Material Constants				
$\bar{E}$ (MPa)	ν	α	α_p	f_0^+ (MPa)	K_0^+ (MPa)	h^+ (MPa)	B^+	q^+
30,000	0.2	0.12	0.2	3.0	3.0	10,000	1.30	1.10

Compressive Material Constants					
f_0^- (MPa)	Q^- (MPa)	b^-	K_0^- (MPa)	B^-	q^-
15.0	120	1000	20	0.15	1.40

8.1.2 Cohesive Interfacial Model

In order to simulate the CNT pull-out process, clear comprehension about the behavior of the CNT and mortar matrix under loads as well as the interfacial properties between the CNT and mortar matrix should be preceded. Since the load transfer mechanisms between the CNT or fiber and matrix are totally dependent on the properties of the interfacial zone between them, it is crucial to understand the behavior of the interface region, where that the reliability of the CNT- or fiber-based composite material model is governed by the modeling technique of the interface region. For the simulation of the single fiber pull-out process, several interfacial models, such as perfect bonding model, spring-like model, and interphase model have been used (Achenbach and Zhu 1989; Jia *et al.* 1999; Liu and Xu 2000; Liu *et al.* 2000; Thostenson *et al.* 2001; Liu and Chen 2003). Especially, the friction model has been commonly used for modeling of the interfacial zone since the energy absorbed by the friction between the fiber and matrix during sliding after debonding is one of the most significant factors that govern the reinforcing effect of the fiber on the matrix.

The cohesive zone model technique is selected since it is considered one of most efficient and simple methodologies to represent interfacial deterioration. It includes fracture mechanics principles to numerically simulate crack nucleation, initiation and propagation at the interface of two materials. The concept of a cohesive zone was originally presented by Barenblatt (1959) and Dugdale (1960) and has been widely used to describe a gradual separation across an interface. In the following micromechanical simulations, the interface is constructed using the zero-thickness built-in cohesive elements available in Abaqus. The mechanical response of these elements is linear elastic prior to the damage initiation. The damage initiates when the element reaches an especial criterion associated with the strength of the interface. After the damage initiates, energy is released and the traction resistance of the interface is reduced. A crack initiates when the element losses completely its traction capabilities. The load this element used to carry is then transmitted to the surrounding elements, promoting the propagation of the crack through the interface. In summary, the mechanical response of the cohesive elements is dictated by the traction-separation law that has three main components: 1) a linear elastic modulus prior to damage initiation, 2) a damage initiation criterion, and 3) a damage propagation criteria (i.e., crack initiation criterion).

In this study, it is assumed that the effect of the energy absorbed by the friction between the CNT and mortar matrix during pull-out process after debonding is negligible because the surface of the natural CNT is very smooth. Therefore, the load transferring between the CNT and the mortar matrix is assumed to occur only during elastic deformation and debonding process. Furthermore, since the interfacial zone

between the CNT and mortar matrix has almost a zero thickness, surface-based cohesive behavior that is primarily intended for simulations in which the thickness of the interface is negligibly small is adopted. Figure 8.4 shows the response of the interface used in the analysis. The linear elastic traction-separation law prior to damage and the energy-based damage evolution with linear softening for cohesive surfaces are assumed. The failure of the cohesive bond is characterized by progressive degradation of the cohesive stiffness, which is driven by the damage process.

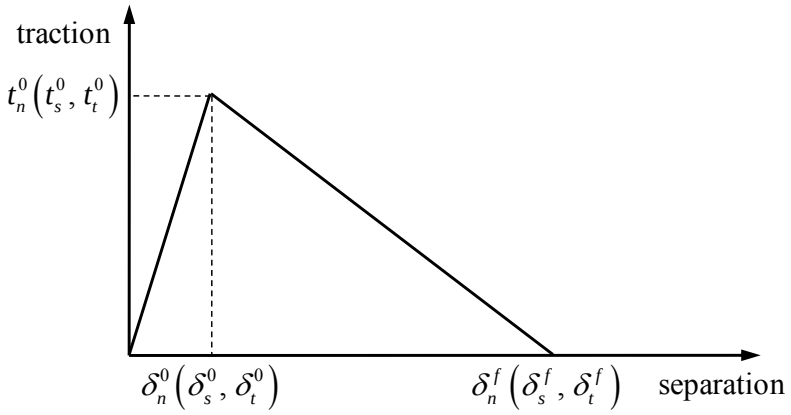

Figure 8.4 Linear traction-separation response of the interface

In three-dimensional problems, the nominal traction stress vector, t, consists of three components: t_n, t_s, and t_t, which represent the normal and two shear tractions, respectively. The corresponding separation to the tractions are denoted by δ_n, δ_s, and δ_t. Then, the elastic behavior can be written as follows:

$$t = \begin{Bmatrix} t_n \\ t_s \\ t_t \end{Bmatrix} = \begin{bmatrix} K_{nn} & K_{ns} & K_{nt} \\ K_{ns} & K_{ss} & K_{st} \\ K_{nt} & K_{st} & K_{tt} \end{bmatrix} \begin{Bmatrix} \delta_n \\ \delta_s \\ \delta_t \end{Bmatrix} = K\delta \tag{8.1}$$

The elasticity matrix K provides fully coupled behavior between all components of the traction vector and separation vector, and the off-diagonal terms are zero for uncoupled traction-separation behavior. Moreover, the maximum separation criterion is adopted for the damage initiation. This criterion means that the damage is assumed to initiate when the maximum separation ratio reaches the value of one, and the criterion can be represented as follows:

$$\max\left\{\frac{\langle \delta_n \rangle}{\delta_n^0}, \ \frac{\delta_s}{\delta_s^0}, \ \frac{\delta_t}{\delta_t^0}\right\} = 1 \tag{8.2}$$

where δ_n^0, δ_s^0, and δ_t^0 represent the peak values of the contact separation, when the separation is either purely along the contact normal or purely in the first or the second shear direction, respectively.

Conceptually, similar ideas to the damage density φ explained in detail in Chapter II, is applied for describing damage evolution on cohesive surfaces. The damage evolution law in the cohesive model describes the rate at which the cohesive stiffness is degraded on the corresponding initiation criterion is reached. A scalar damage variable, D, is employed and represents the overall damage at the contact point. The damage variable initially has a value of zero and monotonically evolves from 0 to 1 upon further

loading after the initiation of damage. Therefore, the contact stress components affected by the damage is expressed as follows:

$$
\begin{aligned}
t_n &= \begin{cases} (1-D)\,\bar{t}_n, & \bar{t}_n \geq 0 \\ \bar{t}_n, & \text{otherwise(no damage to compressive stiffness)} \end{cases} \\
t_s &= (1-D)\,\bar{t}_s \\
t_t &= (1-D)\,\bar{t}_t
\end{aligned}
\tag{8.3}
$$

where $\bar{t}_n$, $\bar{t}_s$, and $\bar{t}_t$ are the contact stress components predicted by the elastic traction-separation behavior for the current separation without damage.

8.1.3 The Effect of the Interfacial Shear Strength

The effect of the interfacial shear strength on the global CNT pull-out strength and ductility is investigated first. In order to observe the sensitivity of the interfacial shear strength, other interfacial properties, such as the cohesive stiffness and the fracture energy are maintained constant. Currently, the studies about the effect of the interfacial shear strength of the CNT/cement composites are very few. Thus, the range of the interfacial shear strength extracted from the pull-out experimental test by Naaman et al. (1991). Naaman et al. (1991) investigated the pull-out strength and the interfacial bond shear stress through the pull-out test of the single steel fiber embedded in the cementitious matrix, and the test showed that the interfacial shear strength varies from 1.47 MPa (for low strength matrix) to 9.73 MPa (for high strength matrix). Based on the experimental test results of Naaman et al., the analytical range of the interfacial shear strength is determined considering normal strength cement matrix.

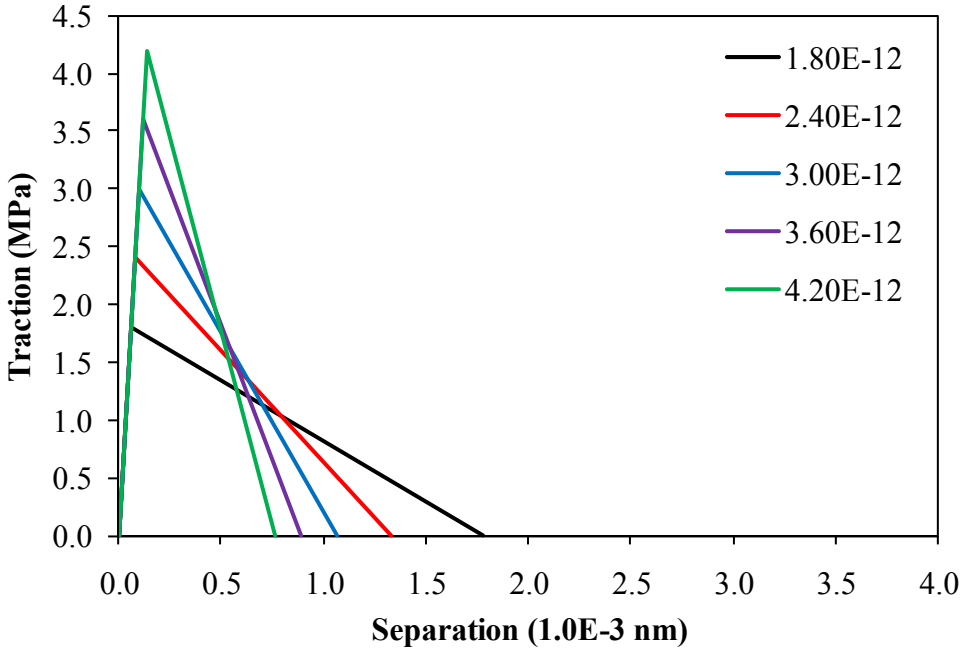

(a)

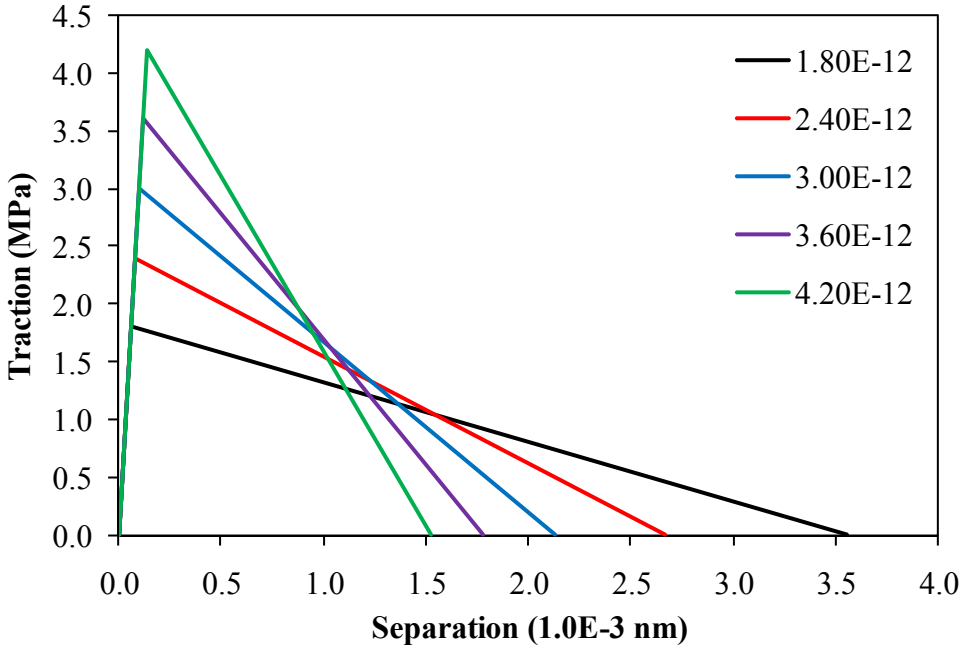

(b)

Figure 8.5 The interfacial shear strength variation: (a) $G = 16\times10^{-16}$ N/nm and (b) $G = 32\times10^{-16}$ N/nm

Figure 8.5 shows the assumed variation of the interfacial shear strength. The interfacial shear strength between the CNT and the cement matrix is varied between 1.8 MPa to 4.2 MPa with the increment of 0.6 MPa, and the magnitude of the fracture energy for model 1 (Figure 8.5(a)) and model 2 (Figure 8.5(b)) are 16×10^{-16} N/nm and 32×10^{-16} N/nm, respectively.

The single CNT pull-out analysis results with varying the interfacial shear strength are shown in Figure 8.6. The global pull-out strength and the ductility are merely affected by the variation of the interfacial shear strength. On the other hand, the increase of the fracture energy causes the rise of both the CNT pull-out strength and the ductility. Moreover, it is noteworthy that the magnitude of the interfacial shear strength does not have a direct influence on the damage distribution in the matrix. Sudden drops in the applied load due to damage evolution in the matrix for some cases can be identified in Figure 8.6(b). It should be noted that there are two reasons causing the drop in the applied load during the pull-out process. One is the material damage in the cement matrix; another is the abnormal energy release accumulated. In case that the interfacial shear strength is 2.4 MPa, the applied load shows several sudden drops due to damage in the cement matrix, and one can notice that the interfacial shear stiffness during reloading, comparing to the elastic shear stiffness of the interface, reduces more and more as the pull-out displacement increases. On the other hand, the decrease of the applied load when the interfacial shear strengths are 3.6 and 4.2 MPa is caused by the abrupt energy release. Regardless of the damage in the cement matrix, the global CNT pull-out strength and ductility are not varied if the fracture energy of the interface is a constant.

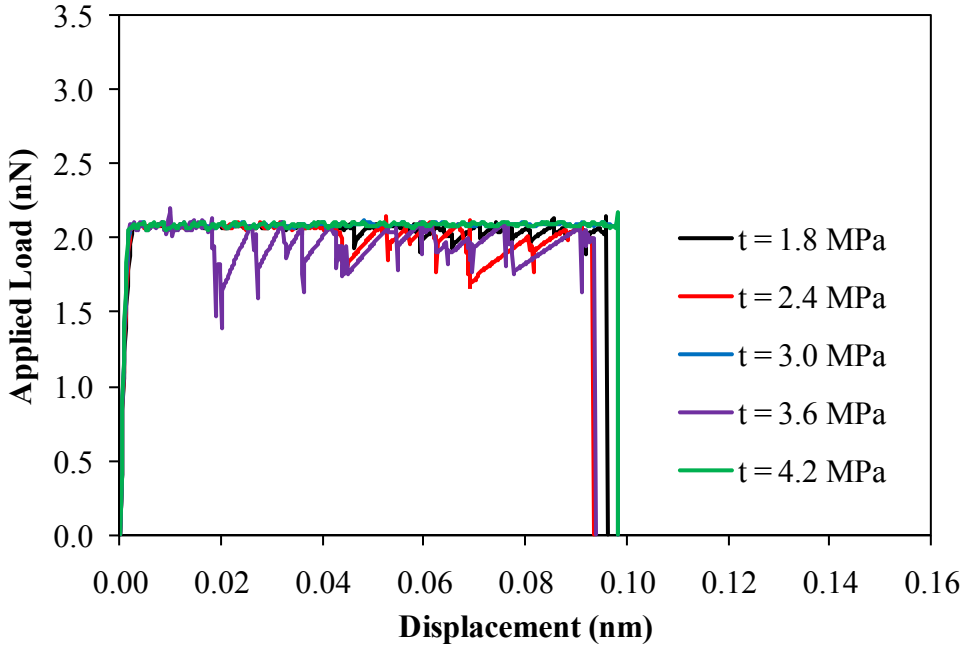

(a)

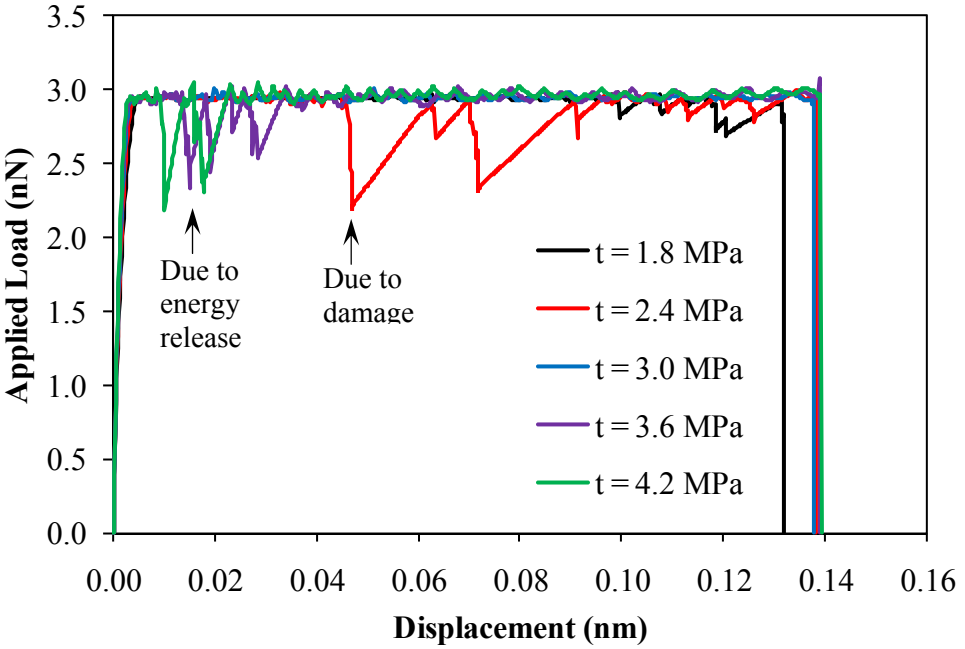

(b)

Figure 8.6 The interfacial shear strength sensitivity analysis results: (a) $G = 16\times10^{-16}$ N/nm and (b) $G = 32\times10^{-16}$ N/nm

The damage initiation and propagation processes in the matrix surrounding the CNT when the interfacial shear strength, t, and the fracture energy, G, are 3.6 MPa and 16×10^{-16} N/nm, respectively (see Figure 8.6(a)) are illustrated in Figure 8.7. In order to clearly show the final debonding between the CNT and the matrix, the longitudinal displacement is magnified 500 times.

As seen in Figure 8.7(a), the first drop of the applied load is not caused by the matrix damage, but caused by the energy release, and the second drop of the applied load is due to the initiation of the damage at the matrix when the CNT is pulled out 0.027 nm. Figure 8.7(b) shows the damage propagation in the cement matrix as the pull-out displacement of the CNT increases, and the final debonding configuration is shown in Figure 8.7(c) with several damage regions. As a result of the simulation, the damage int matrix during pull-out process is not distributed uniformly through the whole length of the matrix, but tends to be localized at some regions, and the damage at matrix always causes the fluctuation of the applied load.

Up to date, it is well known that the fiber pull-out strength is proportional to the strength of the interface between the fiber and matrix. However, it may be said that this statement is partially wrong based on the analysis results shown in Figure 8.6. Since the variation of the interfacial strength is generally accompanied with the variation of the other properties, such as the stiffness and the fracture energy, one cannot draw a conclusion simply that the pull-out strength and the ductility are proportional to only the strength of the interface between the reinforcement and the matrix.

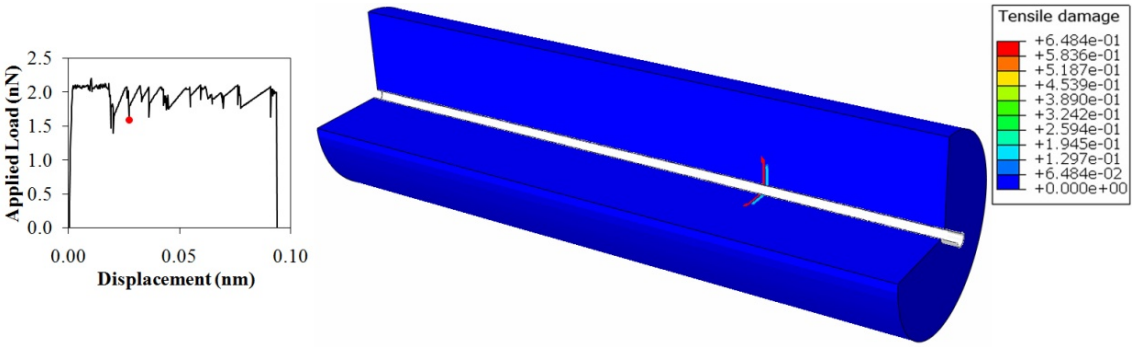

(a)

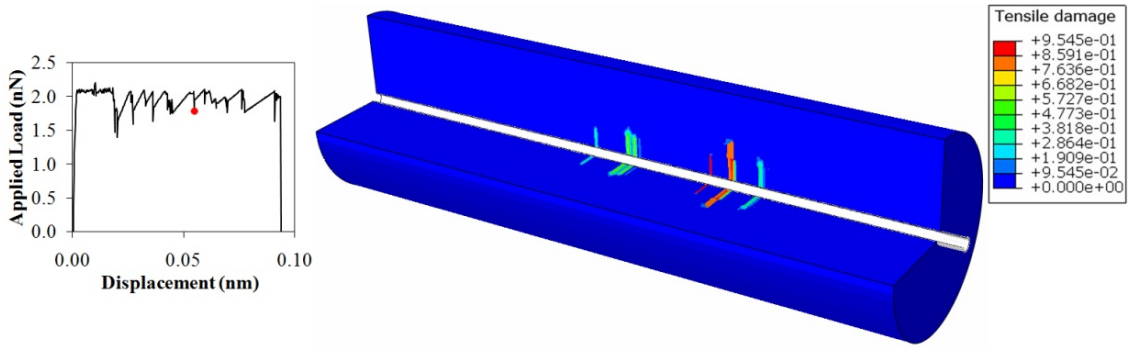

(b)

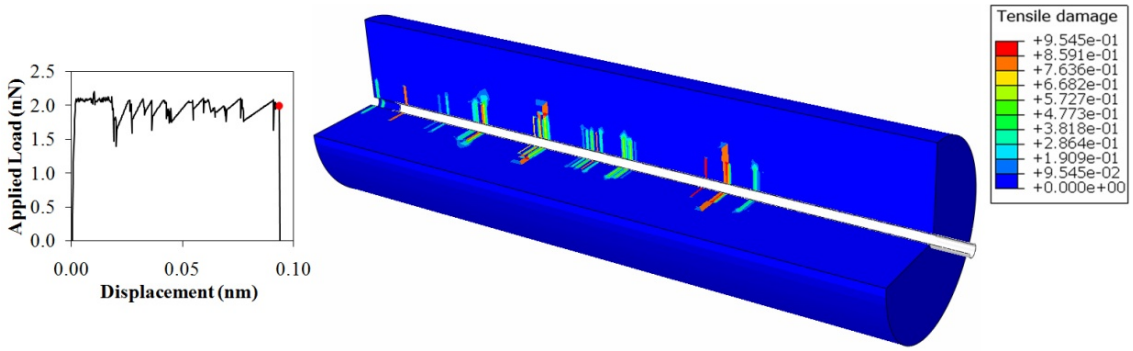

(c)

Figure 8.7 The damage evolution at cement matrix during pull-out process: (a) damage initiation at 0.027 nm pull-out displacement of the CNT, (b) damage propagation, and (c) final debonding between the CNT and the matrix

8.1.4 The Effect of the Cohesive Stiffness

With the constant interfacial shear strength and fracture energy, the peak value of the contact separation δ^0 is chosen as a unique variable in order to investigate the effect of the cohesive stiffness, *K* on the ultimate pull-out strength and ductility. Figure 8.8 shows the interfacial models used in the analysis.

The fracture energy is fixed with 16×10^{-16} N/nm for all three models, and the interfacial shear strength of the model (a), (b), and (c) are 2.4 MPa, 3.0 MPa, and 3.6 MPa, respectively. Since the cohesive stiffness, *K* is defined as the initial slop of the traction-separation relation ($K = t/\delta$), the peak value of the contact separation, δ^0 for each case is chosen for the cohesive stiffness, *K* to be varied from 1×10^{-8} N/nm^3 to 5×10^{-8} N/nm^3.

The cohesive stiffness sensitivity analysis results are shown in Figure 8.9. Although there are several fluctuations of the applied pull-out force due to the damage at matrix or the sudden release of the energy, the ultimate pull-out strength and the ductility are merely affected by the variation of the cohesive. Moreover, the results are independent of the magnitude of the interfacial shear strength. Therefore, it should be noted that the alteration of the cohesive stiffness or the interfacial shear strength only cannot change the strength of the CNT reinforced cementitious composite.

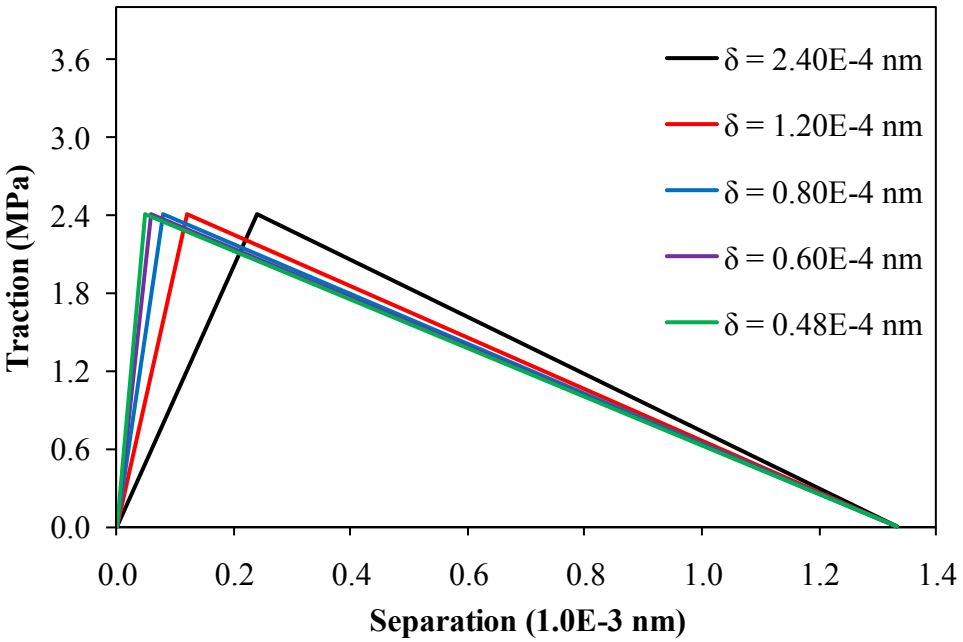

(a)

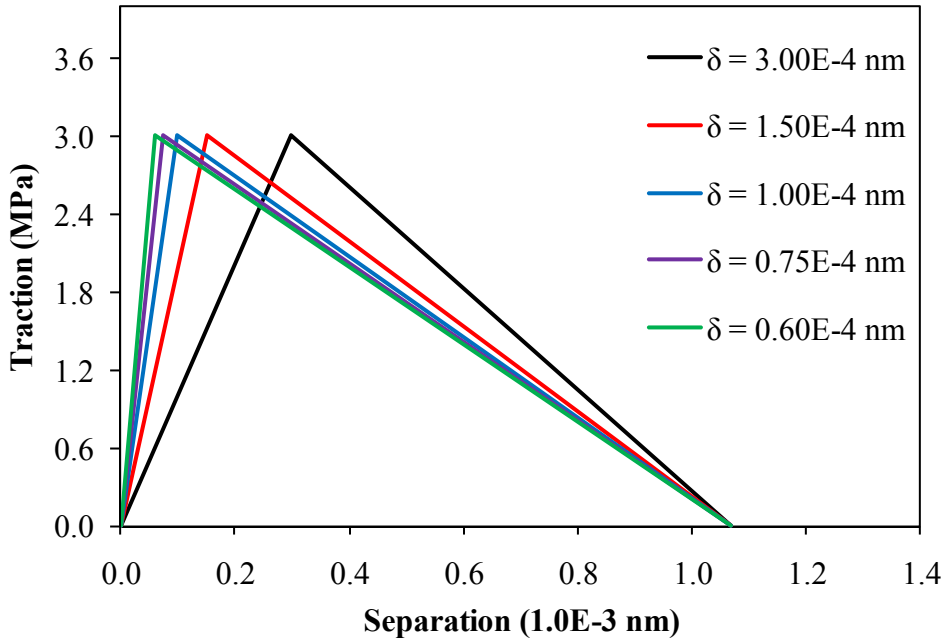

(b)

Figure 8.8 The variation of the cohesive stiffness of the interface between the CNT and the cement matrix: (a) t = 2.4 MPa, (b) t = 3.0 MPa, and (c) t = 3.6 MPa

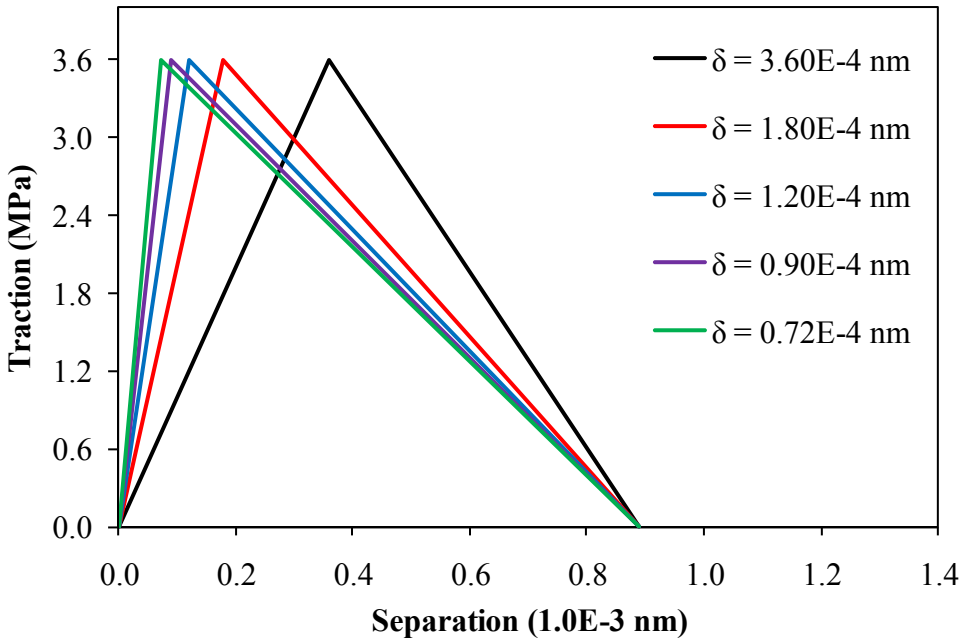

(c)

Figure 8.8 Continued

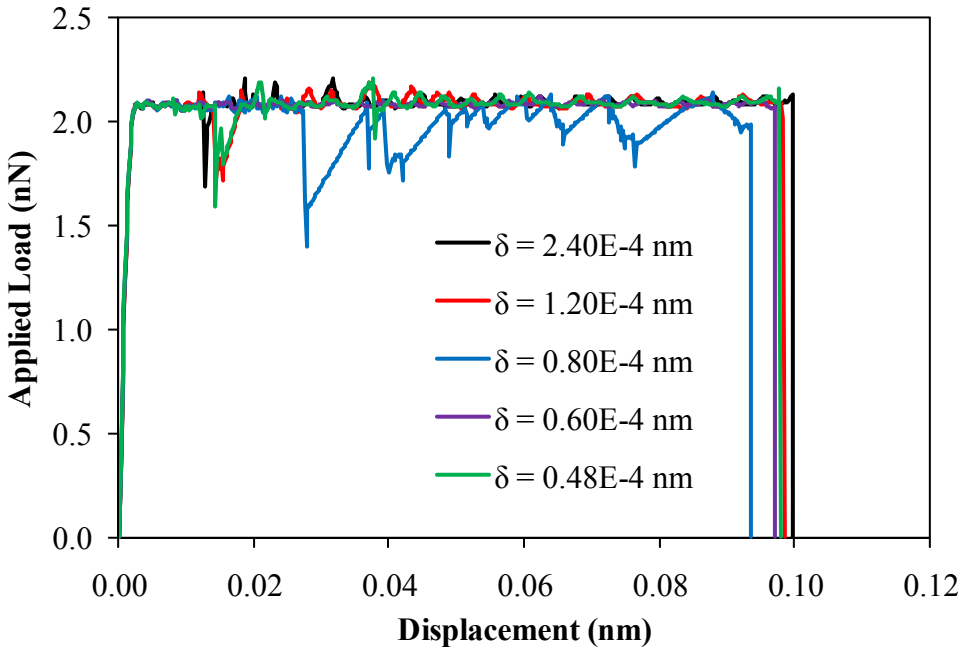

(a)

Figure 8.9 The cohesive stiffness sensitivity analysis results: (a) t = 2.4 MPa, (b) t = 3.0 MPa, and (c) t = 3.6 MPa

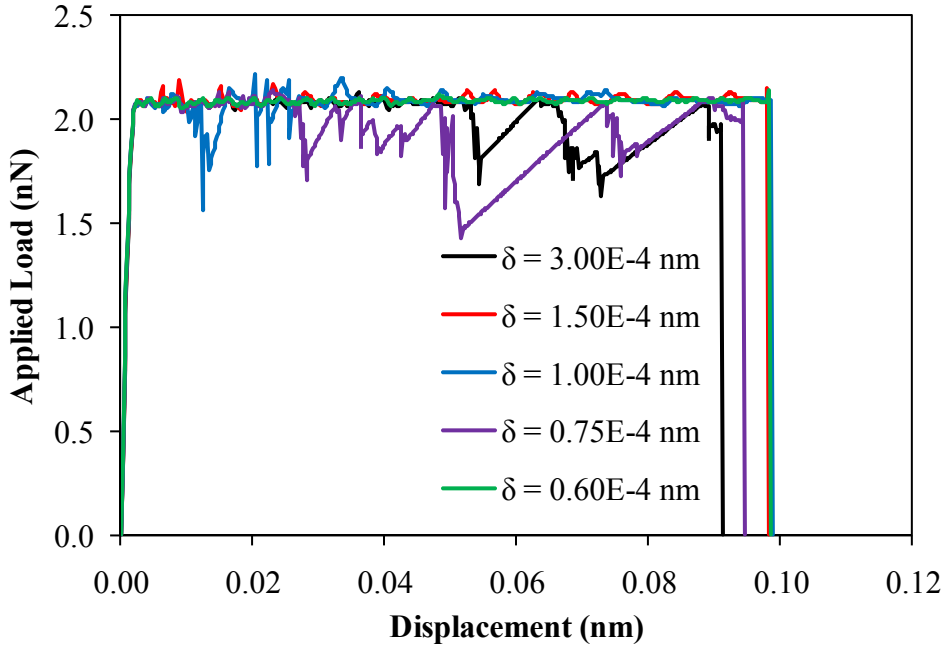

(b)

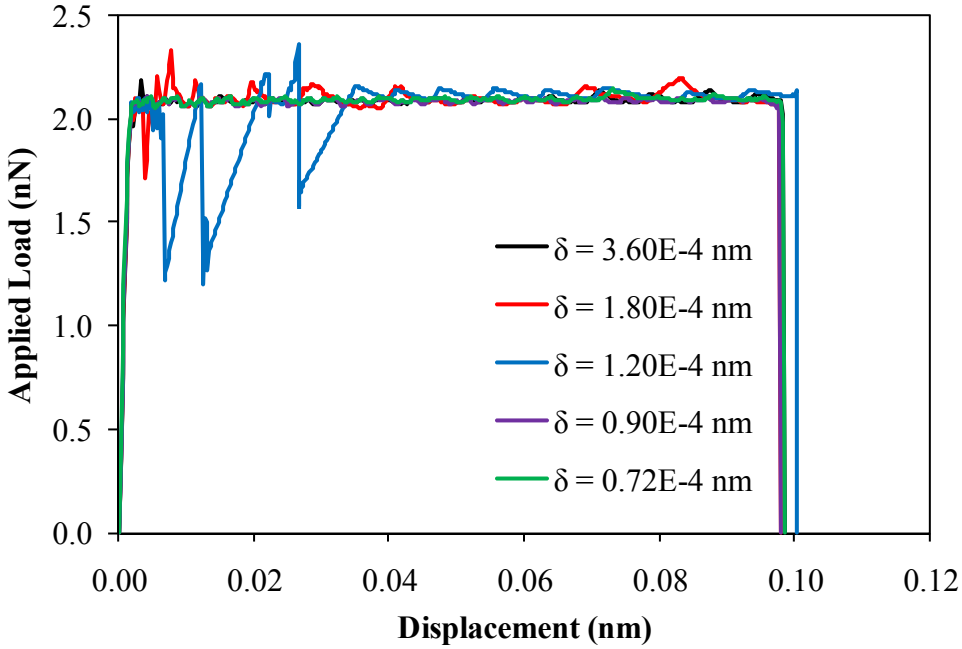

(c)

Figure 8.9 Continued

8.1.5 The Effect of the Interfacial Fracture Energy

In order to investigate the effect of the fracture energy on the global CNT pull-out behavior, the interfacial fracture energy is varied with the constant interfacial shear strength and stiffness. Furthermore, three sets of the interfacial property models having different interfacial shear strength are considered and showed in Figure 8.10. The interfacial shear strength of the model 1, 2, and 3 are 2.4 MPa, 3.0 MPa, and 3.6 MPa, respectively. For the variation of the fracture energy only, the linear softening region after yielding is changed so that the fracture energy varies from 4×10^{-16} N/nm to 68×10^{-16} N/nm with the constant interfacial shear strength and stiffness.

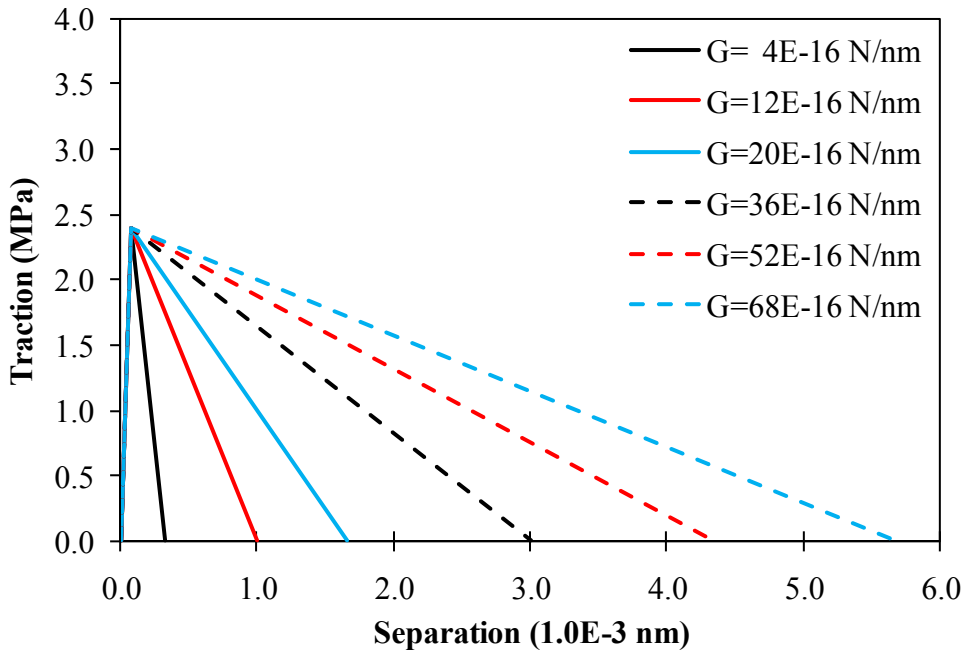

(a)

Figure 8.10 The variation of the fracture energy of the interface between the CNT and the cement matrix: (a) t = 2.4 MPa, (b) t = 3.0 MPa, and (c) t = 3.6 MPa

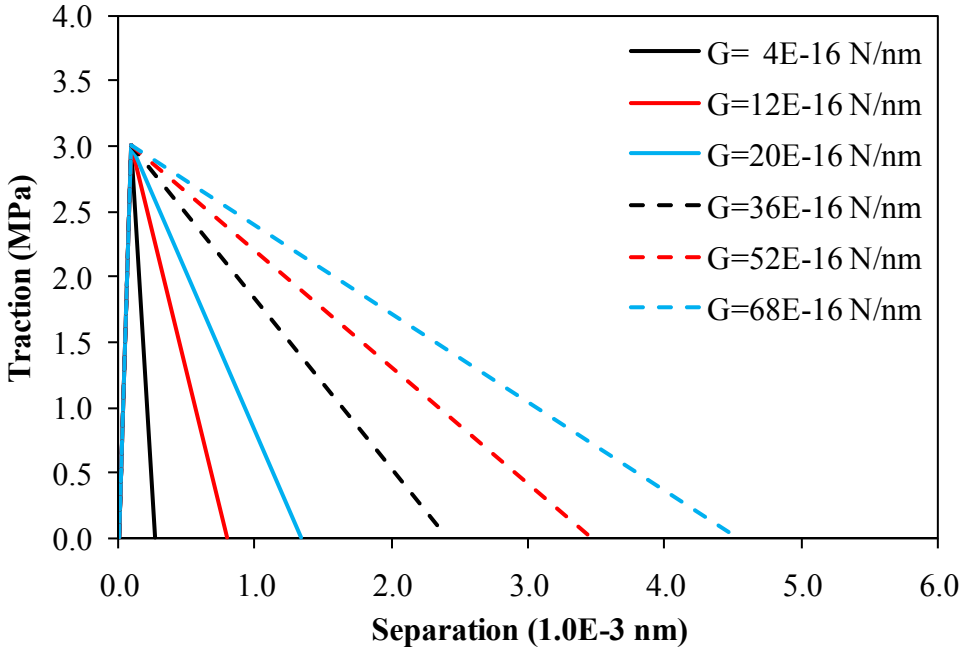

(b)

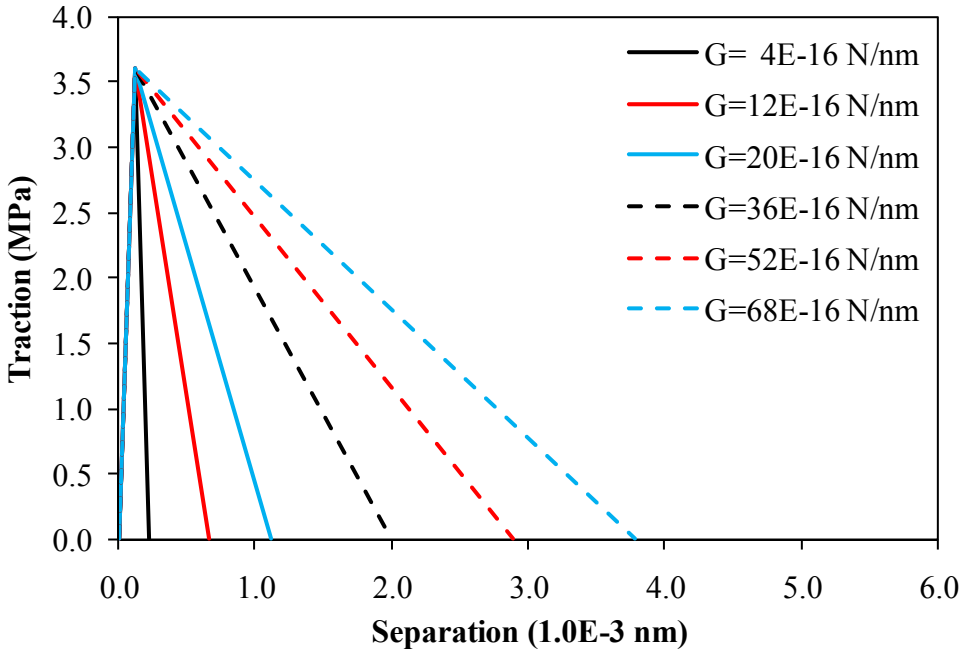

(c)

Figure 8.10 Continued

The results of the fracture energy sensitivity analysis are shown in Figure 8.11. Both the global CNT pull-out strength and the ductility are proportional to the fracture energy for all three cases, and the ultimate pull-out force and the final debonding displacement of the CNT are independent of the damage in matrix as mentioned earlier.

The variation of the ultimate pull-out force and the final debonding displacement of the CNT with the variation of the fracture energy are shown in Figure 8.12. The ultimate pull-out strength and the final debonding displacement are increased linearly as the fracture energy increases, and the same fracture energy gives rise to the same ultimate pull-out strength and ductility. It means that the composite strength between the CNT and cement matrix is governed by the fracture energy of the interface rather than by the interfacial shear strength or the cohesive stiffness.

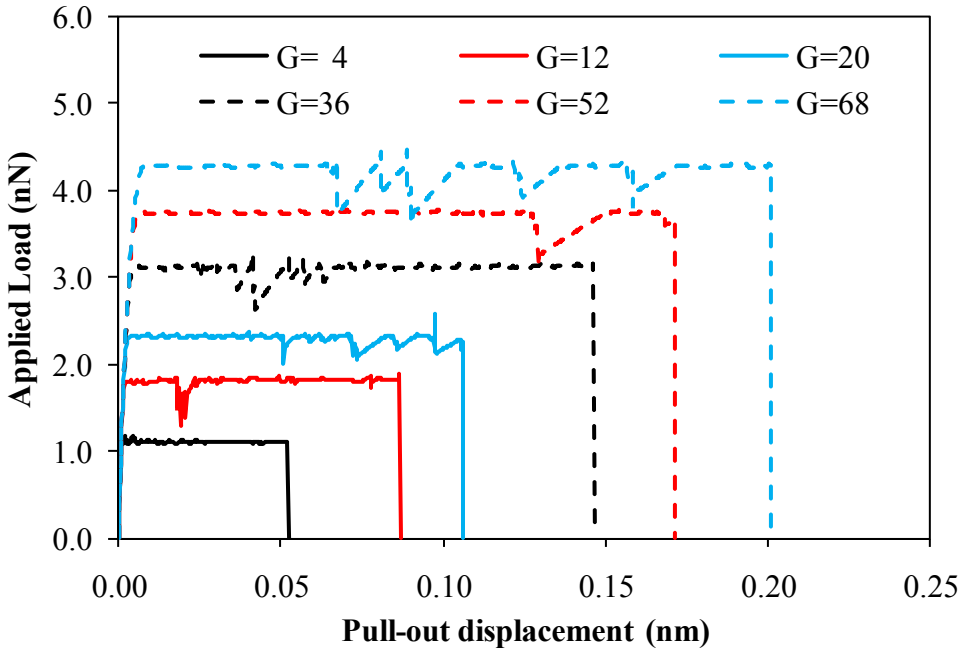

(a)

Figure 8.11 The fracture energy sensitivity analysis results: (a) model 1 (t = 2.4 MPa), (b) model 2 (t = 3.0 MPa), and (c) model 3 (t = 3.6 MPa)

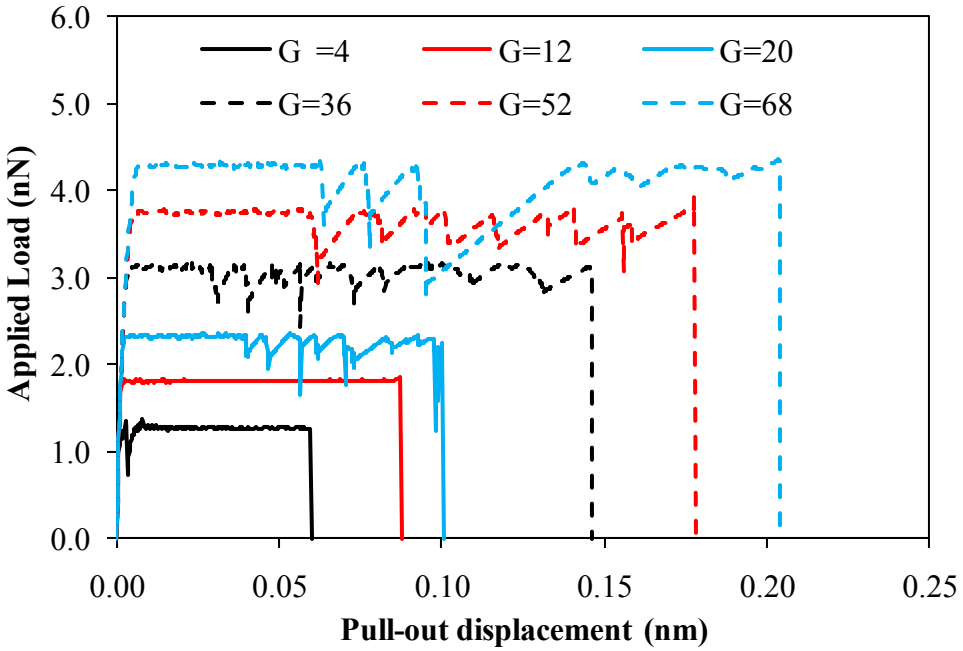

(b)

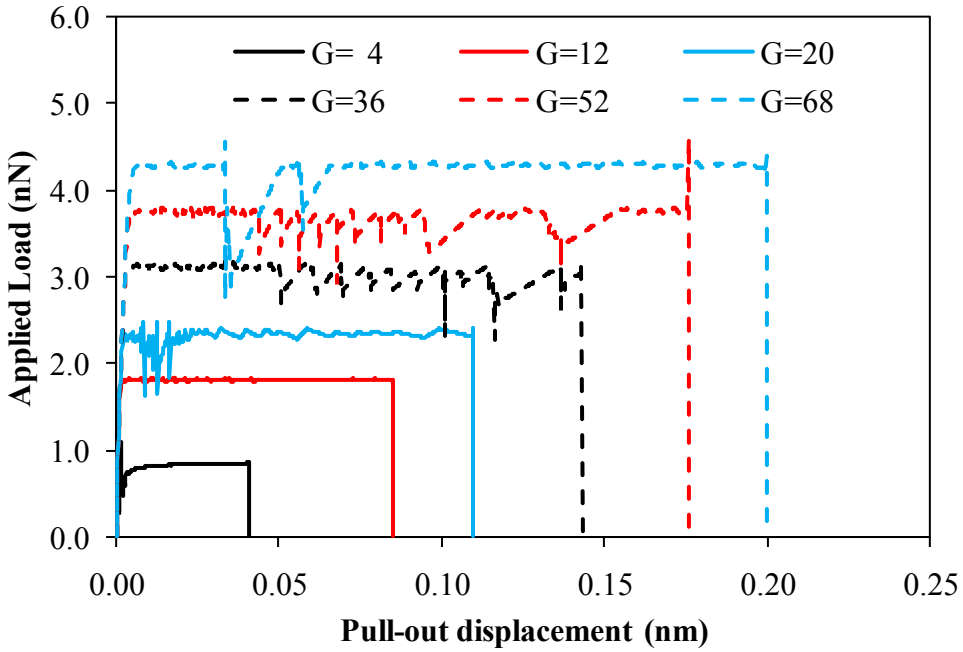

(c)

Figure 8.11 Continued

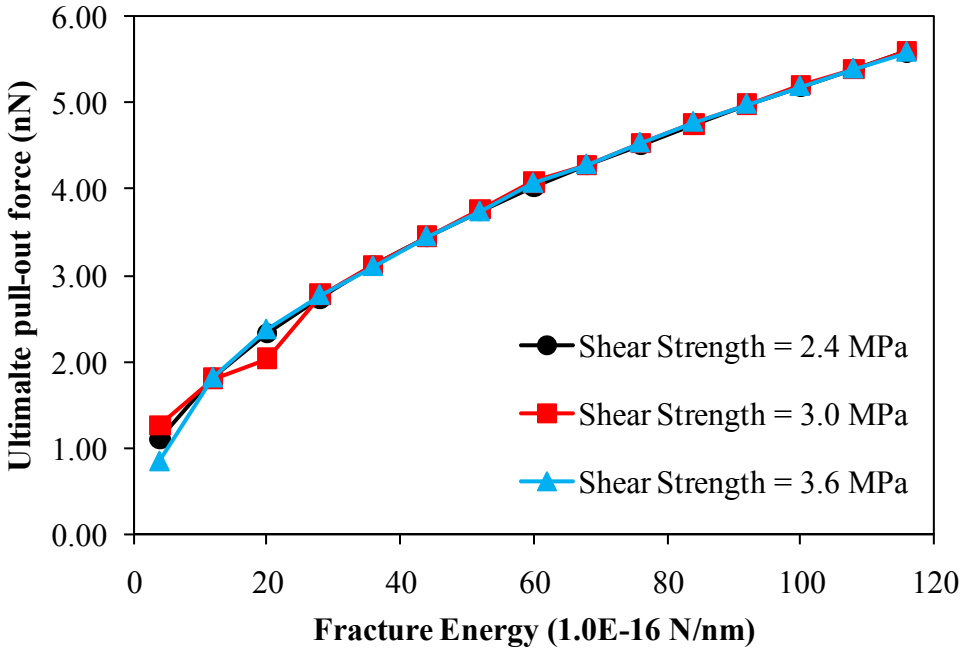

(a)

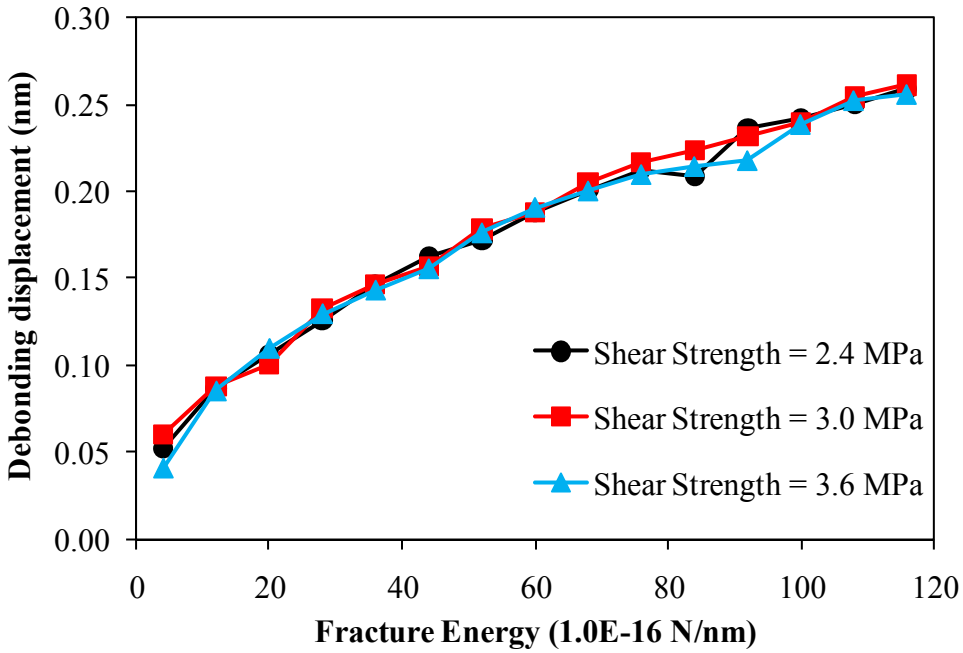

(b)

Figure 8.12 The variation of the ultimate pull-out strength and the ductility by the increase of the fracture energy: (a) ultimate pull-out force and (b) final debonding displacement of the CNT

8.1.6 The Effect of the Embedded Length

The effect of the CNT embedded length on the debonding strength and ductility with the constant interfacial shear strength and the fracture energy is investigated. For the simulation, three different embedded length models, 1000, 2000, and 4000 nm, are adopted, and the two damaged cases, that is when the cement matrix is damaged during pull-out process and when there is no damage in matrix are considered separately with using different interfacial material properties. The interfacial shear strength and the fracture energy used for the undamaged case are 2.4 MPa and 4×10^{-16} N/nm, respectively, and 3.0 MPa and 28×10^{-16} N/nm, respectively for the damaged case. Figure 8.13 shows the embedded length effect analysis results.

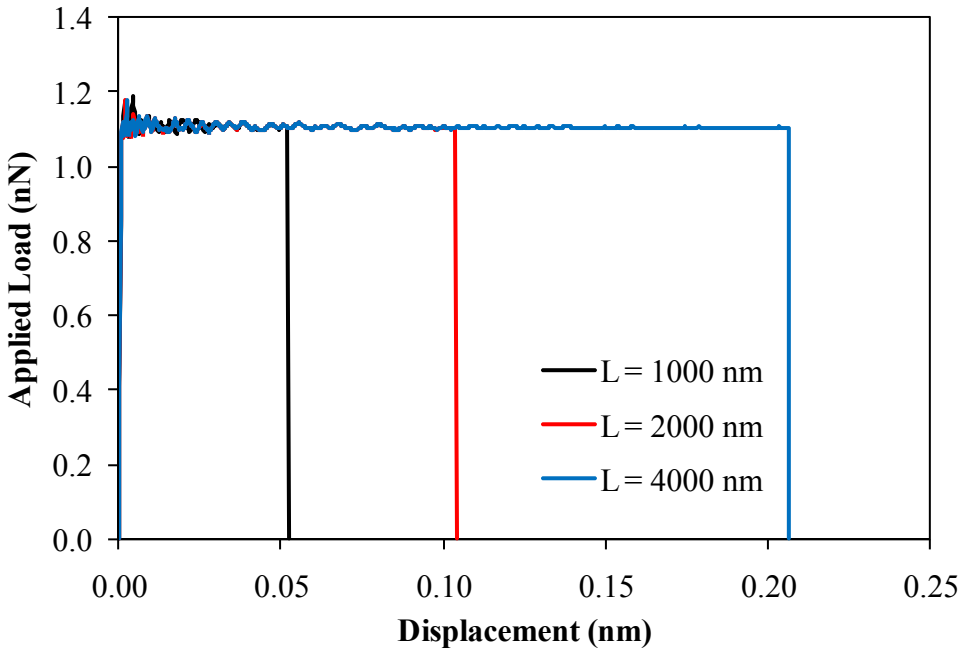

(a)

Figure 8.13 The CNT embedded length effect: (a) undamaged matrix and (b) damaged matrix

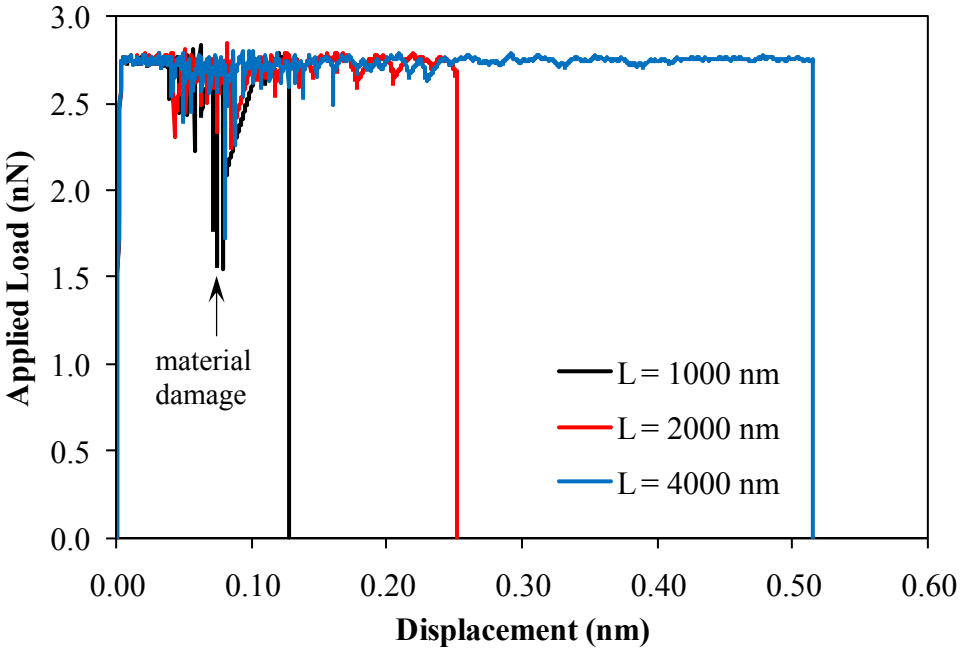

(b)

Figure 8.13 Continued

The ultimate pull-out strength is independent on the embedded length, while the final debonding displacement is linearly increased with the embedded length for both cases. Moreover, the damage position on cement matrix during pull-out process is also not affected by the embedded length of the CNT as shown in Figure 8.13 (b).

8.1.7 The Effect of the CNT and Mortar Matrix Properties

The properties of the CNTs, such as the modulus of elasticity and strength can be varied widely depending on the way of the manufacture, and the pull-out behavior of the CNT from the matrix can largely be affected by the Young's modulus of the CNT. Furthermore, the variation of the Young's modulus and the strength of the matrix can also affect the pull-out behavior and the failure mechanisms of the reinforcement.

Therefore, the variation effect of the properties of the CNT and the matrix on the pull-out strength and the ductility is investigated.

Firstly, the Young's modulus of the CNT varies from 0.25 TPa to 2.0 TPa with a constant Young's modulus of the matrix, and the three different interfacial fracture energy, such as 12×10^{-16} N/nm, 24×10^{-16} N/nm, and 36×10^{-16} N/nm with increasing only the complete failure displacement, δ^f are adopted to each Young's modulus of the CNT in order to examine the interaction between them. Figure 8.14 shows the analysis results of the CNT Young's modulus effect on the CNT pull-out behavior. As the Young's modulus of the CNT increases, the ultimate pull-out force is increased while the final debonding displacement, the ductility is decreased (Figure 8.14 (a)). This is because the larger the CNT Young's modulus is, the smaller the deformation is induced at the same level of force, and then the wider the interfacial contact area is activated and the faster the interfacial debonding is propagated to resist the same amount of the displacement of the CNT. Figure 8.14 (b) and (c) show the variation of the ultimate strength and the final debonding displacement with the change of the CNT Young's modulus and the interfacial fracture energy. The increase of the interfacial fracture energy intensifies the effect of the CNT Young's modulus on the ultimate pull-out strength while weakens on the final debonding displacement. Moreover, the energy absorption capacity, that is, the area of the applied load-final debonding displacement curve in Figure 8.14 (a) by the change of the CNT Young's modulus and the interfacial fracture energy is illustrated in Figure 8.14 (d). The energy absorption capacity of the interface between the CNT and

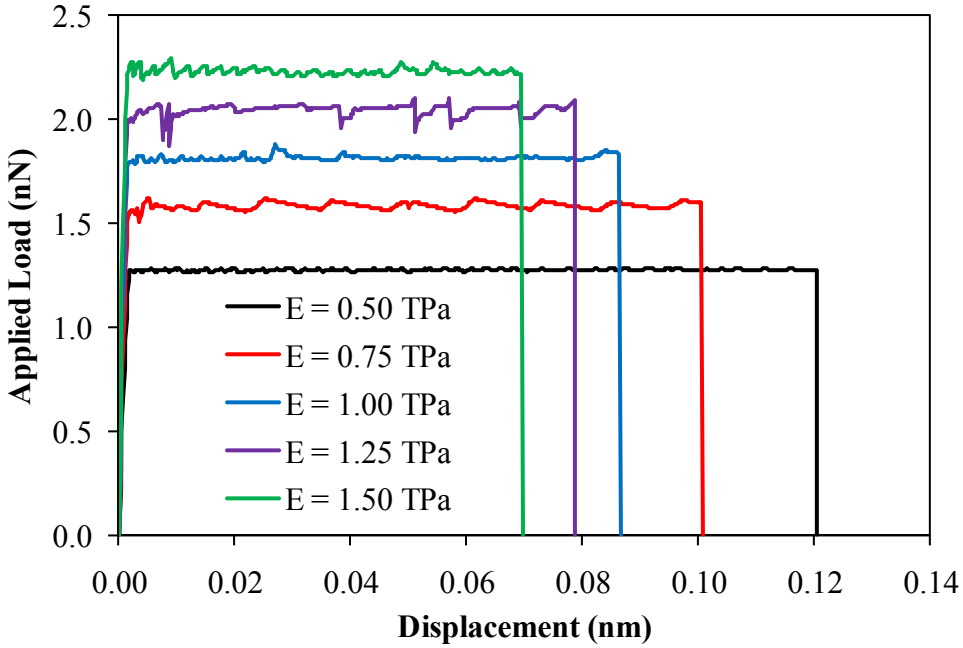

(a)

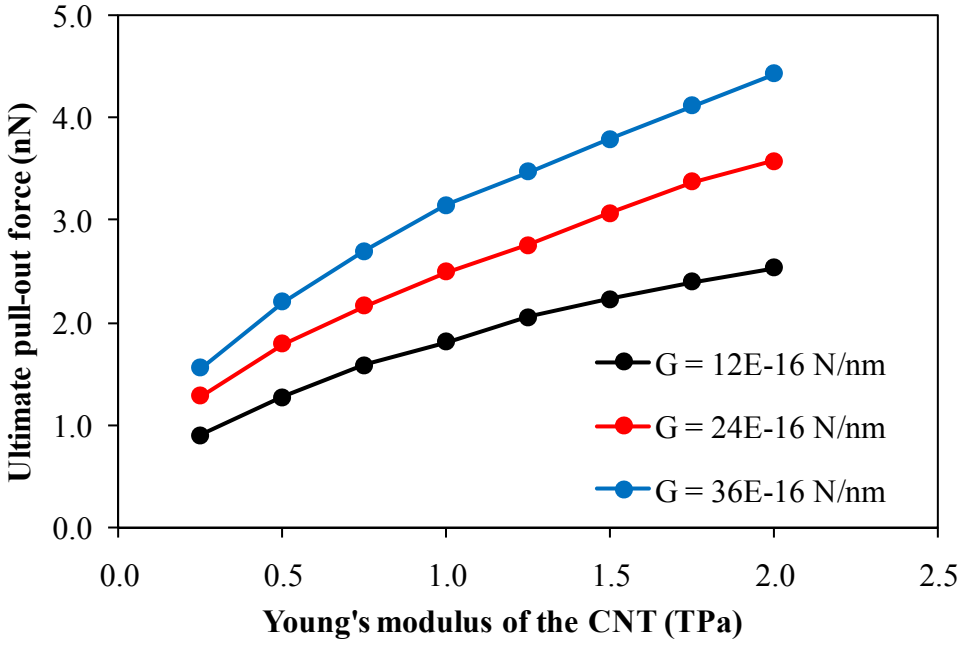

(b)

Figure 8.14 The variation effect of the CNT Young's modulus: (a) applied load-displacement relation, (b) ultimate pull-out force change, (c) final debonding displacement change, and (d) the energy absorption capacity change with the variation of the Young's modulus of the CNT and the interfacial fracture energy

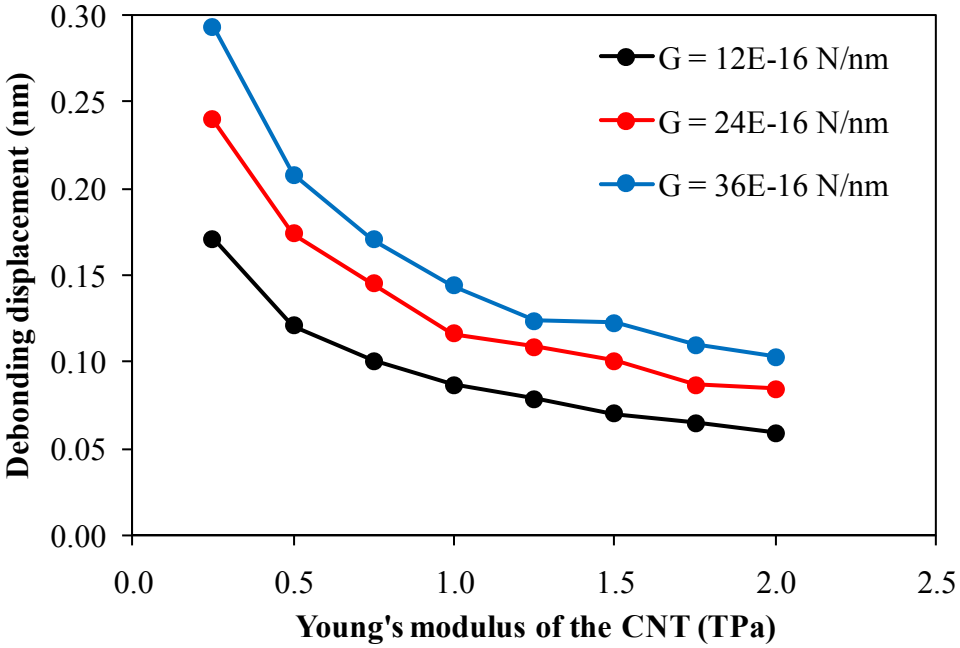

(c)

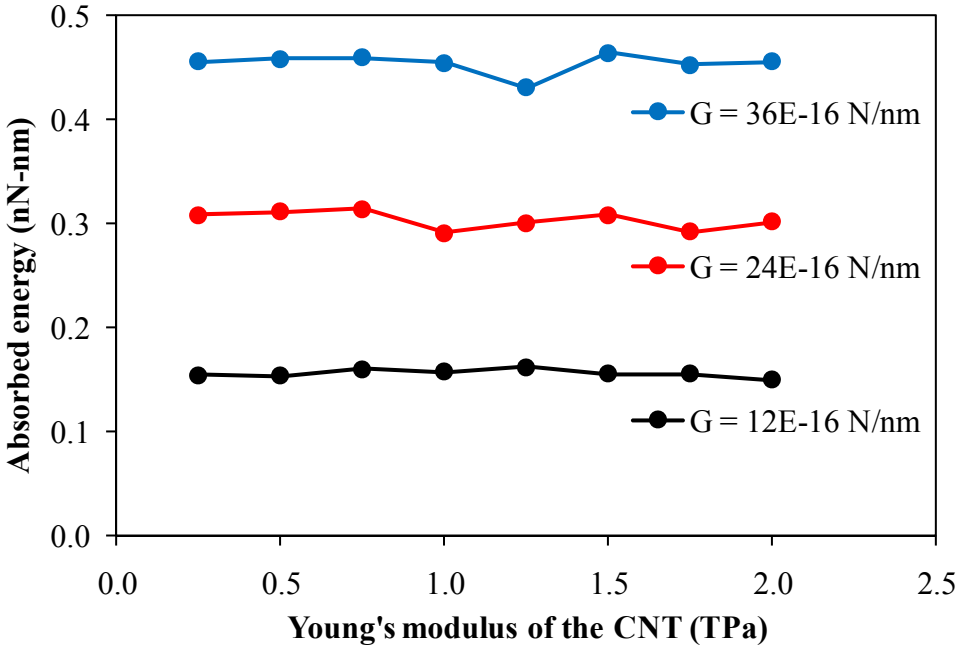

(d)

Figure 8.14 Continued

the matrix is hardly dependent on the variation of the CNT Young's modulus, and the absorbed energy is almost linearly proportional to the amount of the interfacial fracture energy.

Secondly, the effect of the tensile strength and the Young's modulus of the matrix are investigated with the constant CNT Young's modulus. For the matrix strength effect, as shown in Figure 8.15, tensile strength of the cement matrix varies from 1.5 MPa to 6.0 MPa. The Young's modulus of the CNT is 1 TPa, and the shear strength and fracture energy of the interface are 3.0 MPa and 12×10^{-16} N/nm, respectively for case of no damage induced in matrix and 3.0 MPa and 20×10^{-16} N/nm, respectively for case of damage induced in matrix. Figure 8.16 shows the effect of the matrix tensile strength for both cases; undamaged and damaged cement matrix.

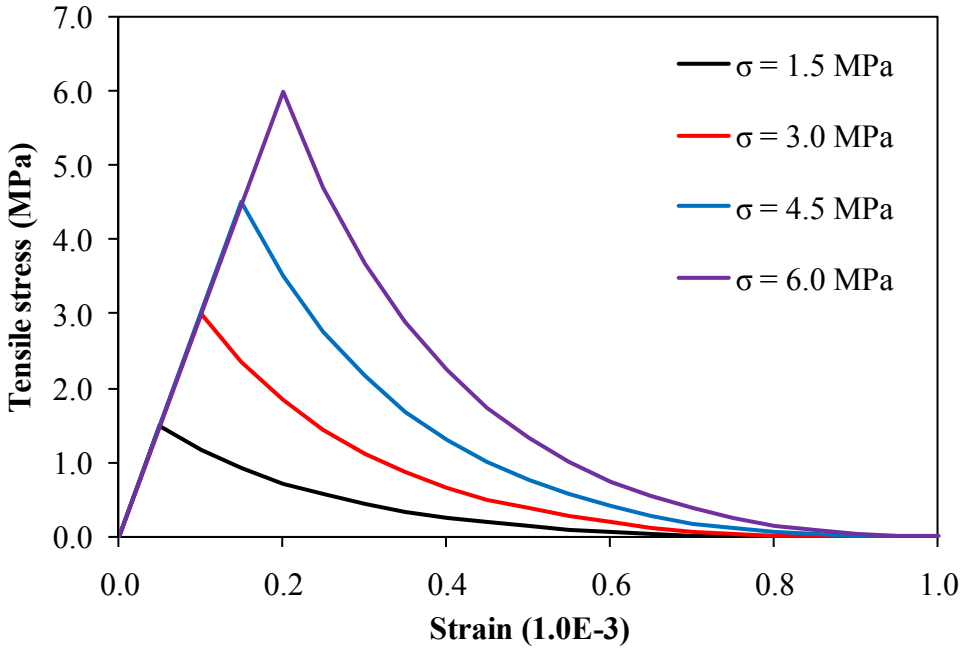

Figure 8.15 Variation of the tensile strength of the mortar matrix

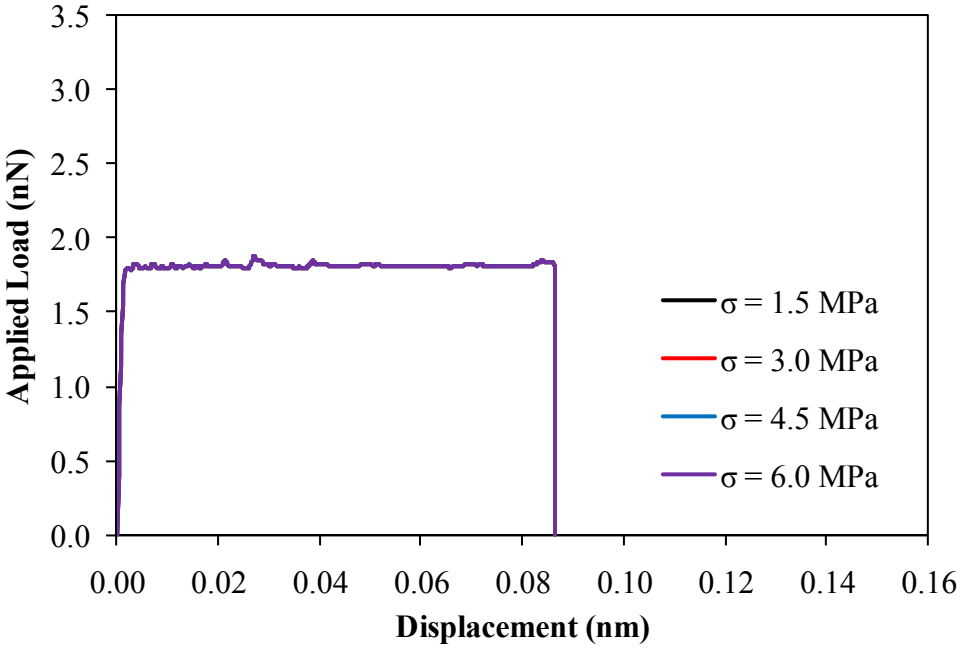

(a)

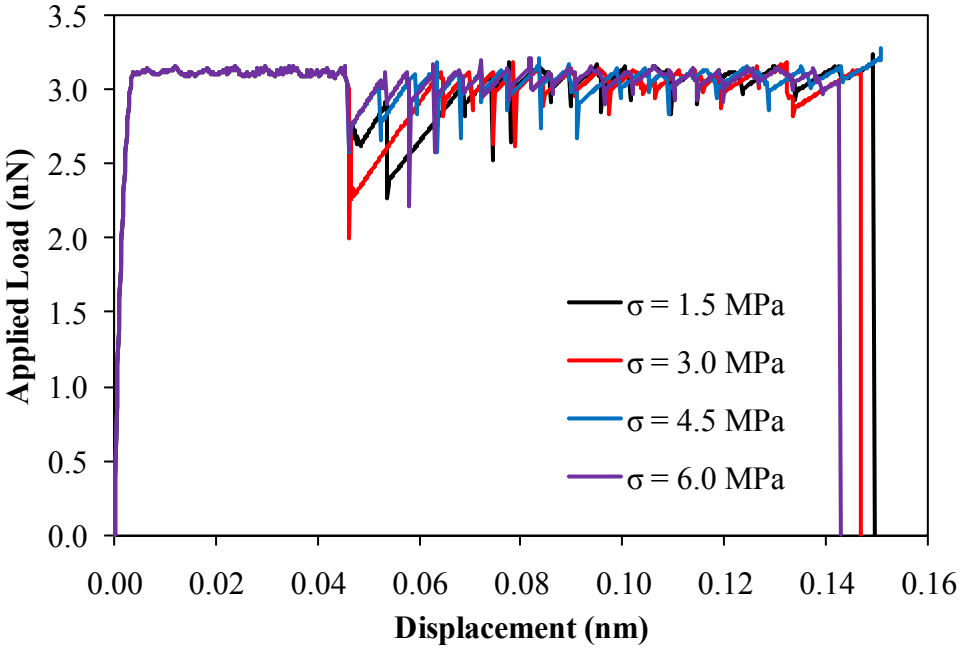

(b)

Figure 8.16 The effect of the matrix tensile strength: (a) no damage induced at matrix (G = 12×10^{-16} N/nm) and (b) damage induced at matrix during pull-out (G = 20×10^{-16} N/nm)

It is worth noting that the variation of the matrix tensile strength with constant interfacial properties, when there is no damage on the cement matrix (Figure 8.16(a)), has no effect on the global pull-out strength and the ductility. Even though the cement matrix is severely damaged during pull-out process (Figure 8.16(b)), the ultimate pull-out strength and the ductility have merely affected by the variation of the tensile strength of the matrix, and the variation of the matrix strength influences simply the intensity of the damage in matrix.

For the investigation of the matrix Young's modulus effect, the matrix is considered as an elastic material since the tensile strength of the matrix has hardly effect on the pull-out behavior of the CNT as above, and in order to consider wide range of the matrix stiffness to the analysis. The shear strength and the fracture energy of the interface are chosen to be 3.0 MPa and 12×10^{-16} N/nm, respectively, and the Young's modulus of the matrix varies from 20 GPa to 500 GPa.

As a result of simulations, the variation of the matrix Young's modulus only with constant interfacial properties has also merely effect on the pull-out behavior of the CNT as seen in Figure 8.17. These results imply that the strengthening of the matrix only without improving the properties of the interface between the reinforcement and the matrix may not guarantee the improvement of the strength of the CNT reinforced composite material. However, in actual, the modification of the matrix properties only may also lead the alteration of the pull-out behavior because the change of the matrix properties is generally accompanied by the change of the interfacial properties.

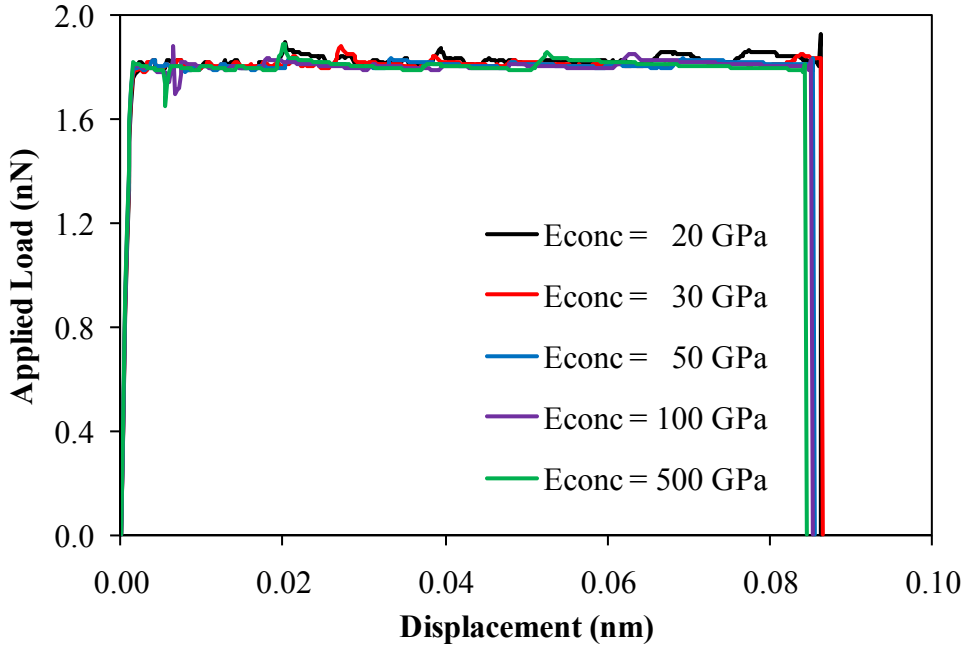

Figure 8.17 The effect of the matrix Young's modulus

8.1.8 The Effect of the Interfacial Surface Area to Volume Ratio

As mentioned above, the CNT pull-out strength is mainly governed by the properties of the interface, and the interfacial surface area between the CNT and the matrix is also one of the crucial factors that shift the strength of the CNT/cement matrix composites because the pull-out strength is generally proportional to the surface area. Thus, the effect of the interfacial surface area with a constant CNT volume ratio on the pull-out strength and the ductility is evaluated. Four axisymmetric models for the interfacial surface area sensitivity analysis are shown in Figure 8.18. The diameters of the CNT used in the analysis are 10, 20, 30 and 40 nm, and the diameters of the cement matrix are 146, 292, 438, and 584 nm, respectively in order to maintain the CNT volume ratio to be 0.47%. Besides, the interfacial shear strength and fracture energy used in the analysis are 3.0 MPa and 12×10^{-16} N/nm, respectively.

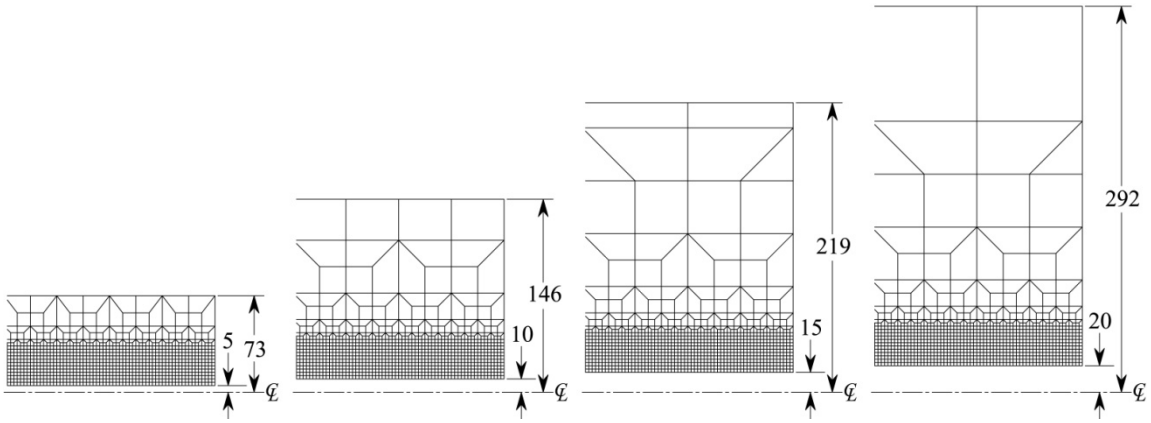

Figure 8.18 Interfacial surface area sensitivity analysis models (units: nm): (a) D_{CNT} = 10 nm, (b) D_{CNT} = 20 nm, (c) D_{CNT} = 30 nm, and (d) D_{CNT} = 40 nm

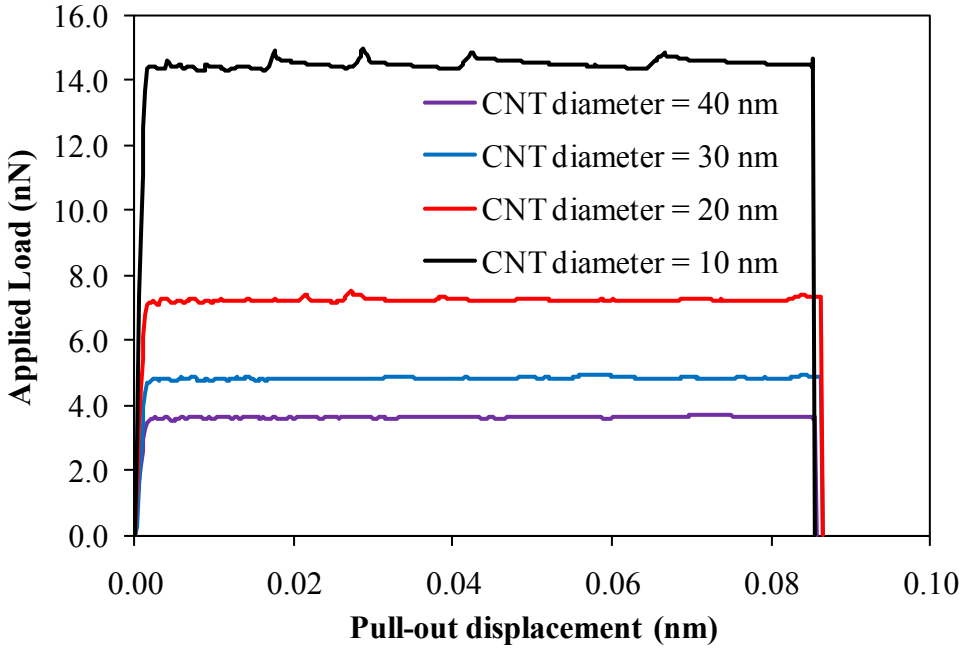

Figure 8.19 Interfacial surface area sensitivity analysis result

The interfacial surface area sensitivity analysis result is shown in Figure 8.19. In order for the comparison of the analysis results of each model, the total volume ratio on the basis of the total volume of the reference model, the 40 nm diameter CNT embedded

model (Figure 8.18(d)) is multiplied to the pull-out strength of each model. As the result of the analysis, the ultimate pull-out strength is inversely proportional to the embedded CNT size or proportional to the surface area of the CNT while the ductility is independent of the variation of the interfacial surface area. It means that the augmentation of the interfacial surface area by using smaller sized CNTs with maintaining the same CNT volume fraction within the limits that the addition of the CNT to the cement matrix allows proper dispersion and workability will guarantee the stronger CNT/cement composite.

8.2 Single Curved CNT Pull-out Analysis

The interfacial friction force F between the CNT and the matrix that is one of the critical factors governing the pull-out behavior of the CNT at sliding stage is simply defined by the multiplication of the friction coefficient μ and the normal force N. The friction coefficient of the CNT which surface is much smoother than other materials can generally be varied from 0.002 to 0.07 according to the surface treatment (Vander Wal *et al.* 2005). Moreover, the normal force applied to the contact surface can also be varied widely by several factors such as, the external force, different thermal expansion coefficient of the CNT and the matrix, the swelling of the matrix, and the bending stiffness of the CNT.

In case of the straight CNT, the normal force N acting on the interface between the CNT and matrix is purely preexisting force that can be generated by the factors mentioned above, and there is no normal force that is caused additionally during pull-out

process. In case of the curved CNT, however, there exists additional normal force induced by the extraordinarily high bending stiffness of the CNT during pull-out process, and the friction force at interface between the curved CNT and matrix, distinguishing the additional normal force with the preexisting normal force, can be expressed as follows:

$$F = \mu\left(N_{preexisting} + N_{additional}\right) \tag{8.4}$$

where $N_{preexisting}$ is the preexisting normal force and $N_{additional}$ is the additionally induced normal force during pull-out process due to the bending stiffness of the CNT. If the preexisting normal force $N_{preexisting}$ is much greater than the additional normal force $N_{additional}$ or the curvature of the curved CNT is small, the additional normal force may be negligible, and the pull-out behavior of the curved CNT will be similar to that of the straight CNT. However, the majority of CNTs embedded in matrix has a high curvature, and the effect of the additional normal force due to the curvature of the CNT cannot be negligible. Moreover, since a major portion of the CNT pull-out process lies on the third stage, the sliding stage, the investigation of the sliding behavior of the curved CNT is more important and interesting than that of the straight CNT.

Therefore, this research is focused on the sliding stage of the curved CNT pull-out process, and the effects of the friction force, the Young's modulus of the CNT and the matrix, and the curvature of the CNT on the sliding behavior of the CNT during pull-out process are investigated with the 3-dimensional analysis model.

8.2.1 Single Curved CNT Pull-out Analysis Model

The representative curved CNT pull-out analysis model is shown in Figure 8.20. Since the analysis model is symmetric with respect to the vertical axis, only the half of the whole model is generated in order to reduce the simulation time. An 8-node 3-D brick element (C3D8) is used for the matrix, and a 4-node doubly curved general-purpose shell element (S4) is used for the CNT. The outer diameter and the thickness of the curved CNT are 20 nm and 0.34 nm, respectively, the diameter of the matrix is 400 nm, and the embedded length of the CNT is 500 nm. Furthermore, the reference Young's modulus of the CNT and the matrix are 1000 MPa and 30 MPa, respectively, and the variation of the properties for the parametric research are listed in Table 8.2.

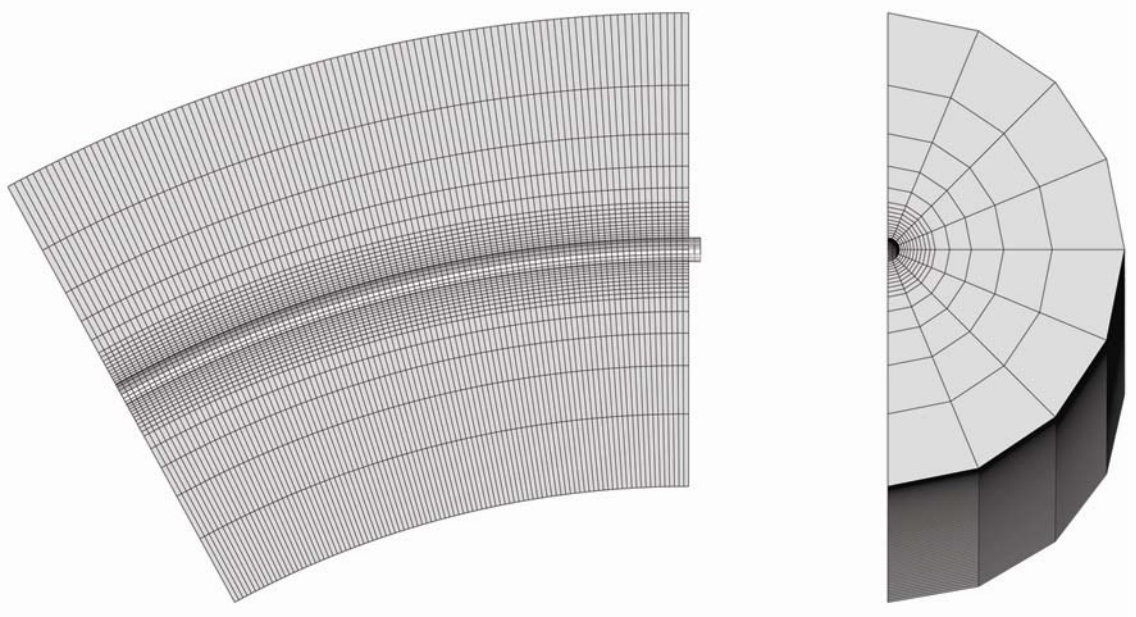

(a) (b)

Figure 8.20 3-D Curved CNT pull-out analysis model. (a) Side view and (b) front view

Table 8.2 Variation of the parameters for the curved CNT pull-out analysis

Variables	Lower bound	Reference	Upper bound
E_{CNT} (GPa)	500	1000	1500
E_{Matrix} (GPa)	10	30	50
Friction coefficient, μ	0.02	0.04	0.06
Normal force , N (nN/nm^2)	0.1	0.15	0.3
Radius of curvature of the CNT, R (nm)	1000	1700	3500

The simulation of the curved CNT pull-out is composed of two steps as shown in Figure 8.21. The external force is loaded to the outer surface of the matrix at the first step in order to generate the normal force at the interface between the CNT and the matrix, and then the horizontal displacement is applied to the exposed end of the CNT at the second step with fixing the horizontal displacement of the outer surface of the matrix and maintaining the magnitude of the normal force.

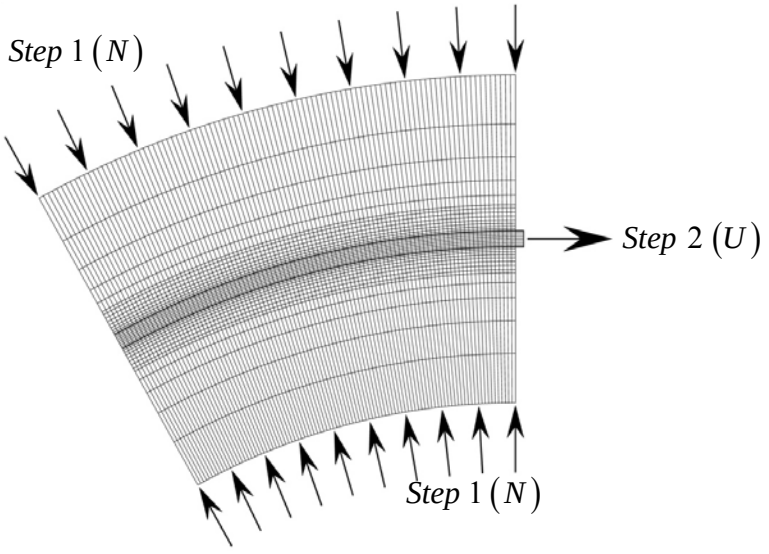

Figure 8.21 Curved CNT pull-out simulation steps

8.2.2 The Effect of the Preexisting Normal Force and the Frictional Coefficient

The interfacial friction force between the CNT and the matrix is the one of the critical factors governing the pull-out behavior of the CNT at the sliding stage, and the effect of the preexisting normal force and the coefficient of friction determining the magnitude of the friction force on the sliding behavior of the CNT is investigated. Furthermore, the straight CNT embedded 3-D analysis model is also generated as seen in Figure 8.22 in order to verify the analysis model and procedure and to compare the analysis results.

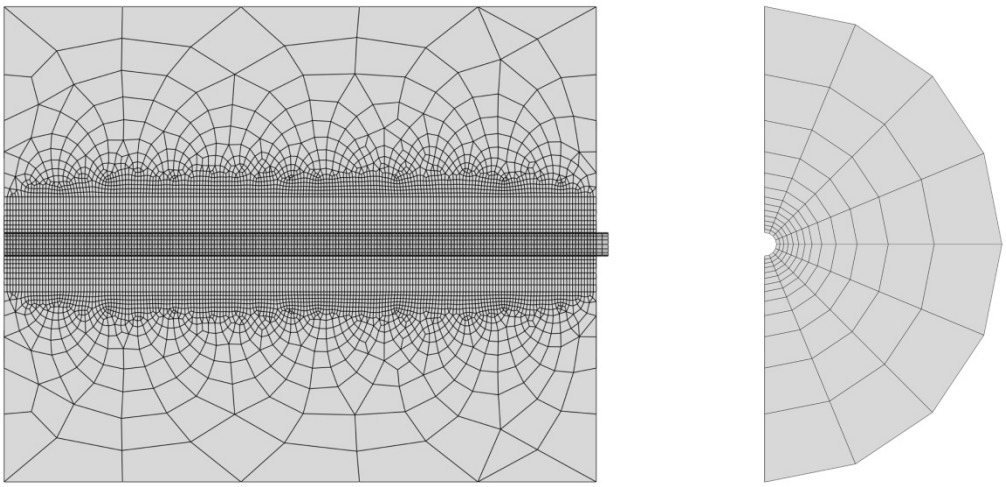

(a) (b)

Figure 8.22 3-D Straight CNT pull-out analysis model. (a) Side view and (b) front view

All resultant outputs are normalized for the easiness of the comparison, and the normalization factor for the pull-out displacement is the embedded length of the CNT, and the for pull-out force it is the ultimate pull-out force of the straight CNT. Figure 8.23 show the sliding behavior of the curved CNT embedded in the matrix is compared with that of the straight CNT.

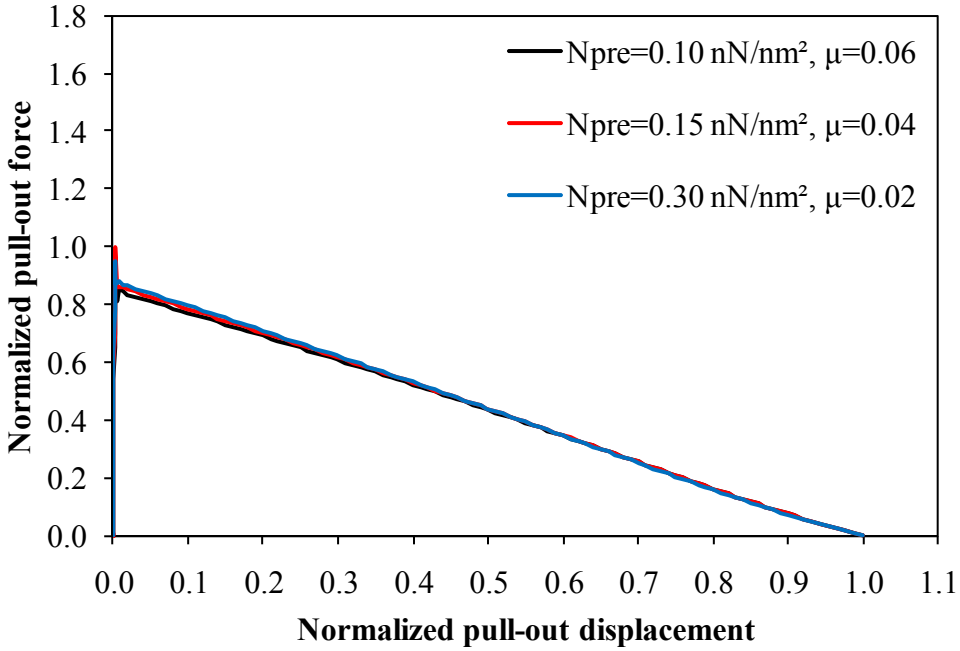

(a)

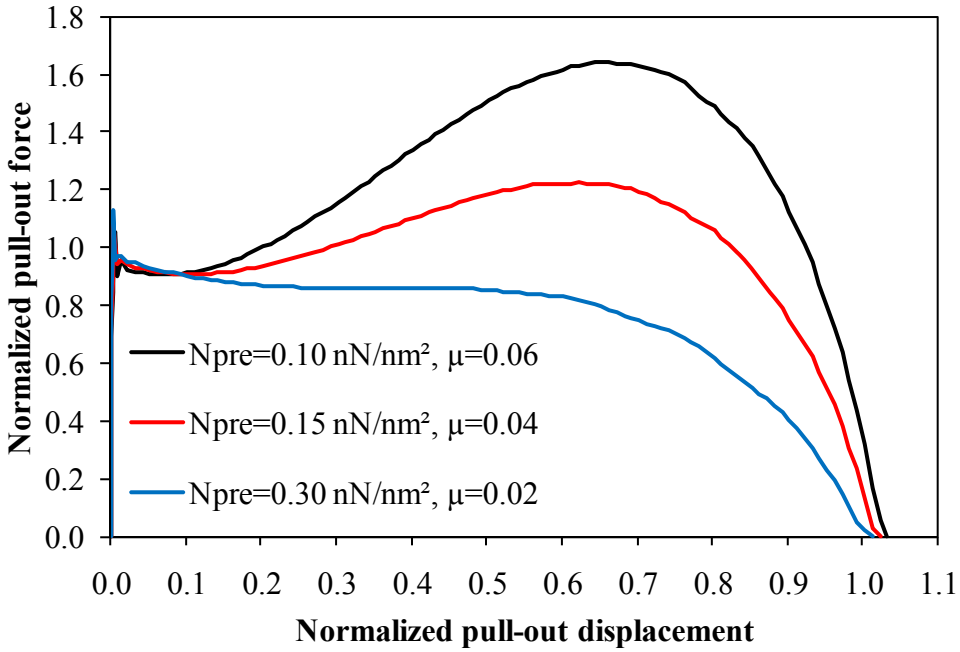

(b)

Figure 8.23 The effect of the combination of the friction force. (a) Straight CNT and (b) curved CNT

Since there is no additional normal force during the straight CNT pull-out process, the variation of the preexisting normal force and the frictional coefficient, if the magnitude of the friction force that is the multiplication of the frictional coefficient and the normal force, has merely effect on the sliding behavior of the straight CNT. On the other hand, the sliding behavior and the ultimate pull-out force of the curved CNT are significantly affected by the combination of the preexisting normal force and the frictional coefficient even though the friction force acting on the interface is a constant. That is, as the preexisting normal force decreases and the frictional coefficient increases, the pull-out force of the curved CNT after the initial sliding is significantly increased due to the effect of the additional normal force induced by the bending stiffness of the curved CNT as shown in Figure 8.24.

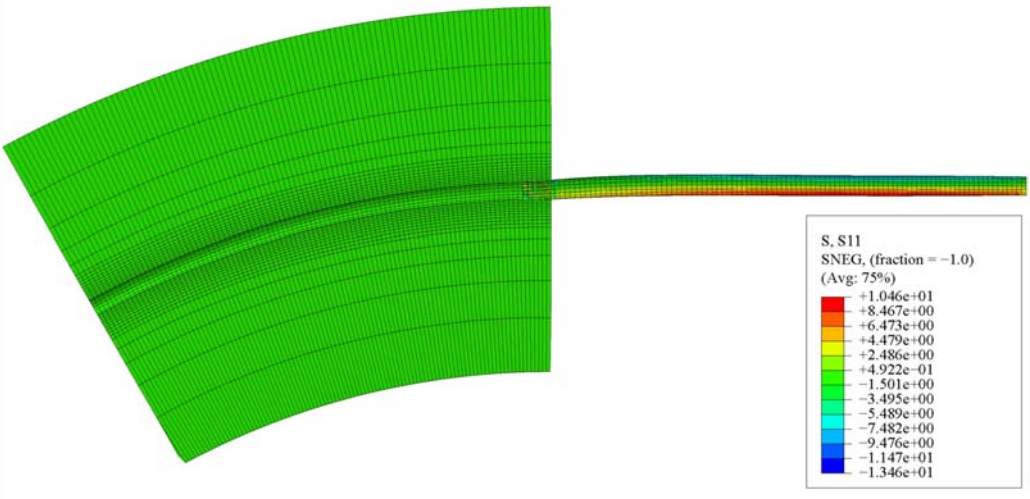

Figure 8.24 The normal stress distribution induced by the bending of the curved CNT

The effect of the frictional coefficient and the preexisting normal force on the pull-out behavior of the curve CNT is investigated separately in Figure 8.25.

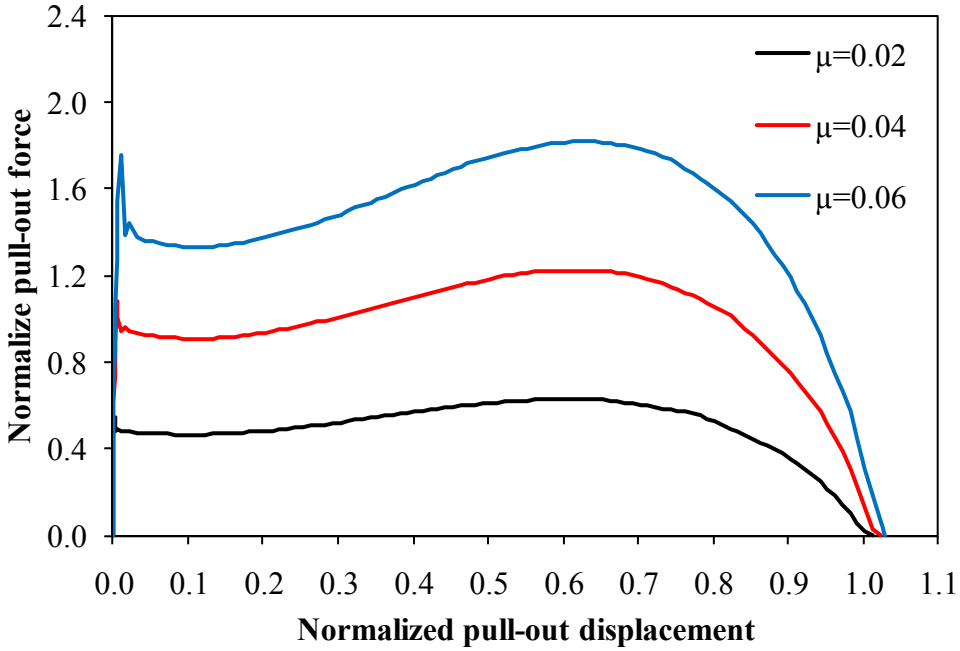

(a)

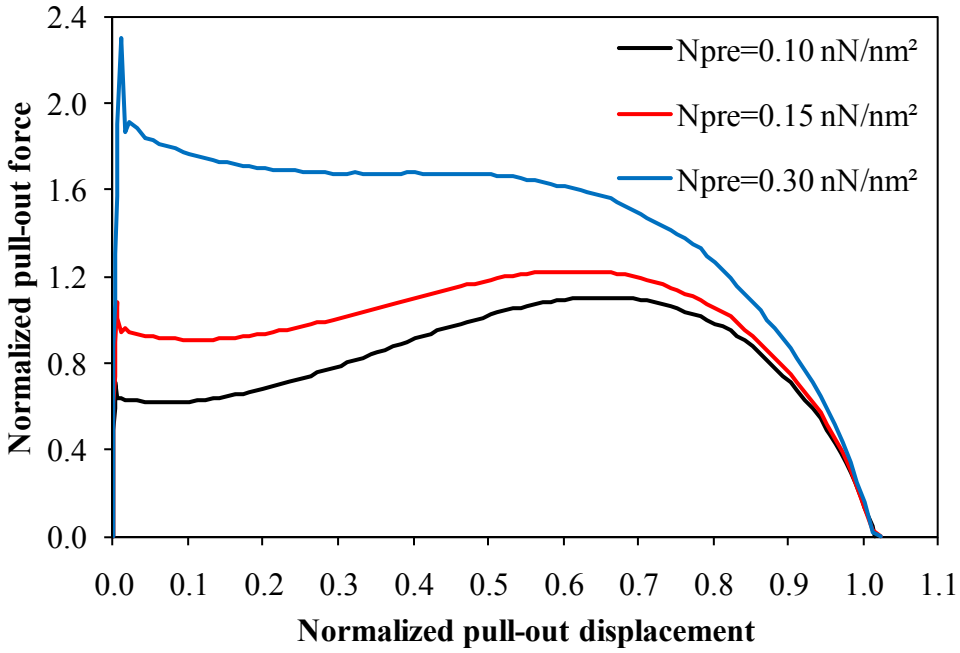

(b)

Figure 8.25 The effect of the frictional coefficient and the preexisting normal force. (a) Frictional coefficient effect ($N_{preexisting}$ =0.15 nN/nm^2) and (b) the preexisting normal force effect (μ=0.4)

As can be seen in Figure 8.25, the variation of the frictional coefficient affects both the initial and the ultimate pull-out force after initial sliding of the curved CNT while the variation of the preexisting normal force changes mainly the initial sliding force. As a result of the analysis, the importance of the additional normal force $N_{additional}$, as explained with Eq. 8.4, is augmented as the preexisting normal force $N_{preexisting}$ decreases. It is noteworthy that the ultimate pull-out force of the curved CNT, according to the contribution of the additional normal force due to the bending stiffness of the curved CNT, can exceed the force that causes initial sliding while the ultimate pull-out force of the straight CNT is always the initial sliding force.

8.2.3 The Effect of the Young's Modulus of the CNT and the Matrix

The effect of varying the Young's modulus of the CNT and the matrix is investigated, and shown in Figure 8.26. As a result, although both the initial sliding and the pull-out force after sliding of the curved CNT is proportional to the variation of the CNT Young's modulus, the effect of varying the Young's modulus of the CNT on the pull-out force after sliding is greater than on the initial sliding force since the additional normal force induced by the bending stiffness of the CNT is linearly proportional to the Young's modulus of the CNT. On the other hand, the variation of the matrix Young's modulus gives totally different results. That is, the increase of the matrix Young's modulus rises the pull-out force after the initial sliding of the curved CNT while lowers the initial sliding force of the curved CNT because the preexisting normal force at the interface between the CNT and the matrix is inversely proportional to the Young's modulus of the matrix.

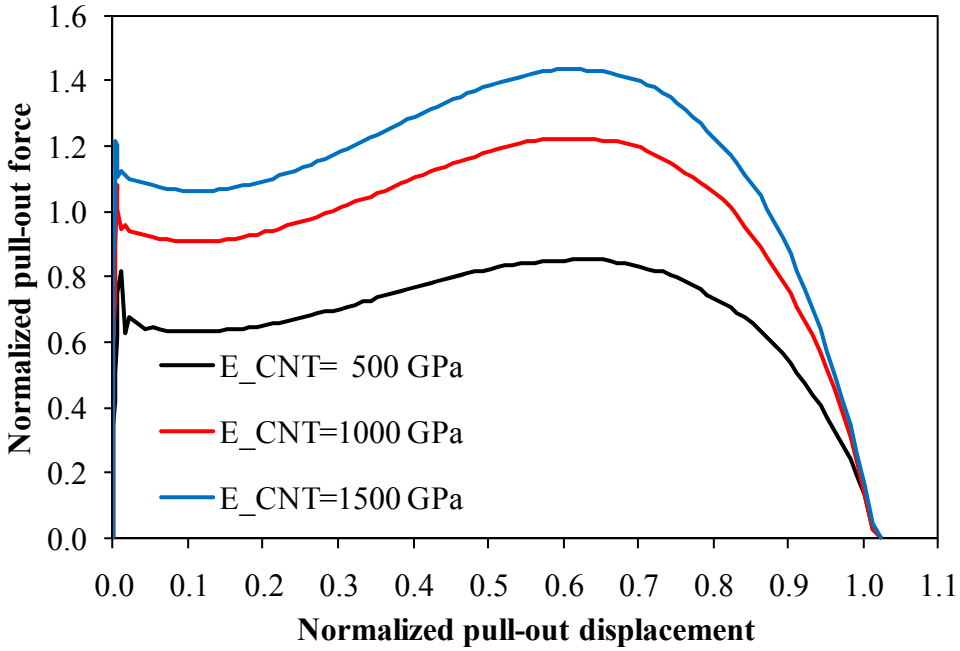

(a)

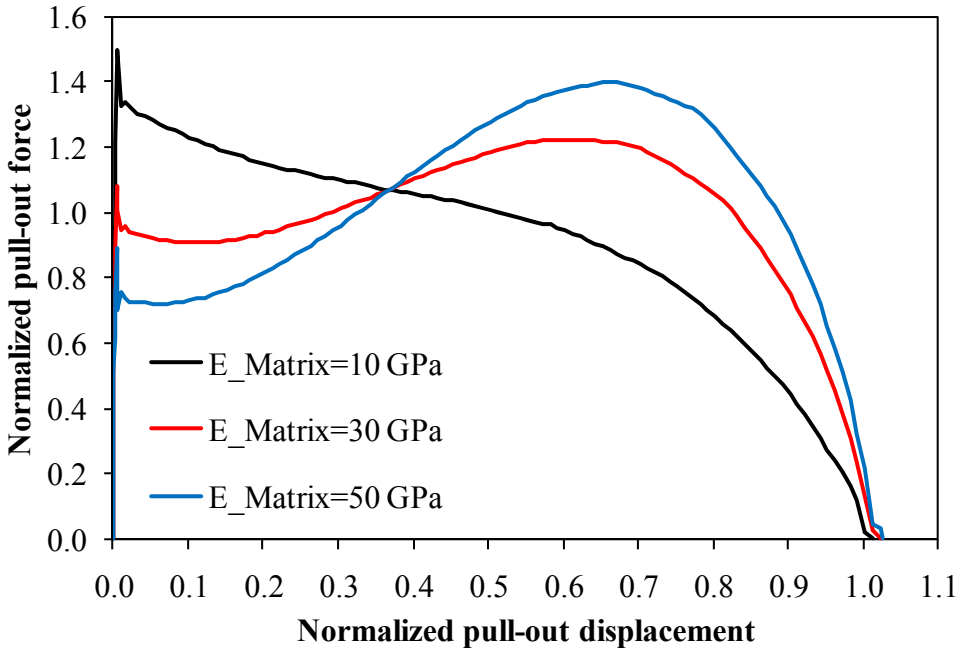

(b)

Figure 8.26 The effect of the Young's modulus. (a) The CNT Young's modulus effect (E_{Matrix} =30 GPa) and (b) the matrix Young's modulus effect (E_{CNT} =1000 GPa)

8.2.4 The Effect of the Curvature of the CNT

As can be seen in Figure 8.24, the exposed part of the initially curved CNT is straightened during pull-out process, and the straightening (or bending) stiffness of the exposed region of the curved CNT has great effect on the pull-out strength of the curved CNT. Moreover, the straightening stiffness of the curved CNT is linearly proportional to the curvature of the CNT. Therefore, the curvature of the CNT is one of the most critical factors control the sliding behavior of the curved CNT, and the effect of the curvature of the CNT is investigated in this section. The radius of curvature of the CNT is varied from 1000 nm to 3500 nm, and the Young's modulus of the CNT and the matrix are 1000 GPa and 30 GPa, respectively. Besides, the frictional coefficient of the interface and the preexisting normal force used in the analysis are 0.06 and 0.1 nN/nm^2, respectively.

Figure 8.27 shows the effect of the radius of curvature of the CNT on the pull-out force of the curved CNT. While the initial sliding force is merely affected by the variation of the radius of curvature of the CNT, the pull-out behavior after the initial sliding is significantly influenced by the curvature of the CNT. When the curvature of the CNT is relatively small (R=3500 nm), the pull-out behavior of the curved CNT resembles the pull-out behavior of the straight CNT, and it means that the additional normal force induced by the bending stiffness of the curved CNT is negligible.

From the curved CNT pull-out analysis, it is noted that when the additional normal force induced by the bending stiffness of the curved CNT is relatively small compared to the preexisting normal force, the pull-out force after the initial sliding does

not exceed the initial sliding force, and the ultimate sliding force of the curved CNT at the sliding stage is governed by the initial sliding force. However, if the contribution of the additional normal force is increased by the variation of the frictional coefficient of the interface, the preexisting normal force, the Young's modulus of the curved CNT, and the curvature of the CNT, then the pull-out force after the initial sliding can exceed the initial sliding force.

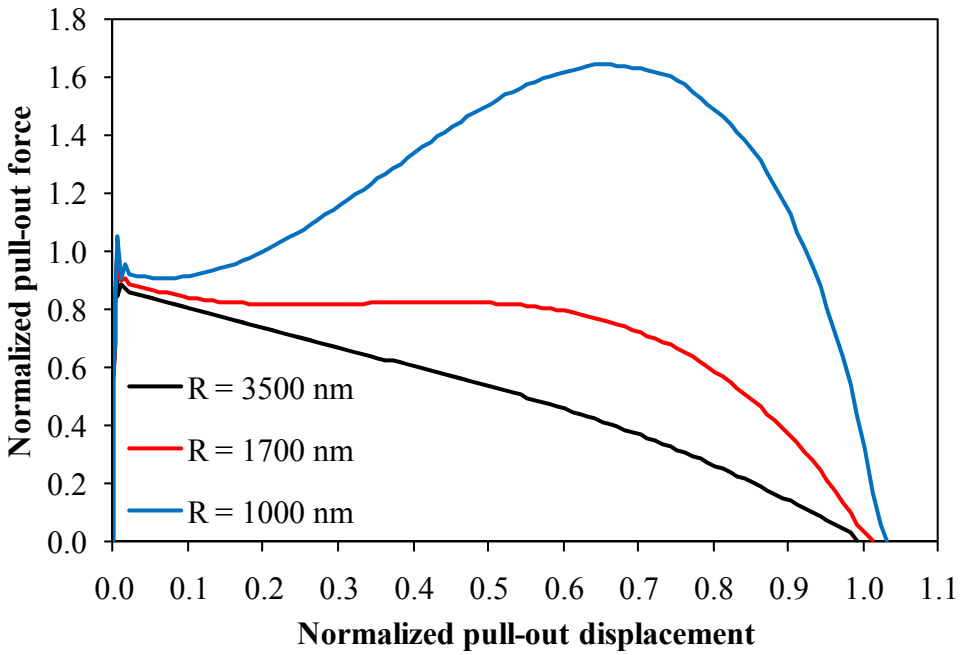

Figure 8.27 The effect of the radius of curvature of the CNT

CHAPTER IX

SUMMARY, CONCLUSIONS, AND FUTURE RECOMMENDATIONS

9.1 Summary

The modified coupled plasticity-damage model for plain concrete on the basis of phenomenological observation that the damaged stiffness varies nonlinearly by the change of the damage density is presented. Two different yield criteria are used in this model: one for plasticity and another for damage, and two different damage evolution laws, the power and exponential damage evolution laws, for both tension and compression are proposed and examined for a more accurate prediction of concrete behavior. The numerical algorithm is coded using the user subroutine UMAT and then implemented in the finite element program Abaqus, and the overall performance of the proposed model is verified by comparing the model predictions to various experimental data in macroscopic level.

Furthermore, the effect of the micromechanical properties of concrete, such as aggregate shape, distribution, and volume fraction, the ITZ thickness, and the strength of the ITZ and mortar matrix on the tensile behavior of concrete is investigated on 2-D and 3-D meso-scale. The tensile damage characteristic of aggregates in concrete is also investigated applying the proposed elasto-plastic damage model to the aggregate in mesoscopic level.

Lastly, the pull-out mechanisms of the single straight CNT embedded in cement matrix and the curved CNT embedded in elastic body are investigated. The CNT is considered as a linear elastic material, and the proposed constitutive model is used to

represent the cement matrix behavior. Moreover, the surface-based cohesive behavior is adopted for the interface model between the single straight CNT and the cement matrix, and the frictional contact is used for the interfacial between the curved CNT and the elastic body.

9.2 Conclusions

The following conclusions are drawn from the work in this dissertation.

(1) In Chapters II, III, IV, and V, it is concluded that the calibration of a plasticity and damage material parameters should be based on loading-unloading or cyclic loading experimental results in order to guarantee the uniqueness of the material constants, and material constants that are identified from simple monotonic loading test cannot be used as reliable values for simulating the damage and failure of concrete structures that are subjected to various loading conditions. It is also shown that the proposed model using the power damage evolution law gives a better prediction than the model using the exponential damage evolution law through the uniaxial loading-unloading tension and compression analyses.

(2) The macro-scale experimental simulations of concrete response, using the newly proposed power damage evolution law, under various loading conditions, such as monotonic uniaxial tension and compression and monotonic biaxial compression, show close agreement with the experimental results. Furthermore, the numerical simulation of the mixed-mode fracture of DEN specimen agrees well with the test

data. This shows that the proposed model with corporation of plasticity and damage provides an effective method for modeling the concrete behavior under various loading conditions such that the model is suitable for three-dimensional structural concrete applications.

(3) From the 2-D meso-scale analysis of the cementitious composites, one can draw a conclusion that the aggregate shape and volume fraction and the strength and thickness of the ITZ are critical parameters that control the global strength of concrete while the aggregate distribution effect is negligible. Moreover, the Young's modulus of concrete is almost linearly proportional to the aggregate volume fraction while the ductility of concrete is inversely proportional, and the ultimate tensile strength of concrete is a minimum at 40% aggregate volume fraction. In case of the 3-D meso-scale analysis, the initial tensile damage at the ITZ doesn't provoke the yielding of the model, but the yielding is occurred as soon as the mortar matrix is damaged. Moreover, the 3-D meso-scale analysis gives a lower ultimate tensile strength but a higher ductility compared to the 2-D meso-scale analysis.

(4) When aggregate is also considered as an elastic damage material in the 2-D meso-scale analysis, the aggregate shape and distribution have a significant effect on the condition of the crack penetration into the aggregate and the yield and ultimate strength of concrete. Moreover, the ratio of the tensile yield strength among the ITZ, mortar matrix, and aggregate is the most important parameter controlling the aggregate damage.

(5) From the pull-out simulations of the single straight and curved CNT embedded in the mortar matrix and elastic body in Chapter VIII, it is concluded that in case of the straight CNT embedded in the cement matrix, the interfacial fracture energy and the Young's modulus of the CNT are key parameters governing the pull-out behavior and the ultimate strength of the straight CNT while the variation of the interfacial shear strength and stiffness only has merely effect on the ultimate CNT pull-out strength and the ductility. In case of the curved CNT embedded in the elastic body, when the additional normal force induced by the bending stiffness of the curved CNT is relatively small compared to the preexisting normal force, the pull-out force after initial sliding does not exceed the initial sliding force, and the ultimate sliding force of the curved CNT in sliding stage is governed by the initial sliding force. However, if the contribution of the additional normal force is increased by the variation of the frictional coefficient of the interface, the preexisting normal force, the Young's modulus of the curved CNT, and the curvature of the CNT, then the pull-out force after initial sliding can exceed the initial sliding force.

9.3 Future Recommendations

Several issues that should be investigated and identified in the near future are considered as an extension of this work:

(1) Updating of the proposed constitutive model to predict the behavior of cementitious materials under triaxial loading condition.

(2) Extension of the proposed model application to the static and dynamic analysis of reinforced concrete structures on macro-scale.

(3) Investigation of the behavior of cementitious composites under compressive loading, bending, and combined loading conditions in meso-scale.

(4) Examination of the relation between the onset of damage at matrix and mechanical properties of the interface between the CNT and cement matrix in nano-scale.

(5) Investigation of the pull-out mechanisms of the curved CNT embedded in cement matrix.

(6) Three-dimensional simulation of the CNTs reinforced cementitious composites under various loading conditions.

REFERENCES

Abu Al-Rub, R.K. and Voyiadjis, G.Z. (2003). "On the coupling of anisotropic damage and plasticity models for ductile materials." *International Journal of Solids and Structures*, 40(11), 2611-2643.

Abu Al-Rub, R.K. and Voyiadjis, G.Z. (2006). "A finite strain plastic-damage model for high velocity impact using combined viscosity and gradient localization limiters: Part I - Theoretical formulation." *International Journal of Damage Mechanics*, 15(4), 293-334.

Achenbach, J.D. and Zhu, H. (1989). "Effect of interfacial zone on mechanical behavior and failure of fiber-reinforced composites." *Journal of the Mechanics and Physics of Solids*, 37(3), 381-393.

Ananiev, S. and Ožbolt, J. (2004). "Plastic-damage model for concrete in principal directions." In V.Li, C.K.Y. Leung, K.J. William, and S.L. Billington (Eds), *Fracture Mechanics of Concrete Structures*, 271-278.

Barenblatt, G.I. (1959). "The formation of equilibrium cracks during brittle fracture. General ideas and hypotheses. Axially-symmetric cracks." *Journal of Applied Mathematics and Mechanics*, 23(3), 622-636.

Bažant, Z. and Oh, B. (1983). "Crack band theory for fracture of concrete." *Materials and Structures*, 16(3), 155-177.

Bazant, Z.P. (1978). "Endochronic inelasticity and incremental plasticity." *International Journal of Solids and Structures*, 14(9), 691-714.

Bazant, Z.P. and Kim, S. (1979). "Plastic-fracturing theory for concrete." *Journal of the Engineering Mechanics Division (ASCE)*, 105(3), 407-428.

Bazant, Z.P., Tabbara, M.R., Kazemi, M.T., and Pijaudier-Cabot, G. (1990). "Random Particle Model for Fracture of Aggregate or Fiber Composites." *Journal of Engineering Mechanics*, 116(8), 1686-1705.

Cervenka, J. and Papanikolaou, V.K. (2008). "Three dimensional combined fracture-plastic material model for concrete." *International Journal of Plasticity*, 24(12), 2192-2220.

Chan, L.Y. and Andrawes, B. (2009). "Characterization of the uncertainties in the constitutive behavior of carbon nanotube/cement composites." *Science and Technology of Advanced Materials*, 10, 1-13.

Chen, A.C.T. and Chen, W.F. (1975). "Constitutive relations for concrete." *Journal of the Engineering Mechanics Division (ASCE)*, 101(4), 465-481.

Chow, C.L. and Wang, J. (1987). "An anisotropic theory of elasticity for continuum damage mechanics." *International Journal of Fracture*, 33(1), 3-16.

Chowdhury, S.C. and Okabe, T. (2007). "Computer simulation of carbon nanotube pull-out from polymer by the molecular dynamics method." *Composites Part A: Applied Science and Manufacturing*, 38(3), 747-754.

Cicekli, U., Voyiadjis, G.Z., and Abu Al-Rub, R.K. (2007). "A plasticity and anisotropic damage model for plain concrete." *International Journal of Plasticity*, 23(10-11), 1874-1900.

Coleman, B.D. and Gurtin, M.E. (1967). "Thermodynamics with internal state variables." *The Journal of Chemical Physics*, 47(2), 597-613.

Cordebois, J.P. and Sidoroff, F. (1979). "Anisotropic damage in elasticity and plasticity." *Journal of Theoretical and Applied Mechanics, Numero Special*, 40-45.

Du, C.-B. and Sun, L.-G. (2007). "Numerical simulation of aggregate shapes of two-dimensional concrete and its application." *Journal of Aerospace Engineering*, 20(3), 172-178.

Dugdale, D.S. (1960). "Yielding of steel sheets containing slits." *Journal of the Mechanics and Physics of Solids*, 8(2), 100-104.

Feenstra, P.H. and De Borst, R. (1996). "A composite plasticity model for concrete." *International Journal of Solids and Structures*, 33(5), 707-730.

Frankland, S.J.V. and Harik, V.M. (2003). "Analysis of carbon nanotube pull-out from a polymer matrix." *Surface Science*, 525(1-3), L103-L108.

Fu, G. and Dekelbab, W. (2003). "3-D random packing of polydisperse particles and concrete aggregate grading." *Powder Technology*, 133(1-3), 147-155.

Gopalaratnam, V.S. and Gettu, R. (1995). "On the characterization of flexural toughness in fiber reinforced concretes." *Cement and Concrete Composites*, 17(3), 239-254.

Gopalaratnam, V.S. and Shah, S.P. (1985). "Softening response of plain concrete in direct tension." *ACI Journal Proceedings*, 82(3), 310-323.

Grassl, P., Lundgren, K., and Gylltoft, K. (2002). "Concrete in compression: A plasticity theory with a novel hardening law." *International Journal of Solids and Structures*, 39(20), 5205-5223.

Grassl, P. and Rempling, R. (2008). "A damage-plasticity interface approach to the meso-scale modelling of concrete subjected to cyclic compressive loading." *Engineering Fracture Mechanics*, 75(16), 4804-4818.

Harik, V.M. (2002). "Mechanics of carbon nanotubes: Applicability of the continuum-beam models." *Computational Materials Science*, 24(3), 328-342.

Jenq, Y.S. and Shah, S.P. (1985). "A fracture toughness criterion for concrete." *Engineering Fracture Mechanics*, 21(5), 1055-1069.

Jia, Z., Wang, Z., Xu, C., Liang, J., Wei, B., Wu, D., and Zhu, S. (1999). "Study on poly(methyl methacrylate)/carbon nanotube composites." *Materials Science and Engineering A*, 271(1-2), 395-400.

Ju, J.W. (1989). " On energy-based coupled elastoplastic damage theories - Constitutive modeling and computational aspects." *International Journal of Solids and Structures*, 25(7), 803-833.

Ju, J.W. (1990). "Isotropic and anisotropic damage variables in continuum damage mechanics." *Journal of Engineering Mechanics*, 116(12), 2764-2770.

Kachanov, L.M. (1958). "On the creep fracture time." *Izv. Akad. Nauk USSR Otd. Tekh.*, 8, 26-31.

Karsan, I.D. and Jirsa, J.O. (1969). "Behavior of concrete under compressive loadings." *Journal of the Engineering Mechanics Division (ASCE)*, 95, 2535-2563.

Kattan, P.I. and Voyiadjis, G.Z. (2001). "Decomposition of damage tensor in continuum damage mechanics." *Journal of Engineering Mechanics*, 127(9), 940-944.

Konsta-Gdoutos, M.S., Metaxa, Z.S., and Shah, S.P. (2010). "Multi-scale mechanical and fracture characteristics and early-age strain capacity of high performance carbon nanotube/cement nanocomposites." *Cement and Concrete Composites*, 32(2), 110-115.

Krajcinovic, D. (1984). "Continuum damage mechanics." *Applied Mechanics Reviews*, 37, 1-6.

Krajcinovic, D. (1985). "Continuous damage mechanics revisited: Basic concepts and definitions." *Journal of Applied Mechanics*, 52(4), 829-834.

Krajcinovic, D. (1996). *Damage Mechanics*, Elsevier Science B.V., North-Holland, Amsterdam.

Kupfer, H., Hilsdorf, H.K., and H., R. (1969). "Behavior of concrete under biaxial stresses." *Journal of the American Concrete Institute*, 66(8), 656-666.

Kwan, A.K.H., Wang, Z.M., and Chan, H.C. (1999). "Mesoscopic study of concrete II: Nonlinear finite element analysis." *Computers & Structures*, 70(5), 545-556.

Lee, J. and Fenves, G.L. (1998). "Plastic-damage model for cyclic loading of concrete structures." *Journal of Engineering Mechanics*, 124(8), 892-900.

Lee, J. and Fenves, G.L. (2001). "A return-mapping algorithm for plastic-damage models: 3-D and plane stress formulation." *International Journal for Numerical Methods in Engineering*, 50(2), 487-506.

Lemaitre, J. (1985). "Continuous damage mechanics model for ductile fracture." *Journal of Engineering Materials and Technology*, 107(1), 83-89.

Lemaitre, J. and Chaboche, J.-L. (1990). *Mechanics of Solid Materials.* Cambridge University Press, New York.

Li, C. and Chou, T.-W. (2003). "A structural mechanics approach for the analysis of carbon nanotubes." *International Journal of Solids and Structures*, 40(10), 2487-2499.

Li, G.Y., Wang, P.M., and Zhao, X. (2005). "Mechanical behavior and microstructure of cement composites incorporating surface-treated multi-walled carbon nanotubes." *Carbon*, 43(6), 1239-1245.

Li, G.Y., Wang, P.M., and Zhao, X. (2007). "Pressure-sensitive properties and microstructure of carbon nanotube reinforced cement composites." *Cement and Concrete Composites*, 29(5), 377-382.

Lilliu, G. and van Mier, J.G.M. (2007). "On the relative use of micro-mechanical lattice analysis of 3-phase particle composites." *Engineering Fracture Mechanics*, 74(7), 1174-1189.

Liu, Y.J. and Chen, X.L. (2003). "Continuum models of carbon nanotube-based composites using the boundary element method." *Electronic Journal of Boundary Elements*, 1(2), 316-335.

Liu, Y.J. and Xu, N. (2000). "Modeling of interface cracks in fiber-reinforced composites with the presence of interphases using the boundary element method." *Mechanics of Materials*, 32(12), 769-783.

Liu, Y.J., Xu, N., and Luo, J.F. (2000). "Modeling of interphases in fiber-reinforced composites under transverse loading using the boundary element method." *Journal of Applied Mechanics*, 67(1), 41-49.

Løland, K.E. (1980). "Continuous damage model for load-response estimation of concrete." *Cement and Concrete Research*, 10(3), 395-402.

Lubliner, J., Oliver, J., Oller, S., and Oñate, E. (1989). "A plastic-damage model for concrete." *International Journal of Solids and Structures*, 25(3), 299-326.

Makar, J.M. and Beaudoin, J.J. (2003). "Carbon nanotubes and their application in the construction industry." *Proceedings of the 1st International Symposium on Nanotechnology in Construction*, Paisley, Scotland, 331-341.

Makar, J.M., Margeson, J., and Luh, J. (2005). "Carbon nanotubes/cement composites – Early results and potential applications." *3rd International Conference on Construction Materials: Performance, Innovations, and Structural Implications,* Vancouver, B.C., 1-10.

Mazars, J. and Pijaudier-Cabot, G. (1989). "Continuum damage theory---Application to concrete." *Journal of Engineering Mechanics*, 115(2), 345-365.

Mohamed, A.R. and Hansen, W. (1999). "Micromechanical modeling of crack-aggregate interaction in concrete materials." *Cement and Concrete Composites*, 21(5-6), 349-359.

Mondal, P., Shah, S.P., and Marks, L.D. (2008). "Nano-scale characterization of cementitious materials." *ACI Materials Journal*, 105(2), 174-179.

Mondal, P., Shah, S.P., and Marks, L.D. (2009). "Nanomechanical properties of interfacial transition zone in Concrete," *Nanotechnology in Construction 3*, Springer Berlin Heidelberg, 315-320.

Murakami, S. and Ohno, N. (1981). "A continuum theory of creep and creep damage. Creep in Structures," *3rd IUTAM Symposium on Creep in Structures,* Berlin, Springer, 422-444.

Mylvaganam, K. and Zhang, L.C. (2004). "Important issues in a molecular dynamics simulation for characterising the mechanical properties of carbon nanotubes." *Carbon*, 42(10), 2025-2032.

Nataraja, M.C., Dhang, N., and Gupta, A.P. (1999). "Stress-strain curves for steel-fiber reinforced concrete under compression." *Cement and Concrete Composites*, 21(5-6), 383-390.

Odegard, G.M., Gates, T.S., Nicholson, L.M., and Wise K.E. (2002). "Equivalent-continuum modeling of nano-structured materials." *Composite Science and Technology,* 62(14), 1869-1880.

Odegard, G.M., Gates, T.S., Wise, K.E., Park, C., and Siochi, E.J. (2003). "Constitutive modeling of nanotube-reinforced polymer composites." *Composites Science and Technology*, 63(11), 1671-1687.

Ortiz, M. (1985). "A constitutive theory for the inelastic behavior of concrete." *Mechanics of Materials*, 4(1), 67-93.

Ortiz, M. and Popov, E.P. (1982). "Plain concrete as a composite material." *Mechanics of Materials*, 1(2), 139-150.

Planas, J. and Elices, M. (1991). "Nonlinear fracture of cohesive materials." *International Journal of Fracture*, 51(2), 139-157.

Poon, C.S., Shui, Z.H., and Lam, L. (2004). "Effect of microstructure of ITZ on compressive strength of concrete prepared with recycled aggregates." *Construction and Building Materials*, 18(6), 461-468.

Rabotnov, Y.N. (1968). "Creep rupture." *In Proceedings of the XII International Congress on Applied Mechanics,* Stanford-Springer, 342-349.

Rosselló, C. and Elices, M. (2004). "Fracture of model concrete: 1. Types of fracture and crack path." *Cement and Concrete Research*, 34(8), 1441-1450.

Schlangen, E. and Garboczi, E.J. (1997). "Fracture simulations of concrete using lattice models: Computational aspects." *Engineering Fracture Mechanics*, 57(2-3), 319-332.

Scrivener, K.L., Crumbie, A.K., and Laugesen, P. (2004). "The interfacial transition zone (ITZ) between cement paste and aggregate in concrete." *Interface Science*, 12(4), 411-421.

Shah, S.P., Konsta-Gdoutos, M.S., Metaxa, Z.S., and Mondal, P. (2009). "Nanoscale Modification of Cementitious Materials." *Proceedings of the Third International Symposium on Nanotechnology in Construction,* 125-130.

Simo, J.C. and Honein, T. (1990). "Variational formulation, discrete conservation laws, and path domain independent integrals for elasto-viscoplasticity." *Journal of Applied Mechanics, Transactions of ASME*, 57, 488-497.

Simo, J.C. and Hughes, T.J.R. (1998). *Computational inelasticity: Interdisciplinary applied mathematics*., Springer, New York.

Simo, J.C. and Ju, J.W. (1987a). "Strain- and stress-based continuum damage models--I. Formulation." *International Journal of Solids and Structures*, 23(7), 821-840.

Simo, J.C. and Ju, J.W. (1987b). "Strain- and stress-based continuum damage models--II. Computational aspects." *International Journal of Solids and Structures*, 23(7), 841-869.

Sinha, B.P., Gerstle, K.H., and Tulin, L.G. (1964). "Stress-strain relations for concrete under cyclic loading." *ACI Journal Proceedings*, 61, 195-212.

Sohlberg, K., Sumpter, B.G., Tuzun, R.E., and Noid, D.W. (1998). "Continuum methods of mechanics as a simplified approach to structural engineering of nanostructures." *Nanotechnology*, 9(1), 30-36.

Taylor, R.L. (1992). FEAP: A finite element analysis program for engineering workstation, Department of Civil and Environmental Engineering, University of California, Berkeley, CA.

Thostenson, E.T., Ren, Z., and Chou, T.-W. (2001). "Advances in the science and technology of carbon nanotubes and their composites: A review." *Composites Science and Technology*, 61(13), 1899-1912.

Tserpes, K.I., Papanikos, P., Labeas, G., and Pantelakis, S.G. (2008). "Multi-scale modeling of tensile behavior of carbon nanotube-reinforced composites." *Theoretical and Applied Fracture Mechanics*, 49(1), 51-60.

van Mier, J.G.M. (1997). *Fracture processes of concrete: Assessment of material parameters for fracture model.* CRC Press, Boca Raton, FL.

Vander Wal, R.L., Miyoshi, K., Street, K.W., Tomasek, A.J., Peng, H., Liu, Y., Margrave, J.L., and Khabashesku, V.N. (2005). "Friction properties of surface-fluorinated carbon nanotubes." *Wear*, 259(1-6), 738-743.

Voyiadjis, G.Z. and Abu-Lebdeh, T.M. (1994). "Plasticity model for concrete using the bounding surface concept." *International Journal of Plasticity*, 10(1), 1-21.

Voyiadjis, G.Z. and Kattan, P.I. (2006). *Advances in damage mechanics: Metals and metal matrix composites with an introduction to fabric tensors,* Elsevier, Oxford.

Voyiadjis, G.Z. and Park, T. (1997). "Anisotropic damage effect tensors for the symmetrization of the effective stress tensor." *Journal of Applied Mechanics*, 64(1), 106-110.

Voyiadjis, G.Z., Taqieddin, Z.N., and Kattan, P.I. (2008). "Anisotropic damage-plasticity model for concrete." *International Journal of Plasticity*, 24(10), 1946-1965.

Wang, Z.M., Kwan, A.K.H., and Chan, H.C. (1999). "Mesoscopic study of concrete I: generation of random aggregate structure and finite element mesh." *Computers & Structures*, 70(5), 533-544.

Wittmann, F.H., Roelfstra, P.E., and Sadouki, H. (1985). "Simulation and analysis of composite structures." *Materials Science and Engineering*, 68(2), 239-248.

Wu, J.Y., Li, J., and Faria, R. (2006). "An energy release rate-based plastic-damage model for concrete." *International Journal of Solids and Structures*, 43(3-4), 583-612.

Wu, K.-R., Liu, J.-Y., Zhang, D., and Yan, A. (1999). "Rupture probability of coarse aggregate on fracture surface of concrete." *Cement and Concrete Research*, 29(12), 1983-1987.

Yao, Z., Zhu, C.-C., Cheng, M., and Liu, J. (2001). "Mechanical properties of carbon nanotube by molecular dynamics simulation." *Computational Materials Science*, 22(3-4), 180-184.

Yazdanbakhsh, A., Grasley, Z., Tyson, B., and Abu Al-Rub, R.K. (2009). "Carbon nanofibers and nanotubes in cementitious materials: Some issues on dispersion and interfacial bond." *ACI Special Publication*, V. SP 254.

Zhang, D.H., Xing, J.B., and Zhu, F.S. (2004). "Study of failure process in concrete samples by using numerical simulation." *Journal of Northeastern University*, 25(2), 175-178.

Zhang, P., Huang, Y., Geubelle, P.H., Klein, P.A., and Hwang, K.C. "The elastic modulus of single-wall carbon nanotubes: A continuum analysis incorporating interatomic potentials." *International Journal of Solids and Structures*, 39(13-14), 3893-3906.

Zhang, Q.Y. (2001). Research on the stochastic damage constitutive of concrete material. Shanghai, China, Tongji University. Ph.D.

Zollo, R.F. (1997). "Fiber-reinforced concrete: An overview after 30 years of development." *Cement and Concrete Composites*, 19(2), 107-122.

VITA

Sun-Myung Kim received his bachelor's degree in the Department of Architectural Engineering from Sejong University, Republic of Korea in 2001, and obtained a master's degree in the Department of Architectural Engineering with emphasis in structural engineering from the same university in 2003. After graduation, he joined the Korea Institute of Construction Technology (KICT) and worked as a researcher. In 2006, he began his doctoral studies at Texas A&M University (TAMU) in the United States under the supervision of Professor Rashid K. Abu Al-Rub, and received his Doctor of Philosophy degree in May 2010. His research interests are computational mechanics, damage mechanics, multi-scale computation analysis, carbon nano-tube or nano-fiber reinforced composite material, and structural optimization.

Permanent Address:

3136 TAMU

College Station, TX 77843-3136

USA

archiksm@hotmail.com